

**Dynamics of intraseasonal variability in the  
north Indian Ocean waveguide**

A Thesis submitted to Goa University  
for the award of the Degree of

**DOCTOR OF PHILOSOPHY**

in

**MARINE SCIENCES**

By

**I. Suresh**

Research Guide

**P.M. Muraleedharan**

**Goa University  
Taleigao, Goa  
2018**

**Dynamics of intraseasonal variability in the  
north Indian Ocean waveguide**

A Thesis submitted to Goa University for the award of the Degree of

**DOCTOR OF PHILOSOPHY**

**in**

**MARINE SCIENCES**

**By**

**I. Suresh**

**Goa University  
Taleigao, Goa  
2018**

*To my beloved mama*

# Statement

As required under the University ordinance OB-9.9 (v-vi), I state that this thesis entitled **“Dynamics of intraseasonal variability in the north Indian Ocean waveguide”** is my original contribution and it has not been submitted on any previous occasion.

The literature related to the problem investigated has been cited. Due acknowledgements have been made wherever facilities and suggestions have been availed of.

I. SURESH

*CSIR National Institute of Oceanography, Goa*

*17 April 2018*

# Certificate

This is to certify that the thesis entitled “**Dynamics of intraseasonal variability in the north Indian Ocean waveguide**”, submitted by I. Suresh to the Goa University for the degree of Doctor of Philosophy, is based on his original studies carried out under my supervision. The thesis or any part thereof has not been previously submitted for any other degree or diploma in any university or institution.

Dr. P.M. MURALEEDHARAN  
Research Guide  
Retd. Chief Scientist, CSIR-NIO

*CSIR National Institute of Oceanography, Goa*

*17 April 2018*

# Acknowledgements

First and foremost, I express my sincere gratitude to my research guide P.M. Muraleedharan without whom I would never have made it. He has been very kind at the personal level and was always available to me, providing help, throughout my PhD. I express my deepest gratitude to Jérôme Vialard, who has been actively involved in this PhD work since its inception, for his guidance and for being with me all through my journey, especially during the toughest times in my career. His immense knowledge, continuous inspiration, and extraordinary patience paved the way for completing this work. The presence of Matthieu Lengaigne at CSIR-NIO (CSIR-National Institute of Oceanography) made every moment of my work enjoyable. Apart from the intriguing discussions on my work, especially in the interannual variability part, his versatility in handling a variety of new challenges has been a great source of motivation for me. I am grateful to Takeshi Izumo for tirelessly spending hours together in the discussions that provided deep insights.

*Well begun is half done.* I am extremely indebted to Fabien Durand, who was concerned about my PhD more than me, for his effort in bringing things together to make a strong beginning of this PhD. This work would not have been possible without the modelling tool of Julian P. McCreary. I am highly indebted to him for his linear ocean model and for his meticulous comments on my work, including the ones that led to a rapid publication at the initial stage of my PhD. Weiqing Han's critical comments significantly improved my manuscripts.

I sincerely acknowledge the support received from the Director, CSIR-NIO and Vice Chancellor (VC), Goa University (GU) in terms of research facilities and infrastructure. I owe special thanks to my Faculty Research Committee members for their comments, encouragement, and technical support in my PhD. I sincerely thank M.R. Ramesh Kumar for agreeing to be my co-guide. I owe my profound gratitude to my VC's nominee T. Pankajakshan for his feedback on my work, his encouragement, and all his support, even personally. I also gratefully acknowledge the help received at various stages from the administrative and technical staffs of CSIR-NIO and GU, particularly, V. Gopakumar and his staff, who carried out the plagiarism check on my

synopsis and thesis. There are many people whose good wishes remained with me throughout my PhD journey - more importantly, R. Shankar, S.W.A. Naqvi, Debasis Sengupta, Raghu Murtugudde, H.L.S. Rao, M. Ravichandran, and S.S.C. Shenoi.

This PhD work was carried out under a Grand-in-aid project sponsored by INCOIS/MoES, Hyderabad under HOOFS program. I acknowledge CSIR, New Delhi for financial support and Institut de Recherche pour le Développement (IRD) for supporting my visits to LOCEAN, Paris.

I express my heartfelt thanks to V. Parvathi for trusting me to mentor her PhD work, and for helping me in my work, especially with the figures and in proofreading this thesis. Sadhvi has been patiently waiting to begin her PhD with me. I wish to place my special thanks to her for her assistance in proofreading some parts of this thesis. I also thank my friends and well-wishers, including Sridhara, Mallik, Rajasekhar and Kavitha, and all my teachers from my schooldays, especially Vasantha miss and Prema miss.

My thesis took away almost all my personal time for years together, subsequently resulting in many personal sacrifices. My heartfelt regards to my brother and his family; they have been taking care of my parents. My Chitti has been waiting for long for my visit. I won't be able to express my love and gratitude to my parents, who have always dreamt of my academic and professional excellence, and have been providing great moral support. My beloved little son Siddhant has been longing to visit the Goan beaches, the Central library, and to play cricket with me. My wife Neetu, who is also my colleague, has been waiting so long for the completion of my thesis and has been coping up with my extremely irregular schedule. Without her cooperation, goodwill, and also her help in the workplace, this thesis would not have materialized. Finally, my beloved Sulaiman mama: forever shall I remain indebted to him for his love and care for me since my childhood, and for nurturing me with all his noble thoughts. I dedicate this thesis to him.

(I. SURESH)

*CSIR National Institute of Oceanography, Goa*

## **Publications from the thesis**

- Suresh I., J. Vialard, M. Lengaigne, W. Han, J. McCreary, F. Durand, and P. M. Muraleedharan (2013), Origins of wind-driven intraseasonal sea level variations in the North Indian Ocean coastal waveguide. *Geophys. Res. Lett.*, 40 (21), 5740–5744, doi:10.1002/2013GL058312.
- Suresh, I., J. Vialard, T. Izumo, M. Lengaigne, W. Han, J. McCreary, and P. M. Muraleedharan (2016), Dominant role of winds near Sri Lanka in driving seasonal sea level variations along the west coast of India. *Geophys. Res. Lett.*, 43 (13), doi:10.1002/2016GL069976.

# Contents

<b>Statement</b> .....	<b>i</b>
<b>Certificate</b> .....	<b>ii</b>
<b>Acknowledgements</b> .....	<b>iii</b>
<b>Publications from thesis</b> .....	<b>v</b>
<b>Acronyms</b> .....	<b>vii</b>
<b>List of Figures</b> .....	<b>x</b>
<b>List of Tables</b> .....	<b>xiv</b>
<b>Chapter 1 General Introduction</b> .....	<b>1</b>
<b>Chapter 2 Background</b> .....	<b>5</b>
<b>2.1 Basic concepts from the linear ocean-wave theory</b> .....	<b>5</b>
<b>2.2 Northern Indian Ocean seasonal variability</b> .....	<b>12</b>
<b>2.3 Northern Indian Ocean interannual variability</b> .....	<b>17</b>
<b>2.4 Northern Indian Ocean intraseasonal variability</b> .....	<b>22</b>
<b>Chapter 3 Data and Methods</b> .....	<b>30</b>
<b>3.1 Introduction</b> .....	<b>30</b>
<b>3.2 Description of observations</b> .....	<b>30</b>
<b>3.3 The ocean model</b> .....	<b>32</b>
<b>3.4 Statistical methods</b> .....	<b>41</b>
<b>Chapter 4 Origin of intraseasonal sea level variability in the Northern Indian Ocean coastal waveguide</b> .....	<b>42</b>
<b>4.1 Introduction</b> .....	<b>42</b>
<b>4.2 Model setup and sensitivity experiments</b> .....	<b>43</b>
4.2.1 Model setup .....	43
4.2.2 Contributions from baroclinic modes .....	43
4.2.3 Sensitivity experiments .....	45
<b>4.3 Results</b> .....	<b>46</b>
4.3.1 Model validation .....	46
4.3.2 Importance of remote forcing .....	48
4.3.3 Seasonality in the forcing contributions .....	51
<b>4.4 Discussion</b> .....	<b>53</b>
<b>Chapter 5 Dynamics of wind-driven intraseasonal sea level variability in the NIO coastal waveguide</b> .....	<b>56</b>
<b>5.1 Introduction</b> .....	<b>56</b>
<b>5.2 The new connection</b> .....	<b>58</b>

5.2.1	Meridional modes of equatorial waves .....	58
5.2.2	Demonstration of EQD connection.....	59
<b>5.3</b>	<b>Intraseasonal wind forcing .....</b>	<b>65</b>
<b>5.4</b>	<b>The processes .....</b>	<b>66</b>
<b>5.5</b>	<b>Model setup and sensitivity experiments .....</b>	<b>69</b>
5.5.1	Model setup.....	69
5.5.2	Sensitivity experiments.....	71
<b>5.6</b>	<b>Results .....</b>	<b>78</b>
5.6.1	Model validation .....	78
5.6.2	Dynamics of sea level ISV.....	82
5.6.3	Process contributions to the sea level ISV in the NIO coastal waveguide .....	87
5.6.4	Seasonality in the process contributions.....	90
<b>5.7</b>	<b>Summary.....</b>	<b>92</b>
<b>Chapter 6</b>	<b>Comparison of sea level dynamics between intraseasonal, seasonal, and interannual timescales .....</b>	<b>93</b>
<b>6.1</b>	<b>Dynamics of seasonal sea level.....</b>	<b>93</b>
6.1.1	Introduction.....	93
6.1.2	Model and the sensitivity experiments .....	96
6.1.3	Overview of basin-scale sea level and wind forcing patterns.....	97
6.1.4	Processes contributing to BoB sea level seasonal cycle .....	104
6.1.5	Processes contributing to AS sea level seasonal cycle .....	106
6.1.6	Robustness of the model results .....	108
6.1.7	Summary .....	109
<b>6.2</b>	<b>Dynamics of interannual sea level .....</b>	<b>111</b>
6.2.1	Introduction.....	111
6.2.2	Model and the sensitivity experiments .....	114
6.2.3	IOD influence on the NIO sea level IAV.....	118
6.2.4	Processes contributing to the NIO interannual sea level .....	124
6.2.5	Summary .....	127
<b>6.3</b>	<b>Comparison of sea level dynamics between timescales .....</b>	<b>129</b>
<b>Chapter 7</b>	<b>Summary and Perspectives .....</b>	<b>134</b>
<b>7.1</b>	<b>Thesis summary .....</b>	<b>134</b>
<b>7.2</b>	<b>Implications and perspectives of this study.....</b>	<b>137</b>
7.2.1	Implications .....	137
7.2.2	Perspectives .....	140

# Acronyms

The abbreviations of model sensitivity experiments pertaining to each chapter are provided in the tables in the respective chapters (i.e. Tables 4.1, 5.1, and 6.1) and the abbreviations of the processes are listed in Table 5.2.

AM	April - May
AS	Arabian Sea
AVISO	Archiving, Validation, and Interpretation of Satellite Oceanographic
BoB or Bay	Bay of Bengal
CTL	Control
DJFM	December to the following March
DMI	Dipole Mode Index
ECI	East coast of India
EICC	East India Coastal Current
ENSO	El Niño - Southern Oscillation
EOF	Empirical Orthogonal Function
EOF $n$	$n$ th Empirical Orthogonal Function
ECMWF	European Centre for Medium-Range Weather Forecasts
ERA-I	ECMWF reanalysis – Interim
ETOPO2	2-minute gridded global relief data
IAV	Interannual Variability
IO	Indian Ocean
IOD	Indian Ocean Dipole
ISV	Intraseasonal Variability
JJAS	June to September
LCS	Linear, continuously stratified
LH/LL	Lakshadweep High/Lakshadweep Low
KW	Kelvin Wave
MEI	Multivariate ENSO Index
MJO	Madden Julian Oscillation
NDJ	November to the following January
NIO	North Indian Ocean
ON	October - November

PC	Principal Component
PC $n$	$n$ th Principal Component
QuikSCAT	Quik Scatterometer
RAMA	Research Moored Array for African-Asian-Australian Monsoon Analysis
RMS	Root Mean Square
RW	Rossby Wave
SBC	Special Boundary Condition
SIO	Southern Indian Ocean
SLA	Sea Level Anomaly
SON	September to November
SSH	Sea Surface Height
SST	Sea Surface Temperature
WCI	West Coast of India
WICC	West India Coastal Current
WOA09	World Ocean Atlas-2009

## List of Figures

No.	Figure Captions	Page No.
2.1	Sea level and zonal current meridional structures of the Kelvin and first Rossby modes	7
2.2	Dispersion diagram for equatorial waves	8
2.3	Dispersion diagram for mid-latitude Rossby waves	10
2.4	Estimates of phase speeds of westward propagating sea level anomalies from TOPEX/POSEIDON altimeter data as a function of latitude.	11
2.5	Seasonal climatology of wind stress and schematic representation of seasonal currents in the NIO for summer and winter	13
2.6	The leaky NIO waveguide	14
2.7	Standard deviation of observed seasonal sea level	16
2.8	Monthly vertical profiles of oxygen and temperature at west coast of India box	17
2.9	Lead-lag correlations of SST anomalies averaged over the eastern equatorial Pacific, the tropical IO, the southwest IO, and the eastern equatorial IO to the November to January average Niño3 index	18
2.10	Schematic illustration of an IOD during its positive and negative phases	20
2.11	Spatial patterns of seasonal anomalies of SST, outgoing longwave radiation, zonal winds, and sea level at the peak of the 1997 IOD event	20
2.12	Time series of the fall interannual thermocline and oxycline depth anomalies off Goa on the WCI	22
2.13	MJO composites of outgoing longwave radiation and 850-hPa wind anomalies during December – February	23
2.14	Composites of outgoing longwave radiation and 850-hPa winds during active and break monsoon days in summer over 1979-1990 period	24
2.15	Standard deviation of intraseasonal SST during summer and winter	25
2.16	Lag-regression of equatorial SSH onto normalized wind index at 70-110 days for AVISO SSH and directly forced model SSH	26
2.17	Spatial patterns of 55 to 110-day band-passed sea level and wind stresses associated with the 55 to 110-day band-passed sea level within the box on the WCI	28
3.1	The WOA09 basin-averaged climatological vertical temperature, salinity, and density profiles and the vertical profile of the Brunt–Väisälä frequency	33
3.2	The characteristic Kelvin wave speeds as a function of mode numbers	34
3.3	The body-force profile used in the LCS model	35
3.4	The model domain	37
4.1	Mode contributions	44

4.2	Set up of the LCS sensitivity experiments	45
4.3	Spatial patterns of intraseasonal wind stress and sea level obtained by lag-regression onto normalized PC of EOF1 of intraseasonal sea level from observations, CTL and EQ experiments	47
4.4	Comparison of PC1s of observed and model intraseasonal sea level	48
4.5	Contribution of equatorial, Bay of Bengal and Arabian Sea wind forcing to the intraseasonal (20-150 day) sea level variations	49
4.6	Seasonality in the ISV forcing and its contributions to the sea level ISV along the east and west coasts of India	52
4.7	Same as Figure 4.5, but for the 30-70 and 70-110-day bands	54
5.1	Sea level meridional structures for equatorial Kelvin and the first, second, and the third meridional mode Rossby waves	59
5.2	Snapshots from the IDLCTL experiment after the initiation of 10 days long westerly wind burst	60
5.3	Snapshots of sea level from IDLCTL, IDLNOSL, IDLST10N, and IDLMEB experiments and the decomposition of total sea level into EQB and EQD processes. Also shown in the sea level (total, EQB and EQD) time series off Goa from each idealized experiment	62
5.4	Maps showing the amplitude of the intraseasonal variability of the wind-stress curl, alongshore wind stress, and the Ekman pumping velocity in NIO	65
5.5	Schematic representation of the processes or the pathways of sea level signals that influence the sea level variability in the NIO, particularly along the coastal waveguide	67
5.6	Mode contributions	70
5.7	Map showing the boxes over which Special Boundary Conditions (SBCs) and dampers are applied for isolating the processes	73
5.8	EOF analysis of the intraseasonal sea level from the CTL run and observations – explained variance of the first five modes, Autocorrelation of PC1 and PC2 and lag-correlation of PC1 and PC2	79
5.9	Spatial patterns of the first two EOF modes from the model and observations, and their explained variance	80
5.10	Comparison of modeled and observed PC1 and PC2	81
5.11	Lag-regression patterns of intraseasonal CTL sea level, wind stresses, wind-stress curl, and alongshore wind stress to the normalized PC of the EOF1 of CTL intraseasonal sea level	83
5.12	Decomposition of the amplitude of intraseasonal sea level from CTL into that from each process	84
5.13	Decomposition of sea level from CTL into that from EQB, EQD, and ST processes	86
5.14	The map showing the distances along the NIO coastal waveguide	87
5.15	Standard deviation of intraseasonal sea level from CTL and its	88

	decomposition into each process and regression coefficient of each process to CTL, both plotted as a function of distance along the NIO coastal waveguide	
5.16	Same as Figure 5.15 but for summer	90
5.17	Same as Figure 5.15 but for winter	91
6.1	Standard deviation of the seasonal Ekman pumping velocity and the alongshore wind stresses	94
6.2	Standard deviation of the seasonal sea level normalized by the square root of the Coriolis parameter, averaged over a 50-km cross-shore extent, plotted as a function of distance along the NIO coastal waveguide from the entrance of BoB waveguide at its eastern rim	95
6.3	Standard deviation of the observed and the modeled seasonal sea levels	96
6.4	Seasonal climatology of CTL sea level, TropFlux wind stresses, curl of the wind-stress field, and alongshore wind forcing during winter, fall inter monsoon, summer, and spring inter monsoon	98
6.5	Decomposition of the amplitude of intraseasonal sea level from CTL into that from each process	99
6.6	Contribution of each process to CTL sea level seasonal cycle	100
6.7	Climatological sea level for winter from CTL and its decomposition into processes	101
6.8	Same as Figure 6.7, but for spring	101
6.9	Same as Figure 6.7, but for summer	102
6.10	Same as Figure 6.7, but for fall	102
6.11	Standard deviation of seasonal sea level from CTL and its decomposition into each process, and the coefficient of regression of seasonal sea level from each process onto CTL solution, both plotted as a function of distance along the NIO coastal waveguide	103
6.12	Standard deviation of interannual anomalies of the wind-stress curl, the alongshore wind stress, the Ekman pumping velocity and the equatorial zonal wind stress	112
6.13	Map of correlation between observed and modeled sea level interannual anomalies	114
6.14	EOF analysis of sea level interannual anomalies, displaying the explained variance of the first five EOFs computed from altimetry and the CTL interannual sea level, respectively Also shown are the modeled and observed first principal component time series	115
6.15	Spatial patterns of the EOF1 and 2 modes, and their explained variance in the sea level IAV from both observations and model	117
6.16	Comparison of CTL PC1 with DMI index. Also shown are the lag-correlations of CTL PC1 and PC2 with SON averaged DMI and NDJ averaged MEI	118
6.17	Patterns of CTL interannual sea level, wind stress, wind-stress curl, and alongshore forcing obtained by lead-lag regression onto the normalized SON DMI index, shown selectively for the	120

	months of August, October, December, and February	
6.18	Monthly time series of the interannual sea level obtained by lead-lag regression onto the SON DMI at coastal locations on the eastern BoB, the ECI, and the WCI for CTL and the processes	122
6.19	Interannual sea level patterns obtained by lead/lag regression to the SON DMI index for October and February: total sea level anomaly from CTL and contributions from the ST, EQD and EQB processes	123
6.20	Contribution of each process: AFBB, ST, AFAS, TrEQ + SIO, EQD, EQB, IBB and IAS to CTL interannual sea level, computed as the regression coefficients of the respective process solution to that of CTL experiment	125
6.21	Standard deviation of CTL interannual sea level and its decomposition into processes, and the regression coefficient of interannual sea level associated with each process to the CTL solution, both plotted as a function of distance along the NIO coastal waveguide	126
6.22	Standard deviation of the sea level at intraseasonal, seasonal, and interannual timescales	129
6.23	Regression coefficient of intraseasonal, seasonal, and interannual sea level from each process to that in CTL as a function of distance along the NIO coastal waveguide	130
6.24	Standard deviation of the zonal wind stress in the equatorial band (2oS-2oN), alongshore forcing and CTL sea level both as a function of distance along the NIO coastal waveguide at intraseasonal, seasonal, and interannual timescales	131
7.1	Spatial map of correlation between the fall interannual anomalies of thermocline and oxycline depths	139
7.2	Multi model mean trend of sea level from the CMIP5 RCP8.5 (Coupled Model Intercomparison Project 5 – Representative Concentration Pathways 8.5) simulations	140
7.3	Map showing the percentage of hypoxic profiles during fall season in a coupled physical-biogeochemical simulation	141
7.4	Schematic of the ocean floor indicating the relevance of the coastal Kelvin wave theory	141

## List of Tables

<b>No.</b>	<b>Table Captions</b>	<b>Page No.</b>
3.1	Summary of the results of LCS model experiments for fixing the model parameters	38
4.1	Summary of the sensitivity experiments pertaining to Chapter 4	46
5.1	Details of LCS model sensitivity experiments pertaining to Chapter 5	72
5.2	The processes and the method for obtaining them using LCS model sensitivity experiments	73
6.1	Contribution from each process to the west coast of India sea level seasonal cycle at 15°N from CTL, EXP500, EXPQSCAT, and EXPRAMP simulations	108

# General Introduction

---

***The seasonal cycle and the North Indian Ocean waveguide:*** The Indian Ocean (hereafter, IO) experiences the strongest monsoon on Earth, owing to the elevated Asian landmass that bounds it to the north. The monsoonal winds are predominantly southwesterlies during boreal summer and northeasterlies during boreal winter. These seasonally reversing monsoon winds drive a strong basin-scale response in the north IO (north of  $10^{\circ}$  S; hereafter, NIO) that has drawn the attention of physical oceanographers for more than two decades. The framework that emerged to help understanding the observed seasonal variability of the sea level and surface currents [e.g., McCreary et al., 1993; Potemra et al., 1991; Yu et al., 1991] revealed the importance of remote forcing (i.e. wind forcing over regions remote from the region of interest). More specifically, the remote equatorial wind forcing has been shown to significantly influence the sea level and surface currents along the NIO coast through equatorial and coastal Kelvin wave (hereafter, KW) propagation [e.g., McCreary et al., 1996; Schott and McCreary, 2001]. The equatorial winds force KWs at the equator. When these eastward-propagating waves reach the eastern boundary (Sumatra coast) of the equatorial basin, a part of their energy is reflected back as equatorial Rossby waves (hereafter, RWs). Some part of their energy also propagates into and around the Bay of Bengal (hereafter, BoB or simply, the Bay) rim, then around Sri Lanka, and further up the west coast of India (hereafter, WCI) [McCreary et al., 1993] as coastal KWs. These seasonal waves are thus responsible for establishing a strong dynamical link between the equatorial and the coastal waveguides, together called the *NIO waveguide*.

***The NIO interannual variability:*** A similar remote forcing by the equatorial winds on the NIO sea level variability has also been discussed [e.g., Han and Webster, 2002] at the interannual (refers to periodicities ranging from a few months to a few years) timescales. At these longer timescales, the NIO sea level and surface currents are significantly influenced by the Indian Ocean Dipole (hereafter, IOD) mode [Saji et al., 1999; Schott et al., 2009], which is an intrinsic mode of IO interannual climate variability associated with strong zonal wind perturbations in the equatorial band during

boreal fall. These wind anomalies can influence the interannual variability (hereafter, IAV) of the sea level and currents in the NIO through equatorial and coastal KW propagation [Clarke and Liu, 1994], as demonstrated by the earlier studies at the seasonal timescale. While most of the previous studies focussed mainly on the BoB [e.g., Aparna et al., 2012 and the references therein], the sea level IAV along the WCI, though weaker compared to that in the BoB, have important consequences for the biogeochemistry in this region. The WCI is home to the world's largest naturally occurring hypoxic system. During boreal summer, the upwelling brings poorly oxygenated subsurface waters from the open ocean Arabian Sea (hereafter, AS) Oxygen Minimum Zone to the continental shelf off the WCI. During some years, these waters turn totally depleted of oxygen, leading to coastal anoxia that have tremendous impacts on the regional ecosystem and fisheries [e.g., Naqvi et al., 2009; Parvathi et al., 2017].

***The NIO intraseasonal variability and the eddies:*** The IO is also home to significant upper ocean variability at timescales ranging from a few days to a few months that are usually referred to as the intraseasonal variability (hereafter ISV). One important source of this variability is meso-scale eddies, which owe their existence to internal instabilities (shear instabilities of the currents systems or baroclinic instabilities). There are energetic eddies both in the BoB and in the AS, as revealed by the altimeter measurements [Chelton et al., 2011], contributing significantly to the ISV of the sea level and currents along the NIO coast [Cheng et al., 2013; Durand et al., 2009]. This thesis will, however, not address the eddy-generated oceanic ISV, but will rather focus on the wind-generated ISV discussed below.

***The NIO response to atmospheric intraseasonal forcing:*** Besides seasonal and interannual forcing, the tropical IO is also subjected to strong atmospheric forcing at intraseasonal timescales. These variations are associated with the dominant sources of ISV over the tropical Indo-Pacific warm-pool, involving a coupling between deep convection and atmospheric equatorial dynamics (see Zhang [2005] for a review), known as the Madden-Julian Oscillation (hereafter, MJO) that dominates during winter, and partly-related active/break cycles (i.e. wet and dry spells) of the Indian monsoon during summer [Goswami, 2005]. These modes provide strong forcing variations to the upper ocean, both in terms of heat flux and wind perturbations. The heat flux perturbations and the resulting variations in SSTs have been addressed well in the

literature (see Jayakumar et al. [2011], Vialard et al. [2012] amongst many others]. This Ph.D. work will therefore focus on the dynamical response to the intraseasonal wind forcing.

***The wind-driven ISV in the NIO waveguide:*** The intraseasonal wind variations induced by MJO and active/break monsoon phases drive a significant sea level and surface currents response. While the dynamical response of the equatorial IO to those intraseasonal wind variations has been relatively well addressed [Masumoto et al., 2005; Sengupta et al., 2007; Iskandar and McPhaden, 2011; Nagura and McPhaden, 2012], studies focusing on the NIO, in general, and on the NIO coastal waveguide, in particular, are scarce. While recent observational studies emphasize the importance of remote forcing [e.g., Shetye et al., 2008; Amol et al., 2012] and propose a basin-scale link between the equatorial and coastal waveguides of the NIO [Vialard et al., 2009], the NIO dynamical response to intraseasonal wind forcing has so far not been characterized in detail. Consequently, many questions about the intraseasonal sea level variability in the NIO are yet to be answered. For example - What are the relative contributions of local and remote wind forcing to the sea level ISV along the coast of India? Are the pathways of those remotely-forced intraseasonal signals from the equator to the NIO similar to those previously described at seasonal and interannual timescales? More generally, how different is the sea level dynamics at intraseasonal timescales compared to that at seasonal and interannual timescales?

***The goal:*** This Ph.D. work aims at exploring the above questions both with observational analysis and through a rigorous modelling approach. The overall goal of this thesis is to understand the dynamics of the wind-driven, intraseasonal variability in the NIO waveguide, mainly focusing on the sea level, and to delineate the differences in the sea level dynamics at intraseasonal timescale from that at seasonal and interannual timescales. In doing so, the thesis will also revisit the sea level dynamics at seasonal and interannual timescales. The thesis is organized as follows.

***Thesis structure:*** *Chapter 2* begins with the basic concepts from the theory of linear ocean waves and provides a review of literature on the NIO dynamics, first at the well-documented seasonal timescale, then at the interannual timescales, and finally at the

intraseasonal timescales, which is the focus of this thesis. The chapter ends with the list of specific questions addressed in this thesis.

*Chapter 3* provides a thorough description of the linear ocean model used in this study, including the details of the governing equations, the method of solution, and the choice of parameters. In addition, this chapter presents a description of the observational datasets used for the analysis as well as for validating the model simulation. The chapter also describes briefly the statistical tool used for analysing the datasets.

*Chapter 4* answers the fundamental question – What is the relative importance of local and remote wind forcing for the intraseasonal sea level variability along the NIO waveguide? This part of the Ph.D. work quantifies the relative contributions from the equatorial, BoB, and AS wind forcing to the sea level ISV in the NIO waveguide using model sensitivity experiments.

*Chapter 5* investigates comprehensively the dynamics of sea level ISV in the NIO, particularly along the coastal waveguide, using model sensitivity experiments. The chapter first demonstrates the existence of a direct connection between the equatorial waveguide and the WCI, in addition to the one involving the coastal KW propagation around the rim of the BoB. The chapter then develops a method of process decomposition that helps evaluating the pathways of the intraseasonal signals and their respective contributions to the sea level ISV in the NIO waveguide.

*Chapter 6* revisits the dynamics of seasonal and interannual sea level variability in the NIO by exploiting the model experiments and the methodology developed in the previous chapter for studying the sea level ISV. This chapter refines the findings from the earlier literature and assesses the importance of the newly established direct connection between the equatorial waveguide and the WCI for the sea level variability at those timescales. Furthermore, this chapter provides deeper insights into the IOD influence on the NIO sea level IAV. Finally, the chapter examines the key differences in sea level variability at intraseasonal, seasonal, and interannual timescales.

*Chapter 7* summarizes the main conclusions of this Ph.D. work, discusses their implications, and outlines the future plan.

## Chapter 2

# Background

---

**Overview:** This chapter provides the necessary background for the thesis. The chapter begins with a brief introduction of the basic concepts from linear ocean-wave theory (in Section 2.1) and subsequently surveys the literature pertaining to this thesis. Studies dealing with the dynamics of sea level and currents in the NIO are reviewed first at the most-studied seasonal timescale (in Section 2.2), then at the interannual timescale (Section 2.3), and finally at the intraseasonal timescale (Section 2.4), which is the focus of this thesis. The chapter ends with a list of unresolved issues concerning NIO sea level ISV.

### 2.1 Basic concepts from the linear ocean-wave theory

**The LCS system and the linear wave solutions:** A variety of ocean models with varying dynamical complexity have been used to study the dynamics of sea level and circulation in the IO [e.g. McCreary, 1985]. While the models with high degree of dynamical complexity (e.g., nonlinear effects included) provide realistic solutions, simpler linear models prove to be extremely useful for isolating the processes and are computationally very efficient. The objectives of the present Ph.D. have been addressed with a simple linear, continuously stratified (LCS) model. A detailed description of the LCS model and its configuration are presented in the next chapter (Section 3.3). The LCS model basically solves the linearized shallow water equations in a rotating frame of reference for a set of orthogonal vertical modes (baroclinic modes) that collectively describe the ocean variability [McCreary, 1980; 1981; 1985]. These baroclinic modes differ by their vertical structure (with largest vertical scale for the gravest mode) and by their typical phase speeds for the horizontal propagation of signals (fastest for the gravest mode; typically  $\sim 2.5$  m/s for the first with an oceanic stratification typical of the tropical oceans). Generally, the first few (two or three) gravest modes are sufficient to describe the oceanic response to wind variations reasonably well in the tropics, as demonstrated later in this thesis. The present section discusses briefly the basic properties of wave solutions of the linear shallow water equations, particularly the

equatorially trapped waves, the coastally trapped waves and the mid-latitude planetary waves. The vertical structure of these waves is described by the corresponding baroclinic mode, and hence the focus here will be on describing their horizontal structure. The presentation here basically follows that of Gill [1982] and Kantha and Clayson [2000].

***The coastal Kelvin waves:*** The coastal KW [Gill, 1982] solutions of the linearized shallow water equations are obtained with no normal flow condition at a lateral boundary (for e.g.  $v=0$  for a zonal boundary), such as continental margins (in case of an oceanic KW) or mountain ranges (in case of an atmospheric KW). In the present context, the shelf geometry is ignored and the coast is considered as a vertical wall, a boundary that acts as a waveguide (where wave energy is trapped), with a trapping scale given by  $\lambda_n = c_n/f$  (where  $c_n$  is the typical phase speed of the  $n^{\text{th}}$  baroclinic mode), which is called the Rossby radius of deformation. The coastal KWs lean against the coast and have an exponential structure ( $e^{-y_1/\lambda_n}$ , where  $y_1$  is the distance from the coast), for both the sea level and the alongshore current. That is, a coastal KW has maximum amplitude at the coast and decays away from it with an e-folding scale  $\lambda_n$ . The coastal KWs are associated with a zero current in the cross-shore direction. This implies that the width of the coastal waveguide varies with latitude, decreasing (increasing) poleward (equatorward). For example, the width of coastal waveguide at  $10^\circ\text{N}$  is  $\sim 100\text{ km}$ , and that at  $15^\circ\text{N}$  is  $\sim 65\text{ km}$ , as computed with a typical first baroclinic speed of  $2.5\text{ m/s}$ . The coastal KWs travel with the coast on their right (left) in the northern (southern) hemisphere. These waves are non-dispersive (i.e. both phase and energy of the wave propagate at the same speed allowing the wave to retain its characteristics over long distances) and can be forced directly by the alongshore wind-stress forcing or generated by the reflection of incident wave energy on a coast (this is what happens when the equatorial KWs reflect at the eastern boundary, as discussed later in this thesis).

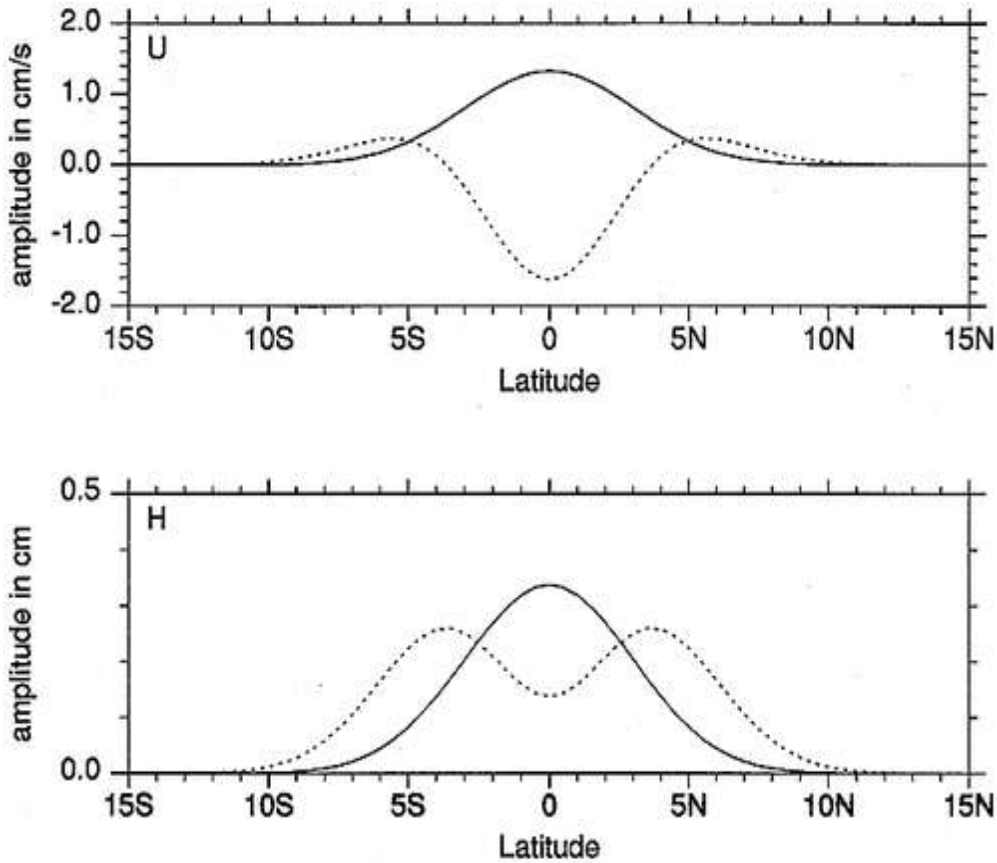


**Figure 2.1:** The amplitudes of the (top panel) zonal current ( $U$ ; cm/s) and (bottom panel) sea level ( $H$ ; cm) as a function of latitude for the Kelvin (solid) and the first Rossby (dotted) modes calculated with a phase speed of 2.5 m/s, illustrating their meridional structures. Reproduced from Boulanger et al. [1997].

**The Equatorial Kelvin waves:** The wave trapping occurs not only at the coast, but also in the equatorial band (due to latitudinal variation of the Coriolis parameter) as illustrated by the equatorial KWs [Matsuno, 1966]. These waves can be viewed as a pair of coastal KWs on both hemispheres leaning against each other symmetrically around the equator that behaves like a virtual boundary (but with a different meridional structure that is discussed below). The equatorial KW [Gill, 1982] is a solution of the linearized shallow water equations in an equatorial  $\beta$ -plane approximation (i.e.,  $f = \beta y$ , where  $f$  is the Coriolis parameter,  $y$  is the meridional distance from the equator (positive northward), and  $\beta$  is the latitudinal gradient of the Coriolis parameter at the equator, a constant given by  $2.3 \times 10^{-11} \text{ m}^{-1} \text{ s}^{-1}$ ). The trapping scale of the equatorial KW is the equatorial radius of deformation given by  $R_n = \sqrt{c_n / 2\beta}$ . The meridional structure (Figure 2.1) of the sea level  $\eta_n$  (and hence the zonal current,  $u_n = \frac{g}{c_n} \eta_n$ ) has a Gaussian shape (maximum at the equator) given by  $\eta_n \sim e^{-\frac{\beta y^2}{2c_n}}$ , with an e-folding (decay) scale

given by  $2R_n$  (i.e.  $\sqrt{2c_n/\beta}$ ). For a typical value  $2.5 \text{ m/s}$  of the first baroclinic mode ( $c_1$ ) in the IO, the trapping scale (or the equatorial radius of deformation) is  $\sim 230 \text{ km}$ , and the typical width of equatorial waveguide is  $\sim 460 \text{ km}$ . The equatorial KW, as the coastal one, is non-dispersive, with its dispersion relation (i.e. the equation that links the zonal wavenumber  $k$  and the frequency  $\omega$ ) given by  $\omega = ck$  (Figure 2.2), implying that it has positive (eastward) phase (i.e. velocity of the waves crest/trough) and group (i.e. velocity at which energy – or the envelope modulating the wave amplitude – propagates) velocities.

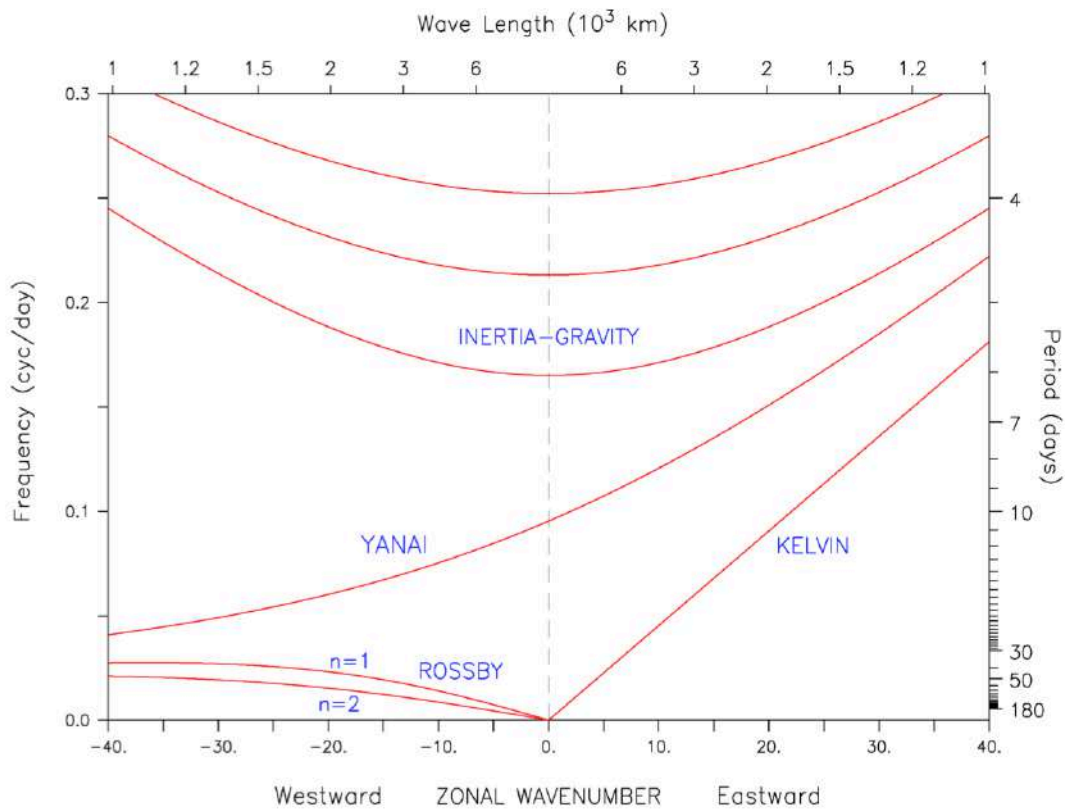


**Figure 2.2:** Dispersion curves corresponding to the dispersion relation, given by  $(\frac{\omega}{c})^2 - k^2 - \frac{\beta k}{\omega} = (2m+1)\frac{\beta}{c}$  (see, Gill [1982]), for waves in the equatorial waveguide. The value  $n=-1$  gives the equatorial KWs and  $n=0$ , the Yanai (also called the mixed Rossby-gravity) waves. For  $n \geq 1$ , the inertia-gravity (also called Poincaré; upper branch of curves) waves occur at high frequencies and the RWs (lower branch of curves), at low frequencies, with the gap in the frequency spectrum filled with KWs and Yanai waves. Yanai waves behave like RWs (inertia-gravity wave) for large negative (positive)  $k$ . Figure courtesy Debasis Sengupta, CAOS/IISc.

**The equatorial Rossby waves:** Besides KWs, the linearized shallow water equations in an equatorial  $\beta$ -plane approximation also allow an infinite set of other equatorially trapped waves [Matsuno, 1966; Gill, 1982] as solutions, with the trapping scale given

by the equatorial radius of deformation, but with varying meridional structures, all together constituting a complete orthogonal set (i.e. any meridional structure can be described mathematically by a combination of those waves). These waves include equatorially trapped inertia-gravity waves, Yanai waves, and RWs. The dispersion relation of all those waves are shown on Figure 2.2 (see its caption), but only the properties of equatorial RWs that are frequently invoked in this thesis are described here. As can be seen from Figure 2.2, the gravity waves occur only at high frequencies (periods  $< 6$  days). Similarly, large spatial scale (i.e. low  $k$ ) Yanai waves also have short periods ( $\sim 10$  days). In contrast, at large spatial scales (low negative  $k$ ), the equatorial RWs represent low frequency motions (periods longer than 30 days) and are quasi-non-dispersive. The dispersion relation of the  $m^{\text{th}}$  meridional mode equatorial RW (Figure 2.2) is:

$$\omega = \frac{-\beta k}{(k^2 + (2m+1)\frac{\beta}{c_n})} \quad \text{-----}(2.1)$$

The above expression indicates that the RWs have westward phase velocities. The short RWs (in the limit  $k \rightarrow \infty$  in the above equation 2.1) have eastward group velocity, i.e. they are dispersive. These short-wavelength waves are not efficiently generated by the large-scale wind forcing considered in this thesis and are damped out quickly due to their fine horizontal scales. Hence these waves in general are not important for the dynamics studied in this thesis. For long RWs (in the limit of  $k \rightarrow 0$  in equation 2.1, an appropriate approximation for the low-frequencies studied in the present Ph.D.; Figure 2.2), the dispersion relation can be approximated by:

$$\frac{\omega}{k} = \frac{-c_n}{(2m+1)}$$

This implies that long RWs are non-dispersive (the phase velocity  $\omega/k$  and the group velocity  $\partial\omega/\partial k$  are both equal to  $-c_n/(2m+1)$ ). This also implies that, for a typical first baroclinic mode phase speed of  $c_1 = 2.5 \text{ m/s}$ , the first meridional mode RW phase speed is  $0.8 \text{ m/s}$ . Thus the first meridional mode (long) equatorial RW requires nearly 3 months to cross the equatorial IO (from east to west) compared to a 1-month time as required by the equatorial KW (from west to east). The higher meridional modes require even longer time. The meridional shapes of odd (even) RWs meridional modes are symmetric (asymmetric) about the equator, with maxima located away from the equator. The sea level meridional structure, computed with  $c_1 = 2.5 \text{ m/s}$ , of the first Rossby mode has its maxima around  $4^\circ$  on either side of the equator (Figure 2.1; first three modes are

shown in Figure 5.1). The current anomaly associated with the first meridional mode RW has maximum at the equator (Figure 2.1).

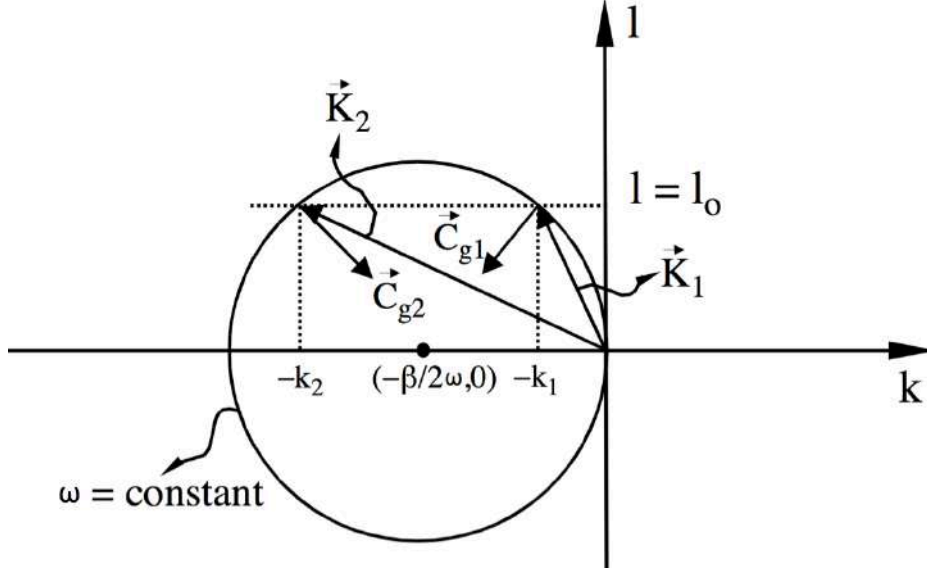


**Figure 2.3:** Dispersion diagram for mid-latitude RWs. Here,  $\omega$  denotes the frequency,  $k$ , and  $l$  are the zonal and meridional wavenumbers, and  $C_g$  is the group velocity. Figure courtesy Debasis Sengupta, CAOS/IISc.

**Mid-latitude Rossby waves:** While mid-latitudes signals can be described by using a large number of equatorial RW meridional modes, it is more straightforward to derive a mid-latitude RW solution from the mid-latitude  $\beta$ -plane approximation  $f = f_o + \beta y$ , where  $f_o$  is the value of the Coriolis parameter at a reference mid-latitude  $\varphi_o$ , and  $\beta$  is the latitudinal gradient of the Coriolis parameter at  $\varphi_o$  given by  $\beta = (2\Omega/R)\cos\varphi_o$ , where  $\Omega$  and  $R$  are the angular velocity and radius of the Earth. The mid-latitude RWs can be derived as solutions of the linearized shallow water equations in Cartesian coordinates on a mid-latitude  $\beta$ -plane [Gill 1982; Kantha and Clayson, 2000]. The corresponding dispersion relation between the frequency  $\omega$  and the zonal ( $k$ ) and meridional ( $l$ ) wave numbers is:

$$\omega = \frac{-\beta k}{k^2 + l^2 + \frac{f_o^2}{c_n^2}}$$

which indicates that the RWs have westward phase speed, but their group velocities can be either eastward or westward. The above dispersion relation can be represented as circles of constant  $\omega$  in the  $(k, l)$  plane, as shown on Figure 2.3. The group velocity, which is the gradient of  $\omega$  in the wave-number plane, is represented by the normal

vector directed radially inward and hence has a westward component for long RWs (small  $k$  negative values) and eastward component for short RWs (large  $k$  negative values, Figure 2.3). The dispersion relation of the long RWs can be approximated as  $\omega/k = -\beta c_n^2/f_0^2 = -\frac{c_n^2 \cos \varphi_0}{2\Omega R \sin^2 \varphi_0}$ , which is non-dispersive and implies a strong inverse relation between the phase speed and the latitude of the form  $\frac{1}{\varphi^2}$ . The estimated phase speeds of sea level from the satellite altimeter observations demonstrate the above strong inverse dependence on the latitude as shown in Figure 2.4, which indicates that the typical phase speed of the 1<sup>st</sup> baroclinic mode RWs in the southern BoB ( $\sim 10^\circ\text{N}$ ) is  $\sim 25 \text{ cm/s}$  and that in the northern BoB ( $\sim 23^\circ\text{N}$ ) is  $\sim 5 \text{ cm/s}$ .

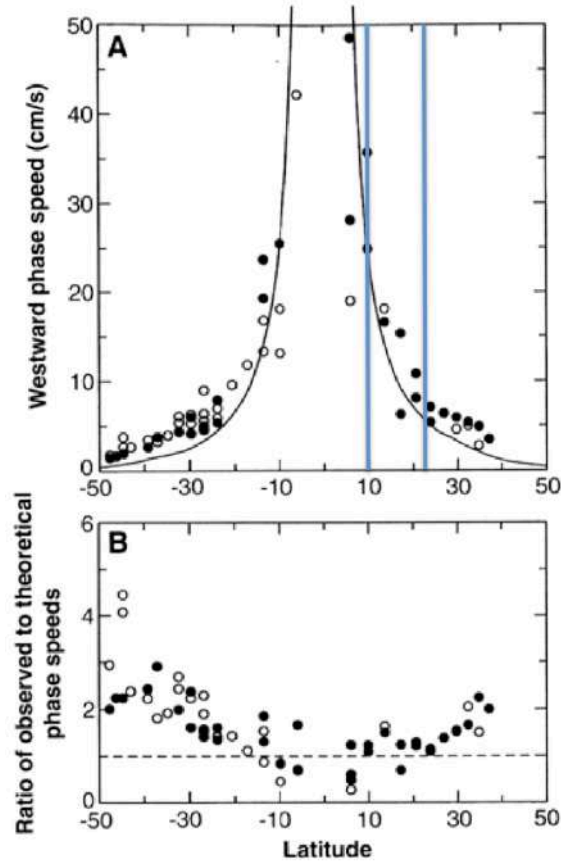


**Figure 2.4:** Estimates of phase speeds of westward propagating sea level anomalies from TOPEX/POSEIDON altimeter data as a function of latitude (abscissa in °N). The solid (open) circles correspond to the estimates from Pacific (Atlantic and IO). The thick black lines on the top panel correspond to the phase speeds of the first baroclinic RW as predicted by linear theory. The two vertical lines on the top panel mark the latitudes of the southern and northern BoB. Adapted from Chelton and Schlax [1996].

**Critical latitude and period:** The maximum frequency of RWs is given by  $\omega_{max} = \beta c_n / 2f_o$ , or the minimum period is given by  $P_{min} = 4\pi y / c_n$  [Gill, 1982]. The latitudinal dependence of the minimum period of planetary waves can alternatively be interpreted as a latitudinal limit poleward of which RWs with certain periods cannot exist. This latitude is called the critical latitude,  $y_c$ . Or alternatively,  $P_{min}$  is called the critical period [Gill, 1982]. For instance, RWs with semi-annual (180-day) period cannot exist poleward of  $\sim 28^\circ$  latitude: this is the critical latitude for the semiannual RW. The critical period,  $P_{min}$ , at  $15^\circ\text{N}$  (with  $c_l = 2.5 \text{ cm/s}$ ) is  $\sim 96$  days. This implies that the coastal sea level signals with period  $< 96$  days remain trapped at the coast as coastal KWs, whereas those with period  $> 96$  days radiate offshore as westward RWs. This “leaking” of sea level signals associated with coastal KWs as RWs has important implications for the dynamics of NIO sea level variability [Shetye, 1998; Shankar et al., 2002] as will be discussed in Section 2.2.

## 2.2 Northern Indian Ocean seasonal variability

**The atmospheric forcing:** The most pronounced feature of the winds over the NIO is their seasonal reversal (Figures 2.5a and 2.5b) associated with the alternating southwest and northeast monsoons [Schott and McCreary, 2001]. The southwest monsoon (boreal summer; June-September; JJAS) winds are, in general, stronger than their northeasterly counterpart (boreal winter; December-March, DJFM), and they form an intense low-level jet, called the Findlater Jet [Findlater, 1969], over the AS. The maximum core of these summer monsoon winds is located over the central AS, with lateral wind-stress variations resulting in strong wind-stress curl forcing away from the core. This wind-stress curl forcing drives Ekman pumping, leading to open-ocean upwelling (downwelling) north (south) of the maximum wind-stress core [Lee et al., 2000]. Furthermore, these southwesterly winds blow almost parallel to the coasts of Somalia, Oman, southern tip of India/Sri Lanka, and the northwestern rim of the BoB (Figure 2.5a), leading to strong alongshore wind-stress forcing that favors coastal upwelling in those regions [Lee et al., 2000; Schott and McCreary, 2001]. During winter, the dry and cool northeasterly trade winds from the Asian landmass cool the ocean surface layer in the northern AS that enhances the convective mixing in the ocean [Prasanna Kumar and Prasad, 1996]. From a dynamical viewpoint, the winter monsoon winds provide a

weaker forcing of opposite polarity compared to their summer counterpart over the above-mentioned coastal (alongshore forcing) and open-ocean (wind-stress curl forcing) regions (Figure 2.5b). Thus NIO is subjected to strong dynamical forcing by the winds during both the monsoon seasons, with the largest seasonal variations of the tropics, and larger than the mean state.

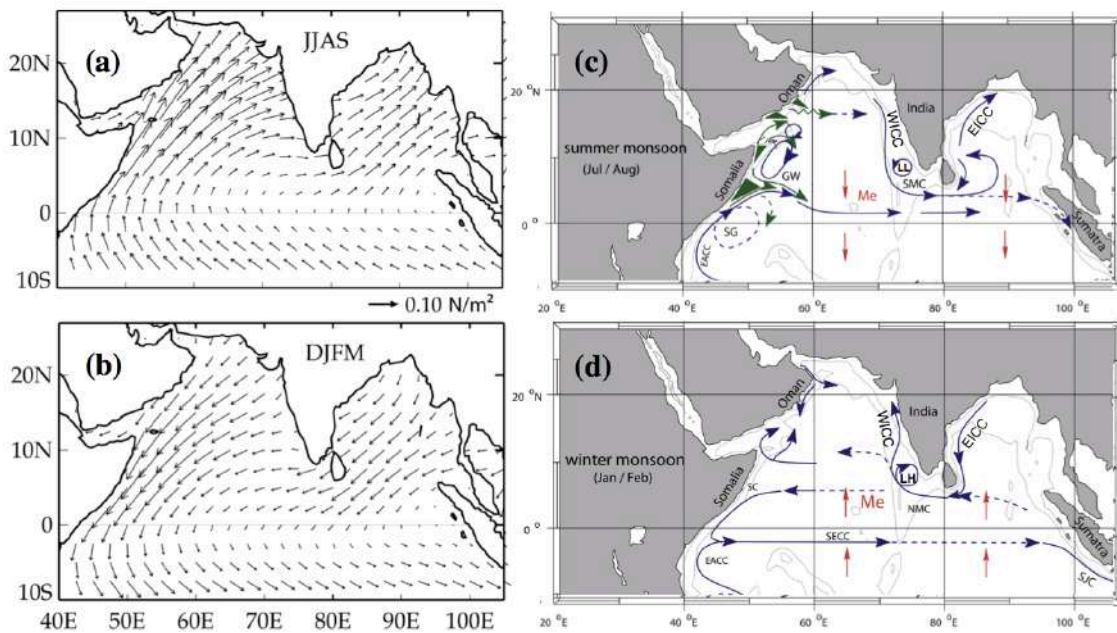


**Figure 2.5:** Seasonal climatology of wind stress ( $N/m^2$ ) in the NIO for (a) boreal summer (JJAS) and (b) winter (DJFM). The wind stresses are from the TropFlux product [Praveen Kumar et al., 2013], described in section 3.2. Schematic diagram of seasonal currents in the NIO during (c) summer and (d) winter, adapted from Schott et al. [2009]. Of interest here are the East India Coastal Current (EICC), the West India Coastal Currents (WICC), the Lakshadweep High (LH) / Low (LL), which are indicated by the arrows.

**The NIO response:** The dynamical response of the NIO to the above wind forcing is best manifested as strong seasonal cycle in the NIO sea level and upper-ocean circulation [Schott and McCreary, 2001]. In the past three decades, numerous studies (review presented below) have focused on describing and understanding the seasonal cycle of the sea level and surface currents in the NIO, particularly of the East India Coastal Current (EICC) along the east coast of India (ECI) and the West India Coastal Current (WICC) along the WCI (Figures 2.5c and 2.5d). Before reviewing the literature on the seasonal variability of sea level and currents along the coast of India, the concept of “leaky waveguide”, which has been proposed to explain the observed seasonal variability, is presented below for ease of the discussion.

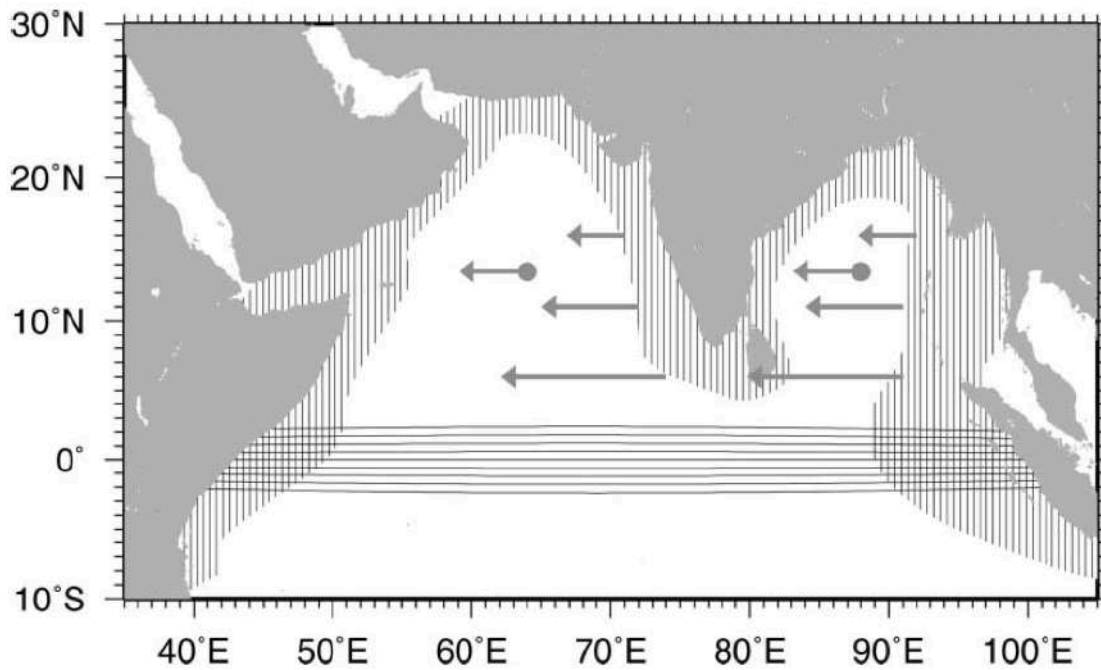


**Figure 2.6:** *The leaky NIO waveguide. The equatorial waveguide is hatched horizontally and the coastal waveguide vertically. The arrows emanating from coastal waveguide correspond to the RW radiation from eastern the boundaries of the BoB and AS basins and those from filled circles indicate the RWs generated by the wind-stress curl forcing in the interior basins. Reproduced from Shankar et al. [2002].*

**The leaky waveguide of the NIO:** The NIO seasonal dynamics has been understood in terms of the “leaky waveguide” (schematically shown in Figure 2.6), a simple conceptual framework proposed within the perspective of linear wave theory [Shetye, 1998; Shankar et al., 2002]. This framework suggests a basin-scale dynamical link between the equatorial waveguide and the NIO coastal waveguide through reflection of equatorial KWs at the eastern boundary of the equatorial IO basin. The equatorial KWs travel eastward and impinge on the coast of Sumatra. The problem of reflection of the equatorial KWs at the eastern boundary is solved mathematically by imposing a no-flow condition across the boundary. Since KWs and RWs of the same polarity (in sea level) have opposite zonal currents at the equator (Figure 2.1), the above boundary condition imposes KWs to reflect into RWs. The reflection at the eastern boundary also involves some of the energy propagating as coastal KWs into the coastal waveguides on the either side of the equator. The northward-branching coastal KWs travel along the NIO coastal waveguide, emphasizing the importance of remote equatorial forcing for the coastal NIO sea level variability. In this conceptual framework, the equatorial waveguide, defined from the equatorial radius of deformation, is  $\sim 500\text{-km}$  wide (cf. Section 2.1) centered on the equator and the coastal waveguide, defined from the e-

folding scale of coastal KWs, at the southern coast of Sri Lanka is  $\sim 200\text{-km}$  wide (cf. Section 2.1). These two regions do not overlap, as the southern coast of Sri Lanka is located more than  $500\text{ km}$  far from the equator. The “leakiness” of the waveguide is related to the westward radiation of RWs (i.e. southward of the critical latitude for a given wave frequency) associated with coastal KW propagation along the eastern rims of the BoB and AS basins (see Section 2.1).

***The ECI seasonal variability:*** The most-striking feature of the BoB circulation is the seasonally reversing EICC (Figures 2.5c and 2.5d), the western-boundary current of the BoB that flows northward (southward) during February – September (November – January), with its peak phase during spring (April – May) season. A detailed description of the EICC based on observations has been presented in several studies; see for e.g., Shenoi et al. [1999], Shetye et al. [1991b, 1993, 1996], and a more recent study by Mukherjee et al. [2014]. The driving mechanisms of the EICC’s seasonal variability have been investigated in many modeling studies way back since 1990s [Yu et al., 1991; Potemra, 1991; McCreary et al., 1993; McCreary et al., 1996; Shankar et al., 1996, Shankar et al., 2002]. Those studies demonstrated that both local (through alongshore wind forcing) and remote (through wind forcing in the interior Bay, along the eastern BoB rim, and in the equatorial region) forcing modulate the seasonal cycle of EICC, but with varying contributions with time.

***The WCI seasonal variability:*** The seasonal cycle of the WICC, the eastern-boundary current of the AS (Figures 2.5c and 2.5d), has been well described based on the observations (see for e.g., Shenoi et al. [1999]; Shetye and Shenoi [1988]; Shetye et al. [1990; 1991a]; Amol et al. [2014] and the references therein) as the poleward-flowing current during winter, with sign reversal during summer. The sea level along the WCI is dominated by the seasonal cycle. Figure 2.7, which shows the standard deviation of the observed seasonal sea level, indicates that the WCI is one of the regions in the NIO with the largest seasonal variability. This variability further extends westward through RW propagation into the southeastern AS, including a region known as the Lakshadweep High (LH)/Low (LL) (Figure 2.5) [Shankar and Shetye, 1997]. Earlier studies [e.g., Yu et al., 1991] proposed that WCI sea level variations are strongly influenced by the remote equatorial wind forcing, through propagation of KWs along the equator and coastal KWs around the rim of the BoB. Using a  $2\frac{1}{2}$ -layer model, McCreary et al.

[1993] demonstrated that the seasonal WCI sea level variations are primarily wind-driven and are largely remotely forced by the BoB winds. Given that the monsoonal winds are almost perpendicular to the WCI (Figures 2.5a and 2.5b), they drive only little sea level variations there. In contrast, the summer (winter) monsoon winds will drive upwelling (downwelling) along the ECI that will propagate to the WCI as coastal KWs. Shankar et al. [2002] performed a series of sensitivity experiments with a 1½-layer model to isolate the effect of alongshore winds in WCI from those along the BoB western rim (including both ECI and Sri Lanka). They concluded that the BoB alongshore winds indeed excite coastal KWs that propagate southward along the ECI, bend around Sri Lanka, and further propagate northward along the WCI to influence the WICC. Those remotely forced sea level signals along the WCI radiate away as RWs, resulting in the formation of LH/LL [Shankar and Shetye, 1997] and impact regions as far as the Somali coast in the western AS [McCreary et al., 1993; Beal et al., 2013].

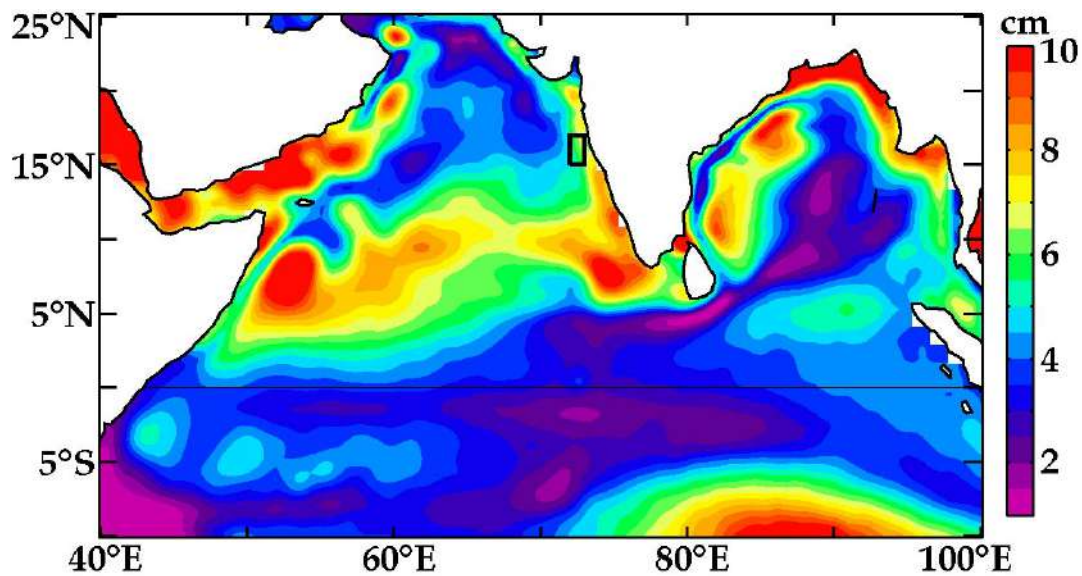


**Figure 2.7:** Standard deviation of observed seasonal sea level (cm). The observations are from the satellite altimeter-based AVISO sea level product described in detail in Section 3.2.

**Implications of WCI seasonal variability:** The seasonal sea-level (and hence the thermocline depth) variability along the WCI and in the LH/LL has strong societal impacts. As discussed above, the remote BoB forcing induces upwelling along the WCI during summer. This seasonal upwelling along the WCI and in the southeastern AS brings nutrients to the surface layer, causes phytoplankton bloom, and thus influences the food chain with a direct impact on fisheries [Madhupratap et al., 2001]. Due to its

intense productivity and weak ventilation, the subsurface AS has one of the most-marked global subsurface Oxygen Minimum Zones [Naqvi et al., 2009]. The seasonal upwelling on the shelf off the WCI also brings very-low oxygen content waters very close to the surface in late summer and fall (Figure 2.8) [Parvathi et al., 2017]. This leads to the formation of the world ocean’s largest natural hypoxic system on the shelf off the WCI, with strong implications for the regional ecosystem and fisheries [Naqvi et al., 2000; 2009]. Finally, the deep thermocline associated with LH favors the development of high SSTs in the southeastern AS before the summer monsoon, well-known as the “Arabian Sea mini warm pool”, that influences the southwest monsoon onset date [Vinayachandran et al., 2007] and total rainfall [Masson et al., 2005], which affects the lives of more than one billion people in India.

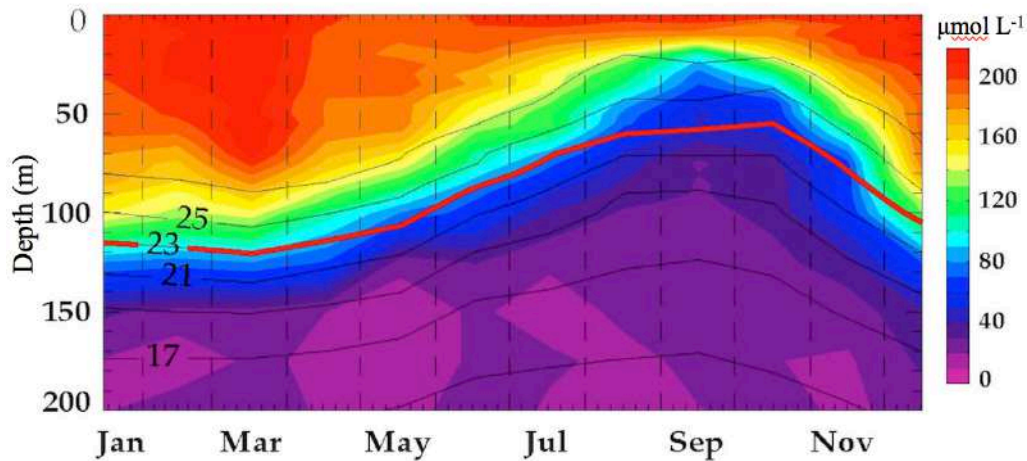


**Figure 2.8:** Monthly vertical profiles of oxygen (color shaded) and temperature ( $^{\circ}\text{C}$ ; black contours) averaged over a box between  $10^{\circ}$  and  $15^{\circ}$  N, extending  $2^{\circ}$  offshore on the WCI. The red line marks the thermocline depth. Figure adapted from Parvathi et al. [2017].

### 2.3 Northern Indian Ocean interannual variability

**Dominant climate modes in the IO:** El Niño - Southern Oscillation (ENSO) and the IOD are the two modes of natural climate interannual variability that affect the year-to-year variability (i.e. IAV) in the IO most prominently [Schott et al., 2009]. Both ENSO and IOD result from strong air-sea interactions, with the former occurring in tropical Pacific and the latter in the tropical IO. Before reviewing the literature on the NIO

interannual variability, a brief discussion on these coupled climate modes, including their impacts on the IO, is presented below.

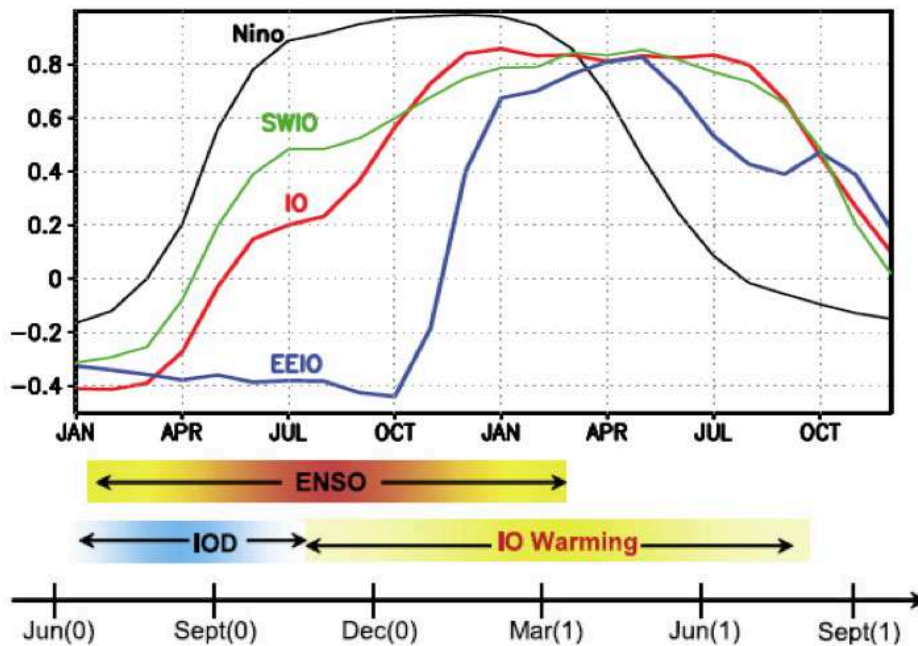


**Figure 2.9:** Lead-lag correlations of SST anomalies averaged over the eastern equatorial Pacific (160–120°W, 5°S–5°N; black: Niño3 region, a typical ENSO index), the tropical IO (40–100°E, 20°S–20°N; red), the southwest IO (50–70°E, 15–5°S; green), and the eastern equatorial IO (90–110°E, 10°S–equator; blue) to the November to January (grey shading) average Niño3 index (and index of El Niño at its peak). In addition, the seasonality of major interannual IO climate modes is indicated at the bottom. The warming in the IO lasts even after the end of an El Niño and the IOD has tendency to co-occur with El Niño. Reproduced from Schott et al. [2009].

**The ENSO and its influence on the IO:** ENSO is the leading mode of Earth’s year-to-year climate variability and is characterized by unusually warm (El Niño) and cold (La Niña) phases. El Niños (La Niñas) are associated with anomalously weak (strong) easterlies and zonal pressure gradients (Southern oscillation) across the tropical Pacific [McPhaden et al., 2006; Schott et al., 2009]. A detailed discussion of the ENSO dynamics can be found, for example, in Philander [1990], Wang and Picaut [2004] or Clarke [2008]. ENSO-related SST anomalies in the eastern Pacific start developing during boreal spring and summer, peak during winter, and subsequently decay during spring (Figure 2.9), thereby lasting for 6-12 months, with a recurrence time of 2-7 years. The ENSO intensity and variability is characterized by many indices [Hanley et al., 2003], such as the Southern Oscillation Index, the NOAA Oceanic Niño Index, and the Multivariate ENSO Index (MEI; see Section 3.2). ENSO influences the worldwide climate through atmospheric teleconnections [e.g. Trenberth et al., 1998] and has

profound socio-economical and environmental impacts [e.g. McPhaden et al., 2006]. Eastward (westward) shifts of the Indo-Pacific Walker circulation induce enhanced (decreased) subsidence over the IO, and hence anomalously high (low) downward surface shortwave fluxes [Klein et al., 1999; Lau and Nath, 2000]. Local air-sea interactions over the IO maintain the anomalous basin-wide warming (cooling) beyond the end of the El Niño (La Niña) event (red curve on figure 2.9; [Xie et al. 2009]). This IO enduring warming hence maintains regional climate anomalies beyond the end of an El Niño event. The warming (cooling) of the tropical IO in response to El Niño (La Niña) favors weaker (stronger) than normal precipitation of the Indian summer monsoon before the ENSO peak [Schott et al., 2009].

**The IOD:** The IOD [Saji et al., 1999; Webster et al., 1999; Murtugudde et al., 2000] is an indigenous mode of interannual climate variability in the IO. A positive (negative) phase of IOD is characterized by a zonal SST gradient in the tropical IO, with an anomalous cooling (warming) in the southeastern equatorial IO and an anomalous warming (cooling) in the central and western equatorial IO, associated with anomalous easterlies (westerlies) in the central equatorial IO (schematically shown in Figure 2.10). The IOD lasts for ~6 months, with its signatures developing during May-June, peaking in fall and rapidly withdrawing by the end of the year (Figure 2.9) [Saji et al., 1999]. The spatial distribution of the SST, the outgoing longwave radiation (a proxy for precipitation observed by satellites), the zonal component of the surface winds, and the sea level anomalies during 1997-98, one of the strongest positive IOD event, are displayed in Figure 2.11 to illustrate the typical patterns associated with an IOD. The SST anomalies (dipole structure) associated with the IOD induce a dipolar rainfall pattern and anomalous easterly winds in the central-eastern equatorial IO. These winds drive downwelling RW response to the west and upwelling KW response to the east, with the latter propagating into the BoB rim as upwelling coastal KWs, thus suggesting an influence of IOD on the NIO sea level IAV. A positive (negative) IOD event often, but not always, tends to co-occur with El Niño (La Niña) (Figure 2.9) [Yamagata et al., 2004; Schott et al., 2009], making it difficult to isolate their relative influences in the observations. The IOD variability is characterized by an index of the zonal SST gradient, called the Dipole Mode Index (DMI; see Section 3.2 for details). The IOD has strong influences on the regional climate of the countries surrounding the IO basin, but with a lesser global extent than ENSO [e.g. Yamagata et al. 2004]. However, it can also

retroact on simultaneous [e.g. Luo et al., 2010] and following year's ENSO [e.g. Izumo et al., 2010] conditions, thereby having an indirect global influence [e.g. Izumo et al., 2014].

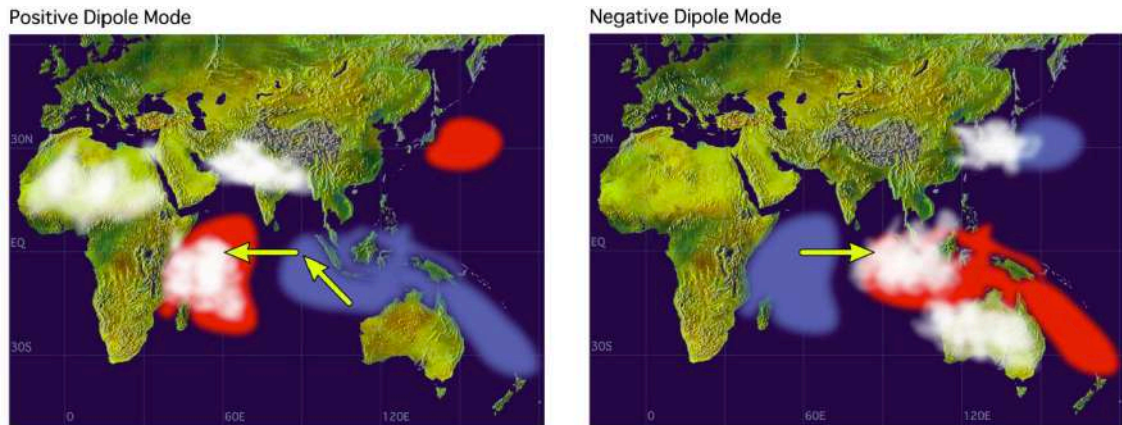


**Figure 2.10:** Schematic illustration of an IOD during its positive (left panel) and negative (right panel) phases. Red (blue) shades indicate warm (cold) SST anomalies, with white shades indicating the convective clouds. The yellow arrows represent wind anomalies, associated with the corresponding IOD event. Picture courtesy JAMSTEC ([http://www.jamstec.go.jp/frcgc/research/d1/iod/iod\\_home\\_s.html.en](http://www.jamstec.go.jp/frcgc/research/d1/iod/iod_home_s.html.en)).

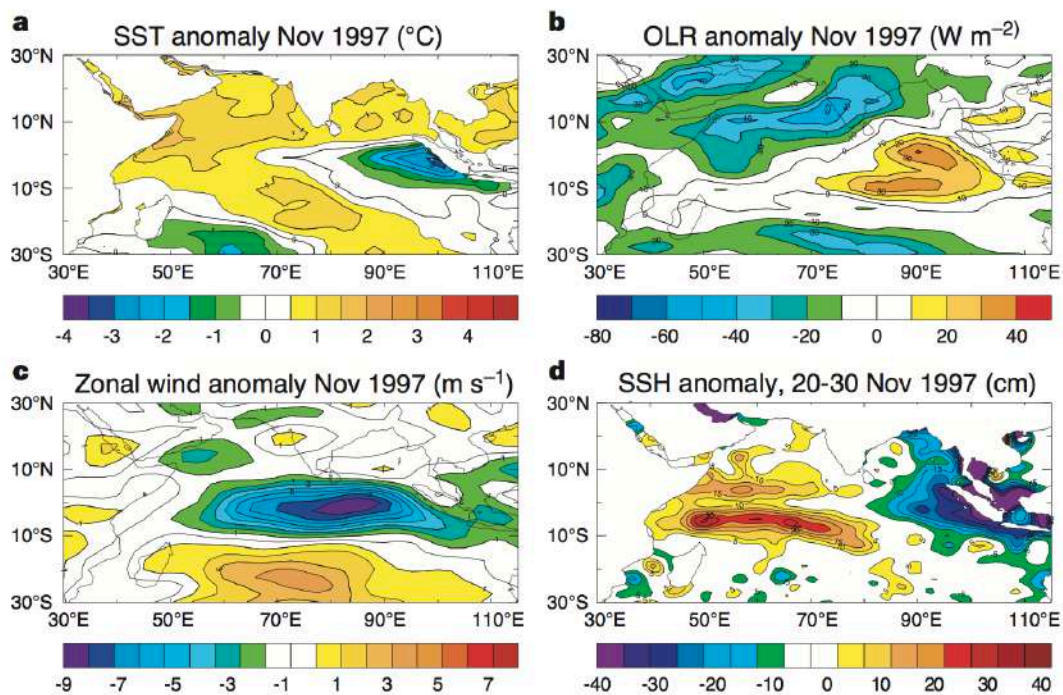


**Figure 2.11:** Spatial patterns of seasonal anomalies of (a) SST (b) outgoing longwave radiation, a proxy for deep atmospheric convection (c) zonal winds (d) sea level at the peak of the 1997 IOD event. Reproduced from Webster et al. [1999].

***NIO Sea level IAV:*** Many studies [e.g., Perigaud and Delecluse, 1992; Rao et al., 2002; Rao et al., 2010] have dealt with sea level IAV in the NIO through both observations and numerical modeling. Clarke and Liu [1994] used monthly sea level records from the coastal stations along the perimeter of the NIO waveguide over a distance of 8000 km, together with a simple linear model, to demonstrate the propagation of the interannual sea level signals forced remotely by the equatorial interannual zonal winds. Han and Webster [2002] used a 4½-layer reduced gravity model to systematically investigate the forcing mechanisms of the sea level IAV in the BoB. They concluded that the IAV in the BoB is primarily wind-driven (both local and remote equatorial winds) and that the surface buoyancy flux, the heat flux and the river discharges into the Bay have negligible effects. The wind stress anomalies associated with IOD and ENSO drive interannual variations in the sea level and currents in the IO [Schott et al., 2009; Singh, 2002; Srinivas et al., 2005], particularly in the BoB, through equatorial dynamics and coastal KW propagation in a fashion similar to the seasonal dynamics. Using tide-gauge and altimeter data, Aparna et al. [2012] showed that ENSO and IOD events have distinct characteristics on the sea level IAV in the BoB, and further investigated their driving mechanisms using a linear model. The SLAs associated with a positive IOD are negative in the BoB and they decrease monotonically attaining a peak during fall. Negative SLAs are observed twice during an El Niño event. These signals reverse in sign, but are weaker, during the negative IOD and the La Niña events. Aparna et al. [2012], however, did not find any clear ENSO/IOD-related signatures on the WCI. On the contrary, a recent study by Parvathi et al. [2017] showed a clear link between the IOD events and the WCI sea level (and thermocline) IAV during fall. Using a coupled physical-biogeochemical model simulation, they demonstrated that the IOD-induced wind anomalies over the southern tip of India/Sri Lanka force coastal KWs that propagate along the WCI and contribute to the sea level IAV there.

***Importance of WCI sea level IAV for biogeochemistry:*** Earlier studies reported a weak sea level IAV on the WCI [Shankar et al. 2010; Aparna et al. 2012]. This weak sea level IAV however has important implications for the regional biogeochemistry. As noted in Section 2.2, the shelf off the WCI becomes one of the world ocean's largest, natural hypoxic systems, following the seasonal upwelling. Substantial interannual changes both in the duration and intensity of the oxygen deficiency along the WCI have been reported [Naqvi et al., 2009]. During some years, waters below the surface become

entirely oxygen depleted over the entire shelf off the WCI – a condition called coastal anoxia [Naqvi et al., 2000; Naqvi et al., 2009], with tremendous impact on the living resources and fisheries. Parvathi et al. [2017] (as mentioned above) showed that the interannual oxygen variability along the WCI is closely linked to the sea level and thermocline IAV (Figure 2.12) during fall, thus emphasizing the importance of WCI sea level IAV.

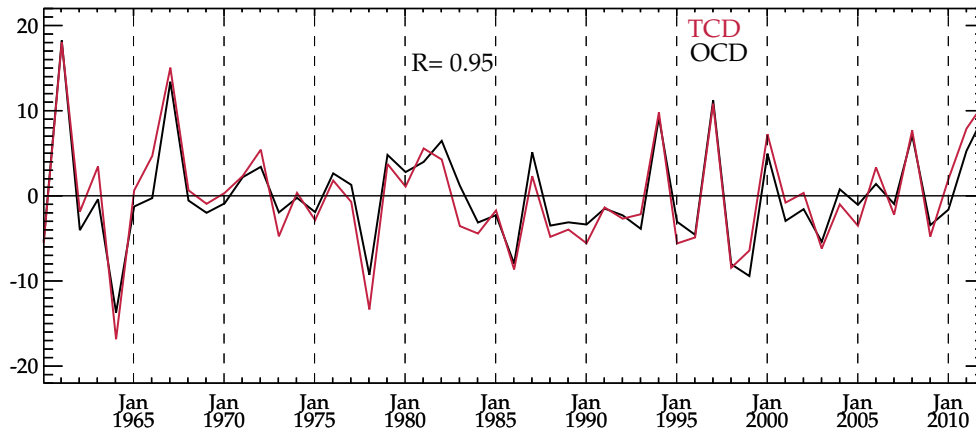


**Figure 2.12:** Time series of the fall (September–November) interannual thermocline (defined as depth of 23°C isotherm) and oxycline (defined as depth of 100  $\mu\text{mol L}^{-1}$ ) depth anomalies off Goa (near 15°N) on the WCI, exhibiting a high correlation of 0.95. Reproduced from Parvathi et al. [2017].

## 2.4 Northern Indian Ocean intraseasonal variability

**The atmospheric ISV:** The tropical IO winds exhibit strong variability at intraseasonal timescales associated with the Madden-Julian oscillation (MJO) and active/break monsoon cycles. These two modes of atmospheric ISV are discussed below. These large spatial scale (of the order of 5000 to 10000 km) modes are characterized by a strong coupling between atmospheric deep convection and dynamics.

**The MJO:** MJO [e.g. Schott et al., 2009; Zhang, 2005; Zhang, 2013 reviews] is the leading mode of the tropical climate variability at intraseasonal timescales and is characterized by basin-scale deep atmospheric convective perturbations, with strong fluctuations in the tropospheric winds at 30 to 90-day timescales. The convective anomalies associated with the MJO originate in the western IO, propagate eastward at a speed of  $\sim 5$  m/s through the IO, maritime continent, and the western Pacific (Figure

2.13). Subsequently they decay when reaching the central Pacific where the surface ocean is not warm enough to sustain deep atmospheric convection [e.g. Gadgil et al., 1984]. The MJO-induced atmospheric variations are the strongest during boreal winter between the equatorial strip and the southern tropics (5-15°S thermocline ridge region) [Zhang and Dong, 2004]. During summer, the convective anomalies associated with the MJO result in intermittent rainy and dry spells of the Indian summer monsoon and are known as the active/break monsoon cycles/phases [Schott et al., 2009; Goswami, 2005] that are discussed below.

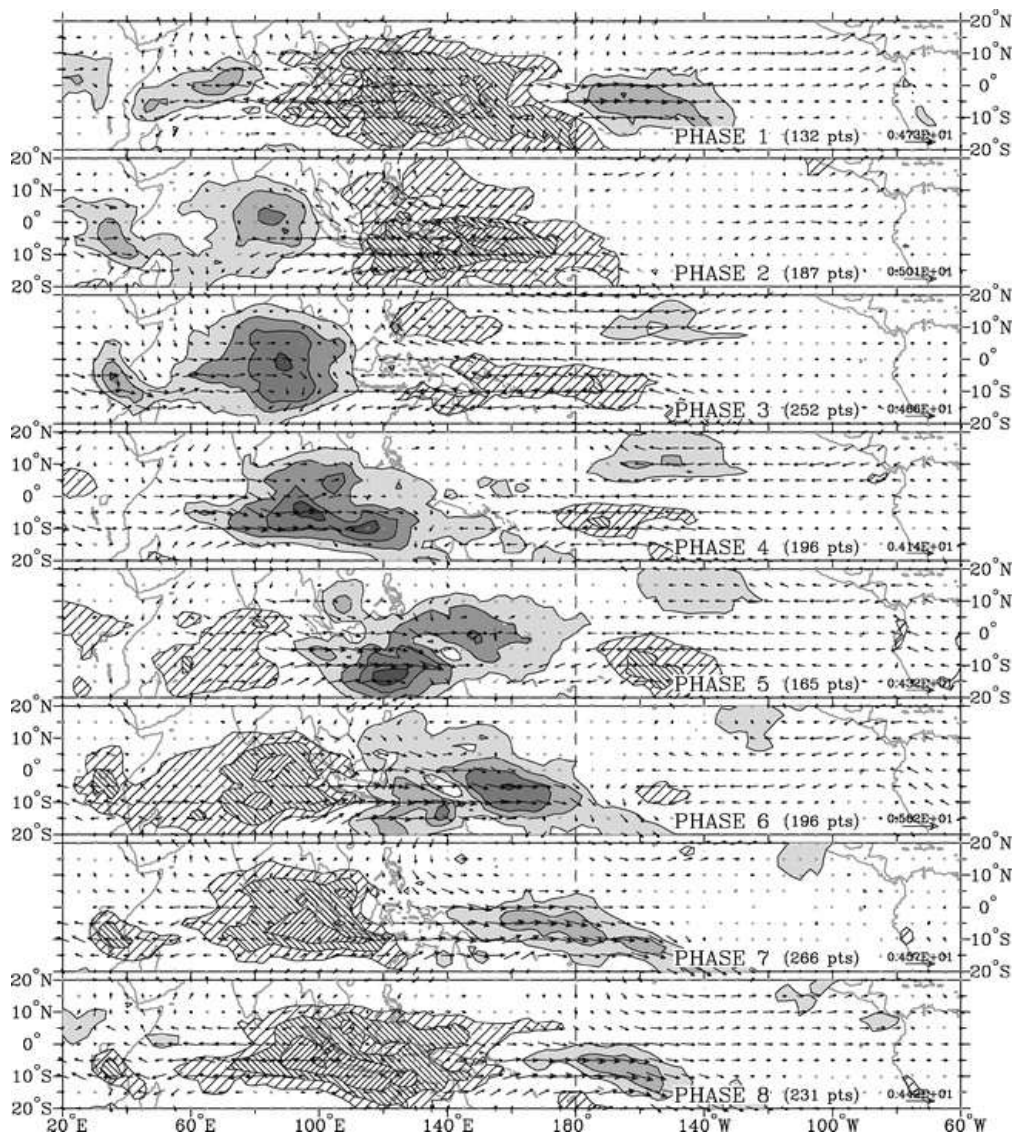


**Figure 2.13:** MJO composites of outgoing longwave radiation (shaded/hatched) and 850-hPa wind (vectors, statistically significant at 99% level) anomalies during December – February. The levels for shading correspond to the values less than -7.5, -15, -22.5 and -30  $W/m^2$ , and those of hatching to values larger than 7.5, 15, and 22.5  $W/m^2$ . Reproduced from Wheeler and Hendon [2004].

**The active/break monsoon phases:** As noted above, the active/break cycles of the Indian summer monsoon can be viewed as the summer variant of the MJO, although the details differ [Goswami, 2005]. The active phases are associated with a strong Findlater jet and intense convection and rainfall across the Indian subcontinent (Figures 2.14a and 2.14b), while the break phases are associated with a weaker Findlater jet that splits into two branches converging on enhanced convection and rainfall on the ocean south of India and on the Himalayan foothills (Figures 2.14c and 2.14d). The convective anomalies propagate northward from the ocean south of India to the Himalayas during break to active conditions [Joseph and Sijikumar, 2004]. The monsoon active/break phases modulate the overall rainfall over India at 30–60-day timescales [Lawrence and Webster, 2002; Schott et al., 2009], somewhat shorter than the winter MJO timescales.

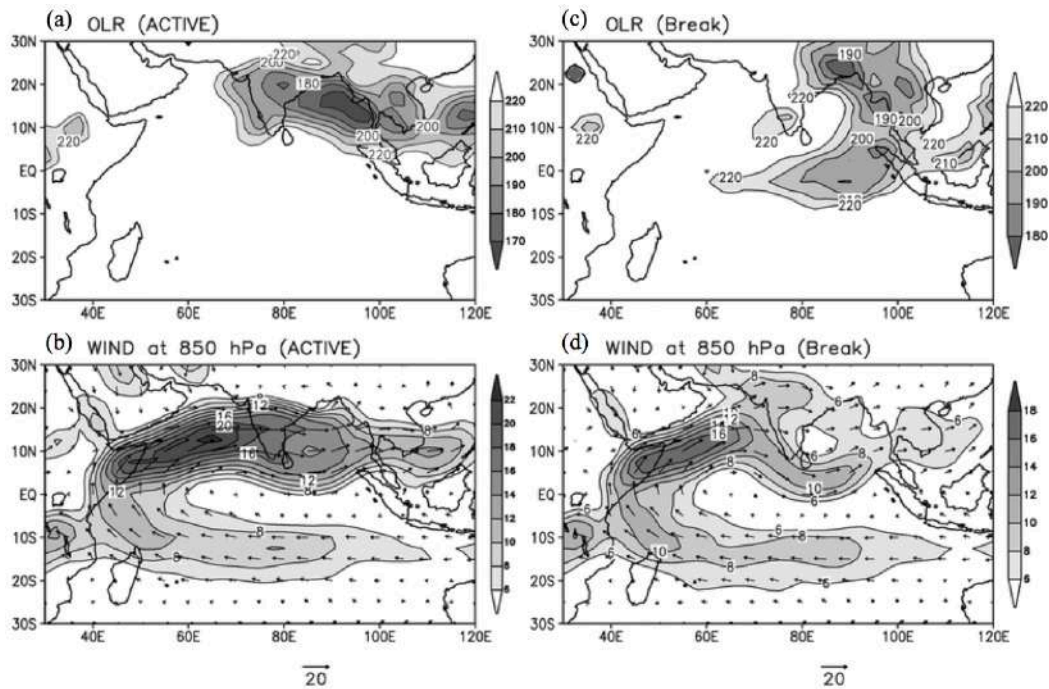


**Figure 2.14:** Composites of (a, b) active and (c, d) break monsoon days in summer during 1979-1990. (a, c) outgoing longwave radiation ( $W m^{-2}$ ) and (b, d) 850-hPa wind vectors ( $m s^{-1}$ ). Reproduced from Joseph and Sijikumar [2004].

**NIO thermodynamical response:** Both MJO and active/break phases are associated with the basin-scale variations of surface winds and air-sea fluxes. This thesis focuses mainly on the *dynamical* response of the IO to surface wind variations associated with the atmospheric ISV. There is, however, also thermodynamical response of the upper ocean to the atmospheric ISV during both the seasons that is briefly reviewed here. During active convective phases, there are reduced downward solar fluxes and

enhanced evaporation due to strong surface winds in both winter and summer [e.g. Vialard et al., 2012; 2013]. This yields typical net surface heat fluxes peak-to-peak variations of up to  $80 \text{ Wm}^{-2}$  depending on the region and season [Vialard et al., 2012; 2013]. In most regions, the SST response to the atmospheric ISV can be well approximated by integrating those flux anomalies over the climatological mixed layer in a slab-ocean model. This suggests that the SST intraseasonal variations in response to the MJO and monsoon active/break phases are generally strong in those regions, where the convective perturbations are strong and the mixed layer is shallow, as in the BoB during summer (Figure 2.15a) [Vialard et al., 2012], and in Seychelles-Chagos thermocline ridge and northwestern Australian basin [Vialard et al., 2013] during winter (Figure 2.15b). The only regions where oceanic processes (upwelling, vertical mixing) seem to play a key role in driving the SST variability in response to the atmospheric ISV are the AS upwelling regions during summer. The intensity of the upwelling (and SST) seems to respond to intraseasonal variations in the alongshore winds [Vialard et al., 2012]. A recent review by DeMott et al. [2015] suggests that intraseasonal SST signatures resulting from the atmospheric ISV feedbacks onto the atmosphere.

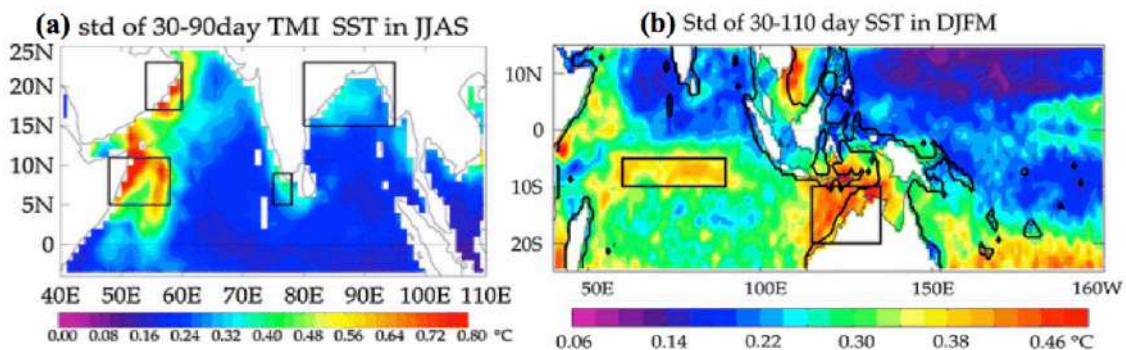


**Figure 2.15:** Standard deviation of intraseasonal SST during (a) summer; Reproduced from Vialard et al. [2012] and (b) winter; Reproduced from Vialard et al. [2013].

**Equatorial IO dynamical response:** As noted above, this Ph.D. addresses the dynamical response of the NIO to the atmospheric ISV. Both MJO and active/break monsoon phases have signatures in the equatorial region, inducing ISV in the equatorial zonal wind field throughout the year. The equatorial oceanic response to that wind ISV has been described in many studies [e.g., Han, 2005; Masumoto et al., 2005; Sengupta et al., 2007; Iskandar and McPhaden, 2011; Nagura and McPhaden, 2012]. Sengupta et al. [2007] showed that the ISV of the zonal surface currents in the equatorial IO is

directly forced by the intraseasonal winds. Han [2005] noticed that the amplitude of the equatorial wind ISV peaked in the 30-60-day band, whereas that of the sea level and the surface currents ISV peaked at 90-day period, which they attributed to the basin-resonance. Using a simple model that retains only the first baroclinic mode Kelvin and first meridional mode Rossby waves, Nagura and McPhaden [2012] studied in detail the dynamics of the response of the equatorial waveguide to wind ISV. In their linear model simulation, the directly wind-forced response dominates the solution (Figure 2.16), with weak reflected waves mainly contributing to strengthening the signal close to the eastern boundary, suggesting that basin resonance is not the main explanation for the dominance of the 90-day signal (basin resonance involves wave reflections that interfere with the directly-forced signal to create nodes).

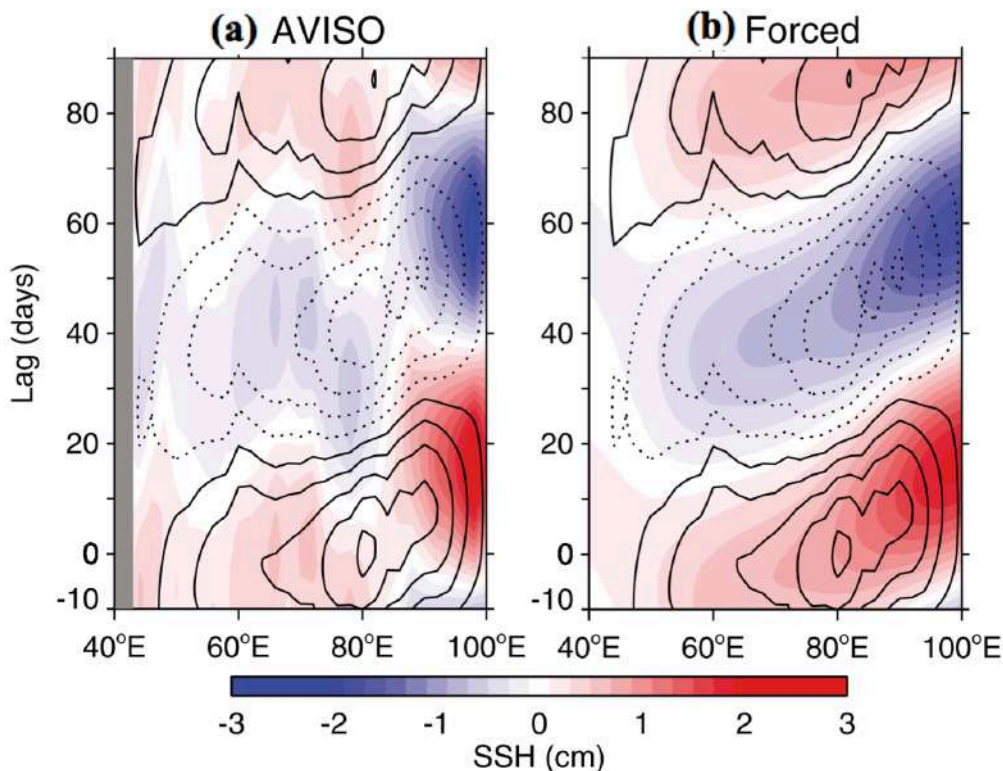


**Figure 2.16:** Lag-regression of equatorial Sea Surface Height (SSH) onto normalized wind index at 70-110 days for (a) AVISO SSH (b) directly forced SSH from a simple model that retains only the two gravest baroclinic mode KWs and first meridional mode RWs. The contours (solid – eastward; dotted–westward) indicate the lag-regressed zonal wind stresses to the above-normalized wind index, beginning with zero contour (not shown) in an interval of  $2.5 \times 10^{-3} \text{ Nm}^{-2}$ . Reproduced from Nagura and McPhaden [2012].

Rather, the main mechanism that seems to strengthen the oceanic response at 90-day timescale is the fact that the atmospheric wind forcing associated with the MJO and the oceanic KW response travel at relatively similar speed, inducing a near-resonant

response at this timescale, as already shown for the equatorial Pacific [Kessler et al., 1995]. Another factor that favors a stronger response at the 90-day period is that the large spatial scales associated with the atmospheric ISV project more efficiently on the first baroclinic mode Kelvin and low-order Rossby equatorial meridional modes at 70-110-day than at 30-60-day timescale, as can be deduced from the dispersion diagram shown in Figure 2.2. Overall, the equatorial IO response to atmospheric ISV has been well described: it is most energetic at 90-day timescale due to the near-resonant response of the ocean at this timescale, and can be described well from the first baroclinic mode Kelvin and first meridional mode Rossby waves: active phases (westerly wind anomalies) force a downwelling KW that dominates the response in the eastern equatorial IO, and an upwelling first meridional mode Rossby wave that dominates the weaker-amplitude response in the western IO. The downwelling KW reflection into a downwelling first meridional mode Rossby wave mostly contributes to the sea level ISV amplitude close to the eastern boundary.

***NIO dynamical response:*** The dynamical response of the NIO, particularly of the coastal waveguide, to the intraseasonal wind variations has been relatively less studied compared to that of the equatorial waveguide. Durand et al. [2009] found significant ISV in the sea level and currents along the ECI that they attributed to the meso-scale eddies, which indeed contribute to the variability in the interior BoB [e.g., Cheng et al., 2013]. Using satellite observations, Vialard et al. [2009] showed that the intraseasonal equatorial KWs propagate into the NIO in the form of coastal KWs. Lead-lag regressions (Figure 2.17) of the basin-scale intraseasonal sea level and wind stresses to the sea level along the WCI reveal that the sea level ISV along the WCI are associated with basin-scale sea level and wind-stress variations resulting from the atmospheric ISV (i.e. MJO and active/break monsoon phases) [Vialard et al., 2009]. In agreement with other studies [e.g. Sengupta et al. 2007; Nagura and McPhaden, 2012], Figure 2.17a shows a clear Kelvin and Rossby-wave response in the equatorial waveguide, with westerlies forcing a downwelling KW to the east and an upwelling RW to the west. The opposite polarity signals at 35-day lead (Figure 2.17a) and 7-day lag (Figure 2.17d) indicate dominance of the 90-day cycle associated with the sea level ISV, in agreement with other studies [Han, 2005; Nagura and McPhaden, 2012]. Thus the study of Vialard et al. [2009] demonstrates a clear link between the equatorial and coastal waveguides in

the NIO at intraseasonal timescales, as was earlier demonstrated at lower frequencies (e.g., seasonal).

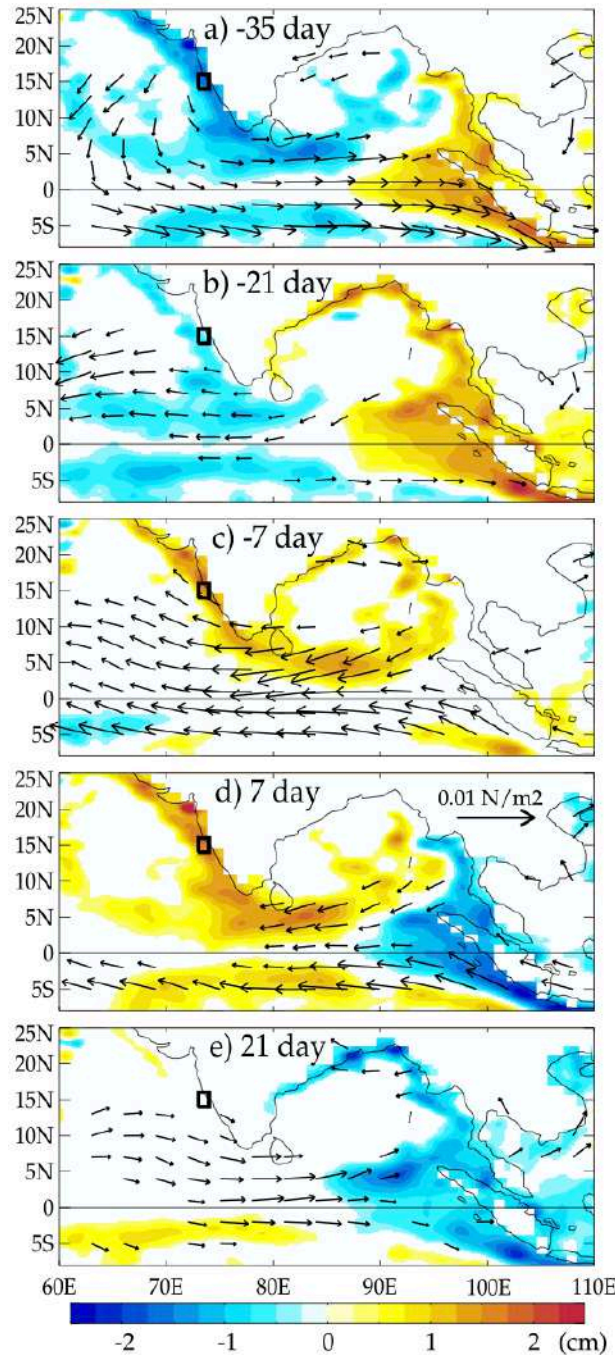


**Figure 2.17:** Lag-regression (lags indicated on the panels) of 55 to 110-day band-passed sea level and wind stresses onto 55 to 110-day band-passed sea level within the box (shown by a black frame) on the WCI. The values shown are significant at 95% confidence level. The wind stresses are from Quikscat product. Reproduced from Vialard et al. [2009].

While Figure 2.17 indicates that most of the large-scale coherent wind stress variations occur in the equatorial waveguide, there are wind variations along the WCI that could contribute to the sea level variations locally (e.g. Figure 2.17c). This poses a

fundamental question on the relative contributions from local and remote forcing to NIO sea level ISV. Analysis of current meter measurements on the WCI further suggested that the remote forcing contributes significantly to the observed intraseasonal currents [Shetye et al., 2008; Amol et al., 2012]. Girishkumar et al. [2013] analysed anomalies of satellite-based winds and SSH, and thermocline depth derived from the moored buoys along 90°E in the BoB and found large ISV at 30-70-day, 90-day and 120-day periods. Their analysis suggested that the 90-day and the 120-day signals are primarily driven by the remote equatorial wind forcing, whereas the 30-70-day variability is dominated by the interior BoB forcing. Recently, Dhage and Strub [2016] used satellite measured SLAs and winds to assess the relative importance of local and remote wind forcing to the sea level ISV along the WCI. Consistent with Amol et al. [2012], this study established high correlations between the sea level along the WCI and the winds at the southern tip of India. Furthermore, WCI intraseasonal sea level is well correlated with that east of Sri Lanka up to the Sumatra coast at increasing lags, emphasizing the importance of reflected equatorial RW signals to the WCI sea level ISV, as hypothesized by some of the earlier studies [Shetye, 1998; Gopalakrishna et al., 2008]. However, their analysis did not allow assessing the relative contributions of coastal KWs travelling through the BoB and those related to the reflected equatorial RWs.

***Unresolved questions concerning NIO sea level ISV:*** The above review on the NIO sea level ISV indicates that there are many questions (also listed in Chapter 1) that still remain unresolved. While many studies emphasize the importance of the remote forcing for sea level ISV in the coastal waveguide, the relative contributions of local and remote forcing have neither been quantified, nor the origins of those remote wind forcing have been identified. Are the equatorial and NIO coastal waveguides connected only at the western and eastern boundaries of the equatorial basin, as suggested by Shankar et al. [2002] (schematically shown in Figure 2.6) or do they intersect at the southern tip of India as speculated by some other studies (e.g. Shetye, [1998]; Vialard et al., [2009]; Dhage and Strub [2016])? If such a connection exists, would it be important for the NIO sea level variability at all (intraseasonal, seasonal, and interannual) timescales? This thesis addresses the above questions with a simple dynamical model that agrees well with the observed sea level variability at all timescales through a suite of sensitivity experiments.

### 3.1 Introduction

The observations (Section 3.2) and the numerical model (Section 3.3) used in this thesis are described in this chapter. The observations include the sea level data for validating the model simulation and the wind-stress fields for forcing the model. These observations are also subjected to analysis for understanding the sea level variability. A more detailed description and explicit mathematical treatment of the ocean model can be found in the previous literature [e.g., McCreary, 1980, 1981; McCreary et al., 1996; Shankar et al., 1996]. The aspects of the model specific to the present study are detailed here. This chapter also describes briefly (Section 3.4) the empirical orthogonal function analysis that has extensively been employed in this work to extract the dominant modes of sea level variability in the observations as well as in the model simulations.

### 3.2 Description of observations

**Sea level product:** The sea level anomaly (SLA) data, produced by Ssalto/Duacs from altimetric observations, is made available by the Archiving, Validation, and Interpretation of Satellite Oceanographic (AVISO) data project on its website <http://www.aviso.altimetry.fr>. The weekly data during the period from October 1993 to August 2013 on a regular spatial grid at a high resolution of  $0.25^\circ$  ( $\sim 25$  km) has been used in this work. Having proven to be extremely useful for studying the large-scale ocean dynamics, the altimeter measurements are not reliable within a distance of 25-50 km from the coast [Saraceno et al., 2008]. In this work, the sea level variability off the NIO coast is dealt with mainly through the coastal KWs that propagate at the shelf break and hence the altimeter-based sea levels still prove to be useful as demonstrated in several studies of the sea level variability along the Indian coast (for e.g., Rao et al. [2010]; Dhage and Strub [2016]).

***Preprocessing of sea level data:*** The long-term linear trend is removed from the SLA time series before subjecting it to any further analysis. The seasonal cycle is constructed as the sum of the first four (annual, semiannual, 120-day and 90-day) harmonics, obtained through a least-square fit. The intraseasonal signal is obtained by applying a 20–150-day band-pass filter, after removing the seasonal cycle. The interannual signal is obtained by subjecting the detrended SLA time series to a band-pass filter with cut-off of less than 150-day and greater than 7-year periods, after removing the seasonal cycle.

***The wind-stress products:*** The surface wind-stress fields are mainly used for forcing the numerical ocean model described in Section 3.3. Two different wind-stress products, namely the QuikSCAT and the TropFlux, are used to assess the sensitivity of the model results to the forcing fields and to ensure the robustness of the results.

***QuikSCAT wind-stress fields:*** QuikSCAT surface wind-stress fields from August 1999 to October 2009 are freely available on the website <http://cersat.ifremer.fr/data/>. This daily data on a  $0.5^\circ$  spatial grid is mapped onto the model grid at  $0.25^\circ$  resolution using bilinear interpolation. Although the wind stresses away from the equator are overestimated [Praveen Kumar et al., 2013], QuikSCAT has been widely used in many studies of the tropical IO ISV [e.g., Senan et al., 2003; Sengupta et al., 2007; Nagura and McPhaden, 2012]. These studies have clearly shown that the model simulation using QuikSCAT wind forcing well reproduces the observed features.

***TropFlux wind-stress fields:*** The more recent TropFlux wind-stress product, primarily derived from ERA-I (European Centre for Medium Range Weather Forecast interim) [Dee et al., 2011] reanalysis data, is available during the 1979-2013 period from <http://www.incois.gov.in/tropflux/> [Praveen Kumar et al., 2013]. This daily data on a  $1^\circ$  spatial grid is mapped onto the model grid at  $0.25^\circ$  resolution using bilinear interpolation. Praveen Kumar et al. [2013] provided a detailed evaluation of the TropFlux wind stresses over tropical oceans and demonstrated its better performance over the other widely used wind-stress products, especially near the equator and for the intraseasonal timescales.

**Preprocessing of wind stress data:** As with the sea level observations, the seasonal wind stresses are constructed as the sum of the first four harmonics obtained through a least-square fit, and the intraseasonal and interannual wind stresses are extracted using the same filters, after removing the seasonal cycle.

**The density profiles:** The vertical density profiles are derived from the climatological vertical temperature and salinity profiles from the World Ocean Atlas-2009 (WOA09) [Locarnini et al., 2010] dataset using the Equation of State [Jackett and McDougall, 1995]. These density profiles are then used for computing the background stratification for the numerical ocean model described in Section 3.3.

**DMI:** DMI characterizes the IOD (described in Section 2.3) intensity and is computed as the SST difference between the western equatorial IO ( $50^{\circ}$ - $70^{\circ}$ E and  $10^{\circ}$ S- $10^{\circ}$ N) and the southeastern equatorial IO ( $90^{\circ}$ - $110^{\circ}$ E and  $10^{\circ}$ S- $0^{\circ}$ ), which in essence, represents the east-west temperature gradient over the tropical IO. Positive (negative) values of DMI represent positive (negative) IODs. The DMI data used in this thesis is downloaded from <http://www.jamstec.go.jp/frcgc/research/d1/iod/DATA/dmi.monthly.txt>.

**MEI:** MEI characterizes the ENSO (described in Section 2.3) magnitude and timing, and performs better compared to other SST-based ENSO indices [Wolter and Timlin, 1998] as it integrates information from the coupled ocean-atmosphere ENSO processes. Besides SST, MEI incorporates five additional observed parameters of the tropical Pacific, namely, the sea-level pressure, the zonal and meridional components of the surface wind, the surface air temperature, and the total cloudiness fraction of the sky, and is computed as the first PC of those fields combined. The MEI data used here is the one downloaded from <https://www.esrl.noaa.gov/psd/enso/mei/table.html>.

### 3.3 The ocean model

**LCS model:** This study uses a linear, continuously stratified (LCS) ocean model, which is a modified version of the one presented in McCreary et al. [1996]. While this section presents most of the aspects of the LCS model, it is recommended to refer to McCreary

[1980; 1981], McCreary et al. [1996] or Shankar et al. [1996], for a more complete description.

**The governing equations:** The model equations of motion are linearized about a state of rest with Brunt–Väisälä frequency ( $N_b(z)$ ) (Figure 3.1d), which is computed from realistic background stratification derived from the basin-averaged ( $40^\circ\text{E}$ - $100^\circ\text{E}$ ,  $15^\circ\text{S}$ - $15^\circ\text{N}$ ) WOA09 climatological vertical density profile shown in Figure 3.1a-c. The model ocean has a uniform depth of  $4000\text{ m}$  (flat bottom). With specific choices on the mathematical forms of the mixing coefficients and the surface and bottom boundary conditions, the solutions of the above linear equations are represented as expansions in vertical normal modes, which are eigenfunctions,  $\psi_n(z)$ , satisfying the equation,  $\left(\frac{1}{N_b^2} \psi_{nz}\right)_z = -\frac{1}{c_n^2} \psi_n(z)$ , subject to the boundary conditions,  $\psi_{nz}(-D) = \psi_{nz}(0) = 0$ , where  $D$  ( $= 4000\text{ m}$ ) is the ocean depth. The eigenvalue,  $c_n$ , of the above equation represents the characteristic KW speed of the  $n$ -th mode (Figure 3.2).

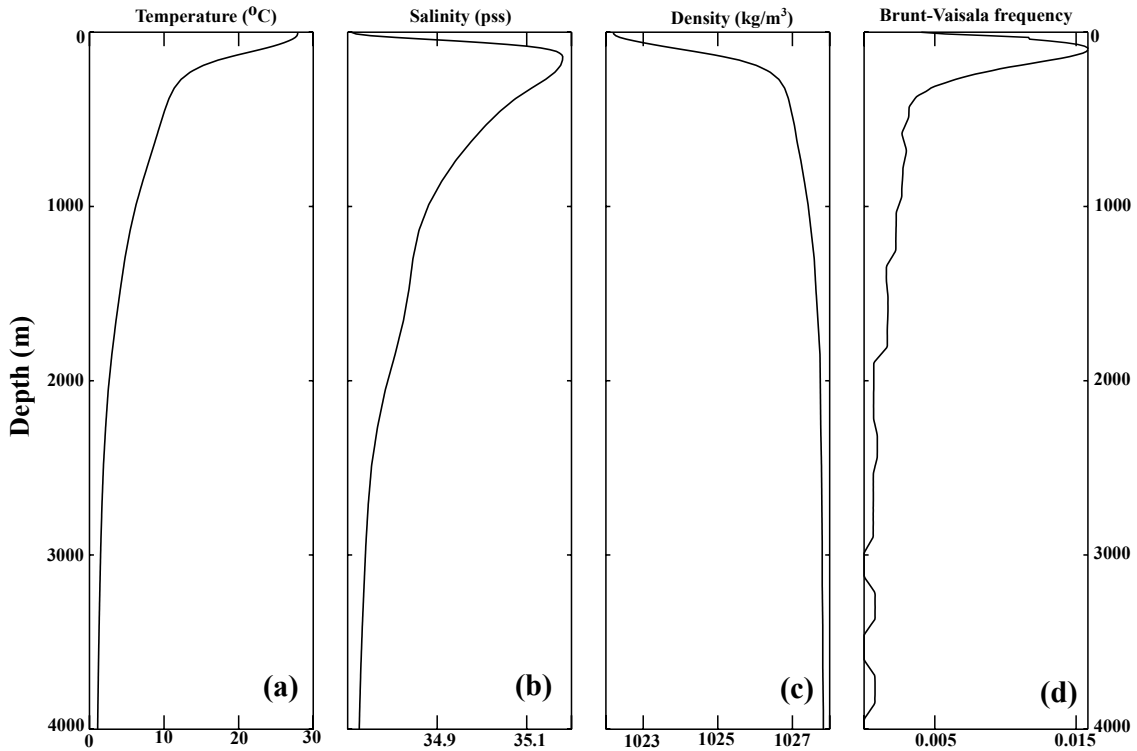


**Figure 3.1:** The WOA09 basin-averaged ( $40^\circ\text{E}$ - $100^\circ\text{E}$ ,  $15^\circ\text{S}$ - $15^\circ\text{N}$ ) climatological vertical (a) temperature, (b) salinity, and (c) density profiles. The density profile is used as the background stratification for the LCS model and is also used for computing the vertical modes, their structures and the wave speeds (see Figure 3.2). (d) The vertical profile of the Brunt–Väisälä frequency,  $N_b(z)$ , computed from the density profile shown in panel c.

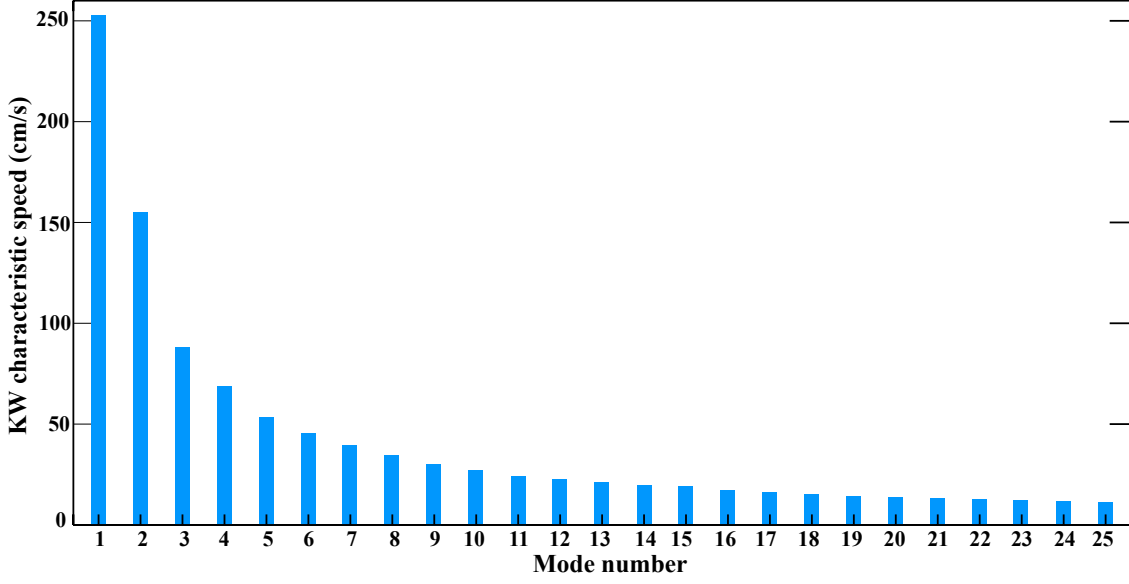


*Figure 3.2: The characteristic KW speeds as a function of mode numbers, computed with the background stratification shown in Figure 3.1.*

The zonal ( $u$ ) and meridional ( $v$ ) velocities, and the pressure ( $p$ ) fields are expanded in terms of the vertical normal modes as

$$u = \sum_{n=1}^N u_n \psi_n,$$

$$v = \sum_{n=1}^N v_n \psi_n,$$

and

$$p = \sum_{n=1}^N \bar{\rho} p_n \psi_n.$$

In the above equations,  $\bar{\rho}$  denotes a typical value of the density of the seawater, the expansion coefficients,  $u_n$ ,  $v_n$ , and  $p_n$ , are all functions of  $x$ ,  $y$  and  $t$  alone, and the above series converge rapidly for small value of  $N$  ( $= 5$ , as demonstrated in Sections 4.2.2 and 5.5.1). The above summations do not include the barotropic mode because of their small contribution to the solution in comparison to that of the baroclinic modes.

The equations for the expansion coefficients take the form,

$$u_{nt} - f v_n + p_{nx} = F_n - \frac{A}{c_n^2} u_n + v_2 \nabla^2 u_n$$

$$v_{nt} + f u_n + p_{ny} = G_n - \frac{A}{c_n^2} v_n + v_2 \nabla^2 v_n$$

$$\frac{p_{nt}}{c_n^2} + u_{nx} + v_{ny} = -\frac{A}{c_n^4} p_n$$

where  $\nu_2$  is the horizontal mixing coefficient and  $f$ , the Coriolis parameter. In essence, these equations themselves represent linearized shallow-water equations for each baroclinic mode  $n$ , and the LCS model amounts to solving those equations individually for each baroclinic mode ( $n$ ) with a characteristic KW speed,  $c_n$  (Figure 3.2), computed from the background stratification shown in Figure 3.1.

**Wind forcing in the model:** The wind forcing is introduced into the ocean as a body force with a profile,  $Z(z)$ . The terms  $F_n$  and  $G_n$  are then given by  $F_n = \tau^x Z_n / (\bar{\rho} H_n)$  and  $G_n = \tau^y Z_n / (\bar{\rho} H_n)$ , where  $\tau^x$  and  $\tau^y$  are the zonal and meridional wind stresses, and  $H_n = \int_{-D}^0 \psi^2 dz$  and  $Z_n = \int_{-D}^0 Z(z) \psi_n(z) dz$  are the coupling factors. The vertical profile,  $Z(z)$ , used here follows that of McCreary et al. [1996], which is constant down to 50 m and ramped to zero at 100 m (Figure 3.3). The wind stress fields for forcing the model are obtained from both QuikSCAT and TropFlux products (described in Section 3.2).

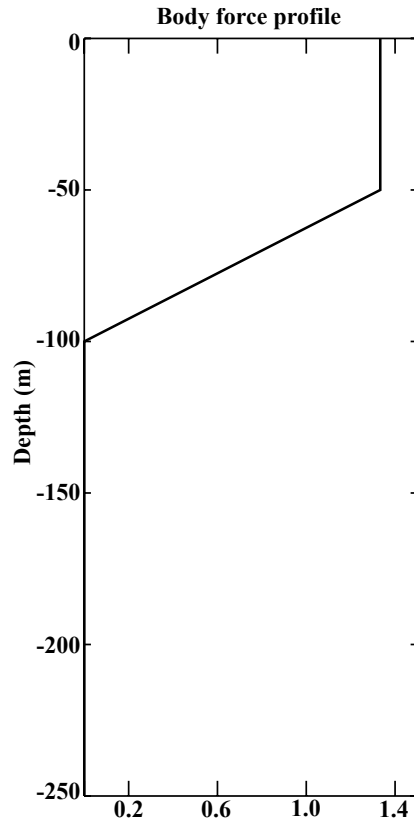


**Figure 3.3:** The body-force profile,  $Z(z)$ , that determines how the wind forcing enters the ocean in the LCS model.

**Background stratification for the model:** The background stratification used here is the one obtained from the averaged (15°S-15°N, 40°E-100°E) WOA09 climatological potential density profile shown in Figure 3.1. The profile of Brunt–Väisälä frequency,  $N_b(z)$ , computed from the above density profile is also shown (Figure 3.1d). The corresponding KW speeds for the first five modes are  $252 \text{ cm s}^{-1}$ ,  $155 \text{ cm s}^{-1}$ ,  $88 \text{ cm s}^{-1}$ ,  $69 \text{ cm s}^{-1}$ , and  $53 \text{ cm s}^{-1}$  and are also shown in Figure 3.2 as a function of mode numbers.

**The model domain, resolution and land-ocean configuration:** The domain of the model (Figure 3.4) covers the IO region from 30°S to 30°N and from 30°E to 110°E. As mentioned above, the model ocean (Figure 3.4b) has a flat bottom and is 4000-*m* deep. The coastline of the model ocean is treated as vertical wall to allow propagation of coastal KWs. The shelf break is a very good approximation for vertical wall than the actual coastline and it occurs at  $\sim 200 \text{ m}$ , as indicated by the IO bathymetric [Smith and Sandwell, 1997] map (Figure 3.4a). Accordingly, coastline of the model ocean is determined from the 200-*m* isobaths (Figure 3.4). The Red Sea and Persian Gulf are closed (modified into land points) in this land-ocean configuration and so is the Palk Strait (Figure 3.4b). Also, any single land point is modified into ocean and vice versa. Any single strip of land is converted to two or more strips of land points to avoid spurious exchange of signals arising from the lateral boundary condition applied at this strip of land points. All these changes made in the land-ocean configuration ensure numerical stability and also optimize the model computational time. The solutions are obtained numerically on a  $0.25^\circ$  (25 *km*) regular grid.

**Lateral Boundary conditions:** The northern and western boundaries of the model domain are closed with the continental land boundary (Figure 3.4b). While the northeastern boundary of the model is closed with the eastern rim of the BoB and Sumatra coast, the southeastern and the southern boundaries remain open (Figure 3.4b). The zero-gradient, open boundary conditions, which when applied at the open boundaries, develop instability along these boundaries. As in McCreary et al. [1996], a damper (on  $u_n$  at the southern and on  $v_n$  at the southeastern boundary), which has maximum value of  $1 \text{ day}^{-1}$  within 150 *km* and ramps linearly to 0 between 150 and 300 *km* of the boundary, has been applied. This allows signals to propagate freely through

these open boundaries. At the continental boundaries, the common no-slip condition is used.

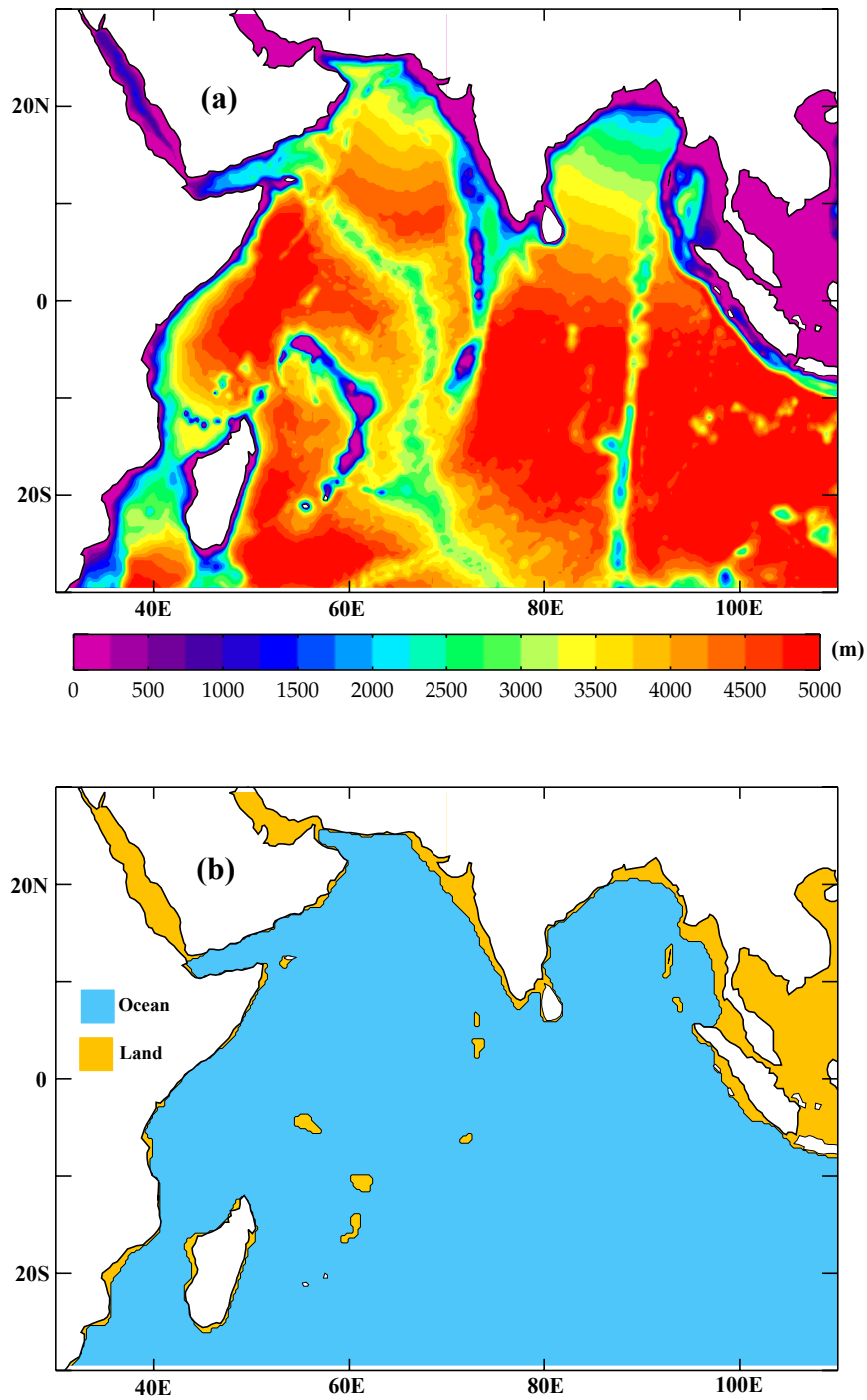


**Figure 3.4:** The model domain. (a) Bathymetry of the IO from ETOPO2 dataset [Smith and Sandwell, 1997] (b) The blue shaded region is the model ocean and the yellow (shelf) and white regions are the model land. This land-ocean configuration is determined from the 200-m depth contour (line of transition between blue and yellow). The actual coastline (line of transition between yellow and white) is shown for a comparison with the model coastline.

**Table 3.1:** Summary of the results of LCS model experiments carried out for fixing the vertical,  $A$ , and horizontal,  $\nu_2$ , mixing coefficients for seasonal and intraseasonal simulations. The evaluation is based on correlation and RMS error (indicated respectively in brackets) of a basin averaged ( $15^\circ\text{S}$ - $15^\circ\text{N}$ ;  $40^\circ$ - $100^\circ\text{E}$ ) sea level between model and observations. The coefficients corresponding to the experiment that shows the best performance have been chosen for the CTL simulation in Chapter 4.

Values of the mixing coefficients	Full timeseries	Seasonal	Intraseasonal
$A = 2.0 \times 10^{-3} \text{cm}^2 \text{s}^{-3}$ (12-month) $\nu_2 = 1 \times 10^5 \text{cm}^2 \text{s}^{-1}$	(0.59, 7.0)	(0.70, 4.0)	(0.29, 3.8)
$A = 2.0 \times 10^{-3} \text{cm}^2 \text{s}^{-3}$ $\nu_2 = 5 \times 10^6 \text{cm}^2 \text{s}^{-1}$	(0.62, 6.7)	(0.72, 3.9)	(0.33, 3.7)
<b><math>A = 2.0 \times 10^{-3} \text{cm}^2 \text{s}^{-3}</math></b> <b><math>\nu_2 = 5 \times 10^7 \text{cm}^2 \text{s}^{-1}</math></b>	<b>(0.65, 6.6)</b>	<b>(0.74, 3.8)</b>	<b>(0.37, 3.5)</b>
$A = 4.0 \times 10^{-3} \text{cm}^2 \text{s}^{-3}$ (6-month) $\nu_2 = 5 \times 10^7 \text{cm}^2 \text{s}^{-1}$	(0.62, 6.8)	(0.70, 4.0)	(0.38, 3.5)
$A = 3.4 \times 10^{-4} \text{cm}^2 \text{s}^{-3}$ (6-year) $\nu_2 = 5 \times 10^7 \text{cm}^2 \text{s}^{-1}$	(0.68, 6.4)	(0.77, 3.7)	(0.36, 3.6)

**The choice of mixing coefficients:** While many of the previous studies (for e.g., McCreary et al., [1996]; Shankar et al., [1996]; Nagura and McPhaden, [2012], Chatterjee et al., [2013]) that used the LCS model already suggest a choice of values for the model parameters, especially the vertical and the horizontal mixing coefficients, a dedicated exercise for fixing those coefficients has been carried out in this study. This exercise involves performing model simulations with different choices of those mixing coefficients and finalizing those values that yield the best performance of the model when evaluated against observations. The best performance of the model is achieved with different values for the mixing coefficients depending on the timescale involved. Table 3.1, for instance, provides summary of the above exercise for intraseasonal and seasonal timescales. The model is forced with QuikSCAT wind stresses and the modeled intraseasonal and seasonal sea levels are evaluated against those from the observations, in terms of basin-averaged sea level correlations and Root Mean Square (RMS) errors. Table 3.1 indicates that the best performance of the model at intraseasonal and seasonal timescales is achieved when the coefficient of the horizontal mixing,  $\nu_2$ , is chosen to be  $5 \times 10^7 \text{cm}^2 \text{s}^{-1}$  and that of the vertical mixing,  $A$ , to be  $2.0 \times 10^{-3} \text{cm}^2 \text{s}^{-3}$ , which corresponds to  $\sim 12$ -month dissipation timescale for the first baroclinic mode ( $c_1^2/A$ ). These values are hence used for the model simulations presented in Chapter 4. This choice for the vertical mixing does not yield the best performance of the model at interannual timescale. For interannual timescale, a similar exercise has been carried out (not shown) and the best performance of the model is found when the vertical mixing

coefficient,  $A$ , is set to  $2.89 \times 10^{-3} \text{ cm}^2 \text{ s}^{-3}$ , which corresponds to  $\sim 7$ -year dissipation timescale for the first baroclinic mode. This choice of  $A$  is also found to yield nearly the same performance of the model for intraseasonal and seasonal timescales (presented in Table 3.1), and hence this value has been used for the simulations in Chapters 5 (intraseasonal) and 6 (seasonal and interannual). A detailed evaluation of the model at intraseasonal, seasonal and interannual timescales is presented in Sections 4.3.1, 5.6.1, 6.1.2 and 6.2.2, respectively.

***The main simulation and sensitivity experiments:*** The LCS model forced with the QuikSCAT (Chapter 4) or TropFlux (Chapter 5) wind-stress fields has been termed as the main or control (CTL) simulation/solution in this thesis. The linearity of the model has been best exploited in this study, in the sense that the processes that make up the CTL solution can be isolated using specially designed experiments, called the sensitivity experiments or process solutions. The linearity of the model ensures that the summation of the process solutions yields the CTL solution. As in McCreary et al. [1996], a process solution is obtained using dampers and/or by applying special boundary condition (SBC) in specific regions.

***Dampers for model sensitivity experiments:*** Simple Newtonian damper [McCreary et al., 1996] with coefficient,  $\delta(x, y)$ , which when applied over a (rectangular) region of interest (value of  $\delta(x, y)$  is maximum,  $c_n / (1.5 \Delta x)$ , within the rectangular box and 0 outside the region), allows the waves to decay rapidly with an e-folding scale of  $1.5 \Delta x$ , where  $\Delta x$  is the grid size. To avoid distortions in the solutions, the damping coefficients are ramped linearly to zero within  $1^\circ$  from the edges of the region. The solution obtained with such a damper will thus be free from the effect of waves emanating out from that region. When using multiple dampers adjacent to each other, it is ensured that the edges of those dampers match and the ramping coefficients add up to 1 in the overlapping region. Section 5.5.2 illustrates the usage of these dampers in the sensitivity experiments for isolating the processes.

***Special boundary conditions for model sensitivity experiments:*** SBC used in this work is of the same form as the one in McCreary et al. [1996].

$$\bar{u}_n = \mathbf{n} \cdot \mathbf{v}_n = -\mathbf{n} \cdot \mathbf{k} \times \frac{F_n}{f}$$

$$\bar{v}_n = \mathbf{k} \times \mathbf{n} \cdot \mathbf{v}_n = 0,$$

where  $\mathbf{n}$  is a unit vector perpendicular to the coast and  $\mathbf{k}$  is an upward-directed unit vector.  $\mathbf{v}_n = (u_n, v_n)$ , with  $\bar{u}_n, \bar{v}_n$ , the horizontal components of velocity parallel and perpendicular to the coast. The effect of the above SBC is to filter out coastal Ekman pumping at the coast by allowing the Ekman flow to pass through the boundaries and hence no coastal KW is generated. The usage of SBC is best illustrated in Section 5.5.2 through sensitivity experiments.

**Wave Trap:** Some of the sensitivity experiments require modifying the land points over a region to ocean, and damping out the signals (using dampers) within that region to isolate specific processes. The region thus behaves like a wave trap, i.e., the waves that enter the region get trapped within that region and the solution remains free from those waves. The technique has been used especially when usage of dampers (over the ocean) might affect the processes other than the one in the context. Usage of wave trap has been illustrated in Section 5.5.2.

**Remark:** A general overview and basic configuration of the LCS model has been provided in this chapter. The model has been used to address specific science questions in the rest of chapters (Chapters 4, 5 and 6) of this thesis. More specific description and set up of the model, including details on the sensitivity experiments for addressing those questions, have been presented in the respective chapters (see Sections 4.2.1 and 5.5.1).

**Preprocessing of model sea level:** As for the observed sea level (Section 3.2), the model sea level seasonal cycle is constructed as the sum of the first four (annual, semiannual, 120-day and 90-day) harmonics, obtained through a least-square fit. The intraseasonal signal is obtained by applying a 20–150-day band-pass filter on the seasonal anomalies. The interannual signal is obtained by subjecting the seasonal anomalies to a band-pass filter with cut-off of less than 150-day and greater than 7-year periods.

### 3.4 Statistical methods

*The Empirical Orthogonal Functions method:* Besides simple statistical analysis such as correlation and regression, the Empirical Orthogonal Functions (EOF) method [e.g. Emery and Thomson, 1998] has been extensively used in this thesis. EOF analysis is a commonly used data reduction method to study the spatial and temporal variability of geophysical fields in terms of orthogonal functions. The method extracts the spatial patterns of variability, their evolution in time, and provides a measure of their importance. EOF analysis involves constructing a covariance matrix of the given field and solving the eigenvalue problem, i.e., finding the eigenvalues and eigenvectors of the covariance matrix. The eigenvectors are the spatial patterns, called the EOF spatial modes, and the eigenfunctions, usually referred to as the principal components (PC), represent their time evolution, their temporal variance being the eigenvalues. The spatial patterns (EOF modes) are ordered with respect to the magnitude of the corresponding eigenvalues. Thus the first EOF, denoted as EOF1 (and associated PC1), corresponds to the eigenvalue with maximum magnitude, EOF2 (and associated PC2) corresponds to the next biggest eigenvalue, and so on. The variance explained by an EOF mode is simply the corresponding eigenvalue divided by the sum of all the eigenvalues, usually indicated in percentage. The EOF spatial modes, which are orthogonal to each other, are uncorrelated in space and represent essentially the standing oscillations in the field. And similarly, the PCs are uncorrelated in time. It should be noted here that the EOF modes do not necessarily represent any physical or dynamical modes of the system. It simply partitions the variance of the given data and hence any relevance to a physical mode is a subjective interpretation. More information on EOF analysis can be found in Björnsson and Venegas [1997].

# Origin of intraseasonal sea level variability in the Northern Indian Ocean coastal waveguide

---

## 4.1 Introduction

**Background for this chapter:** The winds over the IO exhibit strong variability at intraseasonal timescales that are mainly associated with the active/break monsoon phases during summer and the MJO during winter (see Section 2.4). Previous studies discussing this wind variability and the associated oceanic response have been extensively reviewed in Section 2.4. Of particular interest here is the study of Vialard et al. [2009], who found strong ISV in the alongshore currents observed during the 2006-2008 period along the continental slope off Goa (at 15°N) on the WCI. They showed, using a suite of satellite observations and an ADCP measuring the upper ocean currents, that the winds associated with the MJO force equatorial KWs, a part of which enters into the BoB rim as coastally-trapped KWs at the eastern end of the equatorial basin. These coastal KWs travel all around the rim of the Bay, make their path around Sri Lanka and further propagate northward along the WCI. This study thus suggested a clear basin-scale link between the equatorial and the NIO coastal waveguides at intraseasonal timescales, as was demonstrated at the seasonal timescale by earlier studies [for e.g., McCreary et al., 1993; Shetye, 1998]. Although this study paved the way for an improved understanding of the processes driving the ISV in the NIO coastal waveguide, there are still many unresolved issues to be addressed.

**Motivation and aim:** While all previous studies (see for e.g. McCreary et al. [1993], Shankar and Shetye [1997]; Vialard et al. [2009]) emphasized the importance of remote forcing in driving the ISV of NIO sea level and currents, they did not precisely quantify the relative effects of local and remote forcing. Moreover, the exact pathways of remotely forced signals and their relative contributions to the sea level ISV along the NIO coastal waveguide have so far not been explored in detail. The aim of this chapter is to address the above questions in the simplest form: what are the relative

contributions of the basin-wide (equatorial/BoB/AS/Southern IO (hereafter, SIO)) intraseasonal wind forcing to the sea level ISV in the NIO coastal waveguide? Section 4.2 provides details on the LCS model (described in Section 3.3) sensitivity experiments that allow us to quantify the above-mentioned contributions in Section 4.3. Section 4.4 summarizes the results with a discussion.

## 4.2 Model setup and sensitivity experiments

### 4.2.1 Model setup

**Model configuration:** The specifications, in general, of the LCS model are provided in Section 3.3, and those specific to this chapter are detailed here. The vertical mixing has the same form as in McCreary et al. [1996], but with a 12-month dissipation time scale for the first baroclinic mode (see Section 3.3) as in Nagura and McPhaden [2012], implying a  $\sim 5$ -month dissipation timescale for the second baroclinic mode. The horizontal mixing coefficient is set to  $5000 \text{ m}^2 \text{ s}^{-1}$ . The model is forced by intraseasonal (20-150-day filtered), daily, Quick Scatterometer (QuikSCAT) wind-stresses (available from [http://cersat/ifremer.fr/data/](http://cersat.ifremer.fr/data/)) from August 1999 to October 2009 (more details in Section 3.2). Several studies indicate that this wind-stress product yields a realistic intraseasonal oceanic response in the equatorial IO [e.g., Sengupta et al., 2007; Nagura and McPhaden, 2012]. As in Nagura and McPhaden [2012], the model solution considered here is the sum of the first five baroclinic modes, though the first two modes themselves are sufficient to explain most of the variability in the NIO as discussed in the following section.

### 4.2.2 Contributions from baroclinic modes

**First two modes vs. twenty modes:** The solution of the linear model is well converged using only the first five modes, with almost identical results with the first twenty modes. Figure 4.1, which displays the maps of coefficient of linear regressions of the first, second, and the sum of the first two baroclinic modes onto the sum of the first 20 modes, indicates that the sum of the first two baroclinic modes alone can explain more than 90% of the 20-mode solution everywhere in the NIO, except in a narrow equatorial

strip (Figure 4.1c). Even in this narrow band, the two modes explain more than 80% of the 20-mode solution. This is in agreement with Nagura and McPhaden [2012], who show that the first two baroclinic modes are sufficient to reproduce the equatorial ISV in the IO.

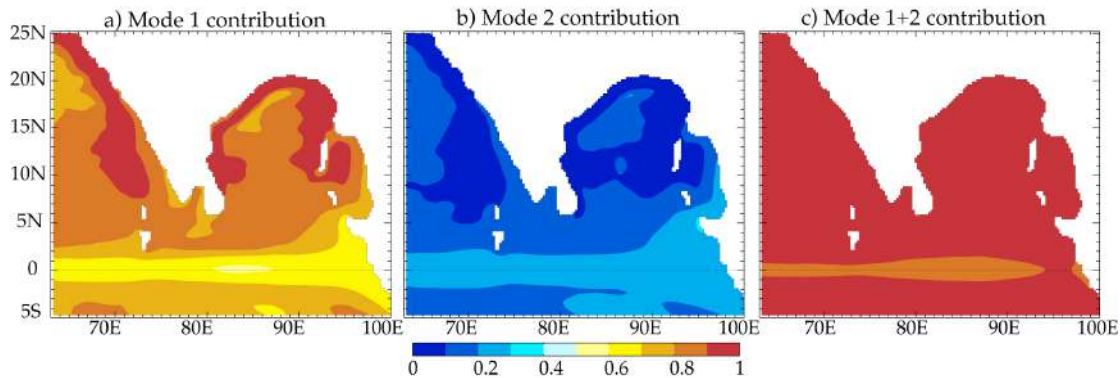


**Figure 4.1:** Regression coefficient of a) first, b) second and c) sum of first two baroclinic modes sea level to the sea level obtained from the sum of the first 20 baroclinic modes.

**Contributions from individual modes:** In the NIO coastal waveguide, the first mode is generally sufficient to explain most of the variability, except south of  $15^{\circ}\text{N}$  in the Andaman Sea and eastern AS (Figure 4.1a). While the second mode explains 20 to 30% of the sea level solution in the equatorial waveguide, it explains at most 20%, and often less than 10% in the coastal waveguide (Figure 4.1b). The Rossby radius of deformation for the second baroclinic mode is less than  $50\text{ km}$  north of  $12^{\circ}\text{N}$  and hence mode 2 would vanish in the model due to insufficient resolution (i.e., 2 grid points in the  $25\text{-km}$  model resolution) and numerical dissipation. Since mode 2 plays a smaller role in the coastal waveguide than at the equator, vertical propagation (downward propagation of energy/upward phase propagation, [Romea and Allen, 1983]) will be more limited in the model’s coastal waveguide than that diagnosed at the equator [Iskandar and McPhaden, 2011] from observations. However, the co-existence of modes 1 and 2 south of  $15^{\circ}\text{N}$  along the WCI (Figures 4.1a and b) will allow some downward propagation of energy in agreement with the inferences of Amol et al. [2012] from the current measurements off the WCI.

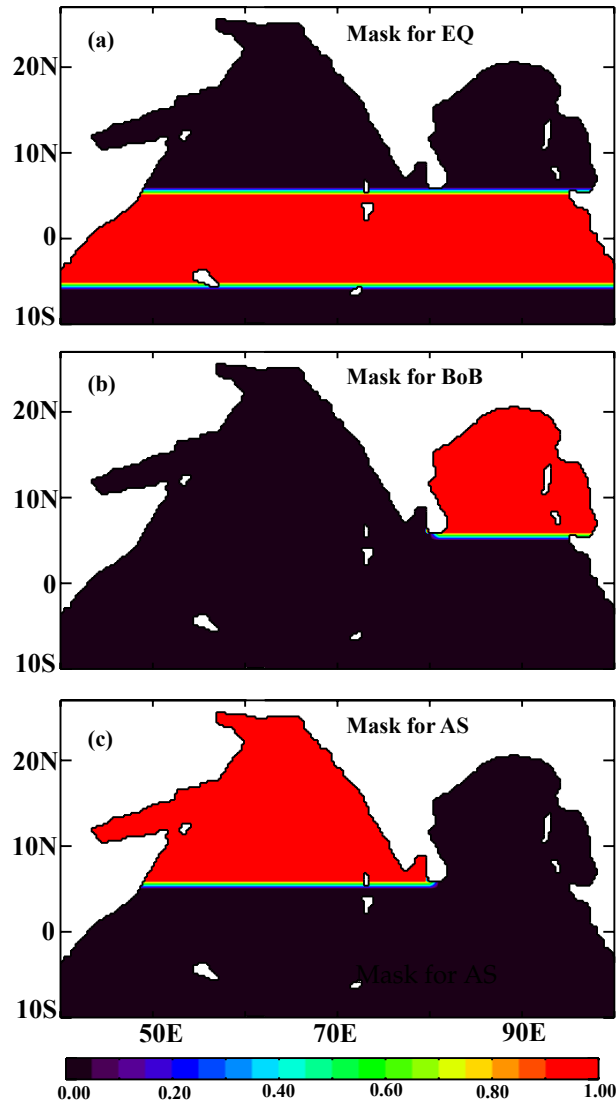


**Figure 4.2:** Set up for the sensitivity experiments described in Section 4.2.3. The shading denotes the mask, which is a value between 0 and 1, which when multiplied with the wind forcing yields the forcing for the sensitivity experiment. For instance, the panel (a) defines the mask values for the EQ experiment. The values are 1 between 5°N and 5°S, and are ramped down to 0 within 1° distance away from these boundaries. These mask values allow applying the wind forcing only within the equatorial band, with a forcing that is smoothly ramped down to 0 within 1° from this equatorial band. (b) BoB denotes the mask for Bay of Bengal and (c) AS for the Arabian Sea.

### 4.2.3 Sensitivity Experiments

**Detail of sensitivity experiments:** The model solution with the QuikSCAT forcing described in Section 4.2.1 above is referred to as the control (CTL) experiment. To assess the relative importance of intraseasonal wind forcing in the equatorial (EQ), BoB, AS, and SIO basins, sensitivity experiments are performed by applying intraseasonal wind forcing only in each of those basins (Figure 4.2). The EQ region is

bounded between 5°N and 5°S; the BoB and AS are confined to the north of 6°N and are divided at 79.75°E (Figure 4.2); the SIO is confined to the south of 6°S. The forcing in each sensitivity experiment is ramped down to zero within 1° of the borders of the forcing region, and the sum of all the forcing (i.e., EQ + BoB + AS + SIO) is equal to the forcing of CTL experiment. The linearity of the model then ensures that the sum of solutions of the sensitivity experiments is equal to the CTL solution. Table 4.1 summarizes the above description of model experiments. The above ramping of the wind forcing near the borders of the forcing region may induce spurious wind-stress curl (and hence Ekman pumping), whose effect has been discussed in Section 4.3.2.

**Table 4.1:** Summary of the sensitivity experiments

<i>Sensitivity Experiment</i>	<i>Regions with full intraseasonal wind forcing</i>
CTL	NIO
EQ	Equatorial band between 5°S and 5°N
BoB	North of 6°N and east of 79.75°E within the Bay of Bengal
AS	North of 6°N and west of 79.75°E within the Arabian Sea
SIO	South of 6°S

## 4.3 Results

### 4.3.1 Model validation

**Validation of EOF patterns:** The large-scale, intraseasonal sea level patterns in the observations and model are extracted using EOF analysis (described in Section 3.4). The first EOF mode is well separated from the rest of the modes in both observations (17% for EOF1 shown in Figure 4.3b and 6% for EOF2) and model CTL experiment (44% for the EOF1 shown in Figure 4.3f and 14% for EOF2), and captures the dominant large-scale intraseasonal sea level signal throughout the basin. The explained variance is larger in the model than in the observations because the model being linear does not produce eddies, which tend to reduce the explained variance in the observations. The correlation between the first PCs of the modeled and observed sea levels (time series) is 0.89 (Figure 4.4), indicating that this linear model captures the phase of the observed basin-scale sea level ISV remarkably well.

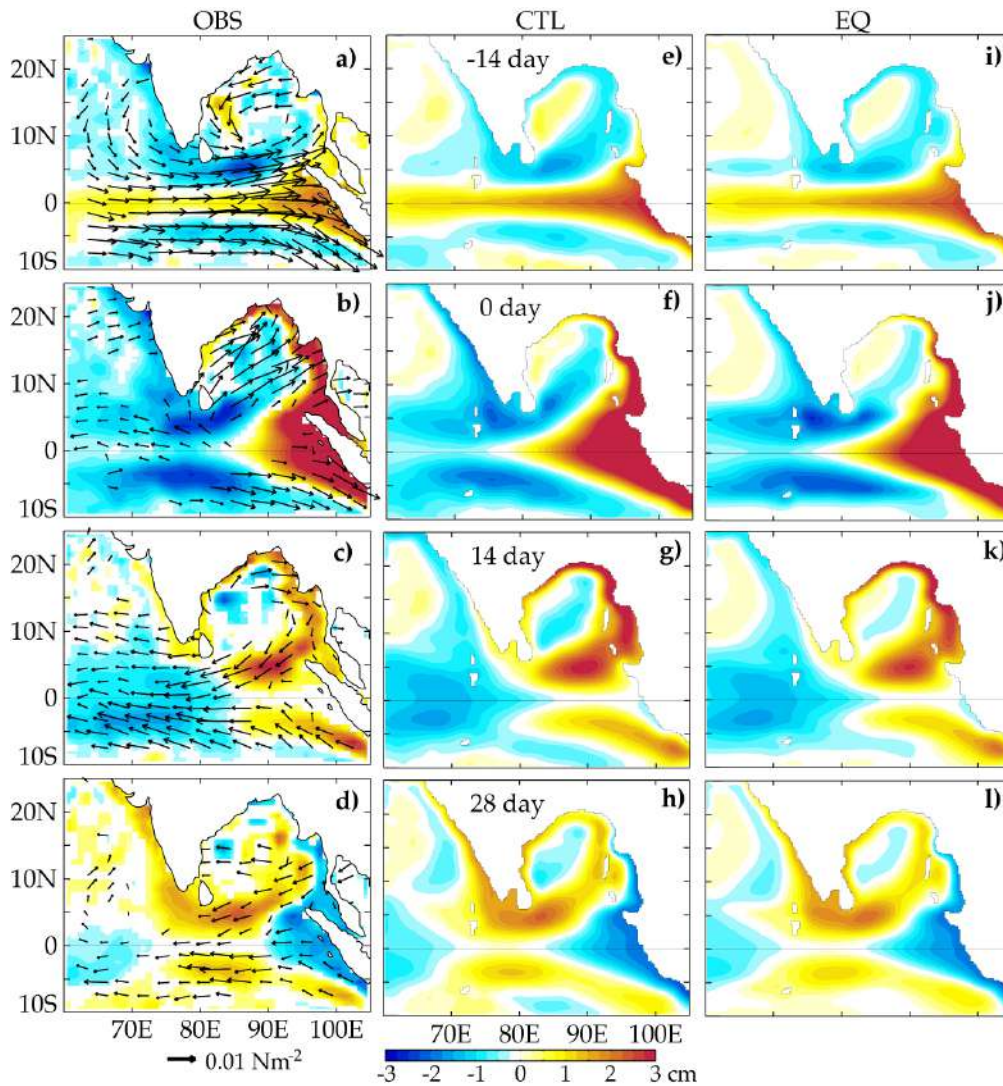


**Figure 4.3:** Lag-regression (lags indicated on the middle column) of 20-150-day filtered QuikSCAT wind stress (first column) and sea level to the normalized PC of the EOF1 of 20-150-day filtered sea level (negative lags for regression maps leading the PC) in: a-d) observations (17% of total variance, second mode 6%), e-h) CTL experiment (44% of total variance, second mode 14%) and i-l) EQ experiment (49% of total variance, second mode 15%). The regression at lag 0 (panels b, f, and j) shows the spatial structure of the first EOF. Values that are not statistically significant at the 95% confidence level are masked (standard *t*-test, with one degree of freedom per 70 days of data, as determined from the lagged autocorrelation of the PC used for the regression).

**Validation of basin-scale patterns:** The wind stress and sea level patterns obtained from a lag-regression to the PCs associated with the first EOFs of observed and modeled intraseasonal sea levels are shown in Figure 4.3. Despite the differences in the method of analysis, the patterns shown here are remarkably similar to those shown in Vialard et al. [2009] and Iskandar and McPhaden [2011], indicating the robustness of these patterns. These patterns reveal that the equatorial westerly wind-stress anomalies force an equatorial downwelling KW (Figures 4.3a,b) that propagates eastward and gets

reflected at the eastern boundary of the equatorial basin (Sumatra coast) as a downwelling equatorial RW (Figures 4.3c,d), with some part of the energy propagating in the form of downwelling coastal KWs into and around the BoB rim (Figures 4.3b and 4.3c) and up the WCI (Figure 4.3d). Figures 4.3e-h show that the CTL simulation captures the observed sea level patterns remarkably well, both in the equatorial band and in the NIO coastal waveguide, suggesting that this model captures the underlying dynamics of ISV and hence is well suited to study the ISV in the NIO waveguide.

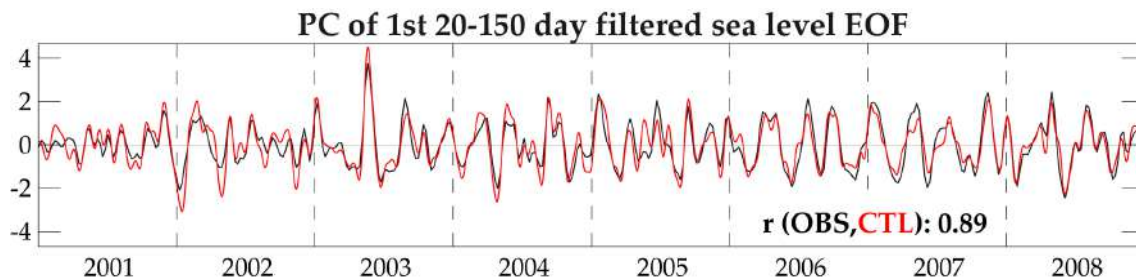


**Figure 4.4:** Comparison of 1<sup>st</sup> PCs of the 20-150-day filtered observed (black) and modelled (red; CTL experiment) sea levels. The correlation coefficient is indicated on the panel.

### 4.3.2 Importance of remote forcing

**Estimation of the forcing contributions:** Spatial maps of contributions of the forcing in each basin are obtained by computing the point-wise regression coefficient of sea level from the respective sensitivity experiments to that of the CTL solution (Figure 4.5). As the regression is computed over the full time series, these maps allow a general evaluation of the contribution of forcing in each basin to the sea level ISV, and not just of those associated with the first EOF shown in Figure 4.3f. The percentage contribution is simply the regression coefficient multiplied by 100. The contribution of SIO to NIO sea level is negligible and hence is not shown here, and henceforth will not be discussed in this chapter.

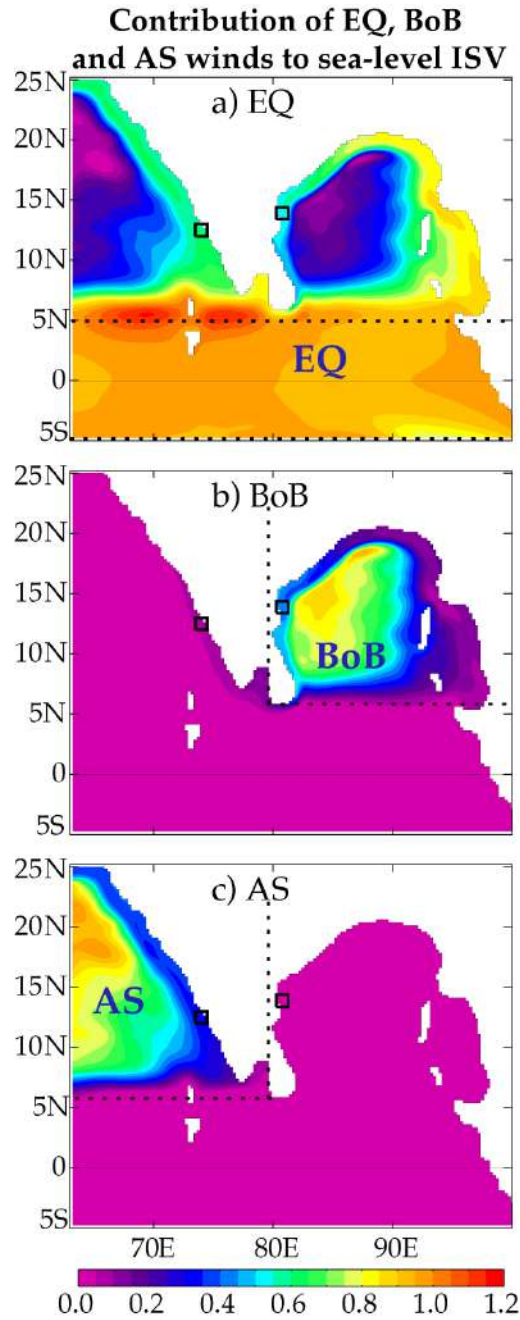


**Figure 4.5:** Contribution of a) equatorial, b) BoB, and c) AS intraseasonal wind forcing to the intraseasonal sea level variations. These contributions are computed as the regression coefficients of 20-150-day filtered sea level of (a) EQ, (b) BoB, and (c) AS experiments to those of CTL experiment. The sum of the contributions is equal to 1 by construction (the SIO wind forcing contribution to the NIO sea level ISV is negligible). The dotted lines indicate the boundaries of the domain in which the EQ, BoB, and AS forcing are applied.

**Dominance of EQ forcing in the equatorial waveguide:** Most of the basin-scale variability is due to the equatorial wind forcing, as shown by the good match in the basin-scale sea level pattern of the EQ solution (Figure 4.3i-l) with that of the observations (Figure 4.3a-d) and CTL solution (Figure 4.3e-h). Consistent with the

previous studies [e.g., Nagura and McPhaden, 2012], the EQ wind forcing explains most of the sea level ISV within the equatorial waveguide, with contributions of more than 95% (Figure 4.5a; regression coefficient  $> 0.95$ ). The ISV amplitude of the EQ solution is larger than that of CTL near  $5^{\circ}\text{N}$  on both sides of the Maldives archipelago (values slightly larger than 1 in Figure 4.5a). This feature is due to spurious Ekman pumping that occurs because the ramping of the wind forcing at  $5^{\circ}\text{N}$  in the EQ experiment artificially increases the wind-stress curl, but it has a negligible effect on the results (other solutions with a less abrupt ramping at the edge of the equatorial waveguide show qualitatively similar results).

***Dominance of EQ forcing in the coastal waveguide:*** The equatorial intraseasonal wind forcing dominates the CTL solution in most of the NIO coastal waveguide. Around the rim of the BoB, the EQ contribution decreases from 80–90% near Myanmar and in the northern Bay down to  $\sim 50\%$  north of Sri Lanka (Figure 4.5a). The EQ forcing contributes to 60–70% of the intraseasonal sea level variations along the WCI.

***Contribution of EQ forcing to the interior basin through RWs:*** The EQ forcing contribution expands westward offshore to the interior ocean from the eastern boundary of both the BoB and the AS up to  $\sim 15^{\circ}\text{N}$ , but is largely confined to the coast farther northward (Figure 4.5a). This offshore extension from the eastern boundary to the interior of the basin is due to the radiation of coastal sea level signals as westward propagating RWs. The RW radiation is restricted to the critical latitude, and to the north of which the signal remains fully trapped at the coast (see Section 2.1). Here, the wave trapping occurs because the first-baroclinic-mode RWs exist only at periods longer than  $\sim 95$  days (critical period, see Section 2.1) north of  $15^{\circ}\text{N}$  [Vialard et al., 2009], whereas the signals that originate from the equator have shorter periods [Han, 2005].

***Contribution of the BoB and AS forcing:*** The wind-stress variations within the Bay contribute to the sea level variations along the ECI through two processes: (1) the arrival of RWs generated in the interior basin and (2) the forcing by the alongshore winds in the BoB coastal waveguide. Both these processes contribute to the generation of KWs along the coast. The southward-increasing contribution of the BoB forcing along the ECI (Figure 4.5b) is likely due to a combination of those two processes. On the other hand, wind variations in the AS can only contribute to sea level ISV along the

WCI through alongshore winds, which excite coastal KWs. The relatively constant value ( $\sim 30\%$ ) of the AS contribution all along the WCI (Figure 4.5c) suggests that the alongshore wind forcing mostly occurs near the southern tip of India. The progressive westward increase of the contributions of BoB and AS wind forcing to sea level ISV in the basin interiors (Figures 4.5b and 4.5c) is due to the contribution of local wind forcing to the RWs as they propagate westward.

### 4.3.3 Seasonality in the forcing contributions

**Seasonality in the wind forcing:** Figure 4.6 presents the wind patterns associated with northern hemisphere winter (panel a) and summer (panel b) basin-scale sea level ISV, obtained by lag-regression of the winds (wind stresses and wind-stress curl) to the PC1 of the intraseasonal sea level for winter and summer seasons respectively. The patterns are remarkably similar to the dominant modes of atmospheric variability: the MJO in winter (e.g., Zhang [2005]) and the active/break monsoon phases in summer (e.g., Goswami [2005]) (see Section 2.4). While the wind-stress amplitude does not change much at the equator between the two seasons, it does become much larger over the NIO during the summer (Figures 4.6a and 4.6b). During summer, the wind-stress curl is strong in the central and southern BoB, and the alongshore wind stress is strong over the northwestern rim of the BoB (Figure 4.6b). In the AS, the winds are generally oriented perpendicular to the coast, except close to the southern tip of India and Sri Lanka, where the winds being parallel to the coast have larger alongshore component, and have larger wind-stress curl during the summer season (Figure 4.6b).

**Seasonality in the sea level ISV on the WCI:** The amplitude of the equatorial, remotely driven sea level ISV on the Indian coast does not change much between the winter and summer seasons (red bars on Figures 4.6c and 4.6d;  $\sim 2$  cm for the WCI and 1 cm for the ECI). On the other hand, the amplitude of sea level ISV due to AS wind forcing (blue bars, Figure 4.6c) is much larger (by greater than 1 cm) in summer compared to that in winter on the WCI (WC box shown in Figure 4.6a). This is probably due to the larger alongshore wind-stress and curl variations close to the southern tip of India during summer (Figure 4.6b). The WC box is representative of what happens over the entire WCI, i.e. the relative contributions of EQ and AS forcing do not vary much along this coast.

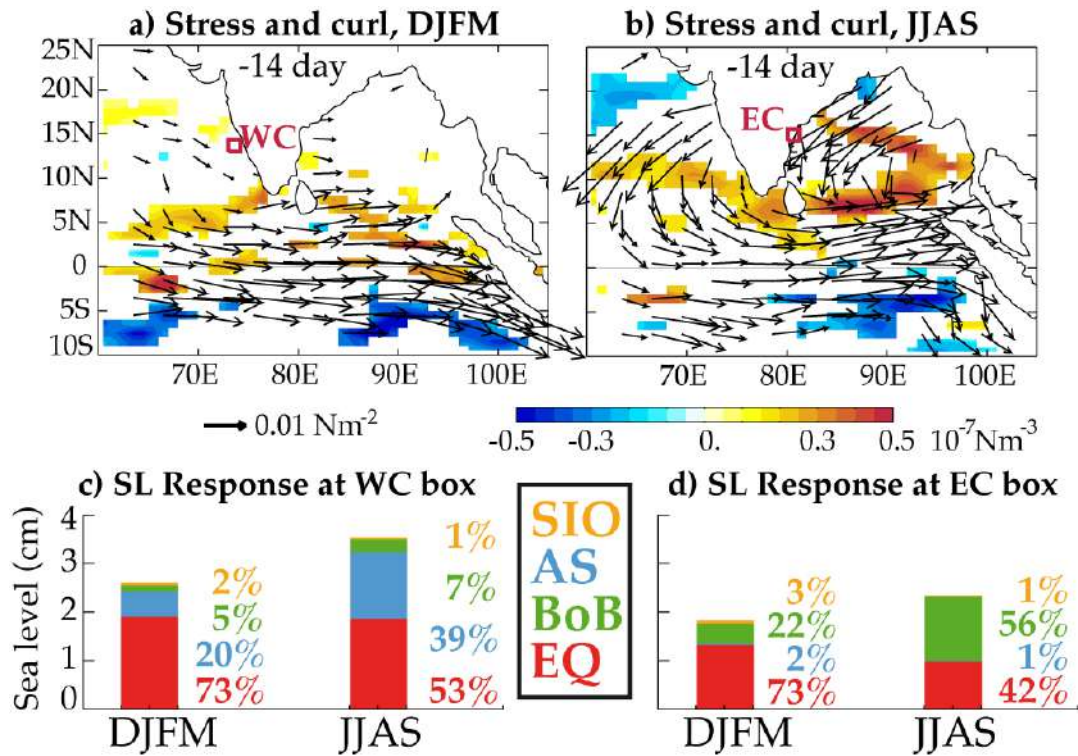


**Figure 4.6:** The 20-150-day filtered QuikSCAT wind stress (vectors) and the wind stress curl (colour shaded) regressed to the normalized PC1 of the 20-150-day filtered observed sea level at 14 day lead, for a) DJFM and b) JJAS. Decomposition of 20-150-day sea level standard deviation (cm, also indicated as a %) in the c) WC (west coast; 73.5°E-74.5°E, 12°N-13°N, cf panel a) and d) EC (east coast; 80.5°E-81.5°E, 13°N-14°N; cf panel b) boxes into contributions from equatorial (red), BoB (green), and AS forcing. Values that are not statistically significant at the 95% confidence level are masked (standard *t*-test, with one degree of freedom per 70 days of data, as determined from the lagged autocorrelation of the PC used for the regression).

**Seasonality in the sea level ISV on the ECI:** On the ECI, there is also a summer-time increase of the contribution in the BoB forcing to sea level variations (green bars, Figure 4.6d). The alongshore wind stresses (Figure 4.6b) over the northwestern rim of the Bay force downwelling coastal KWs that reinforce the remotely driven downwelling sea level signals (Figure 4.3i), while the Ekman pumping in the central and southern Bay (Figure 4.6b) forces upwelling RWs with the opposite sign sea level signals. Thus, the overall positive contribution of BoB forcing is due to the dominance of alongshore wind-stress forcing along the northwestern rim of the Bay. A similar analysis at other locations in the BoB coastal waveguide also indicates larger contribution of local forcing during summer. This contribution, however, diminishes around the rim of the Bay in the clockwise direction.

**Seasonality in the contributions:** The larger wind forcing results in larger variability (standard deviation) in NIO sea level during summer on both coasts of India (Figures 4.6c and 4.6d), with the proportion of regionally-forced to total sea level variability increasing from 20% to 40% on the WCI and up to ~60% on the ECI.

#### 4.4 Discussion

**Summary:** This chapter addresses the fundamental question – How important are the wind forcing over the equatorial, BoB, AS, and SIO basins to the sea level ISV in the NIO coastal waveguide? The wind-driven linear model used here well reproduces the observed intraseasonal sea level patterns in the NIO identified by Vialard et al. [2009], making it well suited to investigate the origins of wind-driven intraseasonal sea level variations in the NIO, particularly in the coastal waveguide. Sensitivity experiments indicate that the wind-forced sea level variations in the NIO coastal waveguide are dominated by the contribution from remote equatorial wind forcing. Around the rim of the Bay, this contribution decreases from 80–90% in the Andaman Sea, to ~50% northeast of Sri Lanka and is 60–70% along the WCI. Furthermore, the contribution of wind forcing to NIO sea level ISV is modulated seasonally. While the equatorial wind contribution to the NIO sea level ISV remains nearly the same for both the seasons, the northward shift of the atmospheric ISV in summer induces stronger variability in the alongshore wind stresses on the northwestern rim of the Bay and also near the southern tip of India, leading to larger sea level ISV and hence a larger contribution of BoB and AS winds to this ISV on both the coasts (~40% west; ~60% east) of India during boreal summer than in winter (~20% on both west and east Indian coasts).

**Sensitivity of results to the timescale:** While the intraseasonal wind-stress variations exhibit maximum power at 30-60-day timescale, the oceanic intraseasonal sea level variations in general peak near the 90-day period [e.g. Han, 2005; Girishkumar et al., 2013]. This has been attributed to the occurrence of resonant response of the IO basin to the wind forcing, near the 90-day period [e.g., Han, 2005; Han et al., 2011]. This study chooses not to distinguish between those two frequencies, but consider them as a whole, by filtering the results in the 20-150-day window.

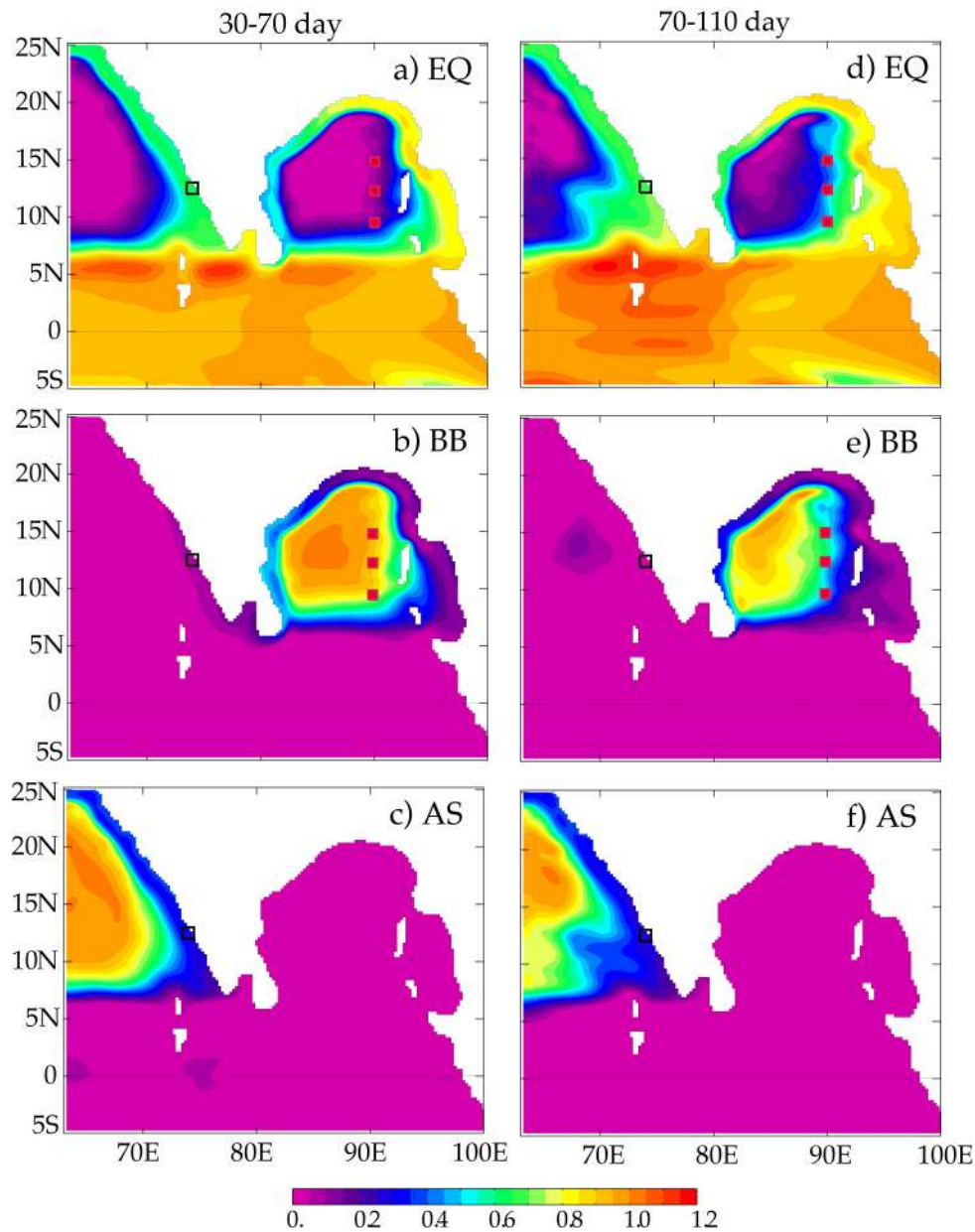


**Figure 4.7:** Same figure as Figure 4.5, but for the 30-70 and 70-110-day bands separately. The colours represent the contribution of wind forcing in the EQ, BoB and AS regions, computed as the regression coefficients of 30-70 or 70-110-day filtered sea level of (a) EQ, (b) BoB, and (c) AS experiments to that of CTL experiment. The sum of the contributions is equal to 1 by construction. The filled red squares indicate the locations of the 8°N, 12°N and 15°N RAMA moorings at 90°E.

The contributions of the various basins remain qualitatively similar even when those two specific periodicities are considered separately, as illustrated by Figure 4.7, which is identical to Figure 4.5, but produced selectively for two frequency bands encompassing the main forcing period (30-70 day) and the 90-day (70-110 day). Inside the equatorial and NIO coastal waveguide, the contributions of the various regions in Figure 4.7 are remarkably similar to those shown in Figure 4.5. There is however a larger contribution of EQ forcing in the southeastern AS and BoB basins in the 70-110-

day band than in the 30-70-day band. This is because the critical latitude (Section 2.1) for the lower frequency signals are farther north compared to that for the higher frequency signals and hence offshore radiation of coastal signals as RWs can occur farther north at lower frequency than at higher frequency [e.g., Vialard et al., 2009].

***Consistency with previous studies:*** Cheng et al. [2013] suggested a significant contribution of equatorial remote forcing in the interior BoB. Girishkumar et al., [2013], who analyzed the temperature observations from RAMA moorings along 90°E at 8°N, 12°N, and 15°N (Figures 4.7b and 4.7e) in the BoB, reported that the thermocline variability at 90 and 120-day periods are primarily driven by the equatorial, zonal wind stress variations. Consistent with those studies, the contribution of equatorial forcing to the 90-day sea level variations is 40-60% at those locations (Figure 4.7e). The results reported here are also consistent with those of Shetye et al. [2008] and Amol et al. [2012], who suggested the variability in the currents along the WCI is influenced by the remote forcing farther south.

## Dynamics of wind-driven intraseasonal sea level variability in the NIO coastal waveguide

---

### 5.1 Introduction

**Lead from the previous chapter:** Previous chapter demonstrated that the sea level ISV originating from the wind forcing in the equatorial region dominates the basin-scale sea level ISV in the NIO coastal waveguide through equatorially trapped and coastally trapped KWs. An intriguing aspect of those remotely forced equatorial signals is that their contribution to the total sea level ISV (Figure 4.5a) is larger along the WCI (60-70%) than along the ECI (50%), suggesting possibility of a direct connection between the equatorial waveguide and the WCI that does not involve coastal KW propagation around the BoB rim.

**The new connection in the literature:** This *direct link* between the equatorial waveguide and the WCI has been speculated by a couple of studies in the literature, but has been neither demonstrated, nor explored in detail. Many studies [e.g., McCreary et al., 1993; Shankar et al., 2002; Shetye, 1998] discussed the seasonal dynamics of NIO sea level and currents under the framework of the linear wave theory and proposed the concept of *leaky NIO waveguide* described in Section 2.2. In this framework, the equatorial and NIO coastal waveguides interact only at the western and eastern boundaries of the equatorial IO basin and remain well separated from each other by  $\sim 100$  km south of Sri Lanka [Shankar et al., 2002; Shetye, 1998] (Figure 2.6). Shetye [1998] noted, however, that part of the energy of an equatorial KW reaching the Sumatra coast is reflected as a westward-propagating RW, which can potentially excite coastal KWs when reaching the east coast of Sri Lanka. Using altimeter sea level data, Gopalakrishna et al. [2008] suggested that this process indeed contributes to the seasonal modulation of the upwelling along the southwest coast of India. At intraseasonal timescales, a recent study [Dhage and Strub, 2016] pointed towards high correlations between sea level along the WCI and that along the RW path between the

east coast of Sri Lanka and the Sumatra coast. Their analysis of altimeter sea level observations did however not allow assessing the respective contributions of coastal KWs travelling through the BoB and those related to this *direct connection* at the Sri Lankan coast. All these studies suggest that the direct pathway between the equatorial waveguide and the WCI can potentially influence the sea level variations along the WCI, but its contribution relative to that of the *classical pathway* through the BoB coastal waveguide remains to be explored.

***Intraseasonal wind forcing:*** Besides the remote equatorial wind forcing, other factors such as the alongshore wind-stress forcing (through coastal KW generation) or Ekman pumping due to wind-stress curl forcing (through RW generation) can also influence the sea level along the NIO coastal waveguide. It is therefore important to identify the regions where wind forcing does matter the most in driving the sea level variations either locally or remotely. Suresh et al. [2016] showed that the seasonal wind variations are strong near the southern tip of India and Sri Lanka, the northwestern boundary of the BoB, and off the east coast of Sri Lanka. Amol et al. [2012] showed that the winds near the southern tip of India exhibit significant intraseasonal variations, particularly in the Gulf of Mannar and off the east coast of Sri Lanka, and hypothesized that these wind variations might significantly influence the currents ISV along the WCI. However, the contribution of the above wind variations to the NIO sea level ISV is yet to be assessed.

***Aim and organization of the chapter:*** This part of the thesis will hence discuss the pathways of NIO intraseasonal signals and estimate the relative contributions of the wind forcing from various regions to the sea level variability in the NIO coastal waveguide. To this end, a series of LCS experiments are carried out and analyzed. The chapter is organized as follows. Section 5.2 illustrates how the equatorial signals can directly propagate to the WCI without transiting through the BoB. Section 5.3 identifies the *hotspots* of intense intraseasonal wind forcing in the NIO. Section 5.4 describes the processes that can potentially influence the sea level ISV in the NIO waveguide. Section 5.5 describes the LCS sensitivity experiments used for isolating those processes. Section 5.6 provides a validation of the model, describes the major sea level ISV patterns, and quantifies the contribution from each of the processes to NIO sea level ISV. The main results of this chapter are finally summarized in Section 5.7.

## 5.2 The new connection

### 5.2.1 Meridional modes of equatorial waves

***Meridional modes and the Sri Lankan southern tip:*** Figure 5.1 shows the sea level meridional structures (cf. Section 2.1; also Figure 2.1) of the first-baroclinic mode equatorial Kelvin and the first, second, and third meridional-mode equatorial RWs, computed with a KW phase speed of  $2.5 \text{ ms}^{-1}$  [Boulangier and Menkes, 1995; LeBlanc and Boulangier, 2001]. The vertical (red) line marks the latitude of the southern tip of Sri Lanka (i.e.  $\sim 5.75^\circ \text{ N}$ ). The first baroclinic KW displays a maximum at the equator and its signal at the southern tip of Sri Lanka reaches only  $\sim 15\%$  of its maximum equatorial value. This will result in weak sea level perturbations at the Sri Lankan coast, and hence a weak response in terms of coastal KWs there. On the other hand, the theoretical sea level structure of the first-baroclinic, first-meridional mode RW has a symmetric shape about the equator, peaking at  $\sim 4^\circ$  latitude on both hemispheres. Its amplitude at the southern tip of Sri Lanka reaches  $\sim 70\%$  of its maximum value and this can, in principle, trigger potentially large coastal KWs. The amplitudes of higher-order meridional modes of RW also peak near the southern Sri Lankan coast. These higher-order modes have even wider meridional extent compared to the first mode and hence they can efficiently contribute to the generation of coastal KW signals not only at the Sri Lankan southern tip, but also at the southern coast of India.

***Possibility of direct connection:*** The above theoretical arguments suggest a new potential connection between the equatorial and the NIO coastal waveguides in addition to the well-known “classical” connection at the western and eastern equatorial boundaries. This new connection will henceforth be referred to as the EQUatorial Direct (EQD) connection. The next section provides a proof of this concept with the help of idealized LCS model experiments. The contribution of EQD connection to the WCI sea level variability is quantified using LCS sensitivity experiments in the later Section 5.6.3.

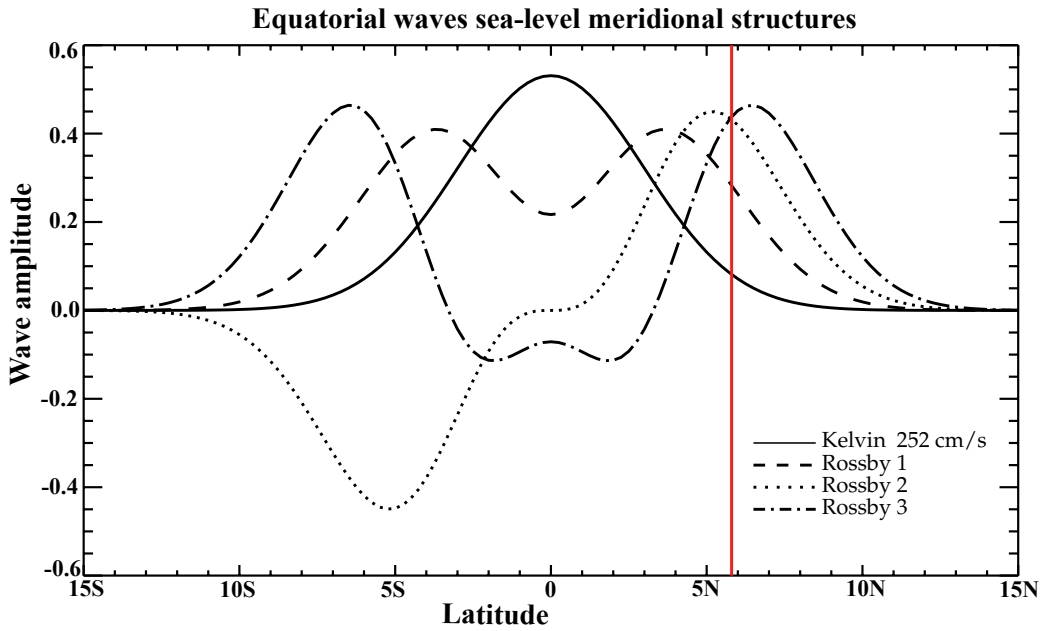


**Figure 5.1:** Sea level meridional structures for equatorial Kelvin and the first, second, and the third meridional mode Rossby waves. The red vertical line marks the latitude of the southern coast of Sri Lanka.

### 5.2.2 Demonstration of EQD connection

**Idealized experimental set up:** An idealized experiment is first performed to illustrate the EQD connection. In this experiment, the LCS model is forced with a westerly wind burst over a rectangular region extending from  $87^{\circ}\text{E}$  to  $93^{\circ}\text{E}$  and  $5^{\circ}\text{S}$  to  $5^{\circ}\text{N}$  in the eastern equatorial IO, lasting for 10 days. The forcing has a Gaussian shape in the meridional direction and is symmetric about the equator, with an arbitrary maximum wind-stress amplitude of  $0.13 \text{ Nm}^{-2}$ . In the zonal direction, the wind stress is constant and is ramped down to zero within  $1^{\circ}$  from the eastern and western edges of the rectangular region. This idealized wind-stress forcing is illustrated on Figure 5.2a. The choice of the forcing pattern ensures that it does not induce a direct coastal KW response at the southern coasts of India/Sri Lanka. A 1-year simulation with this wind-stress forcing is referred to as the IDLCTL simulation.

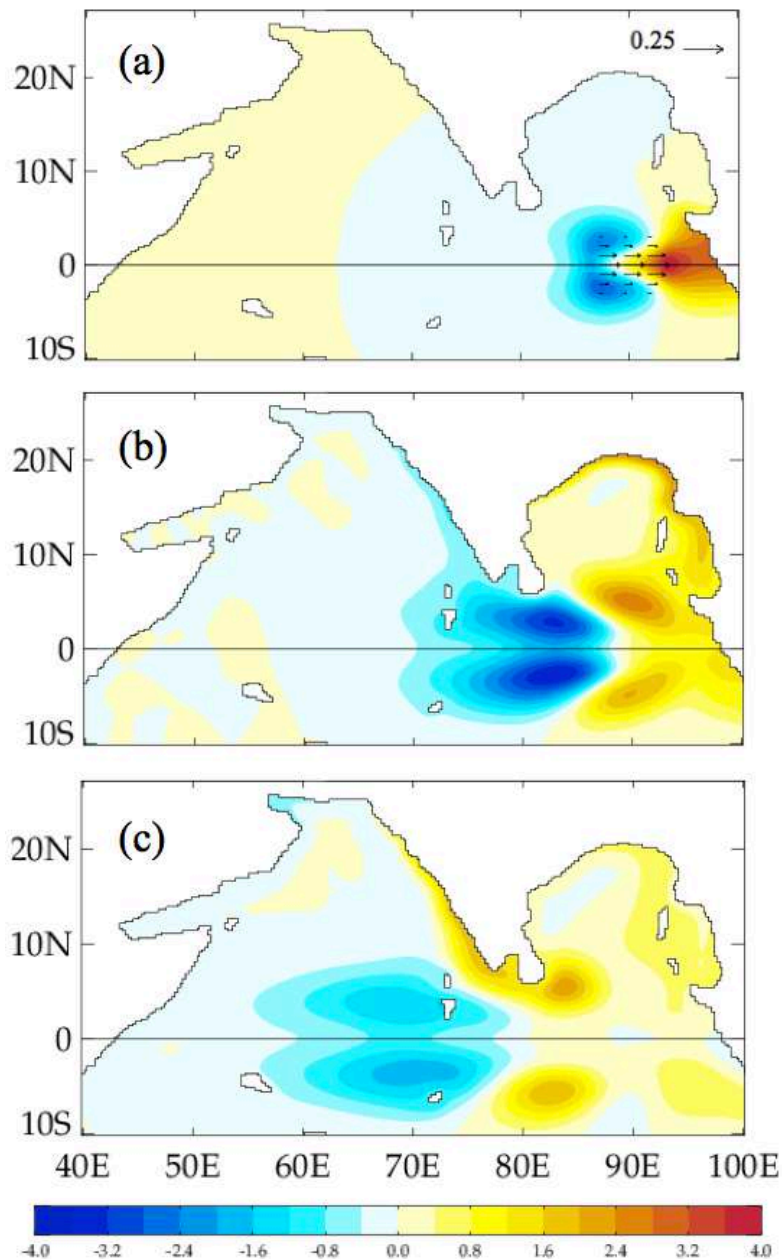


**Figure 5.2:** Snapshots from the IDLCTL experiment at (a) 4 days (b) 24 days, and (c) 44 days after the initiation of 10 days long westerly wind burst shown in panel (a).

**Response to idealized forcing:** As expected, this idealized westerly wind forcing excites a downwelling equatorial KW to the east of the forcing region and upwelling equatorial RW to the west (Figure 5.2a). When the eastward-travelling equatorial KW reaches the Sumatra coast, part of its energy is reflected back into the equatorial region as downwelling equatorial RW, while some of its energy enters into the BoB coastal waveguide (along eastern BoB rim) as downwelling coastal KW (Figure 5.2b). Both the forced upwelling and the reflected downwelling equatorial RWs propagate westward

and set up coastal KWs upon encountering the Sri Lankan coast (Figure 5.3b,c). These coastal KWs signals propagate off the coast of Sri Lanka and climb up the coastal waveguide off the west India, influencing the sea levels there. This illustrates the **EQD** mechanism mentioned in Section 5.2.1. In the mean time, the downwelling coastal KW at the eastern rim of the BoB propagates anticlockwise along the coast. The coastal sea level signal at the eastern rim also radiates away (as constrained by a critical latitude; see Section 2.1) as westward RW that influences the sea level in the interior BoB (Figure 5.2b). When this RW signal reaches the BoB western boundary, it excites a coastal KW, reinforcing the downwelling coastal KW propagating around the BoB rim. All these downwelling signals travelling along the BoB coastal waveguide bend around Sri Lanka and further propagate northward along the WCI (Figure 5.2c). This process, which involves propagation of remote equatorial signals through BoB, will hereafter be referred to as the **EQB** process. It should be noted that the length of the EQB pathway ( $\sim 4500$  km around the BoB rim) is roughly three times of that of the EQD pathway ( $\sim 1500$  km from Sumatra coast to east coast of Sri Lanka). As the EQB signals (coastal KW) travel three times faster than the EQD signals (first-baroclinic equatorial RW), it takes nearly the same time for the reflected RW and the coastal KW to reach the east coast of Sri Lanka.

**Remark:** The idealized experiment does not have any other forcing. Hence, EQB and the EQD are the only processes that can influence the sea level in the NIO and the latter influences the sea level only in the AS, and not in the BoB.

**Separation of processes:** The travel times of EQB and EQD signals along their respective pathways is nearly the same (the distance-speed ratio discussed above). Hence, it is not straightforward to decompose these signals in the observations. The above two processes can however be separated out in the linear model solution with an additional LCS experiment, by imposing a Newtonian damper (described Section 3.3) in the BoB. This damper, delineated by a dashed rectangular frame in Figure 5.3b, filters out the waves entering into the BoB, and hence the solution will only contain the EQD process. The difference between the IDLCTL and the above-mentioned damper experiment would then yield the EQB process.

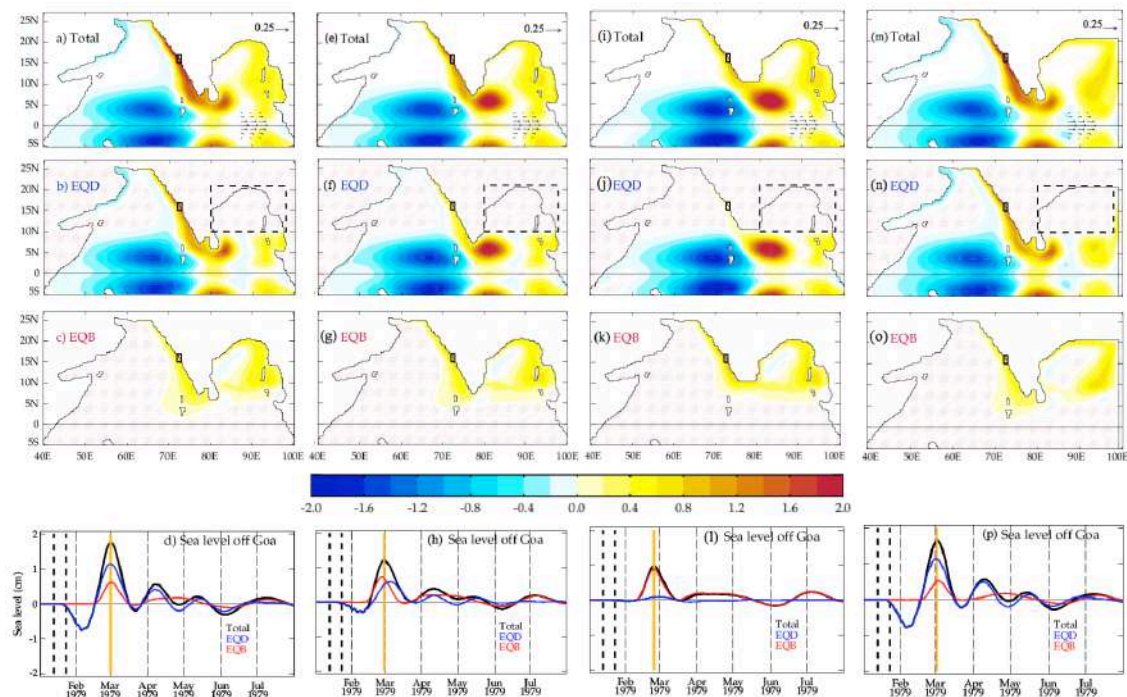


**Figure 5.3:** Sea level patterns corresponding to the maximum sea level off Goa (indicated with a yellow-colored vertical line in bottom panels) and the sea level time series (bottom panels) from idealized, single-pulse LCSM experiments with different Land/Ocean masks (described in Section 5.2.2). The left most panels (a)-(d) correspond to the run with original model coastline (IDLCTL); (e)-(h) without Sri Lanka (IDLNOSL); (i)-(l) without Sri Lanka and “chopped” Indian tip (IDLST10N); and (m)-(p) with a “meridional wall” eastern boundary (IDLMEB). An additional experiment without Maldives archipelago (not shown here) shows similar results to that with original model coastline for the sea level along the WCI. The single pulse wind stress forcing used for these experiments is shown on each of the top panels and its duration (10 days) is indicated in the bottom panels with dashed black vertical lines. The sea level patterns (top 3 rows) correspond to the total, EQD (direct connection between equator and WCI) and EQB (equatorial signals through BoB) sea levels (see Section 5.2.2 for explanation of these processes). The damper used for separating these processes is indicated with a dashed black frame on panels in the 2<sup>nd</sup> row. The off Goa location (WCI box) is indicated with a black box on the maps.

**Analysis of IDLCTL experiment:** The first column (panels a-d) of Figure 5.3 corresponds to the results of the idealized set of experiments described above. Figure 5.3d shows sea level time series at a location off Goa (black box on WCI shown in the snapshots) from IDLCTL simulation (will be referred to as total sea level) and its decomposition into EQD and EQB processes. Figures 5.3a-c display respectively the snapshots of the total, the EQD and the EQB sea level at the time corresponding to the maximum amplitude of total sea level off Goa (indicated by a yellow vertical line on Figure 5.3d). As discussed above, the sea level off Goa (Figure 5.3d) first shows upwelling (coastal KW) signals excited by the forced upwelling equatorial RWs (EQD process) and then the arrival of downwelling signals driven by both the reflected

downwelling equatorial RWs (EQD process) and the downwelling coastal KWs through BoB rim (EQB process). In this experiment, the sea level on the WCI is dominated by EQD, whose contribution off Goa is twice that of EQB (Figure 5.3d). This ratio of amplitudes between the EQD and EQB will however depend on wind forcing applied. For a wind forcing located on the western equatorial IO, the amplitude ratio of EQD and EQB on the WCI may be different.

***Importance of Sri Lanka:*** The presence of the Sri Lankan landmass is essential for an efficient EQD connection. This is demonstrated with an additional set of experiments forced with the same wind-stress forcing as in IDLCTL, but with a modified land-ocean configuration in which the Sri Lankan landmass is removed. A year-long simulation similar to IDLCTL is carried out and is referred to as the IDLNOSL experiment. The EQD and EQB contribution in IDLNOSL are separated out in the same way as in the IDLCTL experiment. The snapshots and the sea level time series corresponding to IDLNOSL are shown in Figures 5.3e-h. As expected, the absence of Sri Lanka results in a weaker interaction between the equatorial and the coastal waveguides. The sea level peak off Goa due to EQD in IDLNOSL is much smaller than that in IDLCTL (blue lines in Figures 5.3h and 5.3d), resulting in a weaker (reduced by half) total sea level amplitude in IDLNOSL compared to that in the IDLCTL experiment (Figure 5.3h vs. 5.3d; black lines), illustrating the importance of Sri Lanka for the EQD pathway. The amplitude of EQB in IDLNOSL, on the other hand, is slightly larger than that in the IDLCTL due to less frictional damping resulting from the shorter length of the pathway of the coastal KW (due to absence of Sri Lanka). This shorter length of the pathway in IDLNOSL also leads to an earlier arrival of EQB signals compared to those in the IDLCTL.

***Importance of southern tip of India:*** As shown in Figure 5.1, the amplitudes of equatorial waves are negligible at 10°N. In a similar set of idealized experiments (IDLST10N; Figures 5.3i-l) as IDLCTL, but with the southern tip of India chopped off to 10°N (and no Sri Lankan landmass), the equatorial RWs propagate unhindered to the west (Figure 5.3j). Therefore, the WCI sea level has almost no contribution from EQD, but is entirely driven by EQB (Figure 5.3k). This further demonstrates that the presence of the southern tip of India (and of course, of Sri Lanka) is crucial for the EQD connection.

***Effect of Maldives:*** The effect of presence of Maldives on the model solution is tested with an additional idealized experiment without Maldives archipelago in its land-ocean configuration. The results (not shown) are same as those with original model coastline (IDLCTL) for the sea level along the WCI, including the EQD and EQB sea level signals, implying that the existence of Maldives islands do not affect the EQD pathway.

***Effect of slanted eastern boundary:*** A comparison of the upwelling RW directly forced to the west of the wind pulse and the reflected downwelling RW at the Sumatra coast indicates that the latter has a larger meridional extent (Figure 5.2b), implying excitation of higher-order meridional modes on reflection. In order to examine if these higher modes are the consequence of the slanted boundary (the Sumatra coast), a last set of experiments (IDLMEB) were carried out with the same set up of IDLCTL, except that the slanted coast was replaced with a meridional eastern boundary as shown in Figure 5.3m. The results of IDLMEB (Figures 5.3m-p) are almost similar to those of IDLCTL (Figures 5.3a-d), including the wider meridional extent of the reflected RW (Figure 5.3n vs. 5.3b), implying that the slanted shape of the eastern boundary has negligible effect on the reflection, which is in agreement with the results of Clarke [1983].

***Limitations of the idealized experiments:*** While the above set of idealized experiments clearly demonstrates the importance of the EQD pathway for the WCI sea level variability, there are still many caveats. The amplitude of EQD signal depends on the choice of the wind forcing. It is indeed different when the wind forcing in IDLCTL is shifted to the central or western equatorial IO, resulting in nearly equal or even weaker amplitude of EQD compared to EQB (not shown). The meridional extent of the forcing also plays crucial role in determining the amplitude of the signal through EQD connection. When the meridional extent of the forcing in IDLCTL is extended to 10°S - 10°N, the amplitude of the initial upwelling signal at the WCI is much larger (not shown) compared to that in IDLCTL, indicating a more efficient EQD connection. Furthermore, the basin resonances reported in the equatorial IO [Han, 2005; Han et al., 2011], particularly the concentration of the 90-day resonant mode in the eastern basin, will have implications for the EQD connection. This calls for a detailed understanding of the EQD process in a realistic model simulation and a quantification of its contribution to the WCI sea level variability.

### 5.3 Intraseasonal wind forcing

*Figure introducing the ISV forcing:* Understanding the characteristics of the intraseasonal wind forcing in the NIO is crucial for studying the NIO sea level ISV. Figure 5.4 therefore details the amplitude of the intraseasonal forcing (namely the alongshore wind stress, the wind-stress curl, and the Ekman pumping velocity) to delineate the main forcing regions.

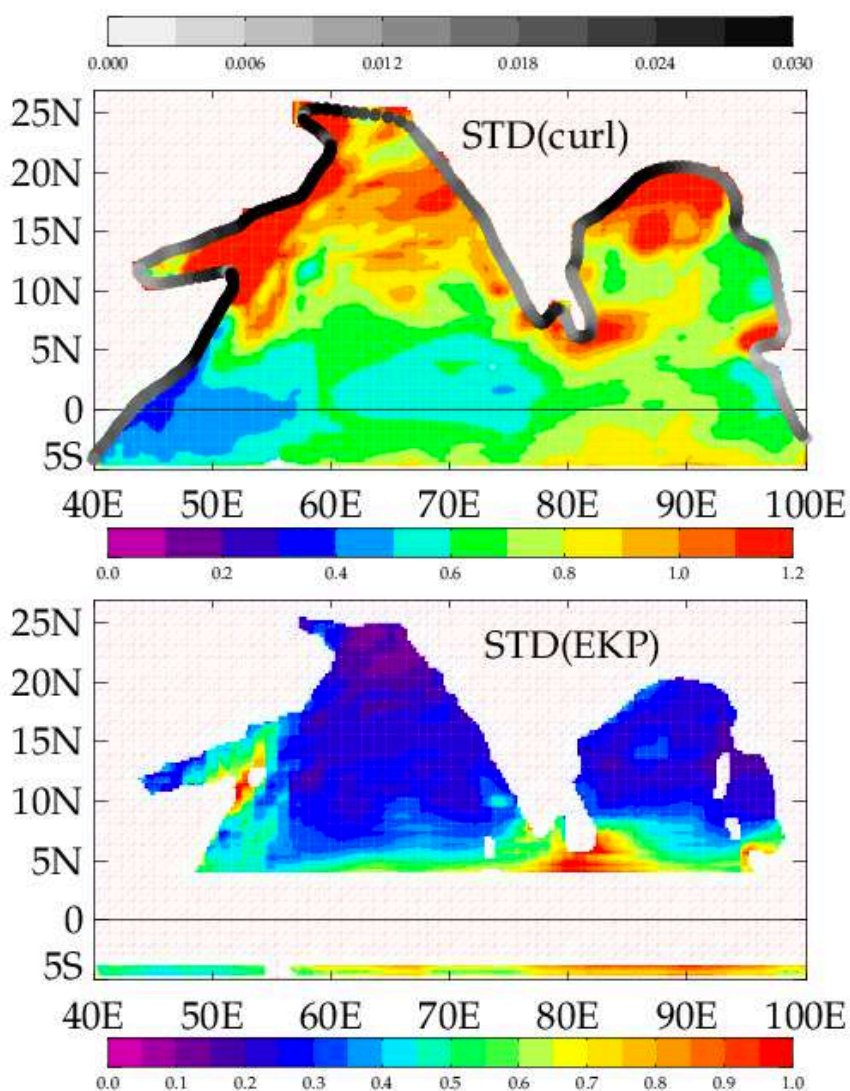


**Figure 5.4:** Amplitude of the intraseasonal variability of (top panel) the wind-stress curl (shaded; scale at the bottom; multiplied by  $10^7$ ;  $N/m^3$ ) and alongshore wind stress (grey shades along the coast; scale at the top of the figure;  $N/m^2$ ) and (bottom panel) the Ekman pumping velocity (m/day).

***The alongshore forcing:*** The seasonal winds are almost parallel to the coasts along the northwestern rim of the BoB and near the southern tip of India and Sri Lanka, resulting in a strong alongshore component of winds along those coasts (Figures 2.5a,b and 6.1) [Suresh et al., 2016]. Figure 5.4a (grey shading) reveals that regions with strong intraseasonal variations in the alongshore forcing coincide with those of strong seasonal variability. These regions are the potential *hotspots* for the coastal KW generation through intense alongshore forcing. Strong intraseasonal variations in the alongshore wind forcing are also found off the coasts of Oman and Somalia. The KWs excited at these coasts would propagate equatorward and enter into the equatorial waveguide at the western boundary of the equatorial IO basin as equatorial KWs.

***The curl and the Ekman pumping:*** The wind-stress curl is strong in the interior and northwestern BoB, in the east and southern coasts of Sri Lanka, in the region adjacent to Sumatra coast, and in the interior and western part of the AS (Figure 5.4a). The amplitude of intraseasonal Ekman pumping velocity is large across the southern BoB and southern AS, with highest values around the Sri Lankan coast (Figure 5.4b). Even though the wind-stress curl at higher latitudes is as strong as that near the equator, the Ekman pumping is weaker because of the higher values of the Coriolis parameter. The RWs triggered by the Ekman pumping would excite coastal KWs upon their arrival at the coast. In summary, Figure 5.4 provides a clear picture of the *hotspots* of strong excitation of coastal KWs. Understanding the pathways of intraseasonal sea level signals requires paying special attention to those regions.

#### **5.4 The processes**

***Remark:*** This section discusses the processes (or pathways of signals) that can potentially influence the wind-driven sea level variability in the NIO, particularly along the NIO coastal waveguide. Note that these processes operate not only at intraseasonal timescales, but also at seasonal and interannual timescales. These processes are summarized in Table 5.2 and are schematically shown in Figure 5.5. Some of the processes are grouped below for simplicity as their contributions are expected to be negligible.

## Schematic of pathways of sea level signals in NIO

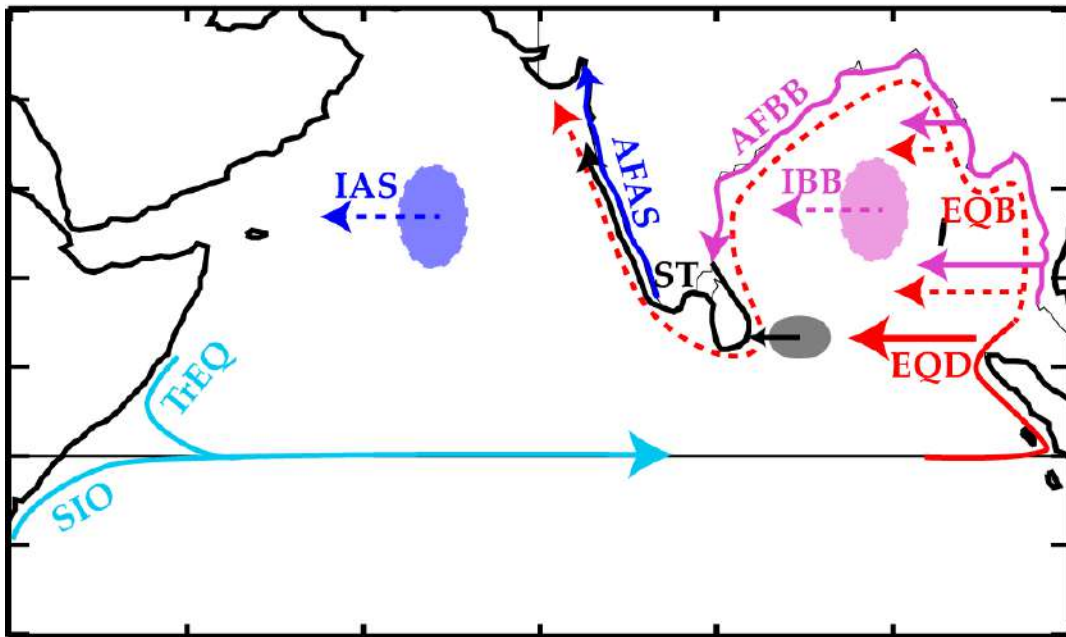


**Figure 5.5:** Schematic representation of the processes or the pathways of sea level signals that influence the sea level variability in the NIO, particularly along the coastal waveguide. The pink color represents the BoB forcing (alongshore – AFBB; interior – IBB), the black color represents the STIP forcing (alongshore – AFST; interior – IST;  $ST=AFST+IST$ ), the blue color represents the AS forcing (alongshore – AFAS; interior – IAS), the red color represents the equatorial forcing (signals through BoB – EQB; signals through direct connection – EQD), and the cyan color represents signals that get into the equator from the western equatorial basin (signals originating from the NIO that propagate into the equatorial band at the western boundary and back into the NIO – TrEQ; signals from the southern IO – SIO). These processes are isolated with sensitivity experiments schematically shown in Figure 5.7 and summarized in Table 5.2. See Section 5.4 and 5.5.2 for more details.

**The equatorial contribution via. EQD and EQB:** The response of the NIO sea level to the remote equatorial wind forcing (including the alongshore forcing at the basin boundaries) involves processes that are grouped into EQD and EQB, which have already been extensively discussed in Section 5.2. In brief, **EQD** refers to the effect of coastal KWs that are generated due to interaction of the equatorial and the coastal waveguides at the Sri Lankan coast and **EQB** refers to the remotely forced equatorial signals that travel through BoB to NIO.

**The BoB forcing:** The winds over the BoB can influence the NIO sea level in two ways: (1) the alongshore forcing (**AFBB**; through coastal KWs) and (2) the interior Bay wind-stress curl forcing (**IBB**; through Ekman pumping, resulting in RW generation).

The coastal signals excited by the alongshore forcing in the eastern rim of the Bay radiate westward RWs, whose effect is also included in the AFBB process.

***Forcing in the vicinity of Sri Lanka/southern tip of India:*** As discussed in Section 5.3, the region near the southern tip of India and Sri Lanka (hereafter, STIP region) is one of the hotspots of intense intraseasonal wind forcing in NIO (Figure 5.4), in terms of both the alongshore forcing (**AFST**) and the strong Ekman pumping velocity in the interior ocean east of Sri Lanka (**IST**). The resulting coastal KWs will influence the AS sea level, particularly along the WCI and this response (combined effect of AFST and IST) will henceforth be referred to as **ST** process

***The AS forcing:*** As with the BoB forcing, the AS winds contribute to the sea level variability both along the coast and in the interior AS through (1) the alongshore wind forcing (**AFAS**; through coastal KWs) and (2) interior AS wind-stress curl forcing (**IAS**; through RWs).

***Contribution of signals that transit through the equator:*** The RWs radiated from the WCI and those generated in the interior AS (by IAS process) ultimately reach the western coastline of the AS and excite coastal KWs there. The coastal KWs in the NIO would also reach the western boundary of the AS after transiting around the rim of the AS. All these coastal signals at the western boundary of the AS propagate equatorward and leak into the equatorial waveguide at the western boundary of the equatorial basin as KWs. In principle, these KWs can contribute to the NIO sea level variability exactly in the same way as that of the EQB and EQD processes, unless the friction damps them out or interfere destructively with other signals. Hence it is important to understand the contribution of these signals transiting through the equator. This process will be referred to as **TrEQ**.

***Signals from the SIO:*** The wind forcing in the SIO can also influence the NIO sea levels through interaction of coastal waveguide along the western boundary of the southern basin and the equatorial waveguide. The signals that reach the equatorial waveguide from the SIO will propagate to the NIO in the same way as the EQD and EQB processes. These signals are grouped together under **SIO** process.

The rest of this chapter is devoted to estimate the relative contribution from each of these processes to the sea level ISV in the NIO, particularly along the NIO coastal waveguide. A series of LCS model sensitivity experiments has been carried out for that purpose and the details of these experiments are presented in the following section.

## 5.5 Model setup and sensitivity experiments

### 5.5.1 Model setup

**Model configuration:** The general configuration of the LCS model is provided in Section 3.3. Model details specific to this chapter are summarized below. The vertical mixing has the same form as the one in McCreary et al. [1996], but with a 7-year dissipation time scale for the first baroclinic mode (see Section 3.3 for details on the choice of mixing coefficients). This ensures that the vertical mixing has negligible effect on the lower baroclinic modes and that the model solutions are suitable for studying the variability even at the interannual timescale (in Chapter 6). The horizontal mixing coefficient is set to  $5000 \text{ m}^2 \text{ s}^{-1}$ . Wind is introduced into the ocean as a body force with the same profile (constant down to 50 m and ramped to zero at 100 m) as in McCreary et al. [1996]. The model is forced with daily TropFlux [Praveen Kumar et al., 2013] wind-stress (available from <http://www.incois.gov.in/tropflux/>) anomalies (long-term mean removed) during the period from 1979 to 2013. As in Nagura and McPhaden [2012], the model solution converges well with the first 5 modes, and the first two modes are indeed sufficient to explain most of the variability in the NIO as discussed below.

**The control experiment:** The model solution with the above TropFlux forcing is referred to as the control (CTL) experiment in this chapter (and is different from the CTL run of Chapter 4). The intraseasonal sea level is obtained by filtering the sea level with a 20-150-day band-pass filter after removing the mean seasonal cycle (see Section 3.2). As demonstrated in Chapter 4, the results are not sensitive to the choice of the filtering bandwidth.

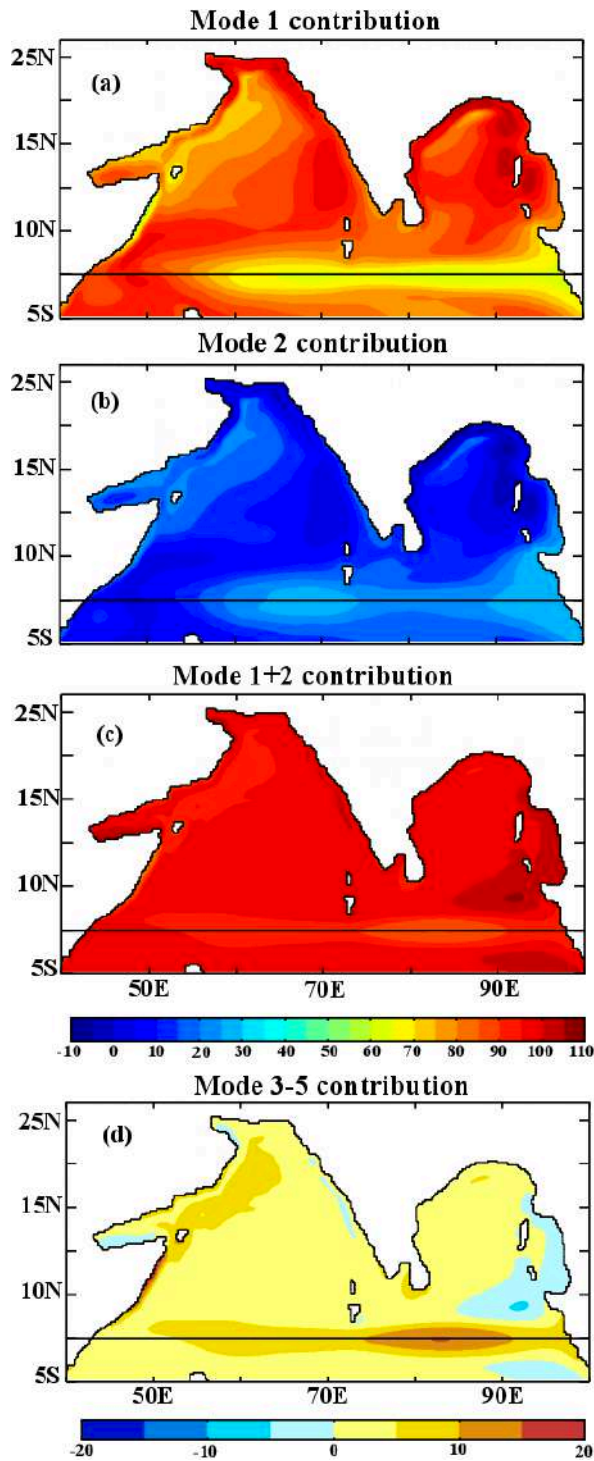


**Figure 5.6:** Regression coefficient of (a) first, (b) second, (c) first two (modes 1+2), (d) modes 3+4+5 intraseasonal sea level to the sum of first five baroclinic modes.

**Contribution from baroclinic modes:** Figure 5.6 (similar to Figure 4.1) shows the spatial maps of coefficients of the linear regressions of the first, the second, the sum of the first two, and the sum of the third to fifth baroclinic modes onto the sum of first five modes. The sum of the first two modes is almost identical to that of the first five modes

over the entire NIO, except in the equatorial region, where the remaining three modes contribute 10-15% to the 5-mode solution. The first mode explains most of the 5-mode solution, with more than 90% in the BoB, the eastern AS, and most of the NIO coastal waveguide. In the central and eastern equatorial IO, the first mode explains ~60% of the solution, with the second mode accounting for most of the rest (sum of modes 3 to 5 has a very weak contribution). The contribution of the first mode to the 5-mode solution progressively decreases westward in the AS, with 70-80% contribution in the Oman and Somalia upwelling regions, where the alongshore forcing is strong. The strong local winds favor generation of the higher modes, with the second mode contributing to 20-30% and little (<10%) contribution from the third, fourth and the fifth modes to the 5-mode solution.

### 5.5.2 Sensitivity experiments

The CTL sea level (denoted as  $sl(CTL)$ ) at any location in the NIO results from the combined effect of the processes described in Section 5.4 (Figure 5.5). The linearity of the model ensures that the sea level from the CTL experiment can be written as:

$$sl(CTL) = sl(EQD) + sl(EQB) + sl(AFBB) + sl(IBB) + sl(ST) \\ + sl(AFAS) + sl(IAS) + sl(TrEQ) + sl(SIO) \quad \text{-----(Eqn. 5.1)}$$

where  $sl(X)$  (on the right hand side) refers to the sea level due to the process ‘ $X$ ’.

Following McCreary et al. [1996], a series of model sensitivity experiments is performed by applying dampers and/or special boundary conditions (SBC) (Section 3.3) in specific regions to isolate the sea level due to each process from the CTL sea level. The details of the LCS model sensitivity experiments are given below and are summarized in Table 5.1. The method for obtaining the sea level corresponding to each process is provided in Table 5.2.

**Table 5.1:** Details of LCS model sensitivity experiments. In the table, “No” implies that the condition is not applied. Dampers are used to damp out the waves within the region encompassed the box boundaries. Special boundary conditions (SBC) are used to filter out the coastal Ekman pumping, and hence no KW is generated along the coastline encapsulated by the box boundaries. The regions specified in the table are shown on Figure 5.7.

LCS model Experiments	Description of Exp. and process	Damper	SBC
NAFBB	Same as CTL, but with SBC imposed off the coast of BoB	No	Coastline within BB box shown in pink color
NAFST	Same as CTL, but with SBC imposed over the coast in the STIP region	No	Coastline within black box
NAFAS	Same as CTL, but with SBC imposed on the coastline in the AS	No	Coastline within blue box
NAFNIO	Same as CTL, but with SBC imposed all over the NIO coastline; Equivalent to NAFBB+NAFST+NAFAS	No	SBC applied over the entire NIO coastline
DSIO	Same as CTL, but with a damper in the southern Indian Ocean	Cyan box [31°E -109°E; 15°S-6°S]	No
NAFNIODSIO	Same as NAFNIO, but with damper in southern Indian Ocean	Cyan box [31°E -109°E; 15°S-6°S]	SBC applied over the entire NIO coastline
DSWT	Same as DSIO, but with SBC over entire NIO and a “wave trap” in Somalia region	1) Cyan box [31°E-109°E; 15°S-6°S] 2) Light-shaded green box on Somalia coast	SBC applied over the entire NIO coastline
DSBWT	Same as DSWT, but with an additional “wave trap” at the entrance of coastal waveguide of Bay of Bengal	1) Cyan box [31°E-109°E; 15°S-6°S] 2) Light-shaded green box 3) Dark-shaded green box	SBC applied over the entire NIO coastline
NAFNIODEQ	Same as NAFNIO, but with a damper in the equatorial region	Red box [35°E-105°E; 4°S-4°N]	SBC applied over the entire NIO coastline
NAFNIODEQBB	Same as NAFNIODEQ, but with an additional damper in the Bay of Bengal	1) Red box [35°E-105°E; 4°S-4°N] 2) Within pink frames over Bay	SBC applied over the entire NIO coastline
NAFNIODEQBBTIP	Same as NAFNIODEQBB, but with an additional damper in the STIP region	1) Red box [35°E-105°E; 4°S-4°N] 2) Within pink frames over Bay 3) Black box over STIP region	SBC applied over the entire NIO coastline

**Table 5.2:** The processes and the method for obtaining the processes using LCS model sensitivity experiments, whose details are provided in Table 5.1. The processes are shown schematically in Figure 5.5.

Process	Process abbreviation	Method
Signals forced by alongshore forcing in BoB	AFBB	$sl(NIO) - sl(NAFBB)$
Signals forced by alongshore forcing in STIP region	AFST	$sl(NIO) - sl(NAFST)$
Signals forced by alongshore forcing in AS	AFAS	$sl(NIO) - sl(NAFAS)$
Signals forced by alongshore forcing in the entire NIO	AFNIO	$sl(AFBB) + sl(AFST) + sl(AFAS)$
Signals due to SIO forcing	SIO	$sl(NIO) - sl(DSIO)$
Signals originating from the NIO that propagate into the equatorial band at the western boundary and back into the NIO	TrEQ	$sl(NAFNIO DSIO) - sl(DSWT)$
Equatorial signals through classical pathway	EQB	$sl(DSWT) - sl(DSBWT)$
Equatorial signals through direct pathway	EQD	$sl(DSBWT) - sl(NAFNIO DEQ)$
Signals forced by interior BoB	IBB	$sl(NAFNIO DEQ) - sl(NAFNIO DEQBB)$
Signals forced by interior AS	IAS	$sl(NAFNIO DEQBBTIP)$
Signals forced by interior forcing in the STIP region	IST	$sl(NAFNIO DEQBB) - sl(NAFNIO DEQBBTIP)$

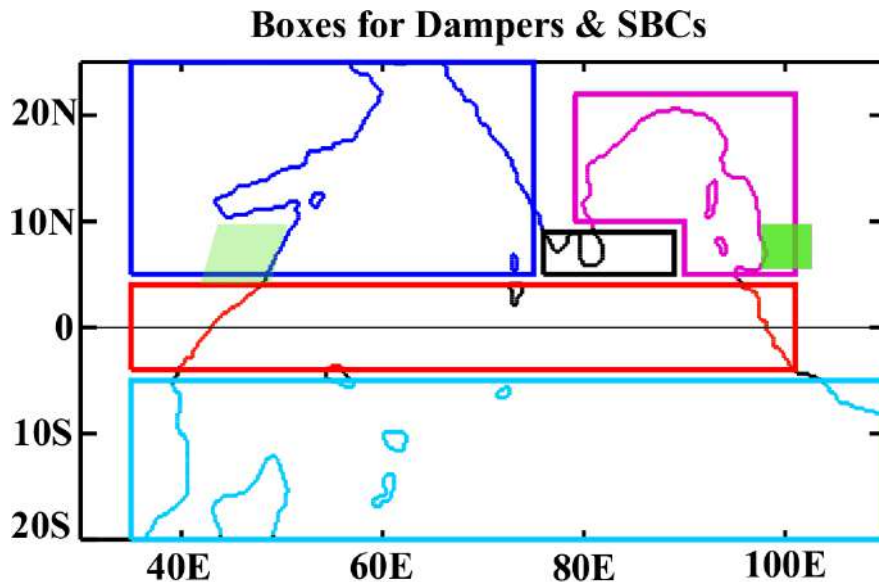


**Figure 5.7:** Map showing the boxes over which Special Boundary Conditions (SBCs) and dampers are applied for isolating the processes listed in Section 5.4 (schematically shown in Figure 5.5 with the same color code). The box boundaries are indicated in Table 5.1.

**Sensitivity experiments for isolating the alongshore forcing:** The effect of the alongshore forcing (the coastal KW generation) over a section of coastline is isolated from the CTL solution with an experiment in which SBC is imposed over that section. For filtering the AFBB process, the SBC is applied over the entire BoB coast starting from (98.5°E, 5°N) to (79.5°E, 9°N), i.e., coastline within the pink color frame in Figure 5.7. This sensitivity experiment is referred to as NAFBB (“No alongshore forcing in the BoB”). The sea level due to AFBB process is then obtained as the difference between CTL and NAFBB.

$$sl(AFBB) = sl(CTL) - sl(NAFBB)$$

The AFAS process is isolated with SBC applied to the AS coastline from (76°E, 9°N) to (40°E, 5°N), i.e. coastline within the blue frame in Figure 5.7 (NAFAS – “No alongshore forcing in the AS”).

$$sl(AFAS) = sl(CTL) - sl(NAFAS)$$

As discussed in Section 5.3,  $sl(ST)$  in Eqn. 5.1 combines the influence of the alongshore forcing (AFST) as well as the Ekman pumping (IST) in the STIP region. That is,

$$sl(ST) = sl(AFST) + sl(IST) \text{ -----(Eqn. 5.2)}$$

The AFST process is extracted in an experiment (NAFST – “No alongshore forcing in the STIP region”) with SBC applied within the black box (Figure 5.7) bounded by 76°E-89°E and 5°N-9°N.

$$sl(AFST) = sl(CTL) - sl(NAFST)$$

The sum of the above sensitivity experiments (NAFBB, NAFST, and NAFAS) is equivalent to applying SBC over the entire NIO coast and will be referred to as NAFNIO (“No alongshore forcing in the NIO”).

$$sl(NAFNIO) = sl(NAFBB) + sl(NAFST) + sl(NAFAS)$$

Equivalently, the effect of alongshore forcing in the entire NIO (AFNIO) is the sum of the effects due to alongshore forcing in the BoB, the STIP region, and the AS. That is,

$$sl(AFNIO) = sl(AFBB) + sl(AFST) + sl(AFAS) \text{ -----(Eqn. 5.3)}$$

Combining Eqns. 5.2 and 5.3, Eqn. 5.1 can now be rewritten as:

$$sl(CTL) = sl(EQD) + sl(EQB) + sl(AFNIO) + sl(IBB) + sl(IST) \\ +sl(IAS) + sl(TrEQ) + sl(SIO) \text{ -----(Eqn. 5.4)}$$

**Separation of SIO process:** The experiment that filters out the effect of SIO process in the NIO sea level has the same set up as the CTL experiment, but with a damper imposed over the cyan box bounded by 31°E-109°E and 15°S-6°S (Figure 5.7), with a 1° ramp at the boundaries to minimize distortion of the signals (see Section 3.3 for a discussion on the ramp). This sensitivity experiment is denoted as DSIO (“Damper in the SIO”). The SIO process is then obtained by taking the difference between the CTL and the DSIO experiments.

$$sl(SIO) = sl(CTL) - sl(DSIO)$$

**Separation of TrEQ process:** Extraction of TrEQ signals involves a set of two sensitivity experiments: DSWT and NAFNIODSIO. The DSWT experimental set up is same as the CTL, but with the following conditions: SBC applied all along the NIO coast (NAFNIO), the damper used for isolating the SIO process (DSIO), and a “wave trap” (see Section 3.3 for a discussion on the *wave trap*) on the Somalia coast as shown by the light-shaded green box in Figure 5.7. The wave trap involves modifying the land points to ocean and damping out the signals within the box. This trap when used at the Somalia coast damps out all the signals at this coast, thereby blocking the signals entering into the equatorial waveguide from NIO, implying that the solution will be free from TrEQ. Thus the overall effect of DSWT is to remove the contribution from AFNIO, SIO and TrEQ. From Eqn. 5.4,

$$sl(DSWT) = sl(EQD) + sl(EQB) + sl(IBB) + sl(IST) + sl(IAS) \text{ ----(Eqn. 5.5)}$$

In NAFNIODSIO experiment, SBC is applied over the entire NIO in addition to imposing the SIO damper in CTL. The resulting sea level is:

$$sl(NAFNIODSIO) = sl(EQD) + sl(EQB) + sl(IBB) + sl(IST) + sl(IAS) + sl(TrEQ) \text{ -----(Eqn. 5.6)}$$

The difference, Eqn. 5.6 – Eqn. 5.5 (or)  $sl(NAFNIODSIO) - sl(DSWT)$ , then yields the sea level due to TrEQ process, that is,

$$sl(TrEQ) = sl(NAFNIODSIO) - sl(DSWT)$$

**Separation of EQB and EQD processes:** The EQB and EQD signals are separated out with a set of three experiments, which are referred to as NAFNIODEQ, DSWT, and DSAWT. NAFNIODEQ experiment is the same as the CTL, but SBC is applied over NIO (NAFNIO) along with a damper imposed over the entire equatorial band extending from 4°S to 4°N (red box in Figure 5.7), with a 1° ramp at the northern and southern edges to reduce distortion of the signal near the edges. The solution with this damper has no equatorial variability, and hence no equatorial signal propagates to the NIO. The equatorial damper also damps out the TrEQ and SIO signals. As a result,

$$sl(NAFNIODEQ) = sl(IBB) + sl(IST) + sl(IAS) \text{ -----(Eqn. 5.7)}$$

The DSWT has already been discussed above and is given by Eqn. 5.5. In addition to the SBC over the entire NIO, SIO damper, and the wave trap at the Somalia coast, DSBWT uses an additional “wave trap” in the eastern boundary of BoB as shown by the dark-shaded green box in Figure 5.7. This trap damps out the coastal KWs (excited on reflection of equatorial KWs at the eastern boundary) that enter the coastal waveguide of the BoB (i.e., the EQB signals are damped out). The DSBWT sea level can then be written as:

$$sl(DSBWT) = sl(EQD) + sl(IBB) + sl(IST) + sl(IAS) \text{ -----(Eqn. 5.8)}$$

The EQB signal is obtained as the difference between DSWT (Eqn. 5.5) and DSBWT (Eqn. 5.8), i.e.,

$$sl(EQB) = sl(DSWT) - sl(DSBWT)$$

and the EQD signal is obtained as the difference between DSBWT (Eqn. 5.8) and NAFNIODEQ (Eqn. 5.7).

$$sl(EQD) = sl(DSBWT) - sl(NAFNIODEQ)$$

**Separation of interior BoB forcing:** When considering the interior BoB forcing, the strong wind-stress curl forcing off the east coast of Sri Lanka (STIP region) is treated separately under the ST process. The interior Bay forcing mainly refers to the forcing by the winds in the pink (BB) box in Figure 5.7 and is extracted using two sensitivity experiments: NAFNIODEQ and NAFNIODEQBB. NAFNIODEQ has already been described above and is given by Eqn. 5.7. NAFNIODEQBB is similar to NAFNIODEQ, but with an additional damper over BB box, which damps out the IBB signals. The resulting sea level is given by,

$$sl(NAFNIODEQBB) = sl(IST) + sl(IAS) \text{ -----(Eqn. 5.9)}$$

The sea level due to IBB process is obtained from the difference, Eqn. 5.9 – Eqn. 5.7.

$$sl(IBB) = sl(NAFNIODEQ) - sl(NAFNIODEQBB)$$

**Separation of IST and IAS processes:** The interior forcing near the southern tip of India and off the east coast of Sri Lanka (IST), and that in the AS are isolated with an additional experiment (NAFNIODEQBBTIP), which involves imposing SBC over the entire NIO and dampers over equatorial region (red box), BB box (pink), and STIP region (black box) (Figure 5.7) in the experimental set up of CTL. This yields:

$$sl(IAS) = sl(NAFNIODEQBBTIP) \text{ -----(Eqn. 5.10)}$$

$sl(IST)$  is computed as the difference between Eqn. 5.9 and Eqn. 5.10:

$$sl(IST) = sl(NAFNIODEQBB) - sl(NAFNODEQBTTIP)$$

The processes isolated using the above-described method of decomposition add up to CTL, with almost negligible residual, thus emphasizing the accuracy of this method. While the focus of this chapter is on the intraseasonal timescale, the method of decomposition of processes presented in this section is independent of the timescale. The above CTL and the process solutions will also be analyzed at seasonal and interannual timescales in Chapter 6. Though many studies [McCreary et al., 1996; Shankar et al., 2002] have already used similar approach for isolating the processes using model sensitivity experiments, the method presented above is quite innovative in that it allows isolating some of the processes (e.g., EQD, TrEQ) that could not be separated by the earlier studies.

## 5.6 Results

### 5.6.1 Model validation

***EOF modes and their relationship in the model and observations:*** The large-scale intraseasonal sea level patterns in the observations and CTL solution are extracted using EOF analysis (see Section 3.4). Because of the strong mesoscale eddy activity in the western AS in observations, the sea level EOF domain is restricted to the east of 55°E in the NIO for both observations and model. In addition, the observations are smoothed spatially over a 2° box before computing the sea level EOF patterns to reduce the influence of eddies within the EOF computational domain (for e.g., western BoB). The sea level patterns corresponding this EOF analysis over the entire NIO domain are obtained through regression onto the normalized PCs. Figure 5.8 shows the explained variance of the first five EOF modes. It clearly indicates that the first EOF mode is well separated from the rest both in model and observations. The first two EOF sea level modes explain 58% of the variance, with EOF1 explaining 42% in the model. The variance explained by the first two modes is much less (35%) in observations due to the influence of mesoscale eddies in the observed intraseasonal sea level, but the ratio

between EOF1 and EOF2 explained variances is reasonably similar to that of the model. Figure 5.8 also shows the lagged auto-correlations of the first and second principal components and the lag correlations between them for both CTL and observations. Auto-correlations of PC1 and PC2 indicate that the first two EOF modes are associated with  $\sim 90$ -day timescale both in model and observations [Han, 2005]. The lag correlations between PC1 and PC2 peak ( $\sim 0.8$  correlation in both model and observation) at  $\sim -21$  days, indicating that the first two EOFs are in phase quadrature, which usually corresponds to propagating signals in EOF analyses. As will be seen later, the remarkable agreement between the EOF2 spatial pattern and patterns of lead-regression to PC1 at 21 days confirms that EOFs 1 and 2 together represent propagating patterns associated with the leading mode of intraseasonal sea level variability. Because of their dominance and the quadrature relationship, only the first two modes are considered for the rest of the analysis.

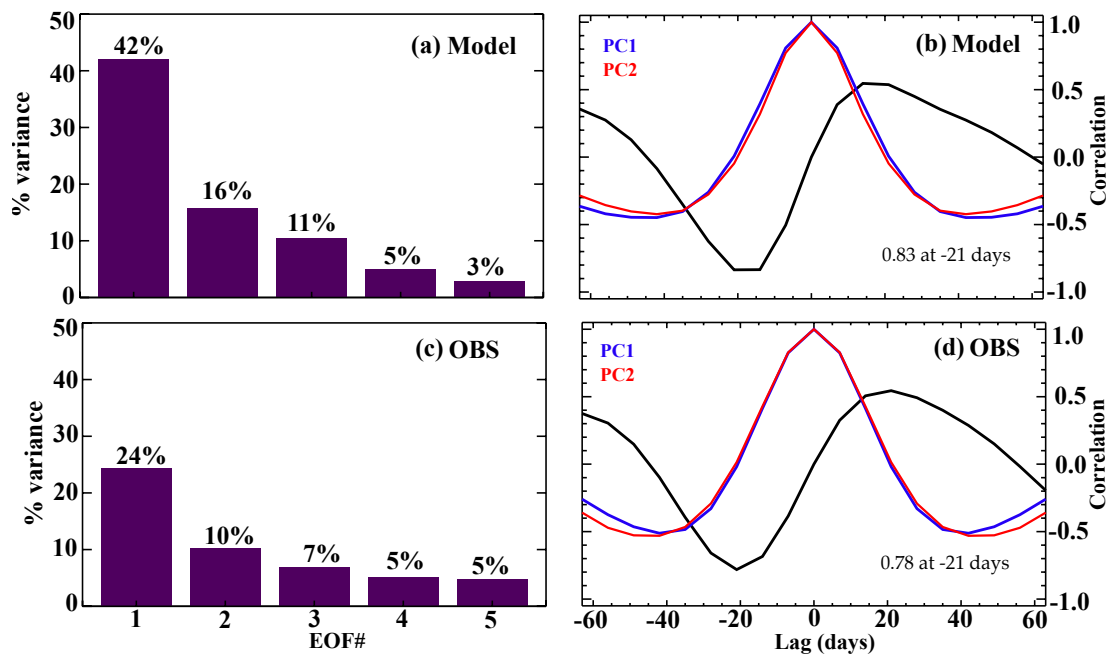


**Figure 5.8:** The EOF analysis of the intraseasonal sea level from the CTL run (top row) and observations (bottom row). (a) Explained variance of the first five EOF modes (modes 1 and 2 explain  $\sim 58\%$  in the model); (b) Autocorrelation of PC1 (blue) and PC2 (red) and lag-correlation (black) of PC1 and PC2 in the model (-ve correlation indicates that PC1 leads PC2). Panels (c, d) are same as (a, b), but for the observations. EOF modes 1 and 2 explain  $\sim 34\%$  in the observations.

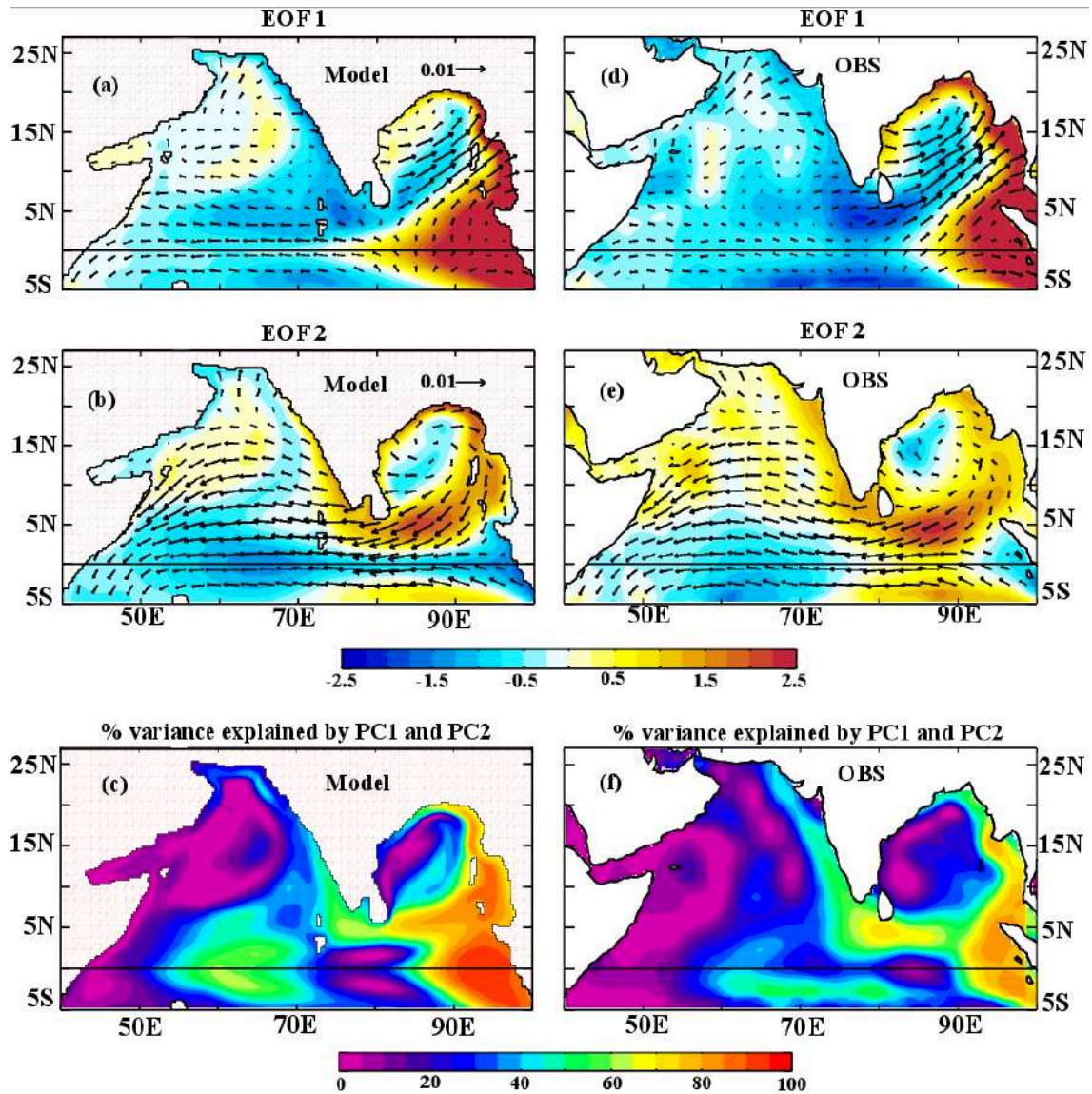


**Figure 5.9:** Spatial patterns of the EOF modes from the model (left panels) and observations (right panels). (a) and (b) show spatial patterns of the 1<sup>st</sup> and 2<sup>nd</sup> EOF modes. (c) Map showing the percentage of variance in sea level ISV explained by EOF modes 1 and 2. (d, e, and f) are same as (a, b, and c), but for observations.

**Validation of basin-scale patterns and their explained variance:** Figure 5.9 displays the spatial patterns of the first two EOF modes for both CTL (Figure 5.9a,b) and observed (Figure 5.9d,e) intraseasonal sea levels and related wind pattern, and the variance explained (in %) by them (Figures 5.9c,f). Despite a slight underestimation in the amplitude, the model is able to capture the observed EOF patterns remarkably well. The first EOF shows the downwelling equatorial KWs reaching the eastern boundary and propagating as the downwelling coastal KW along the BoB rim and the upwelling coastal KW propagation along the WCI. The second EOF shows the same propagating patterns, but with the above-mentioned (discussion on Figure 5.8) quadrature shift in the

90-day timescale. The second EOF shows the downwelling equatorial RWs excited by the reflection of downwelling equatorial KWs and also the downwelling coastal KWs that have already reached the WCI. In the mean time, the equatorial westerly winds have turned to easterlies, leading to generation of upwelling equatorial KWs. In the model, the first two sea level EOF modes together explain more than 80% of variance in the eastern equatorial IO and along the eastern rim of the BoB (Figure 5.9c,f). The explained variance progressively decreases around the rim of the Bay, reaching 20-30% along the ECI, probably due to destructive interference between signals from the equator and those generated by winds in the Bay (e.g., winds associated with PC1 exhibit a positive curl in the Bay favoring upwelling signals). The variance explained by the two modes in CTL sea level along the WCI is 50-60%, as for observed sea level. For the BoB, the eddy activity results in a reduction of explained variance in the observations compared to that in the model. In addition to these spatial EOF patterns, the modeled sea level PCs exhibit a very good phase agreement with that of the observations (Figure 5.10), with a correlation of 0.85 for PC1 and 0.75 for PC2. The good performance of the model suggests that this model is well suited for studying the dynamics of sea level ISV in the NIO.

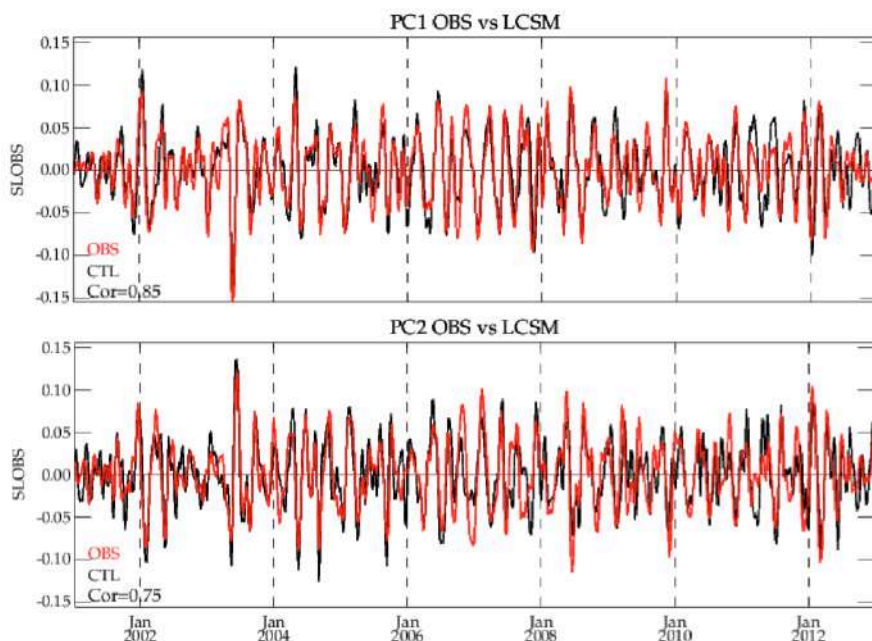


**Figure 5.10:** Comparison of modeled (black line) and observed (red line) PC1 (top panel) and PC2 (bottom panel). Correlation of 0.85 for PC1s and 0.75 for PC2s.

## 5.6.2 Dynamics of sea level ISV

***Basin-scale intraseasonal patterns in the sea level and wind forcing:*** Left panels (a-f) of Figure 5.11 display the modelled sea level and wind-stress patterns obtained from a lag-regression onto the sea level PC1, similar to those shown in Figure 4.3, but for more lags here. In spite of using a different product for the wind-stress forcing in the present CTL simulation (TropFlux) as compared to the one in Chapter 4 (QuikSCAT), the two sea level patterns (Figure 5.11 vs. Figure 4.3) are almost the same and remarkably similar to those in the observations (Figure 2.17) shown by Vialard et al. [2009], though they used a different method of analysis. This suggests that these large-scale intraseasonal patterns are very robust and essentially reveal the same underlying dynamics as that described in Section 4.3.2. The patterns of wind-stress curl and alongshore forcing obtained by a similar lag-regression onto sea level PC1 are also displayed on the right panels (g-l) of Figure 5.11 to allow discussing the main dynamics of sea level ISV in terms of the forcing. The westerly wind anomalies in the equatorial region force a downwelling equatorial KW (Figure 5.11a), which enters into the BoB coastal waveguide as a downwelling coastal KW and further propagates along the rim of the Bay (Figures 5.11a-d). The strong positive curl (Figures 5.11g,h) in the interior Bay from lag -14 to 0 day excites upwelling signals, which propagate westward as upwelling RWs, potentially leading to a destructive interference at the northwestern and western rims of the BoB, thereby diminishing the downwelling KW signals along these coasts. There is a strong coastal alongshore forcing at the southern tip of India and Sri Lanka (Figures 5.11g,h) that can trigger upwelling coastal KW signals at these coasts. The STIP region also exhibits strong positive curl (Figures 5.11g,h) that helps reinforcing the above upwelling signals, which further propagate to the WCI (negative sea level anomalies along WCI in Figures 5.11a-c). From +7-day lag onward (Figure 5.11j-l), the STIP forcing reverses its sign (compared to Figures 5.11g,h) both in terms of alongshore forcing and wind curl forcing, and strengthens further within a week to induce downwelling coastal KW signals along the WCI (Figure 5.11e). In the mean time, part of the energy of the incoming equatorial KW is reflected (Figure 5.11d and e) at the Sumatra coast as downwelling equatorial RW. This westward-propagating RW interacts with the Sri Lankan coast and reinforces the downwelling coastal signal in the STIP region (Figure 5.11e-f) that further propagates poleward along the WCI (Figure 5.11f). At +7-day lag (Figure 5.11d), the equatorial winds (westerlies in Figure 5.11a)

shift to easterlies, which force upwelling equatorial KWs (Figure 5.11e and f), leading to sea level signals of opposite polarity, and hence to the opposite phase, to complete the cycle (of  $\sim 90$  day period; Figure 5.8b).

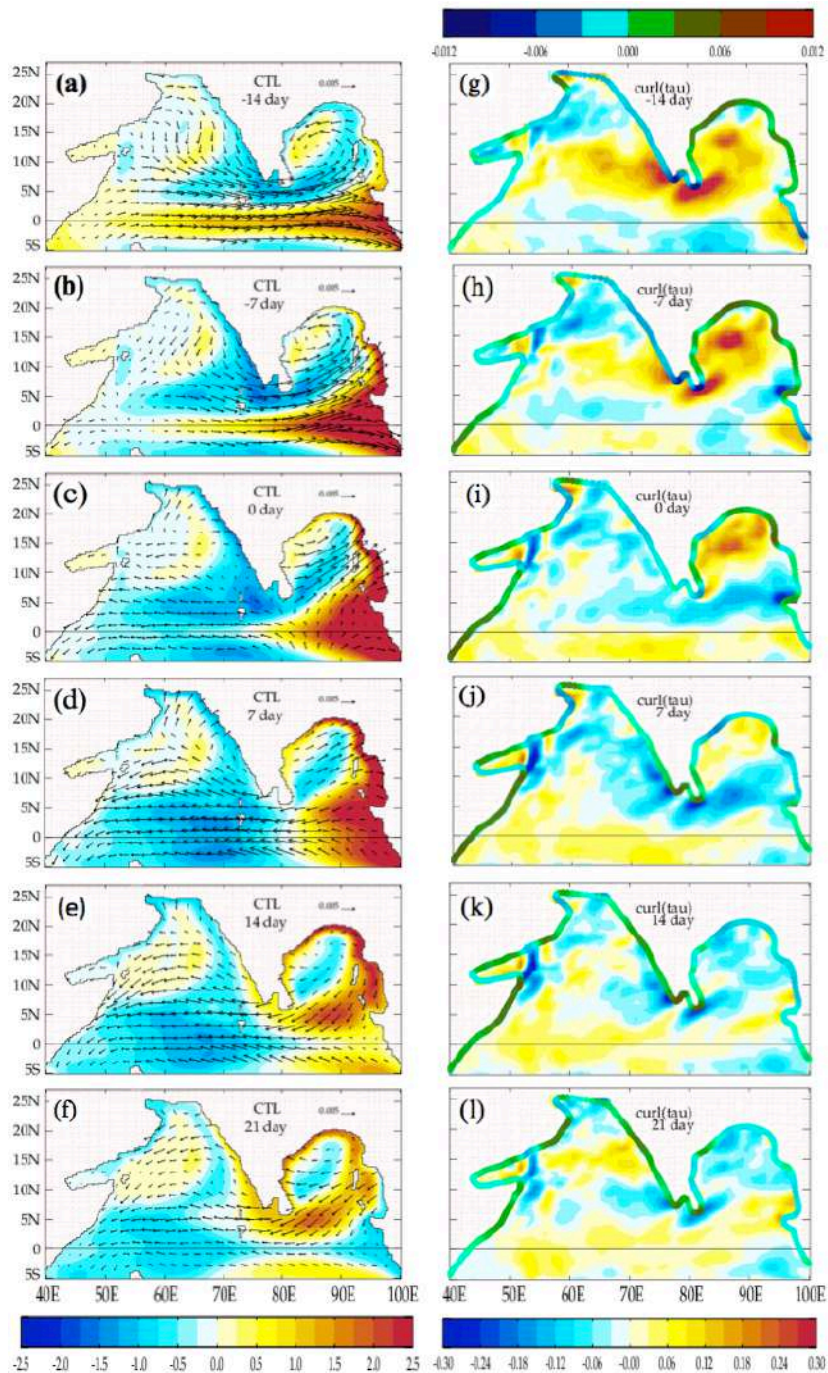


**Figure 5.11:** The lag-regression (the lags are indicated in each panel) patterns of intraseasonal (left panels) sea level (cm; from CTL; color bar below the left column) and wind stress ( $N/m^2$ ), and (right panels) wind stress curl ( $\times 10^7$ ;  $N/m^3$ ; color bar below the right column) and alongshore wind forcing ( $N/m^2$ ) to the normalized PC of the EOF1 of CTL intraseasonal sea level. The sea level pattern at lag 0 shows the spatial structure of the EOF1 (see Figure 5.9a), and negative lags indicate the sea level patterns that lead the PC. TropFlux wind stresses have been used. The alongshore wind forcing is indicated with a different color shading (see color bar above the right column) along the coastline on the right panels.

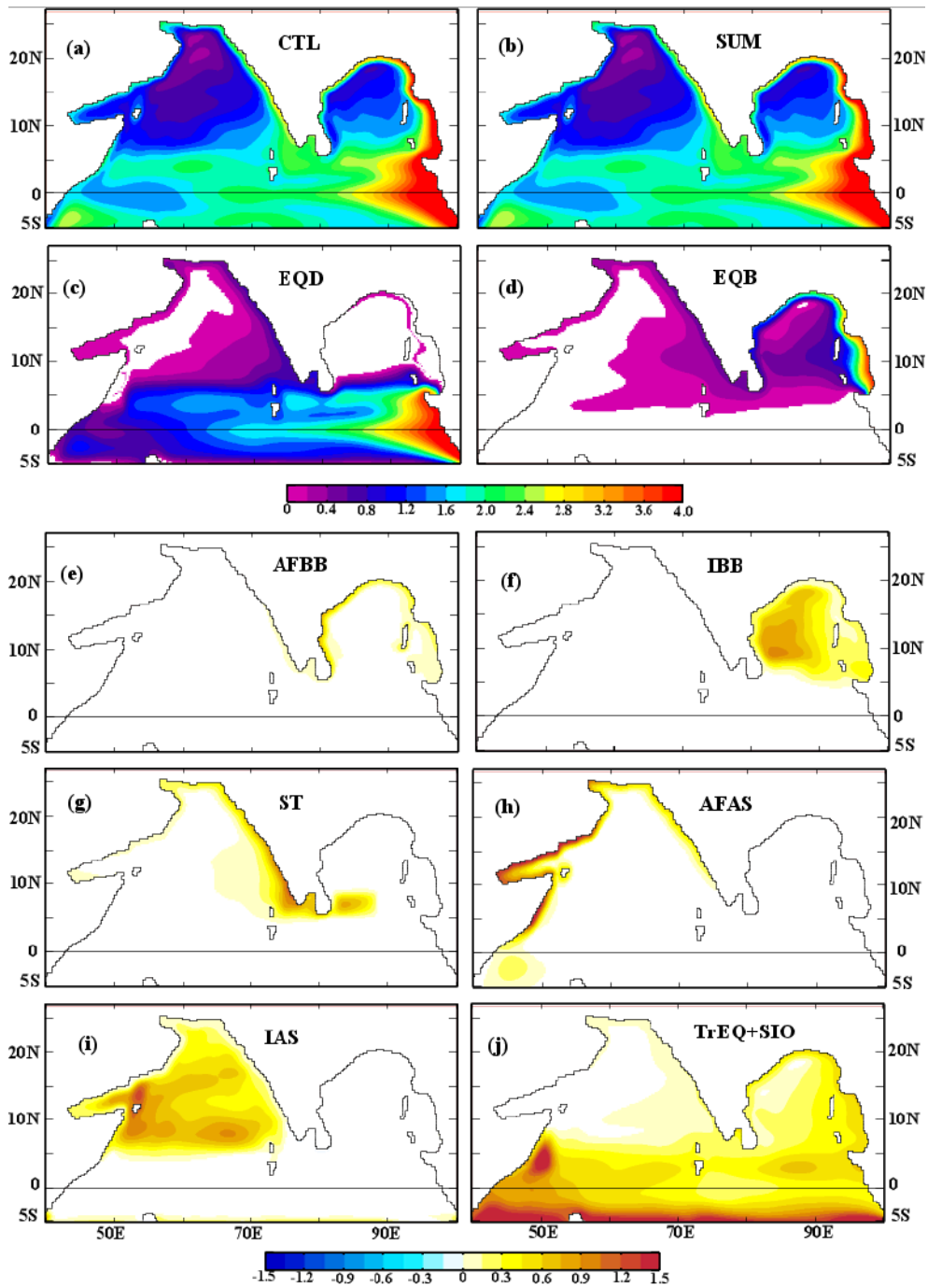


**Figure 5.12:** Decomposition of the amplitude (standard deviation, see Section 5.6.2 for details) of intraseasonal sea level from (a) CTL into that from the process: (c) EQD, (d) EQB, (e) AFBB, (f) IBB, (g) ST, (h) AFAS, (i) IAS, and (j) TrEQ+SIO. Panel (b) shows the sum of the amplitudes of all the processes that add up to the CTL (panel a). The residual (CTL minus sum of all processes) is negligible.

**Decomposition of the CTL into processes:** Figure 5.11 provides qualitative insights on the dynamics of large-scale wind-driven intraseasonal sea level patterns in the NIO. However, it does not allow to quantify the contribution of each process to the sea level ISV, particularly along the NIO coastal waveguide. Figure 5.12 shows the

decomposition of the amplitude of CTL sea level ISV into that of each process, which is calculated as the coefficient of correlation between each process and CTL sea levels multiplied by the standard deviation of the corresponding process sea level (this is same as the regression coefficient of process sea level onto CTL sea level, multiplied with standard deviation of CTL sea level). EQB is the process that contributes most to sea level ISV in the BoB coastal waveguide, whereas EQB, EQD and ST all contribute to the sea level ISV on the coastal waveguide off WCI. Spatial pattern in each map exactly depicts how the process is expected to behave. The amplitude of the signals resulting from the interior forcing increases progressively westward due to integration of forcing along the RW path (Figure 5.12f) and the amplitude of the signals forced by alongshore forcing increasing along the coastal KW path (Figures 5.12e and 5.12h). TrEQ+SIO plays a role in the western equatorial IO, where as EQD dominates east of 60°E. EQB influences the coastal waveguide through coastal KW propagation and the interior Bay and eastern AS through RW radiation from the eastern boundaries. As expected from the critical latitudes of the intraseasonal frequencies (see Section 2.1), the RW propagation is restricted to the southern BoB and AS. Figure 5.12 thus demonstrates that the method of decomposition indeed works as expected.

***Driving processes of the CTL sea level ISV:*** Figure 5.13 shows the decomposition of CTL sea level pattern (shown in Figures 5.11a-f) into each of the above processes. These snapshots clearly demonstrate how each of the processes operates as the CTL sea level evolves. The EQB signals contribute to CTL sea level both along the coastal waveguide and in the interior BoB through coastal KWs and RW radiation from the eastern boundary. This offshore radiation from the eastern rim of the Bay is confined to ~15°N probably because the critical period at this latitude is ~95 days [Vialard et al., 2009; Suresh et al., 2013] (Section 2.1). The equatorial signals have shorter periods [Han, 2005], implying that these waves remain trapped at the coast north of their critical latitude 15°N (Section 2.1). Figure 5.13 also illustrates the EQD process, which involves westward propagation of the reflected equatorial RW and its subsequent interaction with the Sri Lankan landmass (seen especially at lags 7, 14 and 21 days), roughly in 28 days, which is consistent with the phase speed of the first baroclinic first meridional mode ( $50 \pm 10$  cm/s) estimated by Webber et al. [2012] or Dhage and Strub [2016]. The downwelling signal along the WCI at 21-day lag in CTL is mainly driven by EQD. The strong wind forcing (alongshore and Ekman pumping) in the STIP region

(Figure 5.4) drives a KW response, which influence the CTL sea level through ST process (Figure 5.13m-o). A detailed evaluation of the contributions from each of the processes to the CTL sea level ISV is provided in the next section.

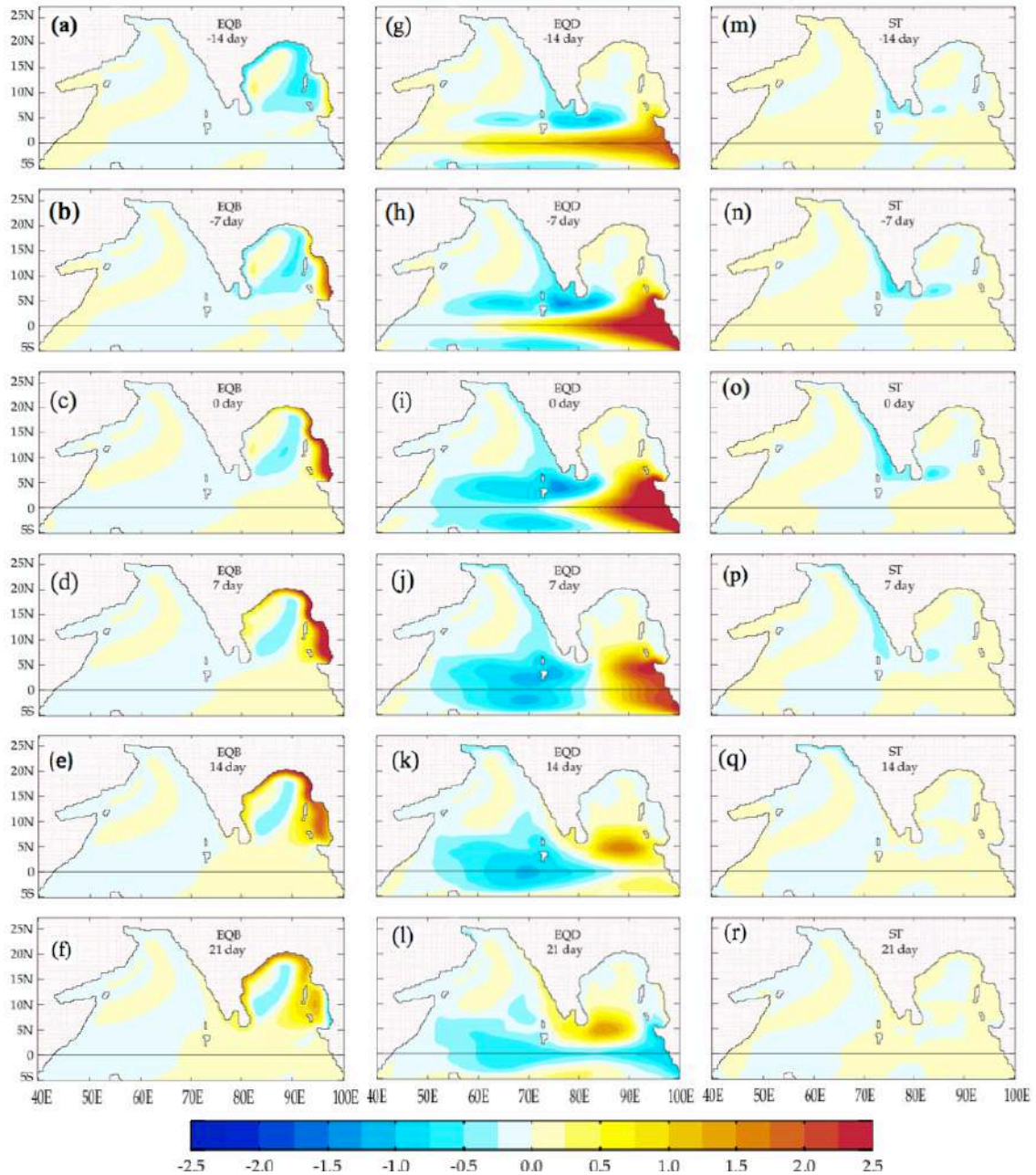


**Figure 5.13:** Decomposition of sea level (cm) from CTL shown in Figure 5.11a-f into that from (a-f) EQB, (g-l) EQD, and (m-r) ST processes at the same lags. Other processes are not shown due to their relatively less contribution to the sea level ISV along the NIO coastal waveguide.

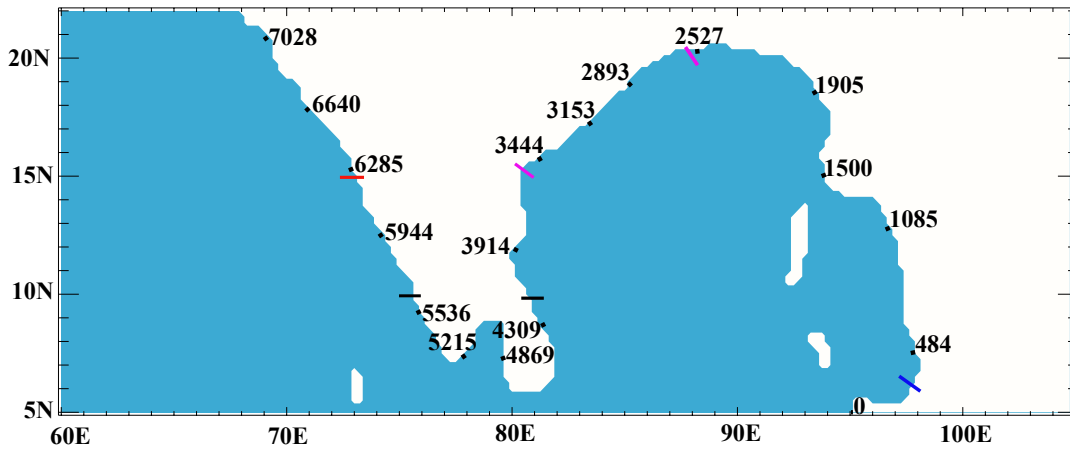


**Figure 5.14:** The map showing the distances along the NIO coastal waveguide to help interpreting the Figures 5.15 - 5.17. The distances are marked in km along the NIO coastal waveguide, starting from the tip of Sumatra (0 km), and form abscissa in the Figures 5.15 - 5.17. The blue tick marks the entrance of BoB coastal waveguide. The region between pink (black) tics is the northwestern BoB (STIP) region. The red tic marks 15°N latitude on the WCI. These color codes are used for shading the corresponding regions in Figures 5.15-5.17.

### 5.6.3 Process contributions to the sea level ISV in the NIO coastal waveguide

**Estimation of process contributions:** Figure 5.15 presents the decomposition of amplitude of the CTL intraseasonal sea level (Figure 5.15a) and the percentage contribution of each process to that sea level variability (Figure 5.15b) as a function of distance along the NIO coastal waveguide starting from the Sumatra coast (Figure 5.14). The percentage contribution is nothing but the regression coefficient of each process sea level to that of CTL, expressed in percentage. As in Section 4.3.2, these contributions are estimated over the entire time series and are not restricted to the sea level associated to the EOF1 (which gives similar results; not shown), allowing a general evaluation of the process contributions. The regression values are averaged over a 20-km cross-shore extent. It is verified that the sea level amplitudes add up to that of the CTL (black dashed line; Figure 5.15a) and that the sum of percentage contributions of processes (Figure 5.15b) almost equal 100%, as expected from the linearity of the model.

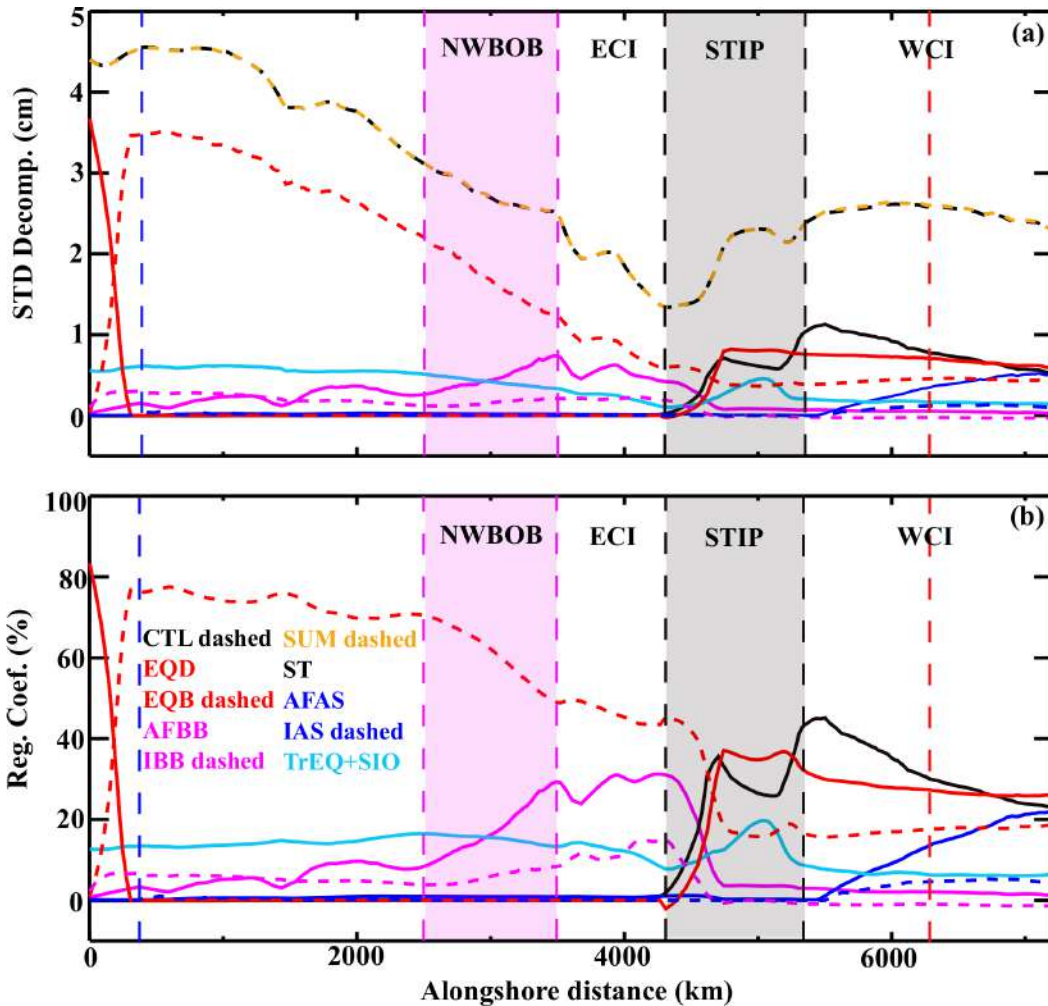


**Figure 5.15:** (a) Standard deviation of intraseasonal sea level from CTL (dashed black curve) and its decomposition into each process (see Table 5.2), as a function of distance along the NIO coastal waveguide (Figure 5.14). The quantities are averaged over a 20-km cross shore extent. The entrance of BoB waveguide (marked with a tic of same color in Figure 5.14) is indicated with dashed blue vertical line at a distance of ~390 km. The region between dashed pink vertical lines (marked with same color in 5.14) indicates the northwestern BoB, where local alongshore forcing is important. The dashed, black vertical lines (tics of same color in Figure 5.14) enclose the STIP region. The dashed, red vertical line (tic of same color in Figure 5.14) at the right extreme (~6300 km) marks the position of WCI box. (b) same as panel (a), but for regression coefficient (given in %) of each process to CTL.

**Process contributions in BoB waveguide:** The CTL intraseasonal sea level amplitude (black dashed curve; Figure 5.15a) is nearly 4.5 cm at the entrance of the BoB waveguide (~390 km) and decreases gradually to ~1.5 cm at the exit north of Sri Lanka (~4200 km). The sea level ISV along the BoB coast is dominated by EQB (red dashed line; Figure 5.15a), whose amplitude decreases from ~3.5 cm at the entrance to ~0.8 cm the end of the rim of the Bay. EQB contributes 80-90% to the sea level ISV in the eastern rim of the Bay (red dashed line; Figure 5.15b), but decreases counter-clockwise around the rim to ~50% along the ECI, in agreement with the results of the previous

chapter (Section 4.3.2). The contribution of the alongshore forcing in the Bay starts increasing in the northwestern rim of the Bay (AFBB; pink line; Figure 5.15b), as expected from the strong alongshore forcing in this region (Figure 5.4) and reaches ~25% along the ECI (~0.5 cm). On the other hand, the interior forcing contributes to less than 10% of the sea level ISV along the East Indian coast (IBB; pink dashed line; Figure 5.15b). There is also a marginal contribution (~10%) from the combined effect of TrEQ and SIO along the rim of the Bay (cyan line; Figure 5.15b), with slightly more contribution from the latter. The rest of the processes do not contribute to the sea level ISV in the Bay, but they become important for the WCI, as discussed below.

***Process contributions along WCI:*** The CTL sea level ISV (black dashed line; Figure 5.15a) is nearly constant along the WCI (~2.5 cm) and results from ST, EQD, EQB, and AFAS (~ 0.9, 0.8, 0.5 and 0.4 cm respectively). The STIP forcing dominates the WCI sea level ISV (black line; Figure 5.15b). Its contribution is maximum at the southern tip of India (~40%) and reduces poleward along the coast, both because of its dissipation/leakage of energy offshore and increasing AFAS contribution, reaching 30% off Goa. The new EQD process also contributes substantially to the sea level ISV along the WCI (red line; Figure 5.15b), driving ~30% of the variability over the entire coast, except for a slight frictional damping on the coastal KW pathway. EQB still contribute ~20% to the WCI sea level ISV (red dashed line; Figure 5.15b), making the total contribution of equatorial forcing to nearly 50%, which is 10-20% lesser compared to the earlier estimate (60-70%) provided in Section 4.3.2. This is because the equatorial signals in the previous chapter do include a part of the STIP forcing, resulting in overestimation of its contribution to the WCI sea level ISV. The contribution of AFAS increases poleward along the WCI due to integration of forcing along the wave path (blue line; Figure 5.15b), reaching ~10% off Goa, in contrast to that estimated as 30% in Section 4.3.2. This is because the AS wind forcing in Chapter 4 includes part of the wind forcing in the STIP region. More precisely, the STIP forcing in the present setup is redistributed among the equatorial (alongshore forcing at the southern tip of Sri Lanka), BoB (Ekman pumping off the east coast of Sri Lanka), and AS (both Ekman pumping and alongshore forcing at the southern tip of India) wind forcing, which led to the above differences in the estimated contributions. Finally, AFBB, which is suggested to be important for WCI at the seasonal timescale [Shankar and Shetye, 1997], contributes only negligibly to the sea level ISV off the WCI (pink line; Figure 5.15b).

### 5.6.4 Seasonality in the process contributions

**Seasonality in the process sea level amplitudes:** Seasonal variations of the intraseasonal wind forcing have already been discussed in detail in Section 4.3.3 (Figures 4.6a,b). The contributions of the processes to the sea level ISV in the NIO coastal waveguide, similar to those shown in Figure 5.15, are presented separately for boreal summer (Figure 5.16) and winter (Figure 5.17). In general, CTL sea level ISV amplitude (black dashed line; Figure 5.16a) during boreal summer is slightly larger than that during winter (black dashed line; Figure 5.17a), in agreement with Section 4.3.3, except for the SIO (cyan lines; Figures 5.16a and 5.17a). During boreal winter, the wind forcing is stronger in the SIO, leading to larger amplitude of SIO during that time. The strong wind forcing in the NIO during summer results in larger amplitudes of the AFBB, IBB, AFAS and ST process sea levels as seen in Figures 5.16 and 5.17.

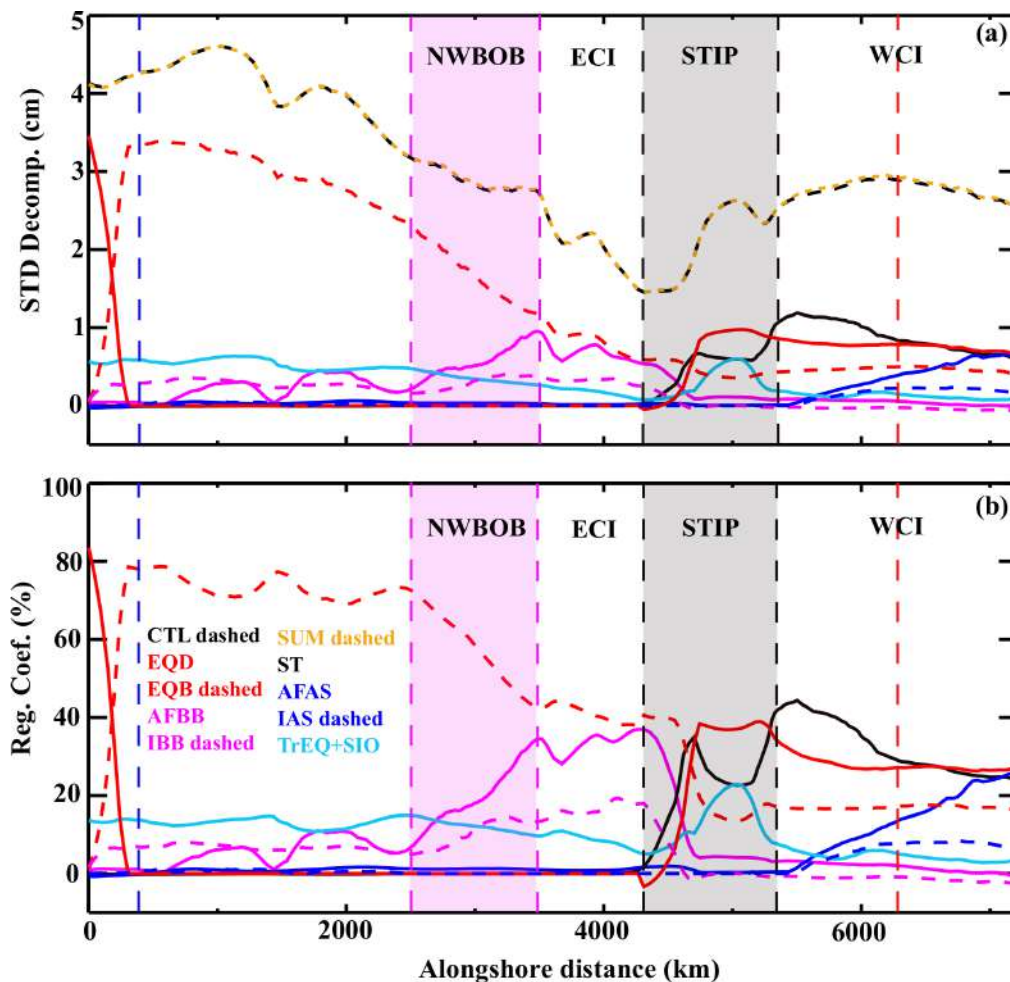


Figure 5.16: Same as Figure 5.15, but for boreal summer (JJAS).

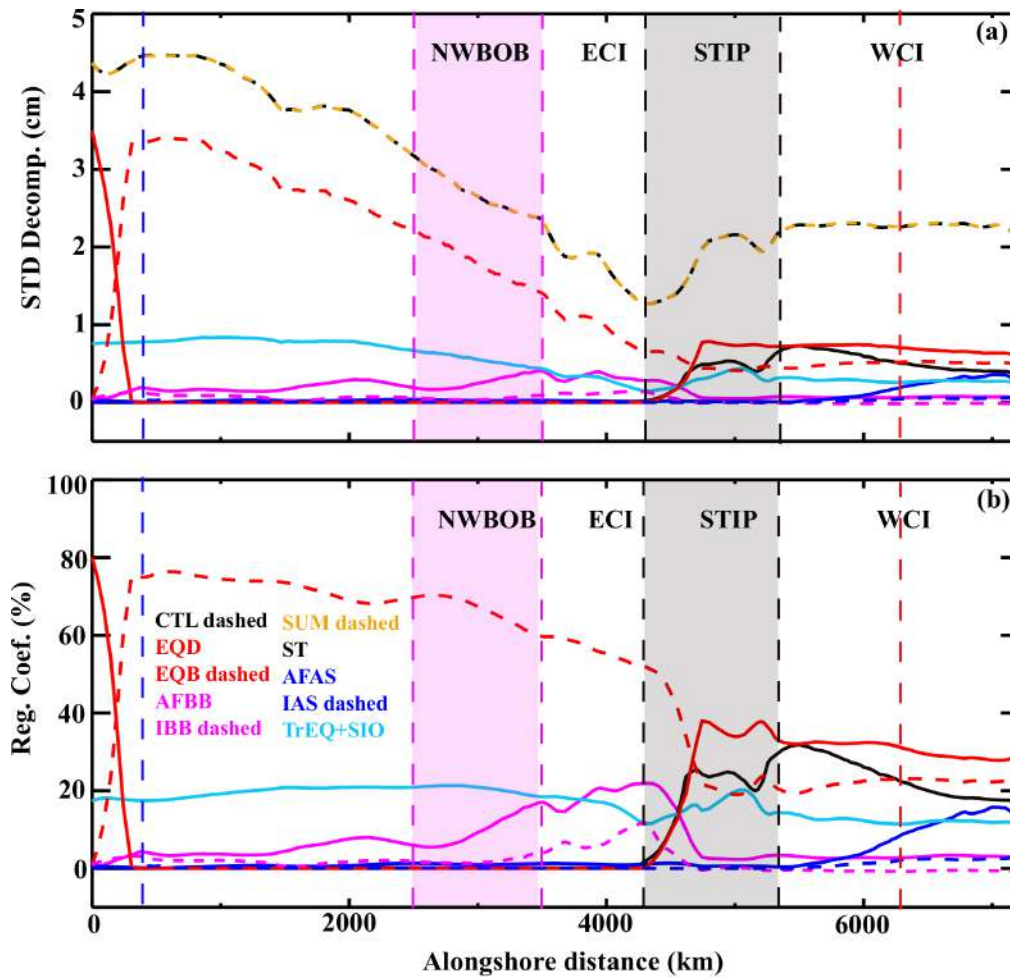


Figure 5.17: Same as Figure 5.15, but for winter (DJFM).

**Seasonality in the process contributions along BoB coast:** The stronger alongshore forcing in the northwestern rim of the Bay results in two-fold increase in the contribution of the AFBB process (pink lines; Figures 5.16b and 5.17b) during summer (up to 35%) compared to winter (up to 17%) along the northwestern and western boundaries of the Bay. Similar increase (10% in summer and 5% in winter) is seen in the IBB contribution (pink dashed lines; Figures 5.16b and 5.17b) along the ECI. This increase in the local forcing of the BoB results in reduced contribution of the EQB signals, from 60% to 40%, along those parts of the BoB coast. On the other hand, the contribution of the SIO signals is larger during winter (20%) than during summer (10%) along the BoB coast.

**Seasonality in the process contributions along WCI:** As with the BoB, the local forcing becomes stronger in the AS, leading to increased contribution of the ST and AFAS processes by 10-15% to the WCI sea level ISV during summer compared to

winter, while the EQD and EQB contributions remain nearly the same at this coast during both seasons.

## 5.7 Summary

**An overview of the chapter:** This chapter investigates extensively the dynamics of the wind-driven, intraseasonal sea level variability in the NIO. Using a series of idealized LCS experiments, this chapter provides the first ever demonstration of the direct link between the equatorial waveguide and the coastal waveguide off the WCI. This connection involves the interaction of equatorial RWs with the Sri Lankan coast, which excites coastal KWs that eventually propagate poleward along the WCI. The chapter also provides new insights on the intraseasonal forcing *hotspots*, namely the regions with strong alongshore forcing and Ekman pumping velocity. With this background, the chapter identifies and gathers an exhaustive list of mechanisms that can potentially drive the NIO sea level ISV. This chapter also develops an innovative method of process decomposition that involves a suite of carefully-designed LCS model sensitivity experiments to extract the processes and to estimate their relative contributions to the sea level ISV along the NIO coastal waveguide.

**Main findings:** The sea level ISV in the coastal waveguide of the BoB is dominated by EQB, whose contribution decreases progressively from 80-90% at the eastern rim of the Bay to ~50% on the ECI. The alongshore forcing in the northwestern rim of the Bay contributes ~25% downstream the coastal KW pathway in the Bay. The WCI sea level ISV is dominated by the wind forcing in the STIP region and the EQD signals, each with ~30% contribution. The EQB signals make their way all through the BoB rim to contribute ~20% to the WCI sea level, with alongshore forcing off the western Indian shelf contributing to the remaining small fraction of the sea level ISV. In addition, the above contributions are modulated seasonally owing to dominant modes of atmospheric variability, namely, the MJO during winter and the active/break phases of the boreal summer, with the local wind forcing (its various components such as alongshore and interior forcing) contribution is higher during summer than winter.

## Comparison of sea level dynamics between intraseasonal, seasonal, and interannual timescales

---

**Overview:** The previous two chapters deal extensively with the dynamics of intraseasonal sea level variability in the NIO coastal waveguide. This chapter examines the differences in the sea level dynamics between intraseasonal and other (seasonal and interannual) timescales. In doing so, this chapter revisits the sea level dynamics at seasonal (in Section 6.1) and interannual (in Section 6.2) timescales and refines the findings from the earlier literature, in wake of the new process decomposition proposed in this thesis (Sections 5.4 and 5.5.2; Figure 5.5; Table 5.2), particularly the role of the newly-established direct connection between the equatorial waveguide and the WCI (EQD process), and the strong localized STIP wind forcing (ST process). Moreover, this chapter (Section 6.2) provides new insights into the IOD influence on the NIO interannual sea level variability. Finally, Section 6.3 provides an inter-comparison between the intraseasonal, the seasonal, and the interannual sea level dynamics.

### 6.1 Dynamics of seasonal sea level

#### 6.1.1 Introduction

**Background:** In the past three decades, numerous studies have focused on describing and understanding the dynamics of sea level and surface currents in the NIO, particularly along the coast of India, at the seasonal timescale based on both observations and numerical models (see Section 2.2 for a review). These studies, however, provided only a qualitative rather than quantitative assessment of the relative importance of remote against local wind forcing for the seasonal variability along the Indian coast. Moreover, these studies did neither assess in detail the forcing fields (the potential *hotspots* of wind forcing, see below), nor account for the EQD pathway, both

of which have been demonstrated in the previous chapter to be important for the sea level ISV on the WCI.

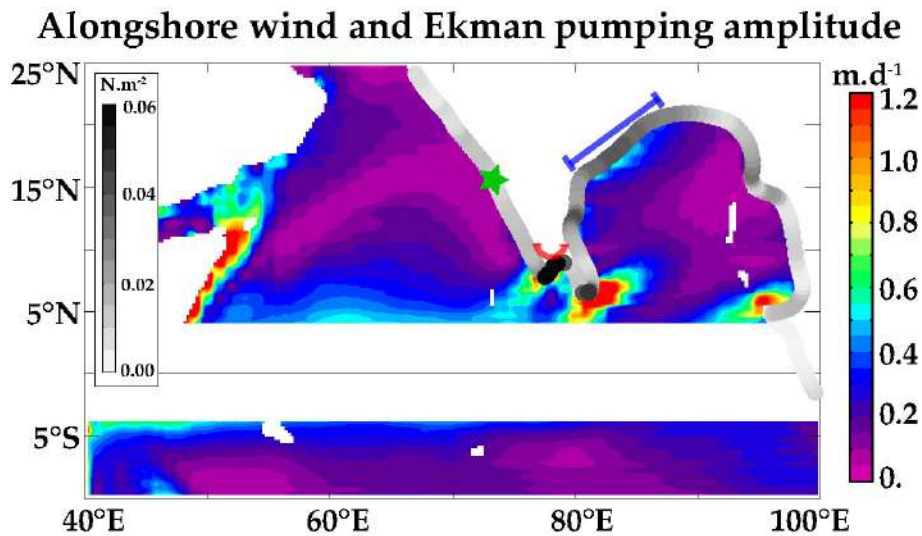


**Figure 6.1:** Standard deviation of the seasonal Ekman pumping velocity (color shaded) and the alongshore wind stresses (grey shades along the coastline; grey scale inset). The coastlines along northwestern BoB and STIP region that are referred to in Figure 6.2 are marked in blue and red colors respectively. The green asterisk marks 15°N on the WCI (off Goa).

**The hotspots of seasonal wind forcing:** Figure 6.1 highlights the regions with strong, localized seasonal variations in the alongshore wind stress and Ekman pumping velocity in the NIO. The hotspots of seasonal wind forcing almost coincide with those of intraseasonal forcing (Figure 5.4). The northwestern BoB and the STIP regions exhibit strong alongshore wind-stress forcing as the southwest and northeast monsoon winds blow parallel to the coast there (Figures 2.5a,b). A strong Ekman pumping signal is also evident off the east coast of Sri Lanka in Figure 6.1. The sea level anomalies that result from the above forcing will propagate westward as RWs and induce signals at the Sri Lankan coast, which can, in principle, set up coastal KWs and impact the sea level and currents downstream along the WCI. Figure 6.2 shows the amplitude (standard deviation) of the observed sea level seasonal cycle in the NIO coastal waveguide. Though coastal sea level amplitude starts increasing in the region of strong alongshore forcing in the northwestern BoB, the increase is far larger in the vicinity of STIP region, strongly suggesting that the wind variations in this region are important for the large-amplitude seasonal cycle (Figure 6.3; see Section 2.2) downstream on the WCI. Thus the alongshore wind stress and offshore Ekman transport variations in the STIP region, which accounts for less than 20% of the total area of the BoB, could play a dominant

role on the WCI seasonal variability. Though the earlier modeling studies [McCreary et al., 1993; Shankar et al., 2002] did include forcing by the STIP wind variations, its importance and a precise evaluation of its contribution to the WCI seasonal cycle has so far not been assessed.

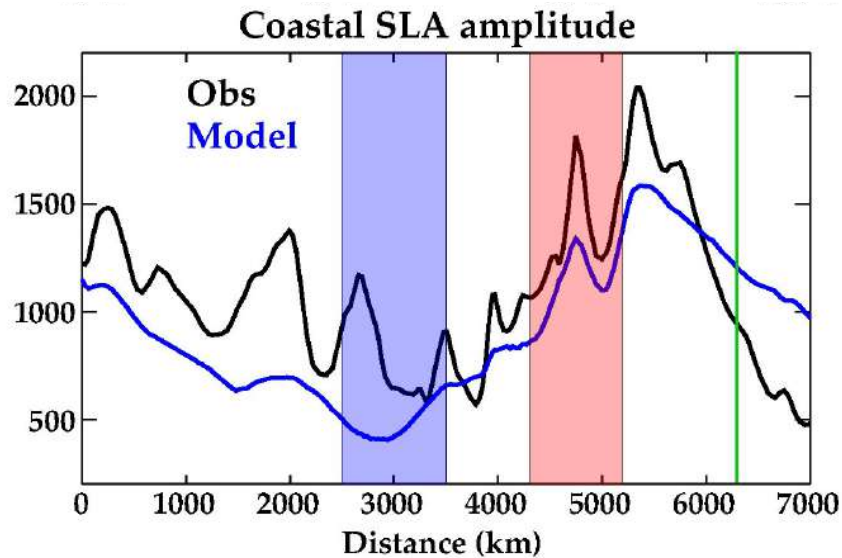


**Figure 6.2:** Standard deviation of the seasonal sea level normalized by the square root of the Coriolis parameter, averaged over a 50-km cross-shore extent, plotted as a function of distance along the NIO coastal waveguide from the entrance of BoB waveguide at its eastern rim (see Figure 5.14). The above normalization eliminates the increasing wave amplitude associated with the narrowing coastal waveguide towards higher latitudes [e.g., Gill, 1982]. The blue (red) shaded vertical band marks the region of strong alongshore forcing in the northwestern BoB (STIP) identified by a marker of the same color in Figure 6.1. The green vertical line marks 15°N on the WCI, also marked with a green star in Figure 6.1 and black frames in Figure 6.3.

**Goal of section 6.1:** In order to evaluate precisely the differences or similarities in the sea level dynamics between intraseasonal and seasonal timescales (later in Section 6.3), it is necessary to perform beforehand a thorough analysis of the seasonal sea level in the NIO coastal waveguide, following the strategy adopted for the NIO sea level ISV in Chapter 5. This section, hence, aims at providing a detailed investigation of the processes that drive the sea level seasonal cycle along the NIO coastal waveguide and to quantify their contributions using the same set of LCS model sensitivity experiments and subsequent process decomposition as in Chapter 5. In particular, the importance of ST and EQD processes for the WCI seasonal sea level variability has been assessed in detail. Robustness of the results of this section to various choices, including the model parameters, has also been evaluated at the end of this section.

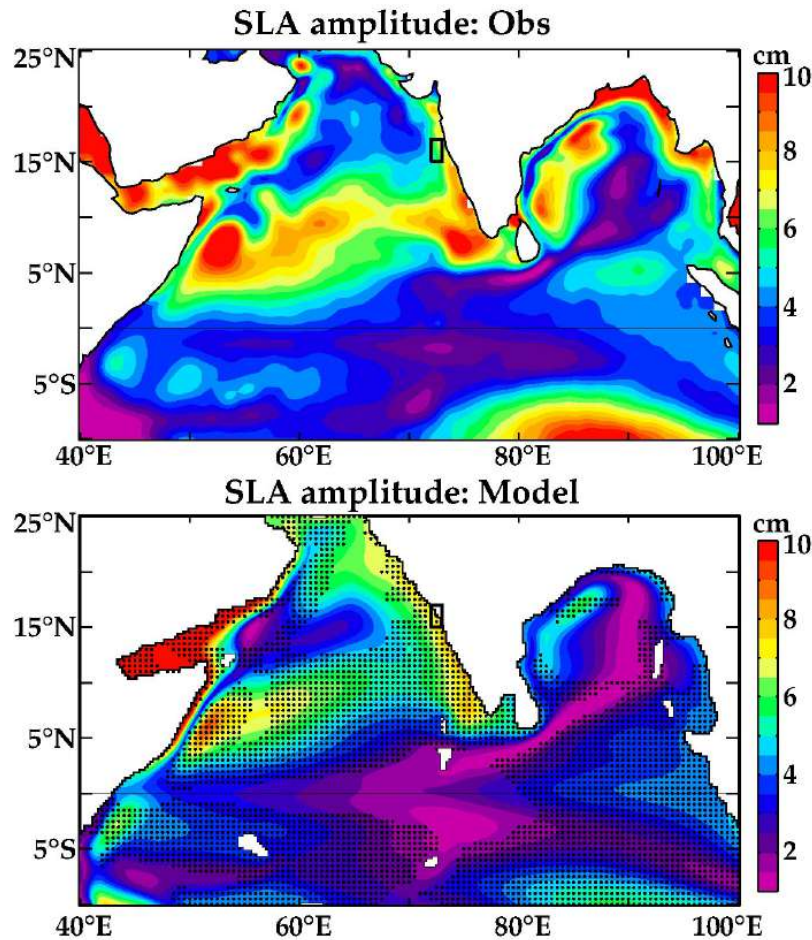


**Figure 6.3:** Standard deviation of the observed (top panel) and the modeled (CTL; bottom panel) seasonal sea levels. The regions, where the correlation between the observed and CTL seasonal sea levels is more than 0.8 are hatched in black in the bottom panel.

### 6.1.2 Model and the sensitivity experiments

**The Model and its validation:** The model configuration and the experimental setup are the same as those described in Chapter 5 and hence only the model validation at the seasonal timescale is presented here. The seasonal sea level from the CTL experiment is validated against the AVISO altimeter observations (see Section 3.2). Figure 6.3 suggests that the linear model correctly reproduces the observed amplitude and phase of the sea level seasonal cycle in most of the basin (hatched regions indicate where the correlation of CTL with the observed seasonal cycle is greater than 0.8), except in eddy-dominated regions (western BoB and western AS), where nonlinear effects are important. The agreement is especially good all along the WCI (correlations exceeding 0.8 along the entire coast). The model also reproduces well (Figure 6.2) the amplitude

of the seasonal cycle all along the rim of the NIO (though with a slight underestimation), particularly the increase in sea level amplitude in the vicinity of the STIP region. The model thus displays a good performance not only at the intraseasonal timescale (validation presented in Chapter 5), but also at the seasonal timescale.

***The Process solutions:*** The method for isolating the processes (Section 5.5.2; Figure 5.5; Tables 5.1 and 5.2) that influence the NIO sea level variability can be applied irrespective of the timescale, and will hence be applied to the seasonal sea level in the present chapter. As with the case of intraseasonal timescale, the results are not very sensitive to other reasonable choices of the dampers used for the process solutions (see Section 6.1.6). In the following, the point-wise contribution of each process to the CTL seasonal sea level over the entire year is quantified by estimating the regression coefficient of the sea level seasonal cycle in each process solution to that in CTL solution. By construction, those coefficients add up to 1 (100%) and can be negative if a process interferes destructively with the other to contribute to the CTL seasonal sea level.

### **6.1.3 Overview of the basin-scale sea level and wind forcing patterns**

***Basin-scale sea level patterns and wind forcing:*** Figure 6.4 presents the spatial patterns of the climatological sea level, wind stress, wind-stress curl, and alongshore forcing during December-March (DJFM; winter), April-May (AM; spring inter monsoon), June-September (JJAS; summer), and October-November (ON; Fall inter monsoon). These patterns are consistent with the description of seasonal cycle of winds and sea level presented elsewhere in the literature [e.g., McCreary et al., 1993; Schott and McCreary, 2001]. Of particular interest here is the STIP forcing. The STIP region displays strong wind-stress curl (and hence intense Ekman pumping velocity) and alongshore forcing (Figures 6.4g,e), which are upwelling (downwelling) favorable during summer (winter). The WCI sea level is consistent with the above forcing, exhibiting upwelling (downwelling) signals during summer (winter), with a phase transition during the inter-monsoon periods. The northwestern part of the BoB also possesses strong wind-stress curl and alongshore forcing in phase with the STIP forcing, but of weaker amplitude (Figures 6.4g,e). In addition, the southeastern BoB region exhibits (Figures 6.4g,e) strong wind-stress curl forcing of opposite polarity to

that of STIP forcing. Figures 6.4c,a also show that the sea level anomalies in those regions are consistent with the above forcing. On the other hand, intrusion of seasonal KWs from the equatorial region into the BoB waveguide is evident in Figure 6.4c (6.4a), with signatures of downwelling (upwelling) signals during summer (winter) along the eastern rim of the BoB as an extension of the equatorial signals. The contributions from various processes to the CTL seasonal cycle of sea level along the NIO coastal waveguide are evaluated below, following the analyses performed in Chapter 5.

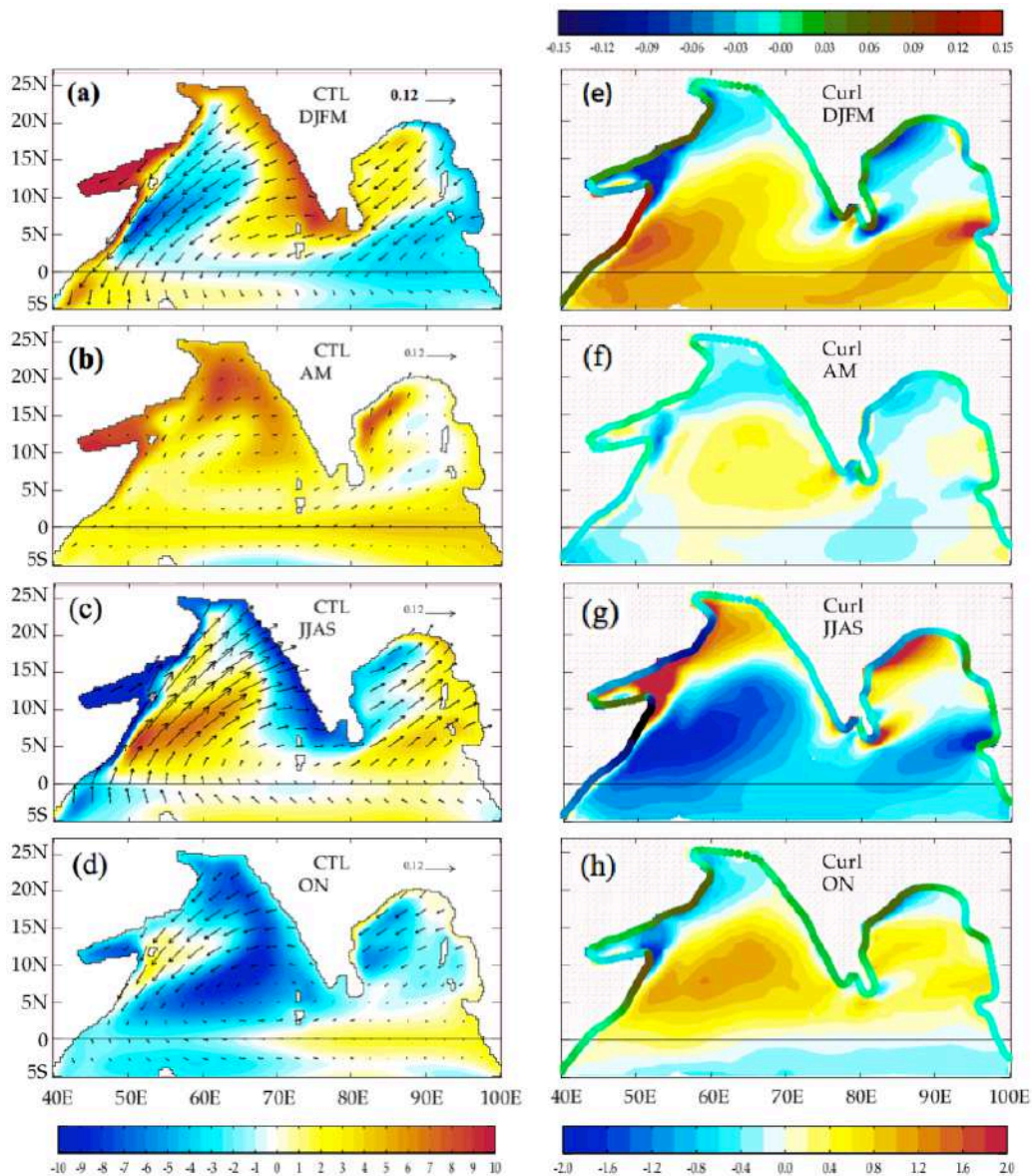


**Figure 6.4:** Seasonal climatology of (a-d) CTL sea level (cm; shaded) and TropFlux wind stresses ( $N.m^{-2}$ ; vectors) and (e-h) curl of the wind-stress field ( $\times 10^7$ ;  $N/m^3$ ; shaded) and alongshore wind forcing ( $N/m^2$ ) during (a, e) DJFM, (b, f) AM, (c, g) JJAS, and (d, h) ON. The alongshore wind forcing is indicated with a different color shading along the coastline on top of the right column (negative values indicating upwelling-favorable winds).

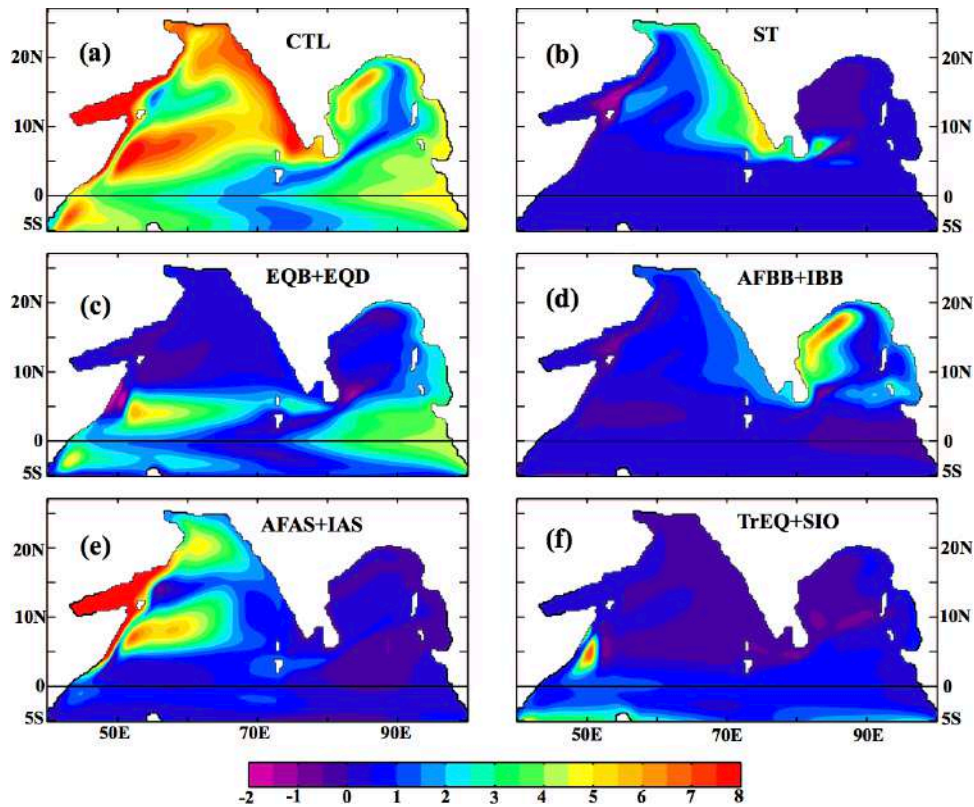


**Figure 6.5:** Decomposition of the amplitude (standard deviation; similar to Figure 5.12) of intraseasonal sea level (cm) from (a) CTL into that from each process (b) ST, (c) EQB + EQD, (d) AFBB + IBB, (e) AFAS + IAS, and (f) TrEQ + SIO. See the text for a justification of grouping some of the processes. The residual (CTL minus sum of all processes) is negligible.

**CTL sea level and evaluation of process contributions:** Figure 6.5 (similar to Figure 5.12 for sea level ISV) shows the decomposition of the amplitude of CTL seasonal sea level into that of each process, calculated as the coefficient of correlation between CTL and process sea levels multiplied by the standard deviation of the process sea level. Additionally, the contributions of each process to the CTL seasonal sea level, computed as regression coefficient of process sea level onto the CTL sea level, are presented in Figure 6.6 (similar to Figure 4.5). As these figures suggest, the seasonal sea level along the eastern rim of the BoB is dominated by the EQB process (Figures 6.5c and 6.6b; note that, by definition, EQD=0 in the BoB) and that along the western rim by a combination of AFBB and IBB processes (Figures 6.5d and 6.6c). The WCI seasonal sea level cycle is dominated by the ST process (Figures 6.5b and 6.6a), with some contribution from the wind forcing in the BoB (combination of AFBB and IBB processes; Figures 6.5d and 6.6c). Due to their moderate contributions along WCI, the AFBB and IBB processes are presented together. The equatorial processes (EQB and

EQD) do not appear to contribute significantly to the seasonal cycle along the WCI (Figures 6.5c and 6.6b; detailed in the discussion of Figure 6.11) and are combined. For a similar reason, the AFAS and IAS are also shown together. However, individual process contributions along the NIO coastal waveguide will be presented later in Figure 6.11 and that will further justify the above choices. The CTL sea level climatological seasonal cycle (Figures 6.4a-d) decomposed into each process (grouped as discussed above) is shown in Figures 6.7-6.10 to help understanding how each process contributes to the CTL seasonal sea level in the NIO.

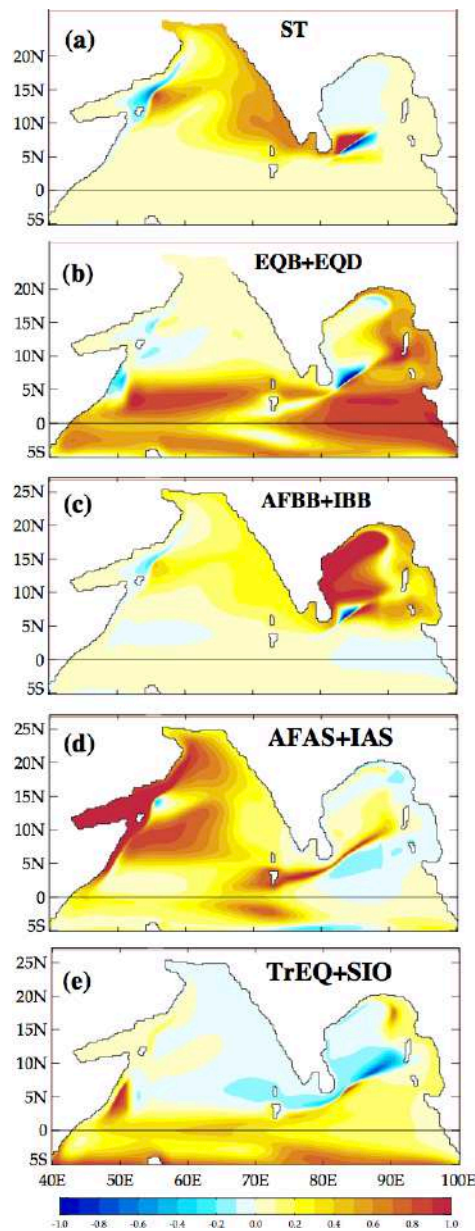


**Figure 6.6:** Contribution of each process (a) ST, (b) EQB + EQD, (c) AFBB + IBB, (d) AFAS + IAS, and (e) TrEq + SIO to CTL sea level seasonal cycle, computed as the regression coefficients of the respective process seasonal sea level to that of CTL experiment. The sum of the contributions is equal to 1 (100%) by construction.

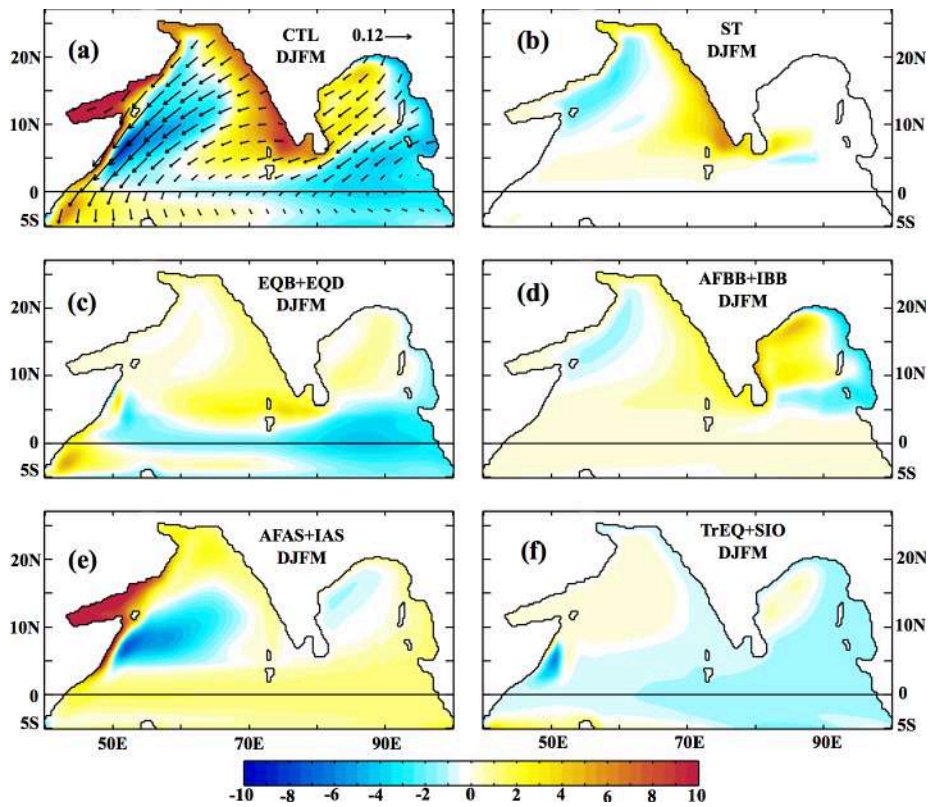


**Figure 6.7:** Climatological sea level (cm) for winter (DJFM) from (a) CTL experiment and its decomposition into processes (b) ST, (c) EQB + EQD, (d) AFBB + IBB, (e) AFAS + IAS, and (f) TrEQ + SIO.

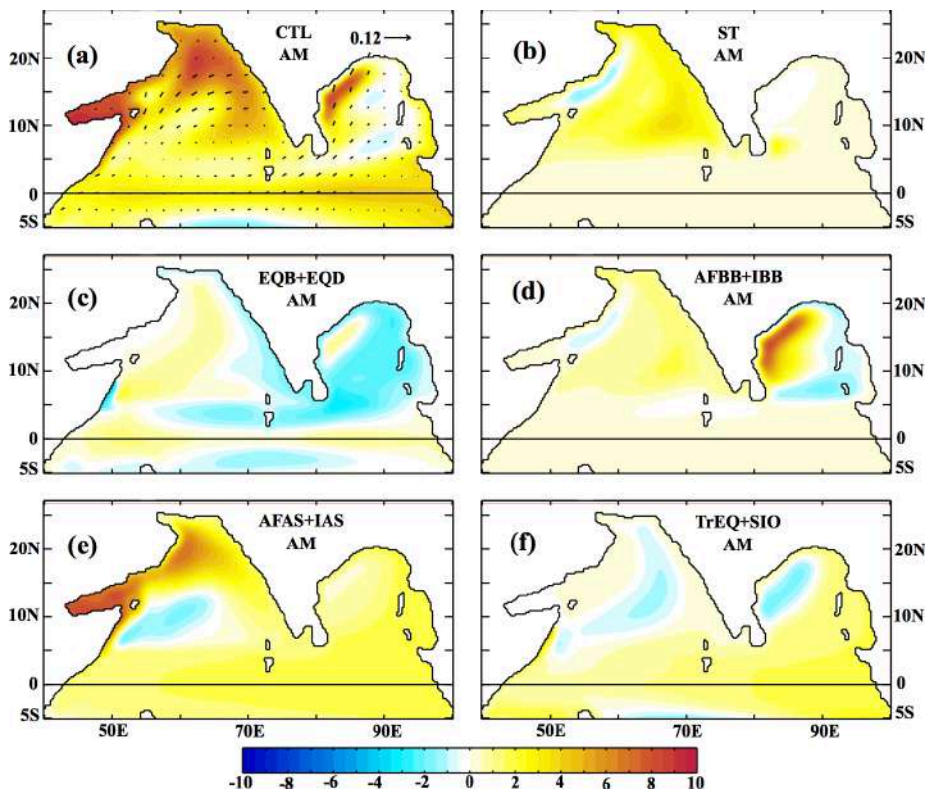


**Figure 6.8:** Same as Figure 6.7, but for spring (AM).

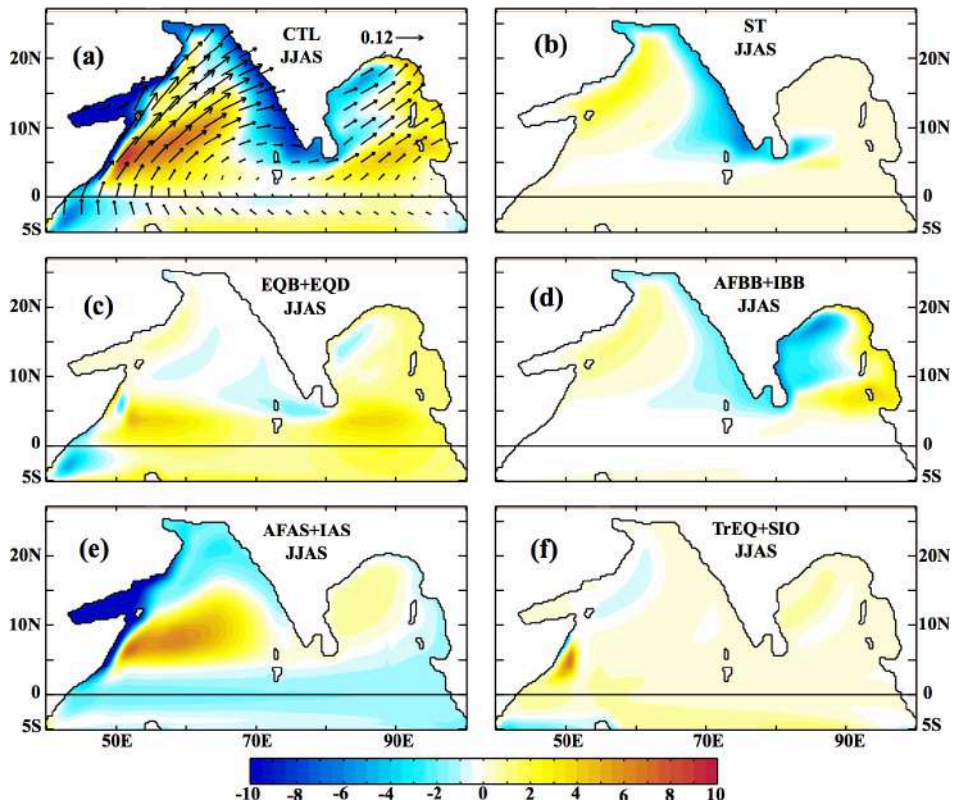


Figure 6.9: Same as Figure 6.7, but for summer (JJAS).

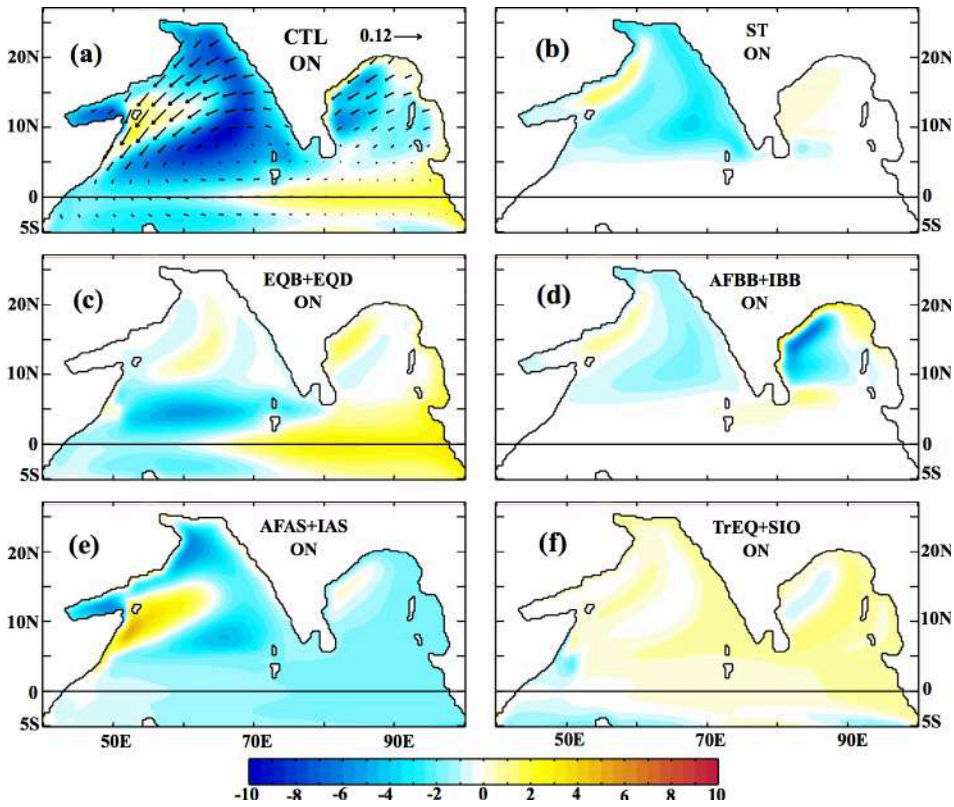
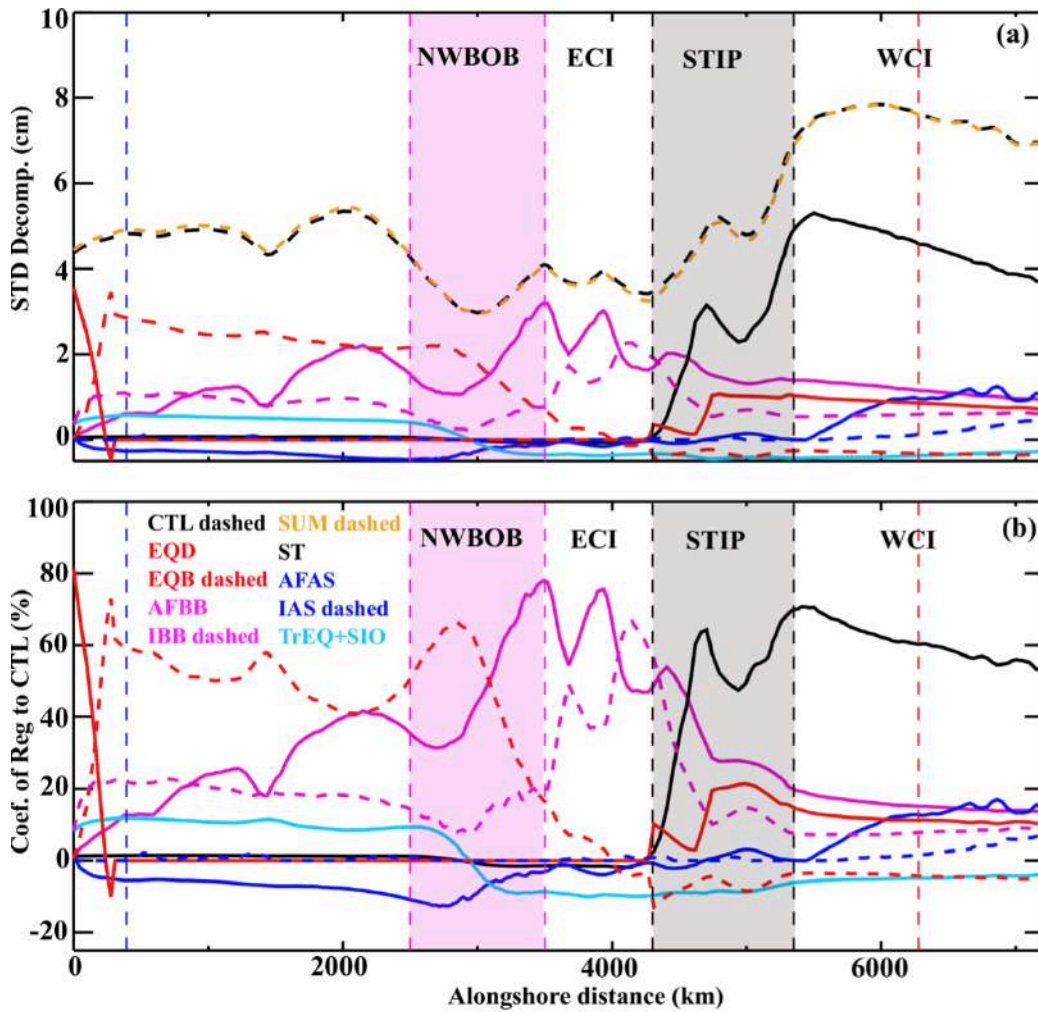


Figure 6.10: Same as Figure 6.7, but for fall (ON).



**Figure 6.11:** (a) Standard deviation of seasonal sea level (cm) from CTL (dashed black) and its decomposition into each process (see Section 5.4 and Table 5.2), plotted as a function of distance along the NIO coastal waveguide. The quantities are averaged over a 50-km cross-shore extent. It is verified that the sum of processes standard deviations (dashed brown) matches the CTL standard deviation. (b) The coefficient of regression (in %) of seasonal sea level from each process onto CTL solution, shown as a function of alongshore distance. In both the panels, the entrance of BoB waveguide (marked with a tic of same color in Figure 5.14) is indicated with dashed blue vertical line at a distance of  $\sim 390$  km. The region between dashed pink vertical lines (marked with same color in 5.14) indicates the northwestern BoB, where local alongshore forcing is important. The dashed, black vertical lines (tics of same color in Figure 5.14) enclose the STIP region. The dashed, red vertical line (tic of same color in Figure 5.14) at the right extreme ( $\sim 6300$  km) marks the position of WCI box.

**Seasonal sea level along the NIO coastal waveguide:** Figure 6.11 (similar to Figure 5.15, but for the seasonal timescale) presents the decomposition of amplitude of seasonal sea level from CTL into that from each process (Figure 6.11a) and the percentage contribution of each process to the CTL seasonal sea level (Figure 6.11b), both as a function of distance along the NIO coastal waveguide. Figure 6.11b is

basically derived from Figure 6.6 by averaging the regression coefficients along the NIO coastline over a 50-km cross-shore extent. This provides better insights into process contributions along the coastal waveguide. The sum of amplitudes of the seasonal sea level from each process is equal to that of the CTL (Figure 6.11a), as ensured by the linearity of the model and the preciseness of the process decomposition.

#### **6.1.4 Processes contributing to BoB sea level seasonal cycle**

***Equatorial forcing contribution:*** The amplitude of the CTL sea level seasonal cycle, on an average, is  $\sim 4\text{-}5$  cm along the BoB rim (Figures 6.5a and 6.11a), and is dominated (2-3 cm) by the EQB process (Figures 6.5c and 6.11a,b) along the eastern and northern rims of the Bay. Figure 6.11b further indicates that the contribution of EQB to the CTL seasonal sea level variations along these coasts is 40-60%. The EQB contribution decreases rapidly in the northwestern BoB, probably due to the following reason. The EQB process includes both the coastal KWs propagating around the BoB rim and the RW radiation transiting through the interior BoB from its eastern rim (Figures 6.7c to 6.10c). These RWs propagate much slowly compared to the coastal KWs around the BoB rim. As a result, the upwelling (downwelling) coastal KW signal during winter (summer) due to EQB is counteracted by the arrival of downwelling (upwelling) signal of the previous cycle RWs at the northwestern and western BoB coasts (Figures 6.7c-6.10c), leading to a rapid southward decrease of the EQB process contribution to the CTL seasonal sea level amplitude along the northwestern rim of the Bay (Figures 6.6b and 6.11a,b).

***BoB forcing contribution:*** The CTL experiment seasonal sea level amplitude displays a local minimum along the northwestern and western rims of the BoB, that is also seen in the observations (Figure 6.3). This minimum can be traced back to the BoB forcing contribution (Figure 6.5d), and in particular the alongshore forcing (Figure 6.11). As a consequence of the BoB geometry and of the alignment of the northeast and the southwest monsoonal winds, the alongshore forcing (Figures 6.4e,g) tends to produce signals of opposite polarity along the eastern and western rims of the Bay (Figures 6.7d and 6.9d). As the propagation time ( $\sim 1$  week) of the coastal KW between the eastern and western BoB rims is relatively short compared to the seasonal timescale, the above-mentioned phase opposition would result in a weak coastal KW amplitude in the

northwestern BoB. The local minimum in coastal sea level amplitude along the northwestern BoB (Figures 6.3 and 6.5a,d) primarily results from the destructive interference of sea levels driven by the local upwelling-favorable winds with those driven by the upstream downwelling-favorable winds during summer (Figure 6.4g) (and opposite signals during winter; Figure 6.4e). The wind-stress curl in the southern Andaman Sea (Figures 6.1 and 6.4e and g) provides for the southern BoB another source of destructive interference: this wind-stress curl indeed forces RWs of opposite polarity to coastal KWs in the western BoB rim (Figures 6.7d and 6.9d). During summer, for example, the anticyclonic wind-stress curl (Figure 6.4g) forces a downwelling RW in the southern BoB that interferes destructively with the upwelling signals propagating in the coastal waveguide east of Sri Lanka (Figure 6.9d). The destructive interferences between eastern and western BoB signals resulting from both alongshore and interior forcing lead to an overall reduction of the amplitude of the coastal KW signals along western and southwestern BoB rim (see the decrease of AFBB and IBB processes contribution to the total sea level amplitude along the east coast of Sri Lanka; Figures 6.11a and b). Though the contribution of AFBB increases sharply to ~80% in the northwestern BoB coast (amplitude ~3 cm; Figure 6.11a) along the coastal KW path, it drops rapidly to ~20% (~1 cm; Figure 6.11a) along the east coast of Sri Lanka, as illustrated by Figure 6.11b. On the ECI, the sea level seasonal cycle is modulated by AFBB (~70%, on average) and IBB (~40%, on average), with a negative (-10%, on an average) contribution from the EQB.

***Process contribution to interior BoB:*** The sea level signals along the eastern BoB rim radiate westward as RWs, which combine with the signals induced by the interior BoB forcing to influence the sea level in the interior BoB. Figure 6.6b indeed demonstrates that the seasonal sea level variations in the eastern BoB are modulated by the RW signals radiated by the coastal KWs associated with EQB. On the other hand, the seasonal sea level in the western BoB is almost entirely due to the interior BoB forcing (Figure 6.6c) through the RWs generated by the strong wind-stress curl forcing (Figures 6.1 and 6.4e-h). The offshore maximum in the seasonal sea level amplitude in the western part of the BoB results from the interior BoB wind-stress curl forcing (Figures 6.5a vs. 6.5d) associated with a wind stress decrease near the coast (Figures 6.4a,c), probably due to stronger friction over land.

### 6.1.5 Processes contributing to AS sea level seasonal cycle

***Dominance of ST process on the WCI:*** Consistent with observations (Figures 6.2 and 6.3), Figure 6.11a indicates that the amplitude of the CTL seasonal sea level along the WCI ( $\sim 7$  cm, on average) is larger than that along the BoB coast (4 cm), mainly as the result of the ST process ( $\sim 5$  cm, on average). As illustrated in Figure 6.9b (Figure 6.7b), the Ekman pumping induced by the strong cyclonic (anticyclonic) wind-stress curl (Figure 6.4g (6.4e)) east of Sri Lanka during summer (winter) results in upwelling (downwelling) RWs, which propagate westward and set up upwelling (downwelling) KWs along the southeast coast of Sri Lanka. This upwelling (downwelling) signal is further reinforced by the winds, which blow parallel to the coast during summer (Figures 6.4g and 6.9b) (winter; Figures 6.4e and 6.7b) monsoon. Figure 6.11b indicates that the ST process dominates the CTL seasonal sea level all along the WCI. The contribution of ST process to the CTL seasonal sea level variability is largest ( $\sim 70\%$ ) near STIP and is 60% at  $15^\circ\text{N}$  (off Goa) on the WCI. Its contribution decreases gradually towards north to  $\sim 55\%$  at the northern end of the WCI (Figures 6.6a and 6.11b), probably due to westward radiation of the RWs from the WCI (Figures 6.7b-6.10b). The  $\sim 60\%$  contribution of STIP forcing to the off Goa sea level seasonal cycle is dominated by alongshore forcing ( $\sim 40\%$ ), with Ekman pumping off the east coast of Sri Lanka contributing to the remaining  $\sim 20\%$  (not shown).

***BoB forcing contribution to the WCI:*** Though BoB wind forcing (AFBB and IBB considered together) is the second largest contributor to the WCI sea level seasonal cycle, it is much weaker ( $< 30\%$ ) than that of the ST process (Figures 6.5d, 6.6c and 6.11a,b). This weaker contribution (amplitude  $\sim 1.5$  cm; Figure 6.11a) from BoB forcing is due to a combination of factors. First, the weak amplitude of coastal KW signals from BoB results from the aforementioned destructive interferences between eastern and western parts of the BoB. Another probable cause for the weaker effect of BoB forcing than STIP forcing is that the Ekman pumping east of Sri Lanka, due to its proximity to the equator, is much stronger than that in the rest of the BoB (Figure 6.1). Finally, the dissipation may act more on the BoB signals, which have a longer pathway along the coastal waveguide to travel to the WCI. All of these factors collectively tend to produce a weak contribution of BoB forcing to the WCI sea level seasonal cycle. The RW

radiation off the WCI also reduces the contribution from BoB forcing as the coastal KWs propagate poleward along the WCI (Figures 6.7d-6.10d).

***Equatorial forcing contribution to the WCI:*** As discussed in the previous section, the amplitude of the signals from EQB process decreases rapidly along the ECI, ultimately resulting in a very weak signal along the WCI. Subsequently, the EQB contribution to the WCI is negligible (Figure 6.11b). The EQD process, on the other hand, contributes 10-15% to the seasonal sea level along the WCI (Figure 6.11b). This weak contribution from EQD ( $\sim 1$  cm) to WCI results from the weak-amplitude, reflected equatorial RW signal at the east coast of Sri Lanka (Figures 6.11a, 6.7c-6.10c). This equatorial wave is relatively weak because the zonal component of seasonal monsoon winds is relatively weak along the equatorial waveguide (cf. Figure 6.24a). Furthermore, this EQD signal interferes destructively with the EQB signals at this coast.

***Local forcing on the WCI:*** The WCI wind seasonal anomalies blow almost normal to the coast during both summer and winter monsoons (Figures 6.4c,g and 6.4a,e), resulting in weak amplitude alongshore component (Figure 6.1). Consequently, the AFAS contribution is rather weak (amplitude  $< 1$  cm, on average) and accounts for only  $\sim 10\%$  (on average,) of the WCI seasonal sea level variations (Figures 6.6d and 6.11b). There is some northward increase in the AFAS contribution that results from the integration of forcing downstream along the wave path (Figures 6.6d and 6.11b). Earlier studies [e.g., McCreary et al., 1993; Shankar et al., 2002] noted that the phasing of the local forcing is not consistent with the WCI upwelling. This study suggests that the remote processes (ST, AFAS+IBB and EQD) drive the WCI upwelling signals and are almost in phase with WCI seasonal sea level over the entire year (Figures 6.7-6.10).

***Processes contributing to the interior AS sea level seasonal cycle:*** The sea level signals along the WCI radiate westward as RWs, which combine with the signals induced by the interior Ekman pumping to influence the sea level in the interior AS (Figures 6.7-6.10). The STIP wind variations, being the dominant process in driving the seasonal sea level along the WCI, extend their strong influence westward into the interior AS through RWs (Figures 6.7b-6.10b). Figure 6.6a indeed demonstrates the dominant role of the STIP forcing ( $\sim 60\%$  contribution) for the LH/LL region. Farther

west, the local AS Ekman pumping dominates the sea level seasonal cycle (Figures 6.6d and Figures 6.7e-6.10e), especially in the Somali upwelling region.

### 6.1.6 Robustness of the model results

**Robustness of the results:** An exclusive exercise has been carried out to test the sensitivity of the model results to the choice of wind forcing, dampers and model parameters. Similar results are obtained by repeating the model experiments using QuikSCAT (details in Section 3.2) wind-stress fields (referred to as EXPQSCAT), which also shows dominance of ST process in driving the WCI seasonal sea level variability (Table 6.1).

**Table 6.1:** Contribution from each process to the WCI sea level seasonal cycle at 15°N (representative of what happens along the entire coast) from CTL (TropFlux forcing, friction coefficient 5000 m<sup>2</sup>/s, 1° ramps near the edges of each damper), EXP500 (TropFlux forcing, friction coefficient 500 m<sup>2</sup>/s, 1° ramps near the edges of each damper), EXPQSCAT (QuikSCAT forcing, friction coefficient 5000 m<sup>2</sup>/s, 1° ramps near the edges of each damper), and EXPRAMP (Tropflux forcing, friction coefficient 5000 m<sup>2</sup>/s, 2° ramps near the edges of each damper) simulations. This table illustrates robustness of the results presented in Section 6.1.

Process	Percentage Contribution (%)			
	CTL	EXP500	EXPQSCAT	EXPRAMP
EQD + EQB	7	-5	10	5
AFBB + IBB	23	25	20	20
ST	60	70	60	65
AFAS	10	10	10	10

The dampers used in the experiments are designed to minimize the distortions in the model solutions, especially at the edges of the dampers by ramping the signals linearly to zero within 1° from the edges (see Section 3.3). Repeating the experiments with a 2°-ramp for dampers (EXPRAMP) yields nearly identical contributions (Table 6.1), indicating that the results are not sensitive to the exact design of these dampers. Experiments with other dampers (e.g., a damper in the eastern IO as in McCreary et al. [1996] to isolate the equatorial process) also give very similar results (not shown). Finally, the lateral friction may also influence the results, since the coastal KWs have narrow offshore structure and propagate over long distances. Reducing the frictional coefficient by an order of magnitude (EXP500) results in contributions similar to those in CTL (Table 6.1), with ST process still being the major driver of the seasonal sea level variations along WCI. The results presented here are thus robust and insensitive to

different observational wind products, the model parameters and the choices of experimental setup, with ST process being the major contributor to the WCI seasonal cycle, followed by a modest contribution of forcing from the BoB forcing (AFBB and IBB processes).

### 6.1.7 Summary

***Salient findings:*** The EQB process contributes 40-60% to the seasonal sea level variations along the eastern and northern coasts of BoB. The strong alongshore forcing arising from the monsoonal winds along the northwestern rim contributes significantly (contribution sharply rising to ~80%) to the sea level seasonality at this part of the coast. This alongshore forcing (~70%, on an average), combined with the interior BoB forcing (~40%, on an average), control the seasonal sea level variability along the ECI. While the RW radiation resulting from the coastal KWs at the eastern BoB rim influences the seasonal sea level variations in the eastern BoB, the interior BoB forcing dominates those variations in the western BoB. The major source (~60% at 15°N) of seasonal sea level variability along the WCI is the seasonal wind variability in a relatively small region (less than 20% of the area of total BoB basin) near the southern tip of India and Sri Lanka (with respective contributions of ~40% by winds along this convoluted coast and ~20% by Ekman pumping induced by the strong wind-stress curl off the east coast of Sri Lanka). Furthermore, the contribution from the BoB, which includes alongshore winds and interior forcing, is less than 30% of the total WCI seasonal sea level cycle. This is partly due to the geometry of the BoB basin and the dominant wind forcing patterns, which result in the partial cancelation of signals forced in the eastern and western portions of the BoB. This refines findings from the previous literature [e.g., McCreary et al., 1993; Shankar et al., 2002]. Using a similar approach to that followed in this chapter, those studies concluded that the west India coastal current and the associated sea level changes along the WCI are primarily driven by the BoB alongshore winds, but did not offer any quantification. The dominant role of wind forcing in the STIP region relative to the rest of the BoB was also not identified before. The equatorial wind forcing, which was also emphasized by the previous studies for the WCI seasonal cycle, contributes less than 15% (EQB and EQD process) to the seasonal sea level along WCI. One reason is that the seasonal monsoon wind patterns have a

relatively weak projection onto equatorial zonal wind stress. Consistent with earlier studies, the local alongshore winds are relatively less important for the seasonal cycle along WCI, with only ~10% contribution, mainly during the summer monsoon. This weak contribution results from the monsoonal wind seasonal variations along WCI (north of 10°N) being nearly normal to the coast, with a weak alongshore component, driving a weak coastal KW response. The STIP wind forcing is also an important contributor (>50%) to sea level seasonal cycle in the eastern AS, especially in the LH/LL region (~60%). Farther west (west of 65°E), the strong interior AS forcing dominates.

## 6.2 Dynamics of interannual sea level

### 6.2.1 Introduction

**Background:** A detailed survey of the studies discussing the IAV of the NIO sea level and circulation is provided in Section 2.3. Though some of those studies did investigate the controlling mechanisms of the NIO sea level IAV, they did not specifically assess the importance of the EQD and ST processes, and focused mainly on the BoB [e.g., Han and Webster, 2002; Aparna et al., 2012]. The WCI sea level IAV has received considerably less attention, probably because of its much weaker amplitude compared to that in the BoB [Aparna et al., 2012]. Nevertheless, the weak amplitude of sea level IAV along the WCI has important consequences for the biogeochemistry in this region, which experiences seasonal hypoxia in conjunction with the WCI upwelling during summer (see Sections 2.2 and 2.3). During some years, these poorly-oxygenated hypoxic waters off the WCI become anoxic by late summer or fall (September – November; SON), with potentially strong impacts on the regional fisheries and ecosystems [Naqvi et al., 2009] (see Section 2.3 for details). Using a coupled physical-biogeochemical model simulation, Parvathi et al. [2017] demonstrated that the interannual oxycline/thermocline/sea level variability off the WCI during SON is strongly influenced by the IOD events: they imprint their signatures on the wind anomalies at the STIP region that, in turn, influence the WCI through coastal KWs. Parvathi et al. [2017] suggested the importance of the ST process for the IAV off the WCI on the basis of correlations between STIP winds and the WCI sea level anomalies, but did not explicitly isolate the signals associated with the STIP winds. Similarly, Parvathi et al. [2017] did not discuss the potential role of the direct connection between the WCI and the equatorial band (EQD process) that has been established to operate at intraseasonal timescales (see Chapter 5). As for intraseasonal and seasonal timescales, there could also be localized *hotspots* of the interannual wind forcing (discussed below) that still remain to be identified.

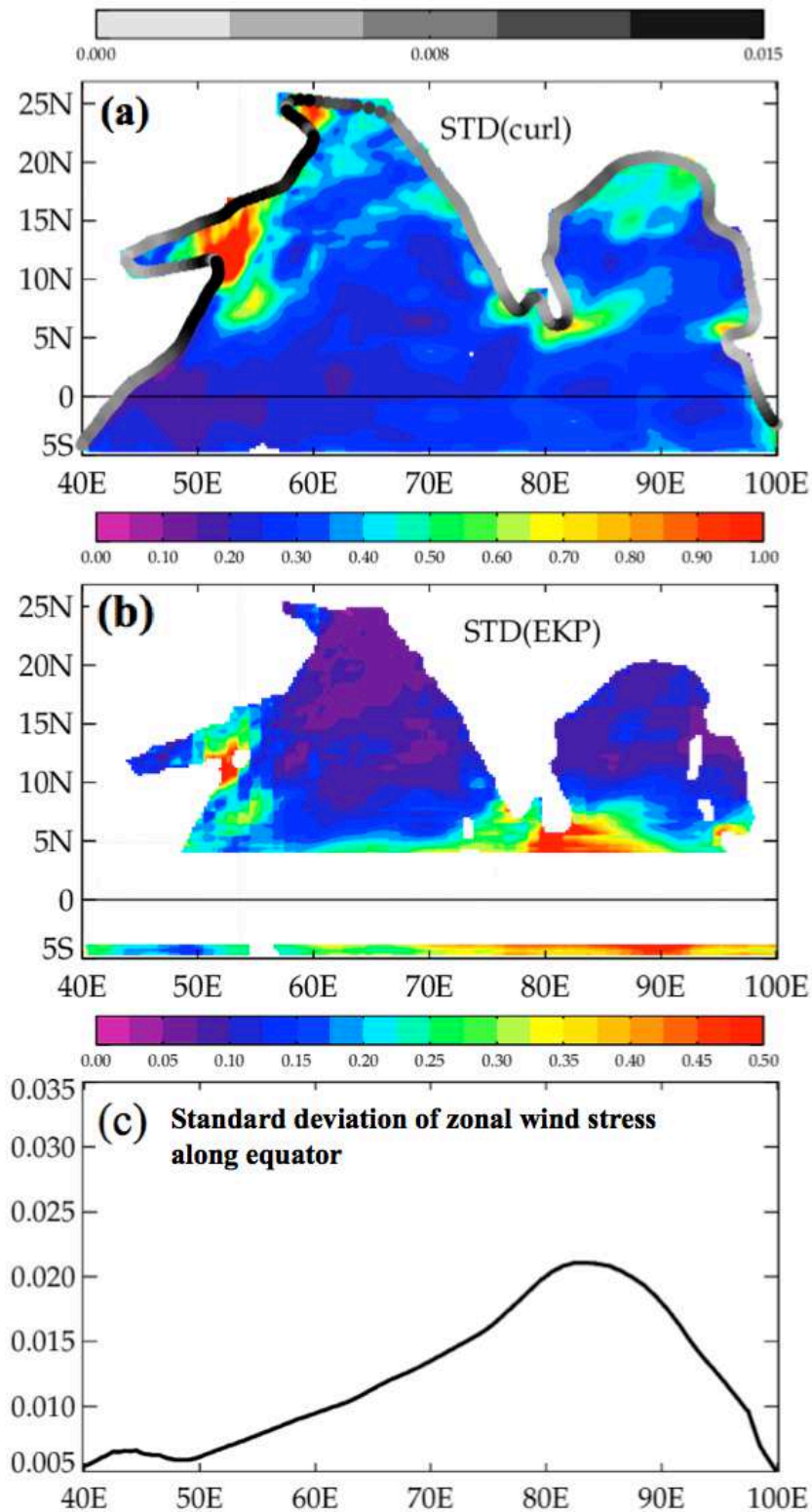


**Figure 6.12:** Standard deviation of the interannual anomalies of (a) the wind-stress curl (shaded; scale at the bottom;  $\times 10^7 \text{ N/m}^3$ ) and alongshore wind stress (grey shades along the coast; scale at the top;  $\text{N/m}^2$ ), (b) the Ekman pumping velocity ( $\text{m/day}$ ) and (c) the  $2^\circ\text{N}$ - $2^\circ\text{S}$  average zonal wind stress  $\text{N/m}^2$ .

**Hotspots of interannual wind forcing:** Figure 6.12 highlights the regions with strong, localized interannual variations in the wind forcing (alongshore wind stress, wind-stress curl, Ekman pumping velocity, and equatorial zonal wind stress) in the NIO. The hotspots of interannual wind forcing almost coincide with those at intraseasonal (Figure 5.4) and seasonal (Figure 6.1) timescales. The northwestern BoB and STIP regions exhibit strong alongshore wind-stress forcing (Figure 6.12a) that can potentially contribute to the coastal sea level IAV by exciting coastal KWs. Strong Ekman pumping signals are found at the STIP region and also off the Sumatra coast (Figure 6.12b). As pointed out earlier for seasonal and intraseasonal timescales, the sea level anomalies excited by the above Ekman pumping signal will propagate westward as RWs and induce signals at the Sri Lankan coast, which can, in principle, set up coastal KWs and impact the sea level and currents downstream along the WCI. The amplitude of the equatorial zonal wind stress (i.e. the forcing in the equatorial waveguide) peaks in the eastern equatorial IO (maximum within 80°-90°E) (Figure 6.12c). The equatorial KWs resulting from this forcing will propagate to the NIO through EQB and EQD processes and influence the sea level IAV there. None of the previous studies have assessed the importance of the above hotspots of wind forcing to the NIO sea level IAV, particularly in the coastal waveguide.

**Goal of section 6.2:** As for the seasonal timescale, a thorough analysis of the sea level IAV on the NIO coastal waveguide will help contrasting the sea level dynamics at intraseasonal and interannual timescales (discussed later in Section 6.3). The goal of this section is hence to provide a description of the NIO sea level IAV and a detailed investigation of its driving processes, especially along the NIO coastal waveguide, and to quantify their contributions using the set of LCS model sensitivity experiments and process decomposition described in Chapter 5. In particular, the importance of the ST and EQD processes for the WCI sea level IAV will be discussed in detail, as this was not done previously. This section also provides a detailed investigation of the IOD influence on the NIO sea level IAV.

## 6.2.2 Model and the sensitivity experiments

**The Model and the process solutions:** The model configuration and the experimental setup for the present study are same as those described in Chapter 5. Moreover, the method described in Chapter 5 (Sections 5.4 and 5.5.2; Tables 5.1 and 5.2) has been employed here for isolating the various processes that contribute to the NIO sea level IAV. As for the seasonal timescale (Section 6.1.4), the results are not very sensitive to other reasonable choices of the dampers used for the process solutions (not shown).

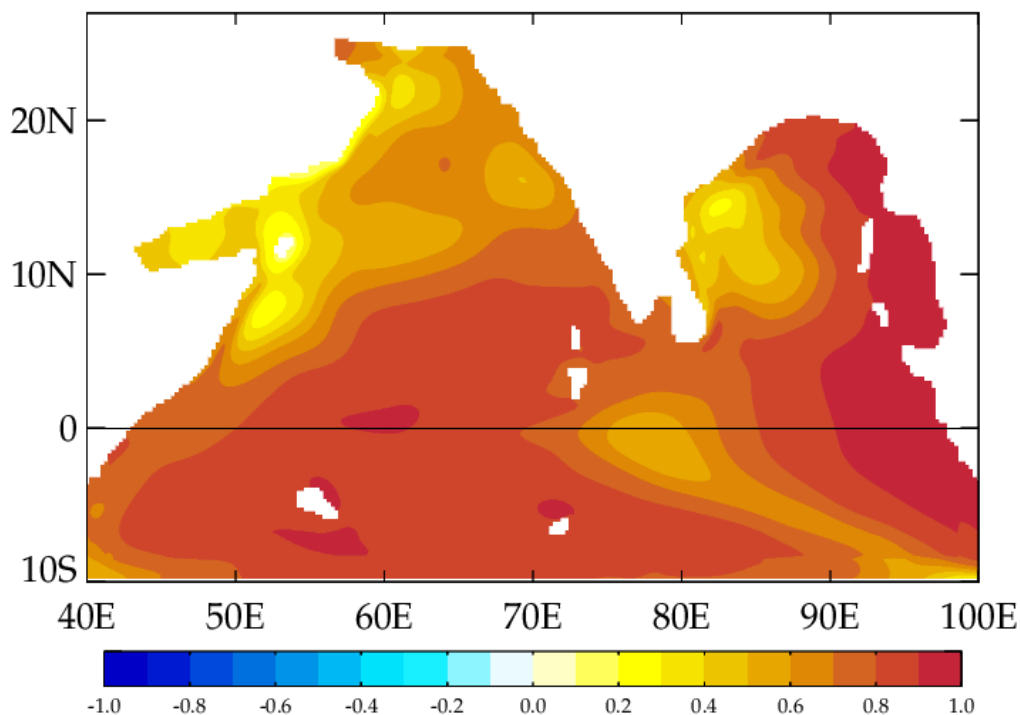


**Figure 6.13:** Map of correlation between observed and modeled sea level interannual anomalies.

**Model validation:** The interannual sea level in the model is validated against AVISO altimeter observations (see Section 3.2). Figure 6.13 indicates that correlations between the modeled and the observed interannual sea level are high over most of the basin except in the eddy-dominated western BoB and western AS, where nonlinear effects are important. The model is particularly accurate in the eastern equatorial IO, all along the eastern and northern rims of the BoB (correlation coefficient greater than 0.8), and along the WCI (0.7 correlation, on average). The model performance is further assessed below through EOF analysis of the interannual sea level from the model and the observations.

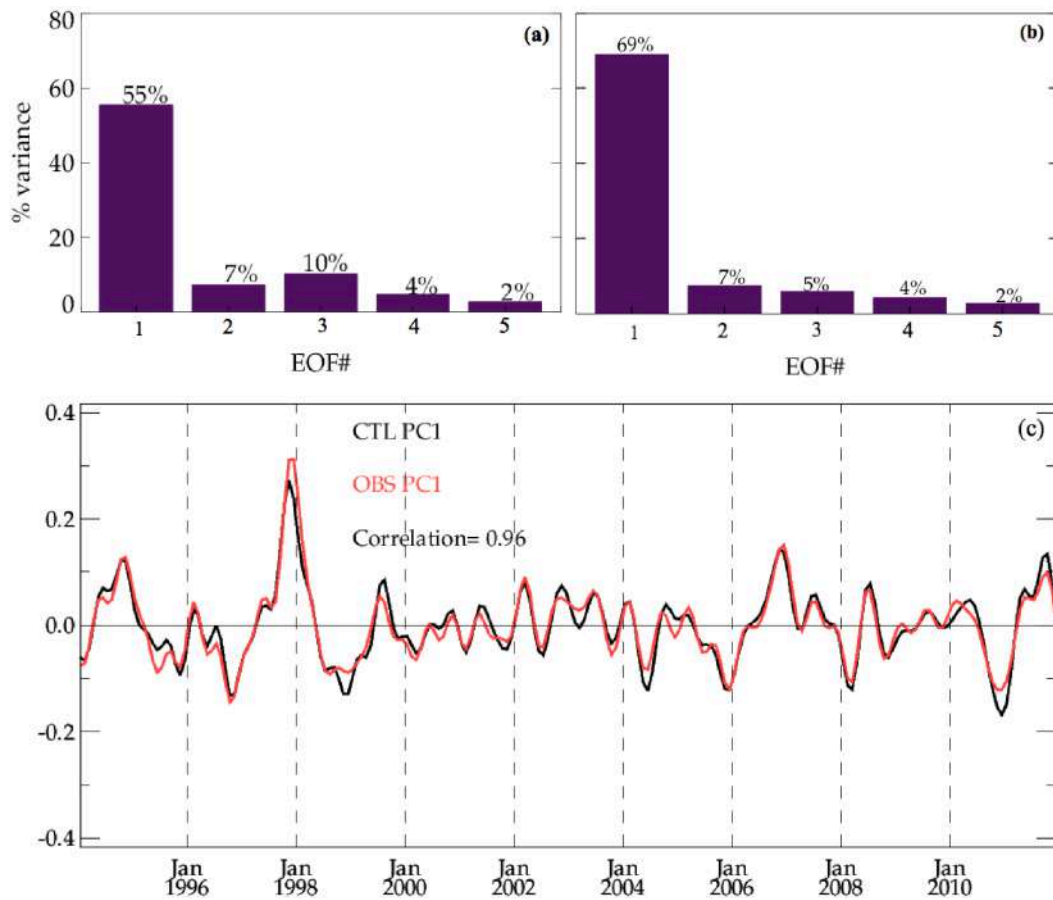


**Figure 6.14:** Sea level interannual anomalies EOF analysis. Note that the observed EOFs 2 and 3 will be interchanged for further analysis, as observed EOF (and PC) 3 is strongly correlated to modelled EOF (and PC) (see text for details) (a) and (b) display the explained variance of the first five EOFs computed from altimetry and the CTL interannual sea level, respectively (modes 1 and 2 collectively explain ~62% of the variance in observations and ~76% in the model); (c) Modeled (black line) and observed (red line) first principal component (Correlation = 0.96).

**EOFs from observations and model:** The large-scale interannual sea level patterns in the observations and in the model (CTL simulation) are extracted using EOF analysis described in Section 3.4. As for the ISV (Section 5.6.1), the EOF analysis of the observed sea level is restricted to the east of 55°E in order to avoid distortions in the EOF patterns arising from the strong meso-scale eddy activity in the western AS. Furthermore, the observed sea level has been smoothed spatially over a 2° box before computing the EOF patterns to reduce the influence of eddies within the EOF computational domain (for e.g., eddy-dominated western BoB region). For the sake of uniformity, the same domain (eastward of 55°E) has been retained for the EOF computations of the modeled interannual sea level, though it is free from eddy effects and the EOF patterns are almost the same (except for slight changes in the explained

variance, not shown) even if the entire NIO domain is considered. The corresponding EOF patterns of the interannual sea level and the wind stresses for the entire NIO domain are obtained through regression onto the normalized PCs. A careful inspection of the spatial patterns of the EOF modes indicates that the second (third) EOF computed from the observations is very similar to the third (second) EOF from the CTL. Moreover, the correlation between observed and modeled PC2 is 0.52, whereas the correlation between observed PC3 and modeled PC2 is 0.67, strongly suggesting that the third EOF mode extracted from the observations represents the same physical mode of variability as the second EOF mode from the CTL experiment. The third and second EOFs from the observations will henceforth be reordered as EOF2 and EOF3, and so are the PCs. Figures 6.14a and 6.14b show the explained variance of the first five EOF modes from the observations and the CTL, respectively. The first EOF mode is well separated from the rest in both observations and model. The first EOF mode in the observations (model) explains 56% (69%) of the variance, while the second and third EOF modes explain, respectively, 10% and 7% (7% and 6%) of the variance. The reduced explained variance by the observed EOF1 compared to that in the model is probably due to the influence of meso-scale eddies, which are not produced in the linear model but present in observations.

***Validation of basin-scale patterns:*** The spatial patterns of the first two EOF modes and the % of variance explained by them are shown on Figure 6.15, both for observed (left panels) and CTL (right panels) interannual sea level along with the wind patterns regressed onto the corresponding PCs. Despite a slight amplitude underestimation, the model reproduces the observed EOF patterns of sea level IAV remarkably well. The EOFs capture the eastern boundary reflection and the subsequent coastal KW propagation in the NIO coastal waveguide. In the model (observations), the first two sea level EOF modes together explain more than 90% (80%) of variance in the eastern equatorial IO and along the eastern and northern rims of the BoB (Figure 6.15f,c). The CTL (observed) explained variance progressively decreases around the rim of the Bay, reaching ~60% (~50%) along the ECI. The variance explained by the two modes in the CTL (observed) interannual sea level along the WCI is ~70% (~30%). The weaker explained variance in the observation could be due to the presence of mesoscale eddies. Besides these spatial EOF patterns, a comparison of the modeled and observed sea level PCs indicates a very good phase agreement of the basin-scale sea level IAV, with a

correlation of 0.96 for PC1 (Figure 6.14c) and 0.67 for PC2 (not shown). The good performance of the model in reproducing the characteristics of EOFs and the corresponding PCs suggests that this model is not only well suited for studying the sea level dynamics at the intraseasonal (see Chapters 4 and 5) and seasonal (Section 6.1.2) timescales, but also at the interannual timescales. In the following section, the climate phenomenon associated with those EOFs in the model and observations have been identified.

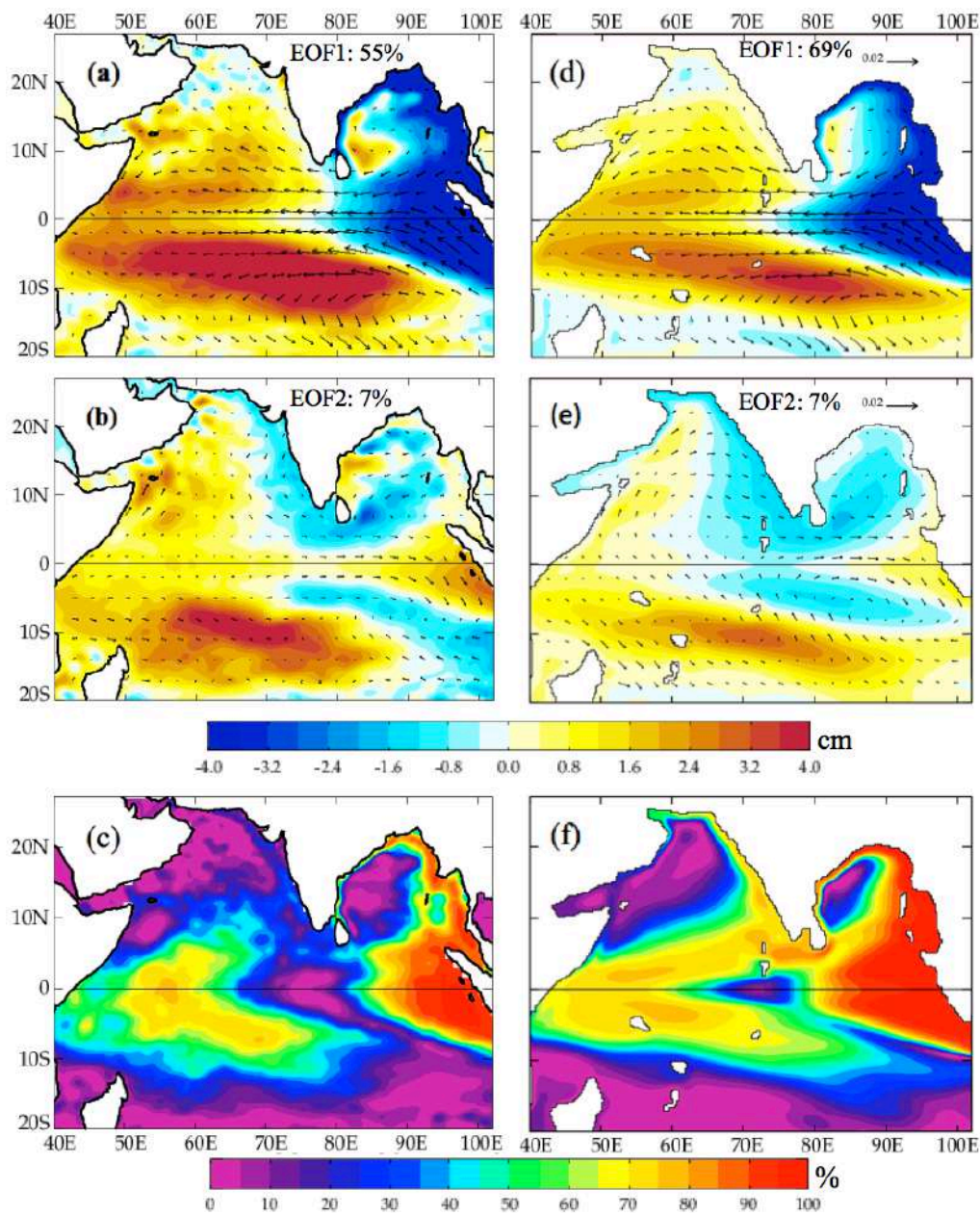


**Figure 6.15:** Spatial patterns of the EOF modes from the observations (left panels) and model (right panels). (a) and (b) show spatial patterns of the 1<sup>st</sup> and 2<sup>nd</sup> EOF modes, respectively. (c) Map showing the percentage of variance in sea level IAV explained by EOF modes 1 and 2. (d, e, and f) are same as (a, b, and c), but for model.

### 6.2.3 IOD influence on the NIO sea level IAV

**Similarity between the EOF patterns and the IOD:** The modelled (Figure 6.15d) and observed (Figure 6.15a) first EOFs are reminiscent of those associated with a positive IOD (see Section 2.3 for a detailed description of the IOD patterns), with easterly wind anomalies in the central equatorial IO forcing negative sea level anomalies in the eastern IO (which further propagate into the BoB as coastal KWs) and positive sea level south of the equator in the central IO, associated with the wind stress curl of the equatorial wind stress anomalies. The main patterns of the second EOF tend to be shifted westward (Figures 6.15e,b), i.e. to represent the typical RW phase propagation. In other words, EOF1 seems to represent the patterns (sea level, winds) of IOD peak in SON, while EOF2 is more representative of the patterns after this peak. It will be verified below if those two EOFs together describe sea level evolution associated with an IOD event.

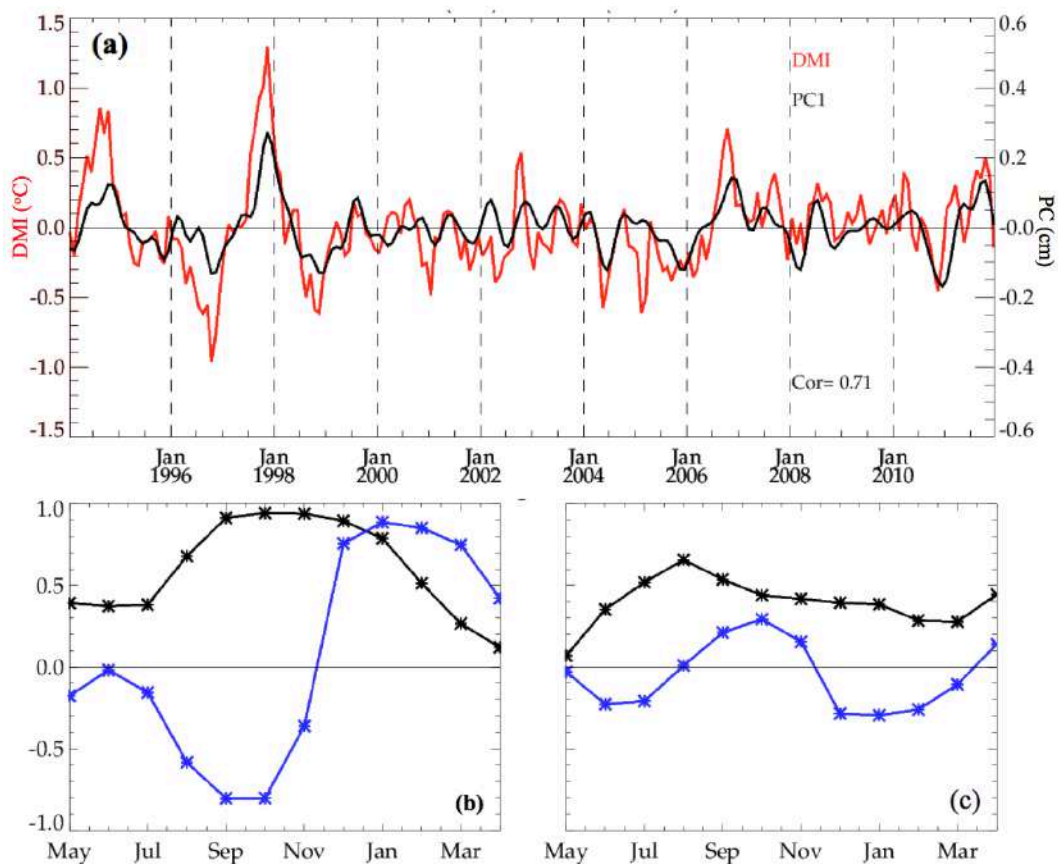


**Figure 6.16:** (a) Comparison of CTL PC1 (black line) with DMI index (red line); Correlation=0.7. (b) Lag-correlation of CTL PC1 (black) and PC2 (blue) with SON averaged DMI. (c) Same as (b) but for NDJ averaged MEI.

***IOD or ENSO?:*** As pointed out earlier in Section 2.3, ENSO and IOD are the two prominent modes of natural climate variability that influence the NIO. It is however sometimes difficult to identify whether a given IO signal is associated with one rather than the other of these two modes, due to the tendency of El Niño (La Niña) events to induce positive (negative) IODs in the IO (e.g. Annamalai et al. [2003]; the correlation between the SON DMI and NDJ (November – January) MEI indices is  $\sim 0.4$  over the period considered). Figures 6.16b and 6.16c display the lead-lag correlations of PC1 and PC2 with the SON DMI and NDJ MEI indices, respectively. The lead/lag correlations with the DMI are systematically higher than those with the MEI, clearly indicating that IO sea level variations are dominated by the IOD, not by ENSO. I.e. in most cases, an El Niño will force a positive IOD, with the sea level signals associated with EOFs 1 and 2. But if the Niño fails to induce an IOD, the sea level signals will be much weaker in the IO, since they occur as a response to the IOD typical wind pattern. This agrees with the results of Currie et al. [2013], who showed using partial regressions applied to a 44-yearlong OGCM simulation that most of the thermocline depth interannual variability in the IO is driven by IOD rather than ENSO.

***Lead-lag relations between PCs and the IOD:*** In SON, PC1 is strongly correlated with the DMI (Figure 6.16a), i.e. EOF1 describes the sea level pattern of an IOD at its peak. By construction, the EOF method ensures that the correlation between PC1 and PC2 is zero at lag zero, i.e. in SON. PC2 is however positively correlated with PC1 during the preceding months (i.e. the IOD development phase) and negatively correlated with PC1 during the IOD decay phase. I.e. the IOD development is described by EOF1+EOF2 and its decay by EOF1-EOF2. Together, those two PCs describe the sea level changes and propagations during an entire IOD event. This is further demonstrated by the fact that the description of the sea level IAV obtained either by lead-lag regression onto the DMI/PC1 (Figure 6.17, described in the following paragraph) or by the projection of the full sea level anomalies onto PC1 and PC2 are equivalent (not shown).

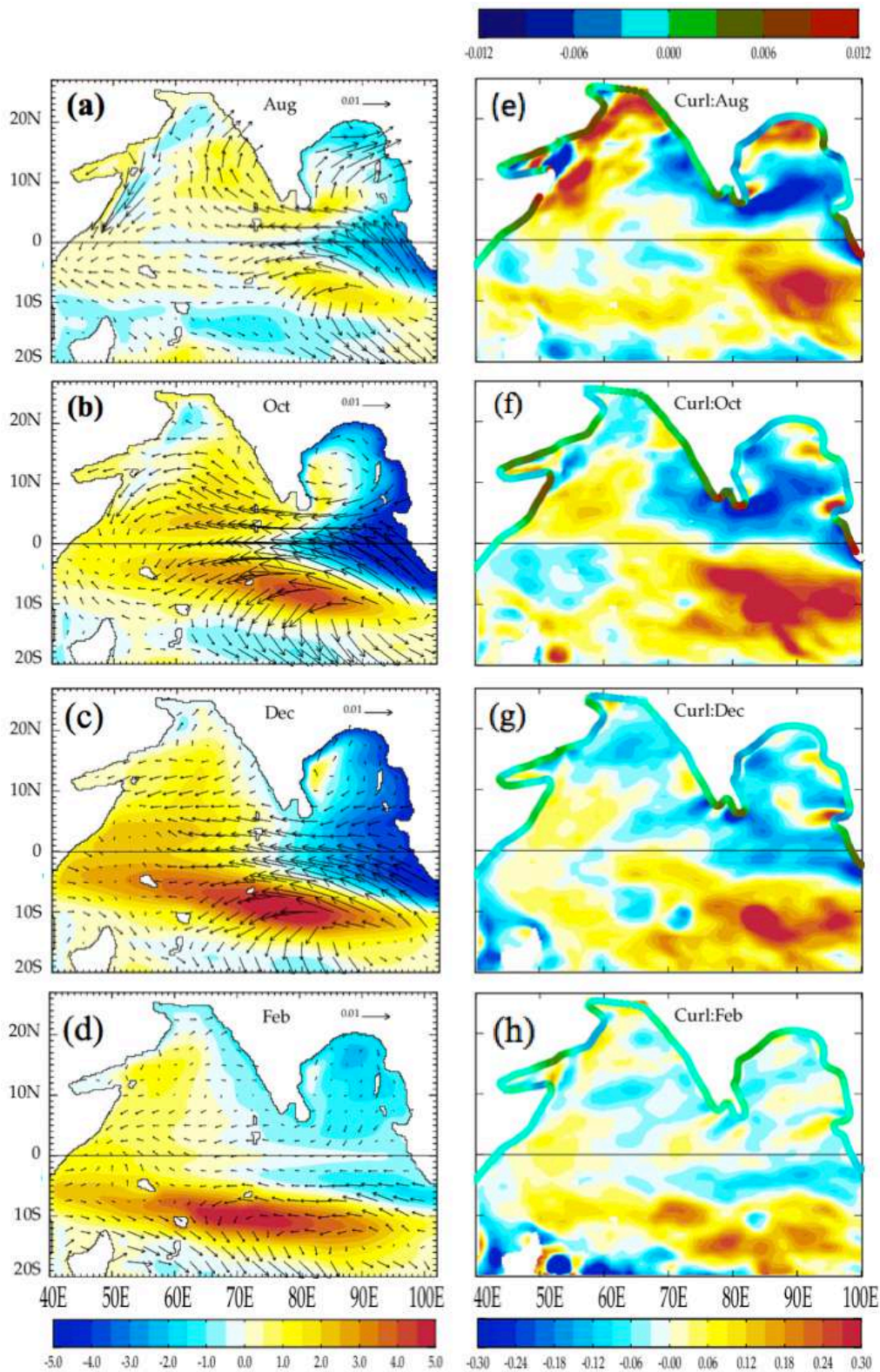


**Figure 6.17:** (a-d) Patterns of CTL interannual sea level (cm) and wind stress ( $N/m^2$ ) obtained by lead-lag regression onto the normalized SON DMI index, shown selectively for the months of (a) August (2 months lead), (b) October (0 month lead), (c) December (2 months lag) and (d) February (4 months lag). Panels (e-h) show the corresponding wind-stress curl ( $X10^7; N/m^3$ ) and alongshore wind forcing ( $N/m^2$ ) patterns. The alongshore wind forcing is indicated with a different color shading (see color bar above the right column panels) along the coastline. TropFlux wind stresses have been used.

**Typical IOD wind stress and sea level patterns:** As already discussed above, the IOD basin-wide pattern more or less remains the same throughout the IOD (left panels on Figure 6.17). Equatorial easterlies drive an upwelling equatorial KW in the eastern equatorial IO, which further propagates around the BoB rim as upwelling coastal KW, in a similar way as that at the intraseasonal timescale. Since the KW propagates fast relative to the timescale of the forcing, this pattern is more or less balanced with the wind stress, being weak in August (onset; Figure 6.17a), peaking in October (Figure 6.17b), starting to decay in December (Figure 6.17c) and having almost disappeared by February (Figure 6.17d). The asymmetric wind pattern south of the equator is associated with a strong curl that drives positive sea level anomalies between 5°S and 15°S (right panels on Figure 6.17), in line with Tozuka et al. [2010]. Since RWs are slower at this latitude, this pattern displays a westward propagation (Figure 6.17a-d) and peaks a bit later than the equatorial KWs (i.e. in December; see Figure 6.17c). During the IOD onset (August), there are relatively strong interannual wind anomalies in the NIO (Figure 6.17a), probably owing to the interaction with the monsoon, which drive negative curl and alongshore anomalies in the BoB. This negative curl remains strong in the southern BoB until October (Figure 6.17e-f). The August, October, December sea level sequence in the NIO is clearly associated with upwelling RWs radiating westward from the BoB eastern rim (Figure 6.17a-c). This is different from what happens at intraseasonal timescales, for which the critical latitude does not allow offshore propagation. In February, there is a clear sea level sign change along the WCI (Figure 6.17d). I.e. the sea level is positive before (and hence cannot be explained by coastal KW propagation from the BoB, where the sea level is negative), and only becomes negative in February. Since this is an important region for biogeochemistry, as discussed in the introduction, the processes that allow this change of sign of IOD-induced sea level signals on the WCI will be assessed in detail.

**Dominant processes in the eastern BoB:** To better grasp how the different processes combine to induce the sea level sequence in the NIO coastal waveguide during a typical IOD evolution, Figure 6.18 provides monthly time series of regressed sea level from CTL and its different contribution onto DMI at three selected coastal locations, representative of the different regions: along the eastern BoB (EBOB box), the western BoB (ECI box) and the WCI (WCI box; boxes shown on Figure 6.17a). Figure 6.19 shows the corresponding regression patterns for the months of October and February. In

the eastern BoB, the dynamics is straightforward: the signal is entirely dominated by remote forcing from the equatorial region, and is hence in phase with the wind forcing due to the fast propagation time of first-baroclinic waves equatorial / coastal KWs to the eastern BoB (1-2 weeks).

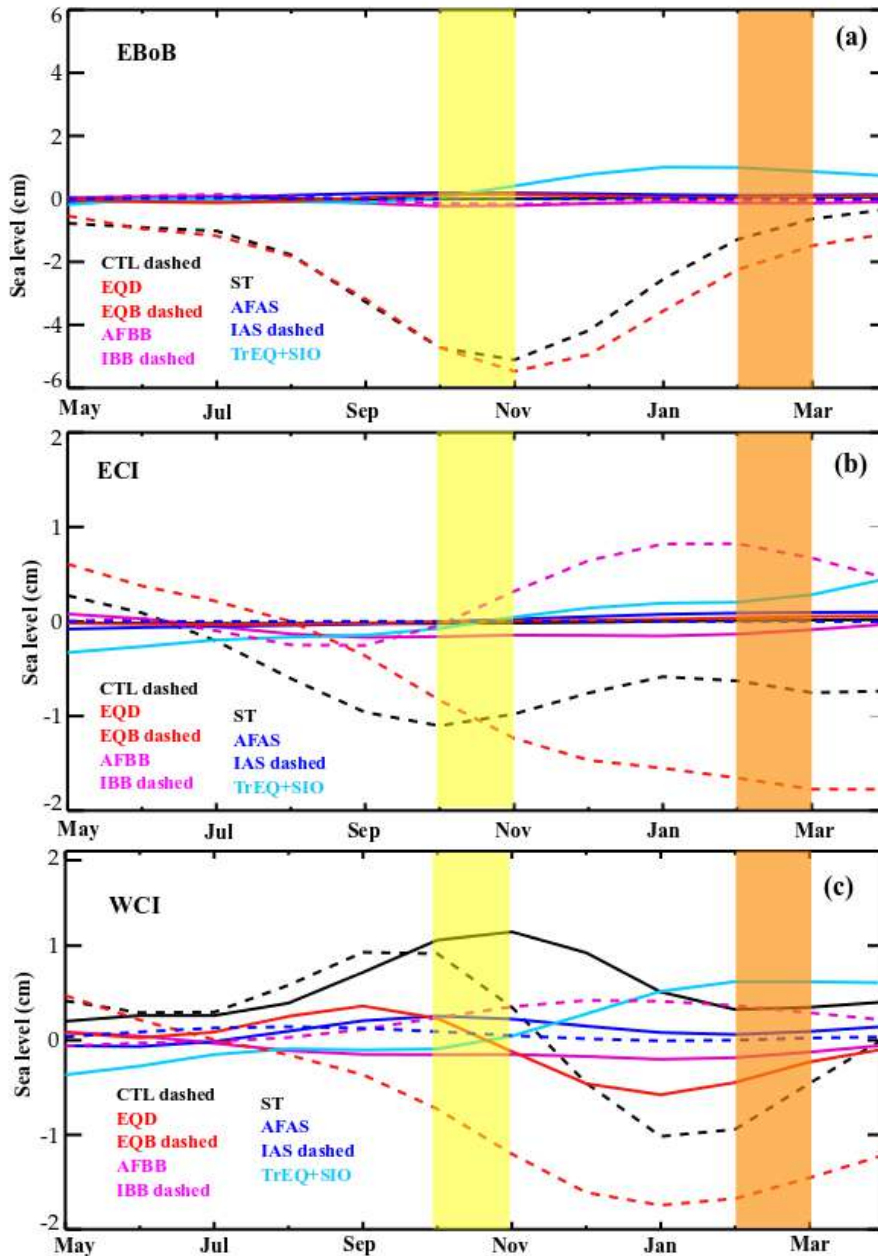


**Figure 6.18:** Monthly time series of the interannual sea level (cm) obtained by lead-lag regression onto the SON DMI at coastal locations (marked with black frames in Figure 6.19e) on the (a) eastern BoB, (b) east coast of India, and (c) WCI for CTL and the processes. The time series is essentially the one derived from Figures 6.17a-d or 6.19 by averaging over the above box locations, but for all months and for each process. It is verified that the sum of processes sea levels equals that of the CTL. The two regimes of IOD influence are shaded with yellow (October) and orange (February) colors.

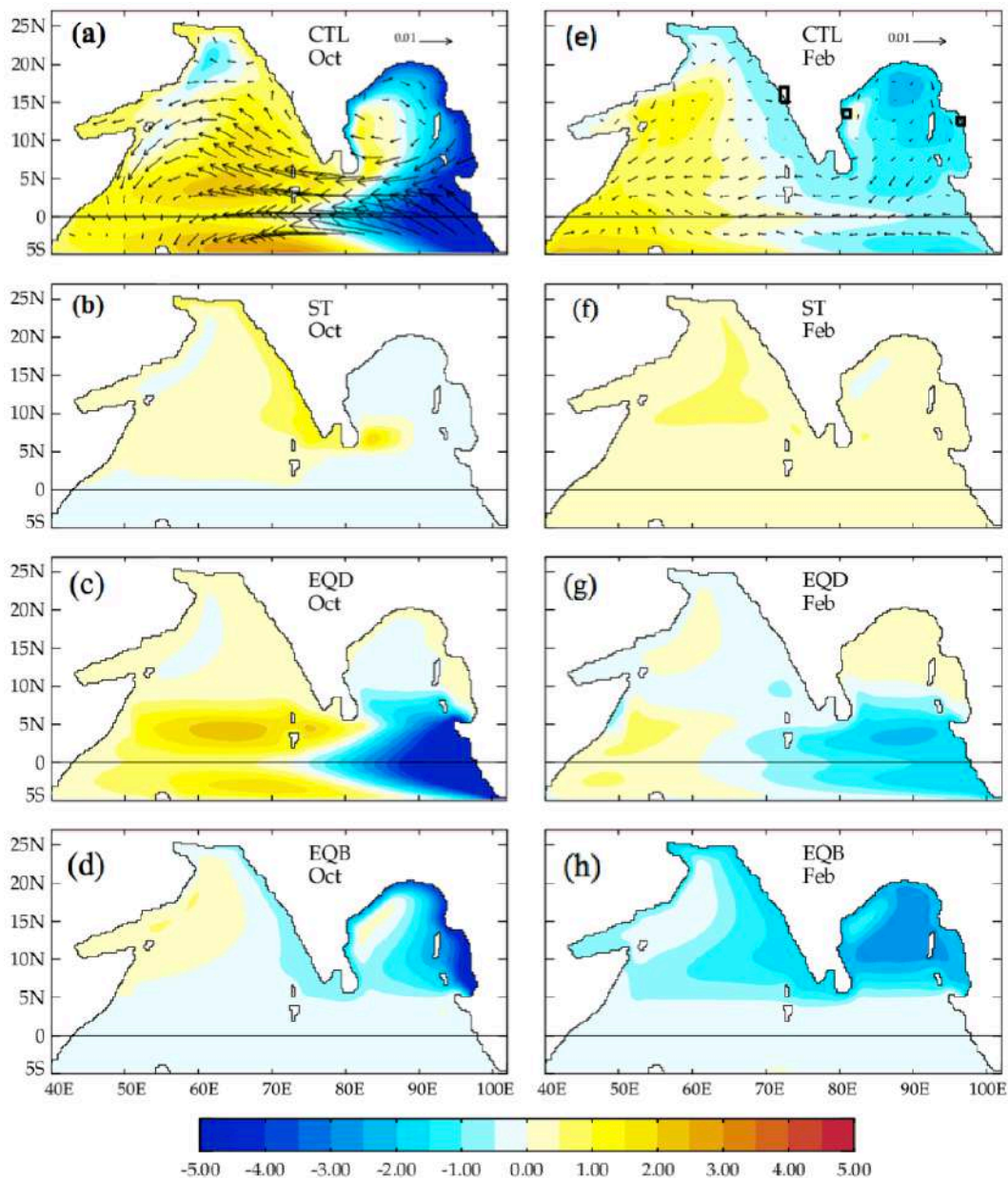


**Figure 6.19:** Interannual sea level patterns obtained by lead/lag regression to the SON DMI index for (a-d) October and (e-h) February: total sea level anomaly (cm) from CTL (panels a and e) and contributions from the ST (panels b and f), EQD (panels c and g), and EQB (panels d and h) processes. The contributions of other processes are not shown due to their relatively minor contribution to the interannual sea level along NIO waveguide. The black boxes in panel e are the WCI, ECI and EBOB boxes used for plotting sea level time series in Figure 6.18.

**Dominant processes along the east coast of India:** The dynamics is more complex for the ECI (Figure 6.18b), with more or less three regimes. The strong wind signals associated with the IOD in July-August in the northern BOB (Figures 6.17a,b) results in an alongshore forcing and positive curl that contributes to the negative sea level signal along the ECI (Figure 6.18b), before the EQB signal picks up. EQB increases more slowly in the ECI box than in EBOB (Figure 6.18ab): this is because the lower

frequency signals allow much more offshore propagation of RWs in contrast to the intraseasonal timescale, as discussed above. As a result, a significant fraction of the EQB signal transits through the interior BoB as slower upwelling RWs rather than following its rim as an upwelling KW. In October, the EQB signal dominates (Figures 6.18b and 6.19). As discussed above, the wind stress curl in the BoB is mainly negative from August to December (Figure 6.17e-g). This negative curl forces downwelling RWs in the BoB interior, which eventually reach the ECI where they interfere destructively with the EQB signal roughly from November to March (Figure 6.18b).

***Dominant processes along the west coast of India:*** As mentioned above, there are two regimes along the WCI, with sea level anomalies shifting from positive values in September - October to negative in January - February (Figures 6.18c). This shift in sign is broadly due to the balance between the positive ST signals and delayed negative EQB signals. The equatorial easterlies induce both downwelling-conducive alongshore anomalies at the STIP and are associated with a strong negative curl (and downwelling) east of Sri Lanka, due to their strong poleward decrease within  $\sim 5\text{-}10^\circ\text{N}$ . The resulting downwelling KW travels quickly to the WCI, yielding a ST signal almost in phase with equatorial zonal wind stress anomalies, with its contribution that peaks in October-November and rapidly decreases afterwards (Figures 6.18c). The upwelling signal associated with EQB has a slower propagating timescale, due to the fact that a significant fraction of the signal transits through the interior BoB as slower RWs (Figure 6.19d). The EQD process is also not negligible during November-February, and has a negative contribution, associated with the reflection of upwelling equatorial KW at the eastern boundary. As discussed on the basis of the idealized experiments of Chapter 5, this process not only involves the first meridional mode RW, but also higher, slower modes, thus explaining its slower timescale relative to the equatorial wind forcing.

#### **6.2.4 Processes contributing to the NIO interannual sea level**

***Evaluation of the process contributions:*** In the following, a more general assessment of the processes contributing to the CTL sea level IAV is provided, without specifically focusing on the IOD-induced variability. Figure 6.20 displays maps of regression coefficients of the interannual sea level from each process onto that from the CTL

experiment. Figures 6.20f indicates that EQB dominates the CTL interannual sea level along the entire BoB coastal waveguide through coastal KW propagation as well as over the eastern part of the interior BoB through RW radiation from the eastern BoB rim. The IBB process (Figures 6.20g) drives most of the sea level IAV over the western interior BoB (off the ECI). On the other hand, the WCI sea level IAV is driven by a combination of processes: ST, EQD and AFAS (Figures 6.20b,e,c). The contribution of IAS process (Figures 6.20h) to the interannual sea level in the interior AS increases westward downstream along the RW path through integration of the wind-stress curl forcing.

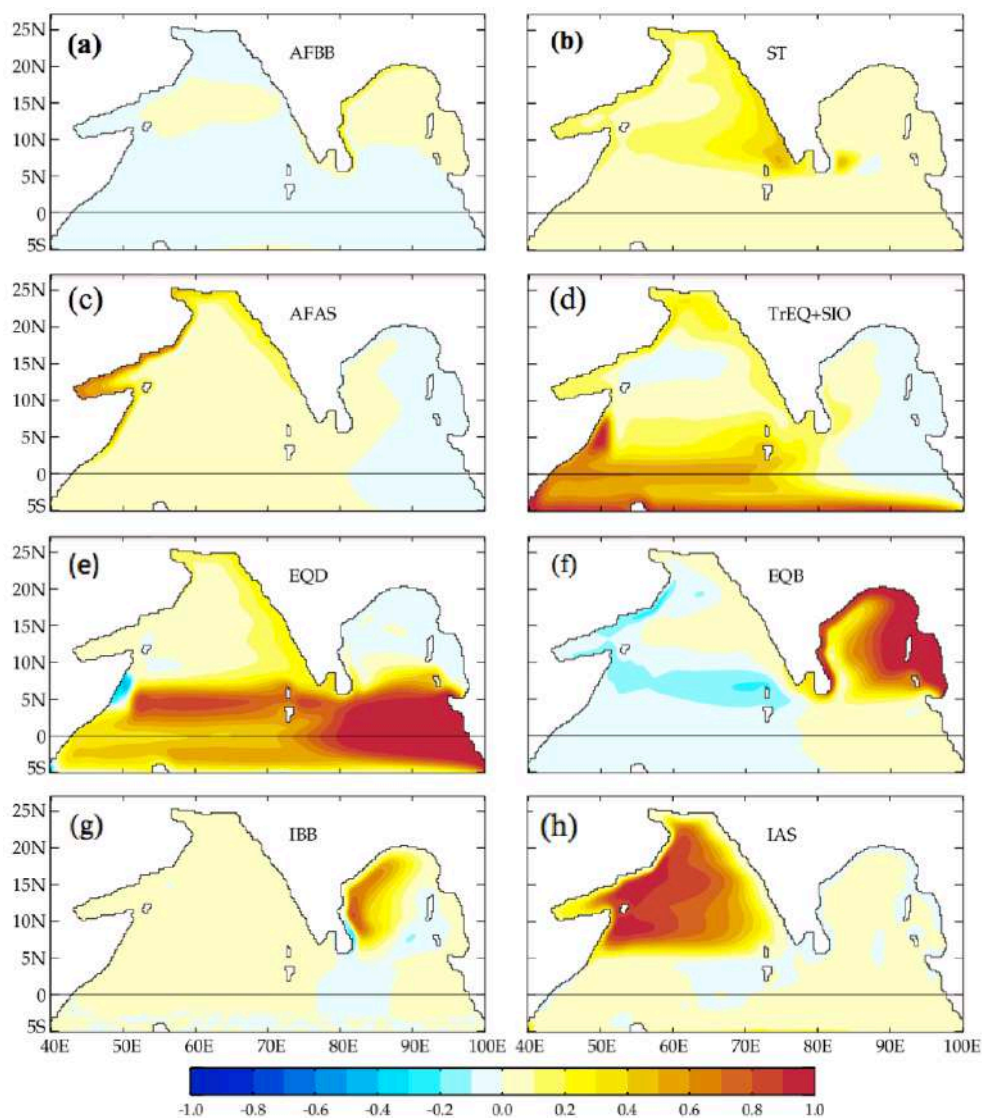


**Figure 6.20:** Contribution of each process (a) AFBB, (b) ST, (c) AFAS, (d) TrEQ + SIO, (e) EQD, (f) EQB, (g) IBB and (h) IAS to CTL interannual sea level, computed as the regression coefficients of the respective process solution to that of CTL experiment. The sum of the contributions is equal to 1 (100%) by construction. Contributions can be negative in case of a negative correlation between a given process and the total variability.

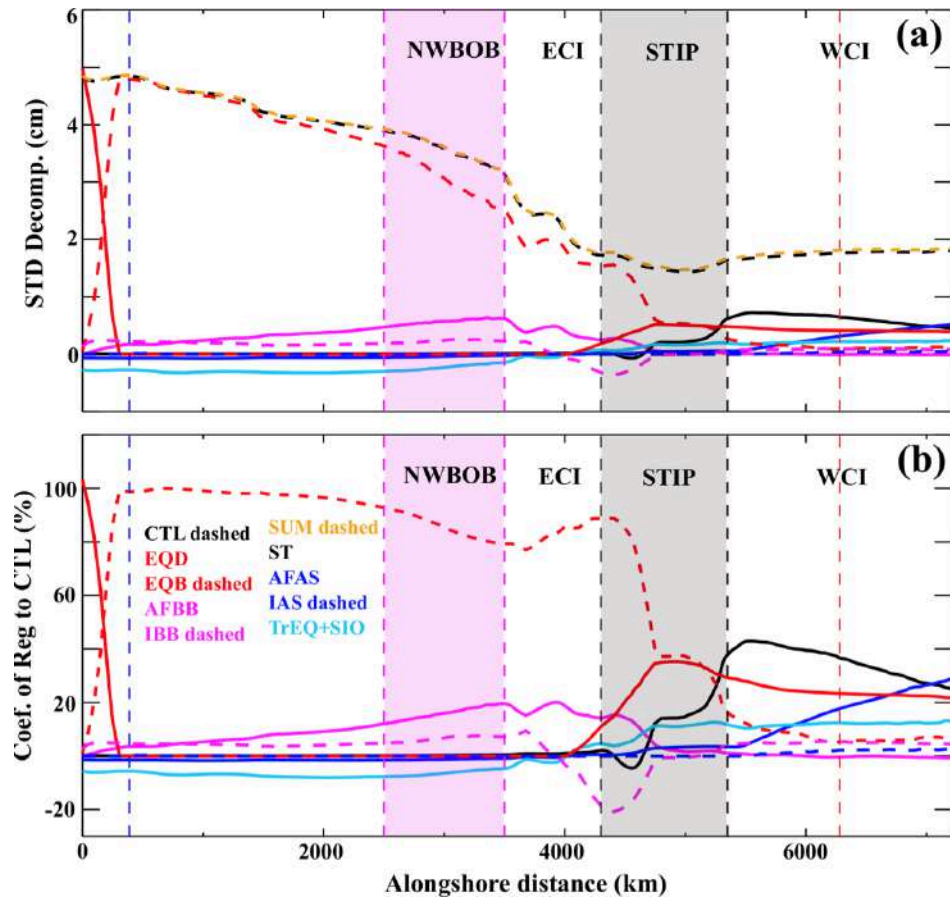


**Figure 6.21:** Similar to 5.15 and 6.11, but for interannual sea level variations. (a) Standard deviation of CTL interannual sea level and its decomposition into processes, plotted as a function of distance along the NIO coastal waveguide. The quantities are averaged over a 50-km cross-shore extent. The sum of contribution from each process (orange dashed) matches the CTL standard deviation (black dashed). (b) Regression coefficient of interannual sea level associated with each process to the CTL solution (in %), shown as a function of alongshore distance. In both the panels, the entrance of BoB waveguide (marked with a tic of same color in Figure 5.14) is indicated with dashed blue vertical line at a distance of ~390 km. The region between dashed pink vertical lines (marked with same color in 5.14) indicates the northwestern BoB, where local alongshore forcing is important. The dashed, black vertical lines (tics of same color in Figure 5.14) enclose the STIP region. The dashed, red vertical line (tic of same color in Figure 5.14) at the right extreme (~6300 km) marks the position of WCI box.

**Overview of dominant processes in the NIO coastal waveguide:** Figure 6.21 finally provides a detailed quantitative assessment of the contribution from each of the processes to the total sea level IAV along the NIO coastal waveguide (similar to Figures 5.15 for intraseasonal and 6.11 for seasonal). As shown on Figures 6.21a, the amplitude of the CTL interannual sea level gradually decreases anticlockwise along the BoB rim, from ~5 cm at the entrance of the BoB waveguide to ~3.5 cm at the northwestern BoB coast, and further to ~2 cm along the east and west coasts of India. CTL sea level IAV is largely dominated by EQB along the BoB coast: it contributes from almost 100% along

the eastern BoB coast to ~80% in the northwestern and western BoB coasts (Figure 6.21b), where alongshore forcing also contributes to some extent (up to 20%). The rather weak contribution from AFBB and IBB mainly results from the weak amplitude BoB wind forcing (Figures 6.12a,b) relative to the equatorial forcing (Figure 6.12c). The sea level IAV along the WCI results from a combination of processes, mainly ST, EQD and AFAS (Figure 6.21b). ST generally dominates CTL sea level IAV but its contribution decreases from 40-50% near the southern tip of India to 20-30% at the northern end of the WCI (Figures 6.21b), probably due to westward radiation of the RWs from the WCI. The contribution of local alongshore forcing increases progressively along the coastal KW path and is ~20% at 15°N (Figure 6.21b). EQD drives 20% of the sea level IAV along the WCI (Figure 6.20b). While the analysis shown on Figure 6.18c indicates a strong role of EQB in driving sea level IAV along the WCI, Figure 6.20f points towards a rather small contribution from EQB: this apparently small contribution stems from the fact that this process is actually in phase quadrature with CTL sea level IAV (Figure 6.18c) and hence results in a weak regression coefficient on Figure 6.20f despite its significant role.

### 6.2.5 Summary

***Process contribution to total IAV:*** This section assesses the dynamics of the NIO sea level IAV, with a particular focus along the coastal waveguide. The process decomposition of the total sea level IAV in the NIO indicates that EQB dominates (>80%) the CTL sea level IAV along the entire BoB rim. The AFBB and IBB processes have a rather modest contribution of 20% along the northwestern and western rims of the BoB, because of the weaker amplitude of the wind forcing within the BoB compared to the much stronger IOD-induced zonal winds at the equator. The WCI sea level IAV is modulated by a combination of ST, EQD and AFAS processes. The contribution from ST process to the WCI sea level IAV decreases from 40-50% near the southern tip of India to 20-30% at the northern end of the WCI. The EQD pathway has a nearly constant contribution of 20% all along the WCI. The contribution of AFAS increases from south to north, with a contribution of ~20% at 15°N.

***The IOD influence:*** EOF analysis reveals that the NIO sea level IAV is dominated by the IOD. The IOD-driven interannual sea level in the BoB waveguide does not change

sign throughout the duration of the IOD. During the entire sequence of a positive IOD, anomalous equatorial easterlies drive upwelling equatorial KWs that propagates at the eastern boundary reflection as coastal KWs along the BoB rim. On the other hand, the IOD-induced sea level anomalies along the WCI change sign, from downwelling signals during the initiation through peak stage to upwelling signal during the termination stage of a positive IOD. These two distinct regimes of IOD influence on the WCI have so far not been discussed in the literature. This arises from the fact that different processes govern the IOD-induced sea level variability on the WCI during the growth and the demise of an IOD event. During a positive IOD peak, the equatorial easterlies induce mass convergence towards the STIP region that drives downwelling coastal KWs downstream along the WCI. Boreal fall is associated with the occurrence of anoxic conditions along the WCI. The positive IOD induces downwelling sea level signals that can prevent the occurrence of anoxic conditions [Parvathi et al., 2017]. In winter, during the IOD demise, the IOD-induced winds have almost receded. The longer time scale associated with RWs propagation from the eastern to the western BoB rims and that from the eastern boundary reflection of the equatorial KWs, however, maintain the upwelling signal associated with the EQB and EQD processes for longer duration, thus yielding an IOD-induced upwelling along the WCI during the winter season. The winter-time IOD-induced signals along the WCI may influence SSTs in the south eastern AS through RW radiation from the western Indian shelf that can in turn set preconditioning for the onset of the Indian summer monsoon [Masson et al., 2005; Vinayachandran et al., 2007].

### 6.3 Comparison of sea level dynamics between timescales

**Differences in the sea level variability:** Having investigated the sea level dynamics at intraseasonal, seasonal, and interannual timescales in the previous sections, this section highlights some of the major differences between them. Earlier studies [e.g. Han et al., 2011; Shankar et al., 2010] have already discussed the sea level variability in the equatorial region at a wide range of timescales (90, 120, 180-day modes and interannual (>17 months)). The discussion here will hence focus mainly on the NIO sea level variability outside the equatorial band. Figure 6.22, which compares the spatial patterns of the sea level amplitude at intraseasonal, seasonal, and interannual timescales, indicates that their amplitudes are strikingly different in the interior BoB, along the WCI, and in the western AS. The specific differences in the sea level variability in the interior BoB and along the WCI, and the main reasons behind those differences are briefly discussed below.

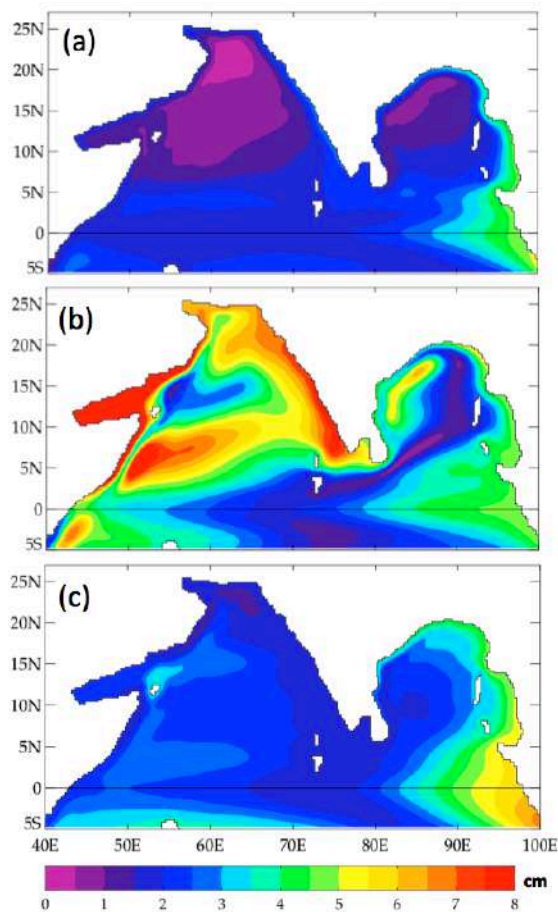


**Figure 6.22:** Standard deviation of the sea level at (a) intraseasonal, (b) seasonal, and (c) interannual timescales.

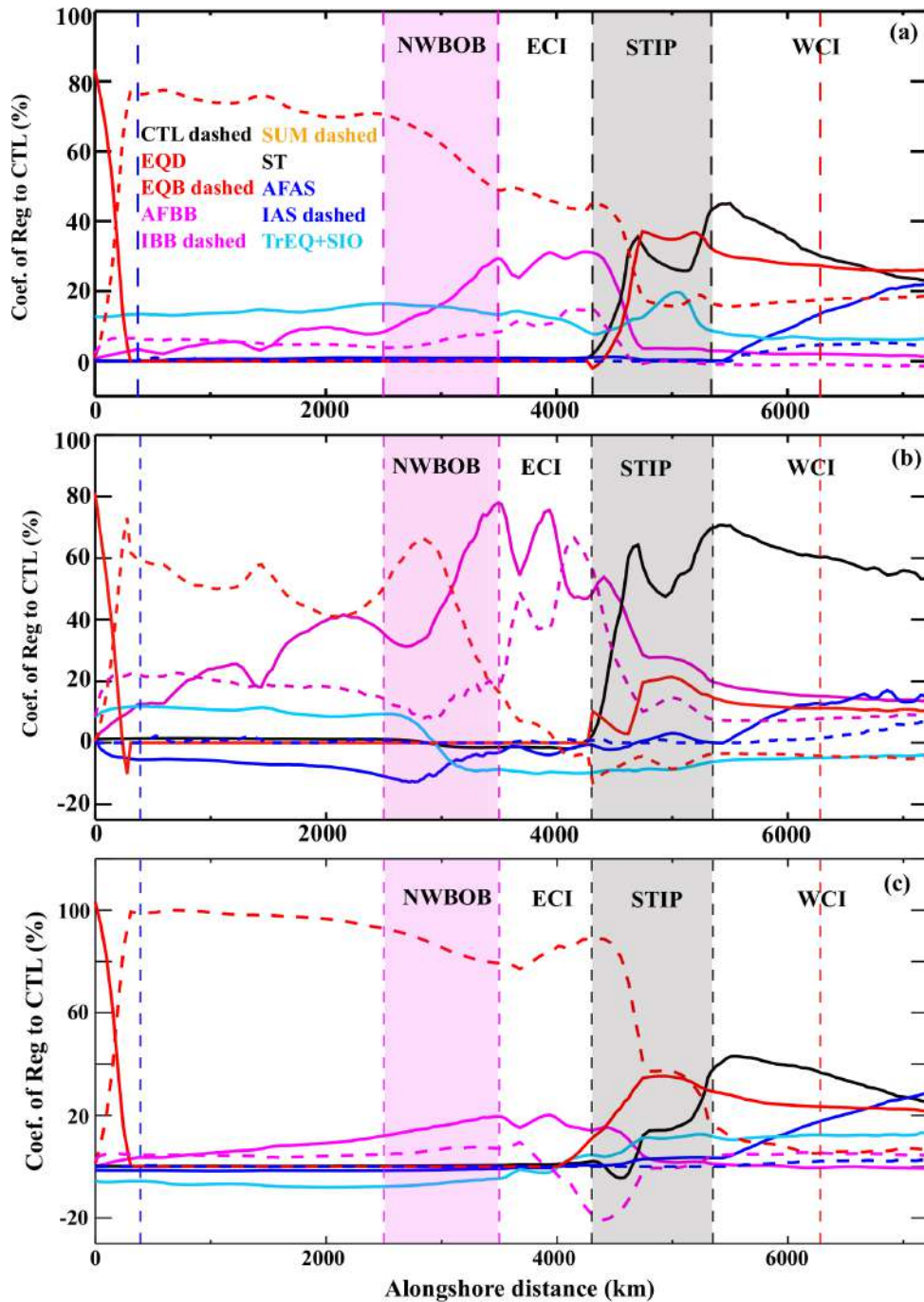


**Figure 6.23:** Regression coefficient (in %) of (a) intraseasonal, (b) seasonal, and (c) interannual sea level from each process to that in CTL as a function of distance along the NIO coastal waveguide (These panels are the same as Figures 5.15b, 6.11b and 6.21b respectively). The quantities are averaged over a 20 km cross-shore extent. The entrance of BoB waveguide (marked with a tic of same color in Figure 5.14) is indicated with dashed blue vertical line at a distance of ~390 km. The region between dashed pink vertical lines (marked with same color in 5.14) indicates the northwestern BoB where local alongshore forcing becomes important. The dashed, black vertical lines (tics of same color in Figure 5.14) enclose the STIP region. The dashed, red vertical line (tic of same color in Figure 5.14) at the right extreme (~6300 km) marks the position of WCI box.

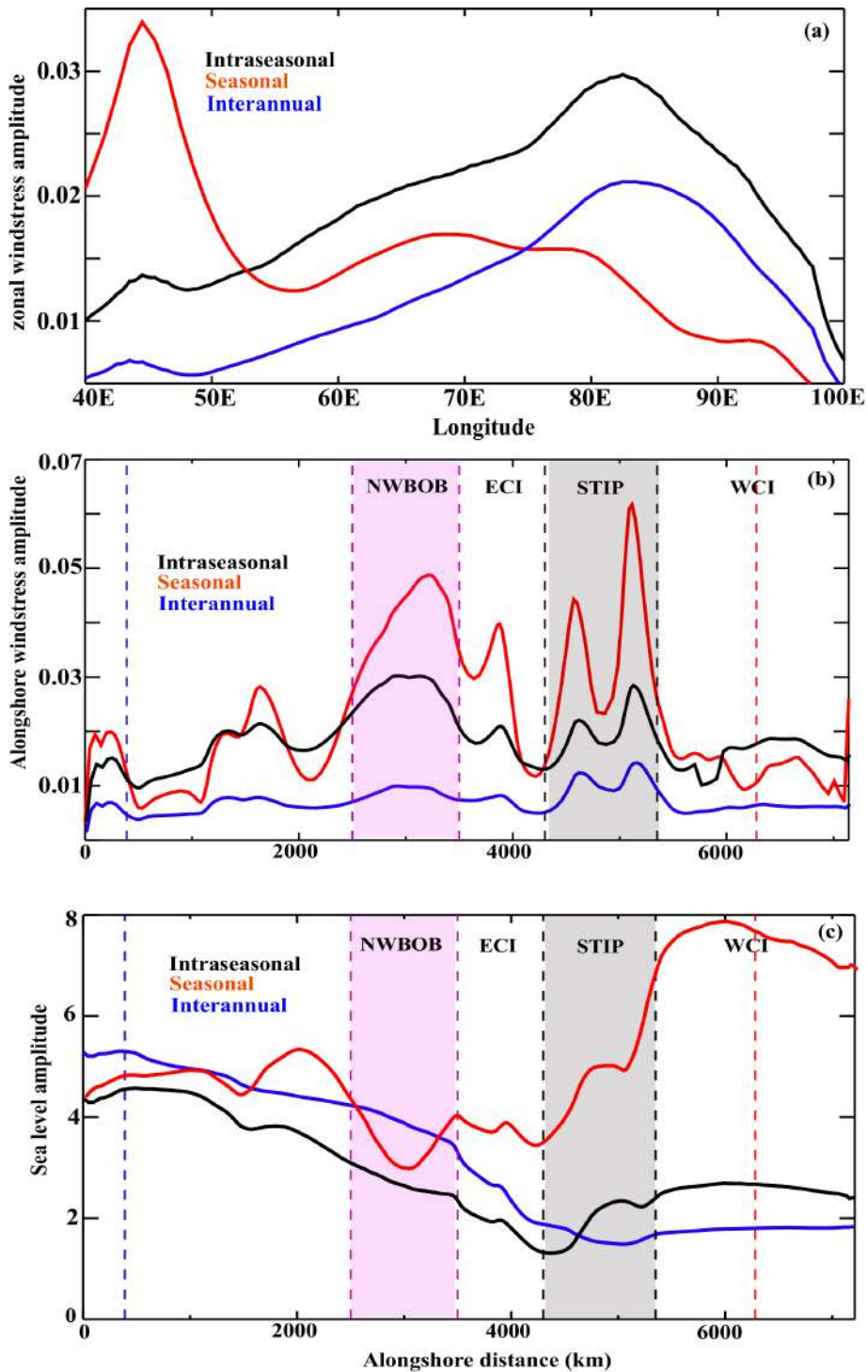


**Figure 6.24:** Standard deviation of the (a) zonal wind stress in the equatorial band ( $2^{\circ}\text{S}$ - $2^{\circ}\text{N}$ ), (b) alongshore forcing and (d) CTL sea level both as a function of distance along the NIO coastal waveguide at intraseasonal (black), seasonal (red), and interannual (blue) timescales. In panels (b) and (c), the entrance of the BoB coastal waveguide is indicated by a dashed blue vertical line at a distance of  $\sim 390$  km (marked by a blue tick in Figure 5.14). The magenta-color shaded vertical band indicates the northwestern BoB rim (coastline within the magenta ticks in Figure 5.14). The black-color shaded band (coastline between the black ticks in Figure 5.14) marks the STIP region. The dashed, red vertical (red tick in Figure 5.14) at the right extreme ( $\sim 6300$  km) marks the position of WCI box. TropFlux wind-stress product (described in Section 3.2) has been used.

**Eastern interior BoB:** The sea level variability in the eastern BoB is more confined to the eastern rim at the intraseasonal timescale (Figure 6.22a), but progressively extends westward into the interior BoB at seasonal (Figure 6.22b) and interannual (Figure 6.22c) timescales. This feature can easily be explained by the critical latitude that increases with decreasing frequency (see Section 2.1 for details), allowing the coastal sea level signals to radiate away as westward RWs more efficiently at interannual and seasonal than at intraseasonal timescales.

**Western interior BoB:** The sea level variability has an offshore maximum in the western interior BoB at the seasonal timescale, but not at other timescales. This strong seasonal variability results from the strong seasonal interior BoB forcing (Figure 6.1) related with the intense monsoonal winds. As this interior wind-stress curl forcing in the western interior BoB is far weaker at intraseasonal (Figure 5.4) and interannual (Figure 6.12) timescales, this precludes existence of an offshore maximum at these timescales.

**Coastal BoB:** The amplitude of the coastal sea level is similar (4 - 5 cm) at the three timescales along the eastern BoB coast (Figures 6.22 and 6.24c) and is dominated by the signals propagating from the equatorial region, i.e. the EQB process (Figure 6.23). This contribution is however weaker at seasonal timescale mainly because the amplitude of the zonal wind stress in the eastern equatorial IO (Figure 6.24a) is rather low at the seasonal timescale, but larger at interannual and much larger at intraseasonal timescales. At all timescales, the alongshore wind forcing (Figures 6.24b) contribution (AFBB) along the BoB rim steadily increases anticlockwise (Figure 6.23) as the sea level integrates the wind forcing along the coastal KW path. However, this process has a larger contribution to the BoB coastal sea level variability at seasonal (Figure 6.23b) than at other timescales (Figures 6.23a,c). This is likely due to the net result of stronger alongshore wind variability (Figure 6.24b) and weaker equatorial wind forcing (Figure 6.24a) at the seasonal timescale compared to other timescales. The orientation of the monsoonal winds in the northwestern rim of the BoB (which are parallel to the coast) indeed allows forcing more energetic coastal KWs at the seasonal timescale. As a result, AFBB dominates the coastal sea level variability along the northwestern and western rims of the BoB at the seasonal timescale (Figure 6.23b).

***Sea level variability along the WCI:*** The WCI sea level variability exhibits a striking difference between the three timescales (Figure 6.22). The seasonal variability is considerably larger compared to intraseasonal and interannual variability (Figures 6.22 and 6.24c). This difference largely results from the wind forcing near the southern tip of India at this timescale, with both largest alongshore forcing at this convoluted coastline (Figure 6.24b) and largest Ekman pumping velocity east of Sri Lanka (cf. Figures 5.4, 6.1, and 6.12) among all three timescales. Consequently, the contribution of ST to the WCI sea level variability is largest at the seasonal timescale (Figure 6.23b) compared to intraseasonal (Figure 6.23a) and interannual (Figure 6.23c) timescales. Finally, the newly established EQD connection for the WCI does operate at intraseasonal (Figure 6.23a) and interannual (Figure 6.23c) timescales, but is weaker at the seasonal timescale (Figure 6.23b). As noted above, the weaker zonal wind variations at the seasonal timescale in the eastern equatorial IO (Figure 6.24a) indeed results in a weaker reflected equatorial RWs, leading to weaker EQD contribution at seasonal timescale than other timescales.

## Summary and Perspectives

---

### 7.1 Thesis summary

***The subject of the thesis:*** The dynamics of the wind-driven, intraseasonal sea level variability in the northern Indian Ocean, particularly in the coastal waveguide, has been extensively investigated in this thesis. In an effort to delineate the differences in the sea level dynamics at intraseasonal timescales from that at the seasonal and the interannual timescales, the thesis goes beyond its initial scope by refining our current understanding on the sea level variability at those timescales. More specifically, this thesis addresses the following intriguing science questions: What is the relative importance of local against remote wind forcing in driving the sea level variability in the northern Indian Ocean? What are the pathways of sea level signals in the north Indian Ocean? Is there a direct connection between the equatorial waveguide and the coastal waveguide off the west coast of India at the southern tip of Sri Lanka, in addition to the previously-known *classical* connection at the eastern and western boundaries of the equatorial Indian Ocean? What are the dominant processes controlling the sea level variability in the coastal waveguide? The above issues are addressed in this thesis with the help of a linear continuously stratified model that, being linear, allows isolating the contribution of each process through sensitivity experiments. The main findings of this Ph.D. work are summarized below.

***Dominant intraseasonal equatorial remote forcing:*** The relative importance of the remote forcing from the equator and the local forcing in the Bay of Bengal and Arabian Sea in controlling the north Indian Ocean intraseasonal sea level variability has been assessed in Chapter 4. This chapter demonstrates that equatorial zonal wind fluctuations drive most of the basin-scale sea level intraseasonal variations, their contribution decreasing anticlockwise along the rim of Bay of Bengal, from 80 - 90% in the Andaman Sea to ~50% northeast of Sri Lanka, and then increasing to 60 - 70% along the west coast of India. The equatorial wind contribution to this variability is modulated seasonally. The northward shift of the atmospheric intraseasonal variability

in summer induces larger fluctuations of alongshore wind stress along the southern tip of India and Sri Lanka and on the western rim of the Bay. This results in larger intraseasonal sea level variations in the north Indian Ocean coastal waveguide as well as a larger contribution of the Bay of Bengal and Arabian Sea winds to this variability on the east (up to ~60%) and west (up to ~40%) coasts of India in that season.

***The EQD connection:*** Chapter 5 demonstrates the existence of a direct connection between the equatorial waveguide and the west coast of India at the southern tip of India and Sri Lanka. This new pathway (referred to as EQD in this thesis) allows equatorial signals to directly propagate northward along the west coast of India without transiting through the Bay of Bengal waveguide. In this scenario, the westward-propagating equatorial Rossby waves, excited by the eastern boundary reflection of the equatorial Kelvin waves, interact with the Sri Lankan landmass and set up Kelvin waves at the Sri Lankan coast. These coastal Kelvin waves travel around the Sri Lankan coast and further off the west coast of India, influencing the sea level there.

***The dynamics of intraseasonal sea level variability:*** Chapter 5 identifies hotspots of intense intraseasonal wind forcing in the northern Indian Ocean and quantifies their individual contributions to intraseasonal sea level variations. After identifying each process that can potentially influence the north Indian Ocean sea level, an innovative method to isolate them using a suite of linear model sensitivity experiments is presented. The equatorial wind forcing dominates the intraseasonal sea level variability along the rim of the Bay through the reflection at the eastern boundary and propagation of coastal Kelvin waves into the Bay (EQB process). This contribution ranges from about 80% in the Andaman Sea to about 50% on the east coast of India, where the remaining variability is largely explained by the alongshore forcing in the Bay of Bengal (AFBB process). This chapter also demonstrates that the intraseasonal sea level variability along the west coast of India is primarily driven by EQD signals (30-40%) and by the remote wind forcing *hotspot* over the southern tip of India and Sri Lanka (~30%) (ST process).

***New insights into the seasonal cycle:*** While there is a wealth of literature on the dynamics of the northern Indian Ocean at the seasonal timescale, there is no precise quantification of the relative importance of the processes contributing to the sea level

seasonal cycle. Hence, Chapter 6 revisited the dynamics of seasonal sea level variability using the same set of sensitivity experiments as in Chapter 5. In consistent with the earlier studies [e.g. McCreary et al., 1993; 1996], this chapter concludes that the EQB process dominates the seasonal sea level variations in the eastern and northern rims of the Bay of Bengal (40-60%), whereas that along the east coast of India is largely driven (~80%) by the alongshore forcing in the Bay (AFBB process) and interior Bay of Bengal wind stress curl forcing (IBB process), due to strong monsoonal winds over the Bay. The most original result of this part of the thesis is related to the large-amplitude sea level seasonal cycle along the west coast of India. Previous studies suggested that the seasonal sea level variability along the this coast was primarily driven by the remote wind forcing from the Bay and the equatorial Indian Ocean through coastal Kelvin wave propagation. This chapter demonstrates that the main driver (~60%) of the seasonal sea level variability off the west coast of India is the wind variability in a relatively small region (less than 20% of the total area of Bay of Bengal basin) near the southern tip of India and Sri Lanka (with respective contributions of ~40% by alongshore winds along this convoluted coast and ~20% by Ekman pumping induced by the strong wind stress curl off the east coast of Sri Lanka).

***New insights into the interannual sea level variability:*** Chapter 6 also revisited the dynamics of interannual sea level variations in the north Indian Ocean using the same decomposition method. The sea level interannual variability is dominated by the dominant mode of natural interannual climate variability in the Indian Ocean, namely the Indian Ocean Dipole (IOD). This thesis brings new insights on the dynamics of IOD-driven interannual sea level variations in the north Indian Ocean. During, e.g. positive IOD events, the equatorial easterly wind anomalies induce negative sea level anomalies in the eastern equatorial Indian Ocean. As already discussed in the literature [e.g. Aparna et al., 2012], those upwelling signals propagate into the Bay of Bengal coast as coastal Kelvin waves (EQB process), and dominate the negative sea level anomalies there. Along the west coast of India, however, sea level signals indicate a transition from downwelling during summer and fall to upwelling during winter. This dual influence of IOD can be tracked back to the seasonally-varying contribution of the EQB and EQD processes. For example, a positive IOD induces easterly wind anomalies near the southern tip of India and Sri Lanka during summer and fall. These winds excite downwelling coastal Kelvin waves at the southern tip of India and Sri Lanka that

dominate the interannual sea level signal along the west coast of India during the IOD onset and peak. But a fraction of the upwelling signal from the eastern equatorial Indian Ocean transits more slowly through the Bay of Bengal as off-equatorial Rossby waves, inducing a delayed negative sea level contribution (EQB process) that eventually yields negative sea level anomalies along west coast of India during winter. While the interannual sea level variability along the west coast of India is relatively weak, it is large enough to strongly influence the year-to-year variability of anoxic events in that region (Parvathi et al. 2017), hence highlighting the potential societal relevance of these results.

**Comparison of timescales:** Similarities and differences in the sea level dynamics between the intraseasonal, seasonal, and interannual timescales are also discussed in Chapter 6. A key difference is that the direct connection between the equatorial band and the west coast of India (EQD process) is important for the sea level variability along the Indian west coast at intraseasonal and interannual timescales, but not at the seasonal timescale. Other differences are related to the difference in wind patterns. The seasonal cycle wind pattern has much larger off-equatorial amplitude, yielding a much more prominent effect of off-equatorial forcing at the seasonal timescale. In particular, the alongshore and wind curl forcing in the vicinity of Sri Lanka and the southern tip of India play a key role for the large sea level seasonal cycle on the west coast of India. The intraseasonal and interannual wind stress variability patterns are quite similar. The main difference between the two timescales is linked to the critical latitude, which allows much more off-equatorial Rossby wave radiation at the interannual timescale, while signals are largely trapped at the coast at the intraseasonal timescale. As a result, signals transit much faster between the equator and west coast of India through the BoB (EQB process) at the intraseasonal than at the interannual timescale.

## **7.2 Implications and perspectives of this study**

### **7.2.1 Implications**

***Eddy-induced sea level variability:*** This thesis deals only with the wind-driven sea level variations in the perspective of the linear wave theory, and not of those induced by meso-scale eddy variability, which owe their existence to the internal instabilities. The

linear model framework used in the thesis cannot allow assessing the variability resulting from the barotropic or baroclinic instabilities. Hence the signals studied in this Ph.D. will be aliased by sea level variations associated with meso-scale eddies. While wind-forced sea level variability dominates in many regions, our results are less relevant in eddy-dominated regions such as the western Bay of Bengal and the western Arabian Sea, where a large fraction of the sea level variations arise from those nonlinearities. However, the results from this Ph.D. remain valid for the deterministic part of the sea level signal in those regions (e.g. to understand mean MJO/ISO signature).

***Coastal sea level prediction:*** The results of this Ph.D. work have important consequences. A thorough understanding of the dynamics in the north Indian Ocean coastal waveguide has direct implications for the forecasting programs, as it could lead to improved predictions of sea level and currents variability along the NIO coast. At intraseasonal timescales, the dominance of the equatorial forcing in driving the sea level variations along the coastal waveguide, especially during winter, implies that the sea level variations along the coasts of Myanmar, Bangladesh, and the west coast of India can be predicted several weeks in advance from those at the eastern equatorial Indian Ocean. It will unlikely be the case for the east coast of India, where the eddy-induced variability dominates the wind-forced signals [e.g., Durand et al., 2009].

***Implications for the Biogeochemistry:*** The shelf off the west coast of India hosts one of the largest, natural, seasonally recurring hypoxic systems of the world oceans [Naqvi et al., 2009]. During some years, the oxygen-deficient hypoxic conditions along the west coast of India become severe, leading to oxygen-depleted anoxic conditions during fall that strongly impact the coastal ecosystem and fisheries. By analysing simulations from a bio-physical coupled model, Parvathi et al. [2017] demonstrated that these interannual oxygen variations along the west coast of India are primarily controlled by the interannual thermocline variations there (Figure 7.1). This Ph.D. work demonstrates the prevalence of the IOD-related wind forcing near the southern tip of India and Sri Lanka in driving the interannual sea level variations along the west coast of India during late summer and fall through coastal Kelvin wave propagation. This relationship between the IOD and the year-to-year variations of seasonal anoxic conditions off the Indian west coast may facilitate advance warning for the possible occurrence of severe anoxic events, given that skilful predictions of mature IOD events in fall can be achieved one

to two seasons ahead [e.g. Luo et al., 2007; Shi et al., 2012; Parvathi et al., 2017]. Results of this thesis may thus have profound implications for the biogeochemistry and fisheries along the shelf off the west coast of India.

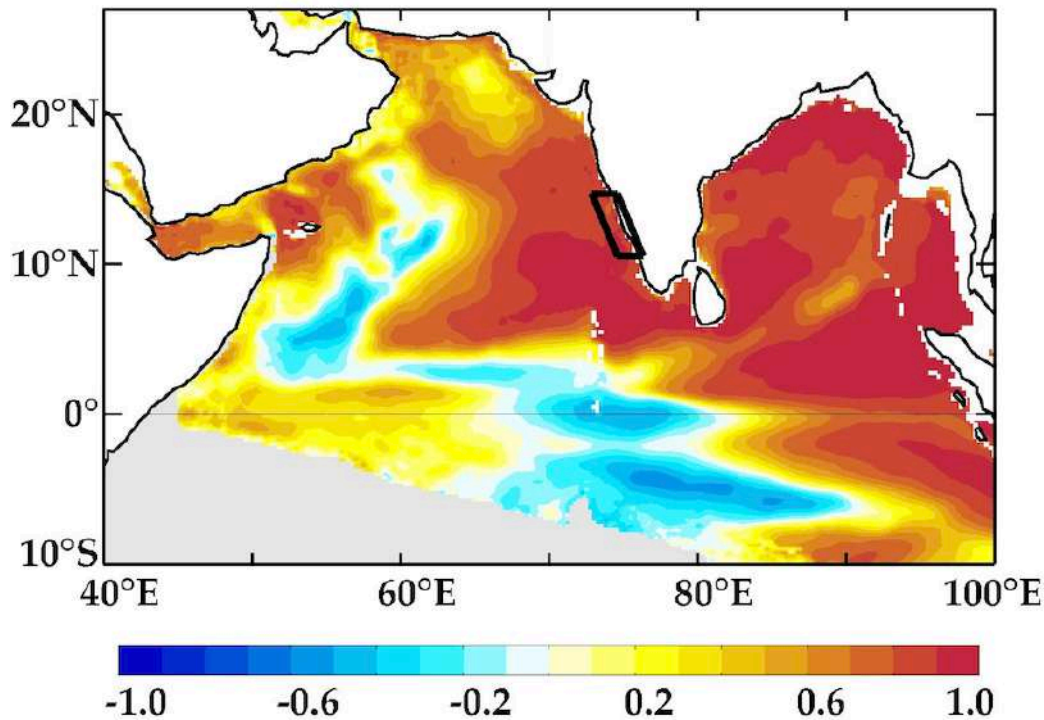


**Figure 7.1:** Spatial map of correlation between the fall (September – November) interannual anomalies of thermocline (depth of 23°C isotherm) and oxycline (depth of 100  $\mu\text{mol.L}^{-1}$ ) depths. Reproduced from Parvathi et al. [2017].

**Implications for the Indian summer monsoon:** This thesis also demonstrates the influence of the IOD on the Indian west coast sea level not only in fall but also in winter. These sea level signatures extend westward into the southeastern Arabian Sea through Rossby wave propagation [Shankar and Shetye, 1997] and modulate the thermocline. The deep thermocline associated with Lakshadweep high favours the development of high sea surface temperatures in the southeastern Arabian Sea before the summer monsoon, well known as the “Arabian Sea mini warm pool”, which influences the southwest monsoon onset date [Vinayachandran et al., 2007], and total rainfall [Masson et al., 2005]. Results from this thesis may lead to an improved understanding of the processes controlling the thermocline and sea surface temperature variability in such sensitive climatic regions, and hence to an improved predictability of the southwest monsoon onset.

## 7.2.2 Perspectives

**Long-term sea level variability and the related implications:** Understanding the processes controlling sea level variability is an important endeavour as this variable is a good proxy for the thermocline variability [Fukumori et al., 1998], which in turn affects the surface layer oxygen variability (Figure 7.1) [Parvathi et al., 2017; Prakash et al., 2013] and its productivity. The strategy adopted in this thesis should be extended to decadal and multi-decadal timescales. This should lead to a better understanding and quantification of the processes responsible for the present and future low frequency sea level variations in the Indian Ocean, either from natural or from anthropogenic origin (Figure 7.2). This would in turn contribute to better ascertain the expected evolution of the oxygen variability in the north Indian Ocean, especially along the Indian coast, and would contribute to address the following key questions: will the anoxic conditions along the west coast of India intensify in future? As indicated by Parvathi et al. [2017], will the Bay of Bengal turn anoxic in future (Figure 7.3)?

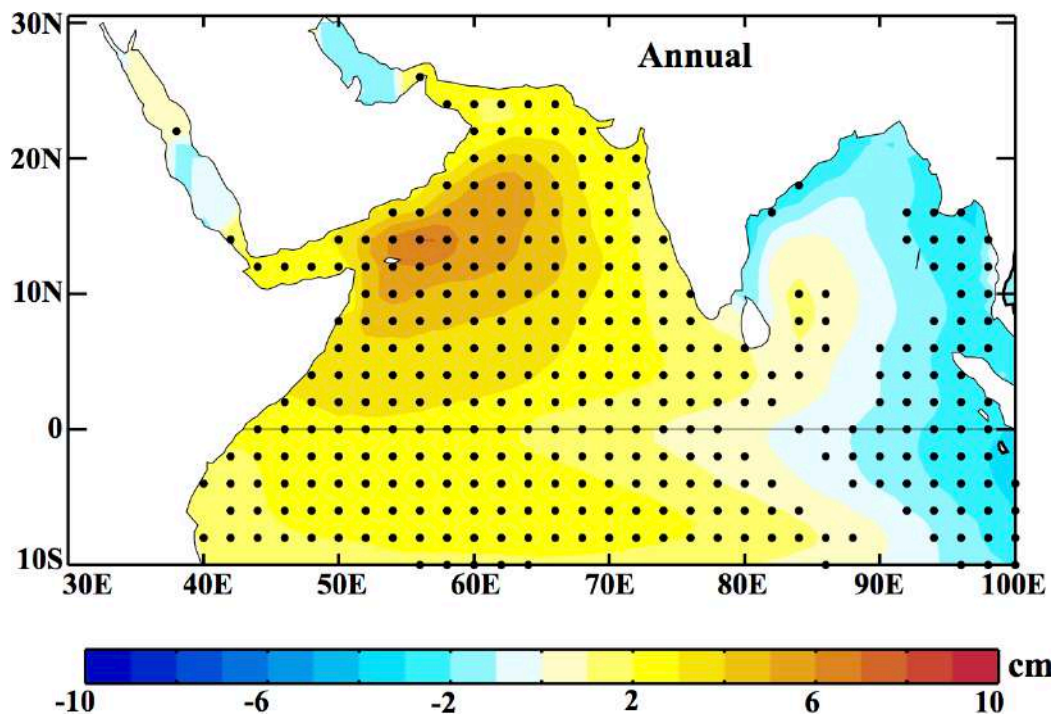


**Figure 7.2:** Multi model mean trend of sea level (cm) from the CMIP5 RCP8.5 (Coupled Model Intercomparison Project 5 – Representative Concentration Pathways 8.5) simulations. Black dots indicate 70% agreement amongst the models on the change.

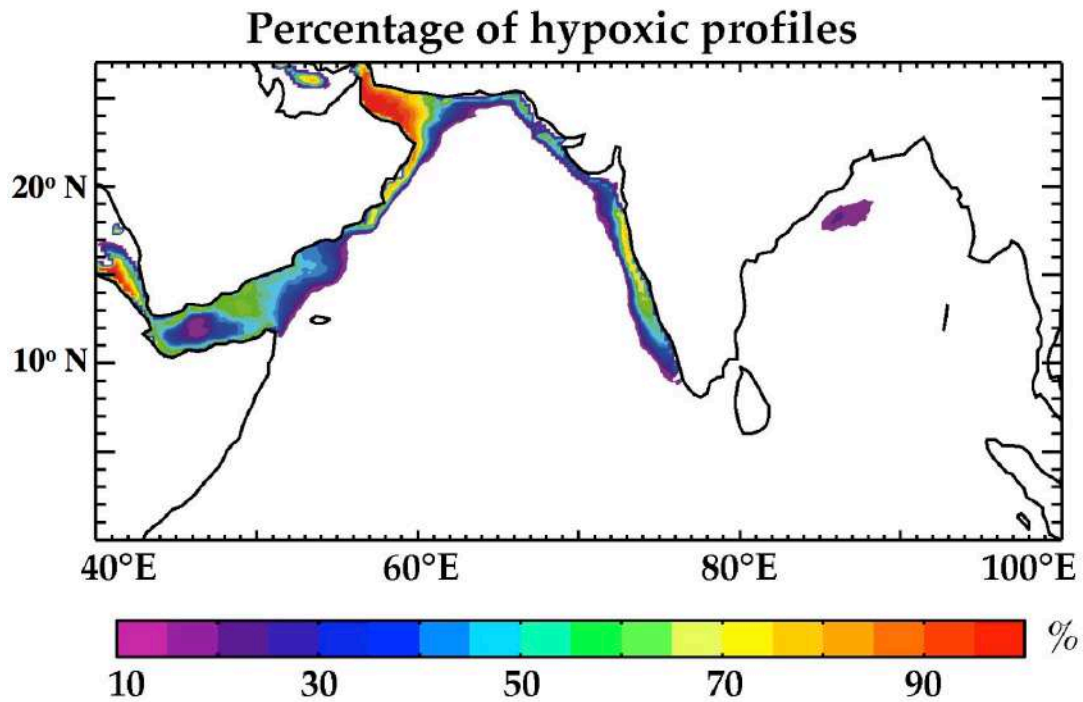


**Figure 7.3:** Map showing the percentage of hypoxic profiles during fall season in a coupled physical-biogeochemical simulation. Reproduced from Parvathi et al. [2017].

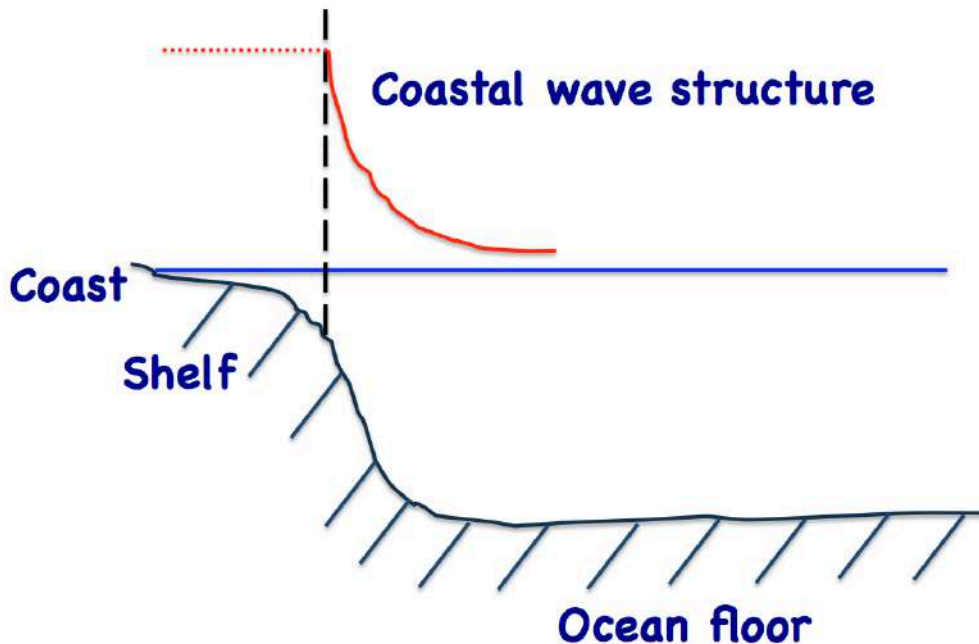


**Figure 7.4:** Schematic of the ocean floor indicating the relevance of the coastal Kelvin wave theory. The dashed black vertical line marks the shelf break, considered as a vertical wall for coastal KW propagation. The thick red line indicates the coastal KW sea level structure, which has maximum at the coast and decays exponentially away from the coast. Studying the open ocean – shelf interaction will help understanding the sea level signals on the shelf that is marked with dotted red line.

***Shelf-Open Ocean Interaction:*** This thesis explores the sea level dynamics along the coastal waveguide in the coastal Kelvin wave theory framework, which treats the shelf break as a vertical wall. It hence essentially deals with the off-shore (model coastline defines as the 200-m isobath) sea level variations as predicted by the coastal KW theory and does account neither for the shelf or near coast bathymetry, nor for the near coast processes such as the local hydrographic conditions that can significantly influence the coastal sea level. This should be kept in mind in interpreting the results of this thesis for the coastal sea level. A more detailed future plan to extend the present results towards the coast is presented below. Using a more complete linear theory of “shelf waves” that accounts for the off-shore variations in ocean depth and for the local stratification [Brink, 1982a,b; Brink and Chapman, 1987] could allow to examine how these coastal waves are modified in a more realistic context. The comparison to ocean general circulation model experiments could also be helpful in that respect. It is still unclear how these signals at the shelf break are related to the signals on the shelf or very near the coast (Figure 7.4). This is especially important for the shelf off the west coast of India, as its width increases from less than 50 km in the south to more than 200 km in the north (Figure 3.4). Exploring how this large-scale sea level variability in the open ocean is transmitted to the shelf region is a natural extension of this thesis work that will require an in-depth analysis of more accurate coastal sea level observations such as those provided by altimeter measurements from SARAL-AliKa [Verron et al., 2015]. This will in turn help to understand how the coastal waves affect the near-shore environment, not only the sea level, but also the currents and temperatures. There are a number of fine-scale processes that play a strong role on open ocean-shelf exchanges, such as internal waves, submeso-scale circulation on the shelf, tides, bottom friction, etc. Studying these open ocean - shelf interactions may also benefit from the development of a model with a nested grid of very high horizontal resolution (e.g., < 10 km) along the Indian west coast that could complement these coastal sea level observations.

## Bibliography

---

- Amol, P., Shankar, D., Aparna, S. G., Shenoi, S. S. C., Fernando, V., Shetye, S. R., Mukherjee, A., Agarvadekar, Y., Khalap, S., & Satelkar, N. P. (2012). Observational evidence from direct current measurements for propagation of remotely forced waves on the shelf off the west coast of India. *J. Geophys. Res.*, *117*, C05017, doi:10.1029/2011JC007606.
- Amol, P., Shankar, D., Fernando, V., Mukherjee, A., Aparna, S.G., Fernandes, R., Michael, G. S., Khalap, S. T., Satelkar, N. P., Agarvadekar, Y., Gaonkar, M. G., Tari, A. P., Kankonkar, A., & Vernekar, S. P. (2014). Observed intraseasonal and seasonal variability of the West India Coastal Current on the continental slope. *J. Earth Syst. Sci.*, *123*(5), 1045–1074, doi:10.1007/s12040-014-0449-5.
- Annamalai, H., Murtugudde, R., Potemra, J., Xie, S. P., Liu, P., & Wang, B. (2003). Coupled dynamics over the Indian Ocean: spring initiation of the Zonal Mode. *Deep-Sea Res. Pt. II*, *50*, 2305–2330, doi:10.1016/S0967-0645(03)00058-4.
- Aparna, S. G., McCreary, J. P., Shankar, D., & Vinayachandran, P. N. (2012). Signatures of Indian Ocean Dipole and El Niño–Southern Oscillation events in sea level variations in the Bay of Bengal. *J. Geophys. Res.*, *117*, C10012, doi:10.1029/2012JC008055.
- Beal, L. M., Hormann, V., Lumpkin, R., & Foltz, G. R. (2013). The response of the surface circulation of the Arabian Sea to monsoonal forcing. *J. Phys. Oceanogr.*, *43*(9), 2008–2022, doi:10.1175/JPO-D-13-033.1.
- Björnsson, H., & Venegas, S. A. (1997). *A manual for EOF and SVD analyses of climate data*, CCGCR Rep. 97–1, McGill University, Montréal, QC, Canada, 52 pp.
- Boulanger, J., Delecluse, P., Maes, C., & Lévy, C. (1997). Long equatorial waves in a high-resolution OGCM simulation of the tropical Pacific Ocean during the 1985–94 TOGA period. *Mon. Wea. Rev.*, *125*, 972–984, [https://doi.org/10.1175/1520-0493\(1997\)125<0972:LEWIAH>2.0.CO;2](https://doi.org/10.1175/1520-0493(1997)125<0972:LEWIAH>2.0.CO;2).
- Boulanger, J.-P., & Menkes, C. (1995). Propagation and reflection of long equatorial waves in the Pacific Ocean during the 1992–1993 El Niño. *J. Geophys. Res.*, *100*(C12), 25041–25059, doi:10.1029/95JC02956.

- Brink, K.H. (1982a). The effect of bottom friction on low-frequency coastal trapped waves. *J. Phys. Oceanogr.*, *12*, 127–133.
- Brink, K.H. (1982b). A comparison of long coastal-trapped wave theory with observations off Peru. *J. Phys. Oceanogr.*, *12*, 897–913.
- Brink, K. H., & Chapman, D. C. (1987). *Programs for computing properties of coastal-trapped waves and wind driven motions over the continental shelf and slope*. Technical report, Woods Hole Oceanographic Institution.
- Chatterjee, A., Shankar, D., McCreary Jr., J. P., & Vinayachandran, P. N. (2013). Yanai waves in the western equatorial Indian Ocean. *J. Geophys. Res. Oceans*, *118*, doi:10.1002/jgrc.20121.
- Chelton, D. B., & Schlax, M. G. (1996). Global observations of oceanic Rossby waves. *Science*, *272*, 234–238.
- Chelton B. D., Schlax, M. G., & Samelson, R. M. (2011). Global observations of nonlinear mesoscale eddies. *Progress in Oceanography*, *91*, 167-216.
- Cheng, X., Xie, S.-P., McCreary, J. P., Qi, Y., & Du, Y. (2013). Intraseasonal variability of sea surface height in the Bay of Bengal. *J. Geophys. Res.*, *118*, 816-830, doi:10.1002/jgrc.20075.
- Clarke, A. J. (1983). The Reflection of Equatorial Waves from Oceanic Boundaries. *J. Phys. Oceanogr.*, *13*, 1193–1207.
- Clarke, A. J. (2008). *An Introduction to the Dynamics of El Niño & the Southern Oscillation*. Elsevier, Academic Press.
- Clarke, A. J., & Liu, X. (1994). Interannual sea level in the northern and eastern Indian Ocean. *J. Phys. Oceanogr.*, *24*, 1224–1235.
- Currie, J. C., Lengaigne, M., Vialard, J., Kaplan, D. M., Aumont, O., Naqvi, S. W. A., & Maury, O. (2013). Indian Ocean Dipole and El Niño/Southern Oscillation impacts on regional chlorophyll anomalies in the Indian Ocean. *Biogeosciences*, *10*, 6677–6698, doi:10.5194/bg-10-6677-2013.
- Dee, D. P., Uppala, S.M., Simmons, A.J., Berrisford, P., et al. (2011). The ERA-Interim reanalysis: configuration and performance of the data assimilation system. *Q.J.R. Meteorol. Soc.*, *137*, 553–597, doi:10.1002/qj.828

- DeMott, C. A., Klingaman, N. P., & Woolnough, S. J. (2015). Atmosphere - ocean coupled processes in the Madden - Julian oscillation. *Rev. Geophys.*, *53*, 1099–1154, doi:10.1002/2014RG000478.
- Dhage, L., & Strub, P. T. (2016). Intra-seasonal sea level variability along the west coast of India. *J. Geophys. Res. Oceans*, *121*, doi:10.1002/2016JC011904.
- Durand, F., Shankar, D., Birol, F., & Shenoi, S. S. C. (2009). Spatio temporal structure of the East India Coastal Current from satellite altimetry. *J. Geophys. Res.*, *114*, C02013, doi:10.1029/2008JC004807.
- Emery, W. J., & Thomson, R. E. (1998). *Data Analysis Methods in Physical Oceanography*. 634 pp., Pergamon, Kidlington, U.K.
- Findlater, J. (1969). A major low-level air current near the Indian Ocean during the northern summer. *Q. J. R. Meteorol. Soc.*, *95*, 404, 362-380.
- Fukumori, I., Raghunath, R., & Fu, L. (1998). Nature of global large scale sea level variability in relation to atmospheric forcing: A modeling study. *J. Geophys. Res.*, *103*, 5493–5512.
- Gadgil, S., Joseph, P. V., & Joshi, N. V. (1984). Ocean-atmosphere coupling over monsoon regions. *Nature*, *312*, 141-143.
- Gill, A. E. (1982). *Atmosphere–Ocean Dynamics*. 664 pp., Academic Press, New York.
- Girishkumar, M. S., Ravichandran, M., & Han, W. (2013). Observed intraseasonal thermocline variability in the Bay of Bengal. *J. Geophys. Res. Oceans*, *118*, 3336–3349, doi:10.1002/jgrc.20245.
- Gopalakrishna, V. V., Rao, R.R., Nisha, K., Girishkumar, M.S., Pankajakshan, T., Ravichandran, M., Johnson, Z., Girish, K., Aneeshkumar, N., Srinath, M., Rajesh, S., & Rajan, C.K. (2008). Observed anomalous upwelling in the Lakshadweep Sea during the summer monsoon season of 2005. *J. Geophys. Res.*, *113*, C05001, doi:10.1029/2007JC004240.
- Goswami, B. N. (2005). *South Asian monsoon, in Intraseasonal Variability in the Atmosphere–Ocean Climate System*. edited by Lau, W. K. M., & Waliser, D. E., pp. 19– 55, Springer, Berlin.
- Han, W. (2005). Origins and dynamics of the 90-day and 30–60-day variations in the equatorial Indian Ocean. *J. Phys. Oceanogr.*, *35*, 708–728, doi:10.1175/JPO2725.1.

- Han, W., McCreary, J. P., Masumoto, Y., Vialard, J., & Duncan, B. (2011). Basin Resonances in the Equatorial Indian Ocean. *J. Phys. Oceanogr.*, *41*, 1252–1270, <https://doi.org/10.1175/2011JPO4591.1>
- Han, W., & Webster, P. J. (2002). Forcing mechanisms of sea level interannual variability in the Bay of Bengal. *J. Phys. Oceanogr.*, *32*, 216–239.
- Hanley, D.E., Bourassa, M.A., O'Brien, J.J., Smith, S.R., & Spade, E.R. (2003). A Quantitative Evaluation of ENSO Indices. *J. Climate*, *16*, 1249–1258, [https://doi.org/10.1175/1520-0442\(2003\)16<1249:AQEOEI>2.0.CO;2](https://doi.org/10.1175/1520-0442(2003)16<1249:AQEOEI>2.0.CO;2)
- Iskandar, I., & McPhaden, M. J. (2011). Dynamics of wind-forced intraseasonal zonal current variations in the equatorial Indian Ocean. *J. Geophys. Res.*, *116*, C06019, doi:10.1029/2010JC006864.
- Izumo, T., Lengaigne, M., Vialard, J., Luo, J. J., Yamagata, T., & Madec, G. (2014). Influence of Indian Ocean Dipole and Pacific recharge on following year's El Niño: interdecadal robustness. *Climate dynamics*, *42*(1-2), 291-310.
- Izumo, T., Vialard, J., Lengaigne, M., de Boyer Montegut, C., Behera, S. K., Luo, J. J., ... & Yamagata, T. (2010). Influence of the state of the Indian Ocean Dipole on the following year's El Niño. *Nature Geoscience*, *3*(3), 168.
- Jackett, D. R., & McDougall, T. J. (1995). Minimal adjustment of hydrographic profiles to achieve static stability. *J. Atmos. Ocean. Technol.*, *12*(4), 381-389.
- Jayakumar, A., Vialard, J., Lengaigne, M., Gnanseelan, C., McCreary, J. P., & Praveen Kumar, B. (2011). Processes controlling the surface temperature signature of the Madden-Julian Oscillation in the thermocline ridge of the Indian Ocean. *Clim. Dyn.*, *37*, 2217-2234, doi:1007/s00382-010-0953-5.
- Joseph, P. V., & Sijikumar, S. (2004). Intraseasonal variability of the low-level jet stream of the Asian summer monsoon. *Journal of Climate*, *17*(7), 1449-1458.
- Kantha, L. H., & Clayson, C. A. (2000). *Numerical models of oceans and oceanic processes*. In: *International Geophysics Series*, Vol. 66. Academic Press, San Diego, 940 pp.
- Kessler, W. S., McPhaden, M. J., & Weickmann, K. M. (1995). Forcing of intraseasonal Kelvin waves in the equatorial Pacific. *Journal of Geophysical Research: Oceans*, *100*(C6), 10613-10631.

- Klein, S. A., Soden, B. J., & Lau, N.-C. (1999). Remote sea surface temperature variations during ENSO: Evidence for a tropical atmospheric bridge. *J. Climate*, *12*, 917–932.
- Lau, N.-C., & Nath, M. J. (2000). Impact of ENSO on the variability of the Asian–Australian monsoons assimilated in GCM experiments. *J. Climate*, *13*, 4287–4309.
- Lawrence, D. M., & Webster, P. J. (2002). The boreal summer intraseasonal oscillation: Relationship between northward and east-ward movement of convection. *J. Atmos. Sci.*, *59*, 1593–1606.
- Le Blanc, J.-L., & Boulanger, J.-P. (2001). Propagation and reflection of long equatorial waves in the Indian Ocean from TOPEX/POSEIDON data during the 1993-1998 period. *Clim. Dyn.*, *17*, 547-557.
- Lee, C., Jones, B., Brink, K., & Fischer, A. (2000). The upper-ocean response to monsoonal forcing in the Arabian Sea: seasonal and spatial variability. *Deep Sea Research Part II: Topical Studies in Oceanography*, *47* (7-8), 1177-1226.
- Locarnini, R. A., Mishonov, A. V., Antonov, J. I., Boyer, T. P., et al. (2010). *World Ocean Atlas 2009, Volume 1: Temperature*. Levitus, S., Ed. NOAA Atlas NESDIS 68, U.S. Government Printing Office, Washington, D.C., 184 pp.
- Luo, J. J., Masson, S., Behera, S., & Yamagata, T. (2007). Experimental forecasts of the Indian Ocean dipole using a coupled OAGCM. *J. Climate*, *20*, 2178–2190.
- Luo, J. J., Zhang, R., Behera, S. K., Masumoto, Y., Jin, F. F., Lukas, R., & Yamagata, T. (2010). Interaction between El Niño and extreme Indian Ocean dipole. *Journal of Climate*, *23*(3), 726-742.
- Madhupratap, M., Gopalakrishnan, T. C., Haridas, P., & Nair, K. K. C. (2001). Mesozooplankton biomass, composition and distribution in the Arabian Sea during the Fall Intermonsoon: Implications of oxygen gradients. *Deep Sea Res., Part II*, *48*, 1345–1368.
- Masumoto, Y., Hase, H., Kuroda, Y., Matsuura, H., & Takeuchi, K. (2005). Intraseasonal variability in the upper layer currents observed in the eastern equatorial Indian Ocean. *Geophys. Res. Lett.*, *32*, L02607, doi:10.1029/2004GL021896.
- Matsuno, T. (1966). Quasi-geostrophic motion in the equatorial area. *J. Meteorol. Soc. Japan*, *44*, 25–42.

- Masson, S., Luo, J.-J., Madec, G., Vialard, J., Durand, F., Gualdi, S., Guilyardi, E., Behera, S., Delecluse, P., Navarra, A., & Yamagata, T. (2005). Impact of barrier layer on winter-spring variability of the southeastern Arabian Sea. *Geophys. Res. Lett.*, *32*, L07703, doi:10.1029/2004GL021980.
- McCreary, J. P. (1980). *Modelling wind-driven ocean circulation*. Tech. Rep., HIG-80-3, pp. 64, Hawaii Inst. of Geophys., Honolulu.
- McCreary, J. P. (1981). A linear stratified ocean model of the coastal undercurrent. *Philos. Trans. R. Soc. London A*, *302*, 385-413.
- McCreary, J. P. (1985). Modeling equatorial ocean circulation. *Ann. Rev. Fluid Mech.*, *17*, 359-409.
- McCreary, J. P., Jr., Kundu, P.K., & Molinari, R. L. (1993). A numerical investigation of dynamics, thermodynamics and mixed-layer processes in the Indian Ocean. *Prog. Oceanogr.*, *31*(3), 181–244, doi:10.1016/0079-6611(93)90002-U.
- McCreary, J. P., Han, W., Shankar, D., & Shetye, S. R. (1996). Dynamics of the East India Coastal Current: 2. Numerical solutions. *J. Geophys. Res.*, *101*, 13, 993–14,010, doi:10.1029/96JC00560.
- McPhaden, M.J., Zebiak, S.E., & Glantz, M.H. (2006). ENSO as an integrating concept in earth science. *Science*, *314*(5806), 1740–1745. doi:10.1126/science.1132588.
- Mukherjee, A., Shankar, D., Fernando, V., Amol, P., Aparna, S. G., Fernandes, R., Michael, G. S., Khalap, S. T., Satelkar, N. P., Agarvadekar, Y., Gaonkar, M. G., Tari, A. P., Kankonkar, A., & Vernekar, S. P. (2014). Observed seasonal and intraseasonal variability of the East India Coastal Current on the continental slope. *J. Earth Syst. Sci.*, *123*, 1197–1232
- Murtugudde, R., McCreary, J.P., & Busalacchi, A.J. (2000). Oceanic processes associated with anomalous events in the Indian Ocean with relevance to 1997–1998. *J. Geophys. Res.*, *105*, 3295–3306.
- Nagura, M., & McPhaden, M. J. (2012). The dynamics of wind-driven intraseasonal variability in the equatorial Indian Ocean. *J. Geophys. Res.*, *117*, C02001, doi:10.1029/2011JC007405.
- Naqvi, S. W. A., Jayakumar, D. A., Narvekar, P. V., Naik, H., Sarma, V. V. S. S., D'Souza, W., Joseph, S., & George, M. D. (2000). Increased marine production of N<sub>2</sub>O due to intensifying anoxia on the Indian continental shelf. *Nature*, *408*, 346–349.

- Naqvi, S. W. A, Naik, H., Jayakumar, D. A., Pratihary, A. K., Narvenkar, G., Kurian, S., Agnihotri, R., Shailaja, M. S., & Narvekar, P. V. (2009). Seasonal anoxia over the Western Indian continental shelf. *Geophysical Monograph Series*, 185, 10.1029/2008GM000745.
- Parvathi, V., Suresh, I., Lengaigne, M., Ethe, C., Vialard, J., Levy, M., Neetu, S., Aumont, O., Resplandy, L., Naik, H., & Naqvi, W. (2017). Positive Indian Ocean Dipole events prevent anoxia along the west coast of India. *Biogeosciences*, 14 (6), 1541-1559, <https://doi.org/10.5194/bg-14-1541-2017>.
- Perigaud, C., & Delecluse, P. (1992). Interannual sea level variations in the tropical Indian Ocean from Geosat and shallow water simulations. *J. Phys. Oceanogr.*, 23, 1916–1934.
- Philander, S. G. H. (1990). *El Niño, La Niña, and the Southern Oscillation*. 293 pp., Academic, San Diego, Calif.
- Potemra, J. T., Luther, M. E., & O'Brien, J. J. (1991). The seasonal circulation of the upper ocean in the Bay of Bengal. *J. Geophys. Res.*, 96(C7), 12667–12683, doi:10.1029/91JC01045.
- Prakash, S., Prakash, P., & Ravichandran, M. (2013). Can oxycline depth be estimated using sea level anomaly (SLA) in the northern Indian Ocean? *Remote Sensing Letters*, 4, 1097–1106, doi:10.1080/2150704X.2013.842284.
- Prasanna Kumar, S., & Prasad, T. (1996). Winter cooling in the northern Arabian Sea. *Current Science*, 71, 11, 834 – 841.
- Praveen Kumar, B., Vialard, J., Lengaigne, M., Murty, V. S. N., McPhaden, M. J., Cronin, M., Pinsard, F., & Gopala Reddy, K. (2013). TropFlux wind stresses over the tropical oceans: Evaluation and comparison with other products. *Clim. Dyn.*, 40, 2049–2071.
- Rao, A. S., Behera, S. K., Masumoto, Y., & Yamagata, T. (2002). Interannual subsurface variability in the tropical Indian Ocean with a special emphasis on the Indian Ocean Dipole. *Deep Sea Res., Part II*, 49, 1549–1572, doi:10.1016/S0967-0645(01)00158-8.
- Rao, R. R., Girish Kumar, M. S., Ravichandran, M., Rao, A. R., Gopalakrishna, V.V., & Thadathil, P. (2010). Interannual variability of Kelvin wave propagation in the wave guides of the equatorial Indian Ocean, the coastal Bay of Bengal and the southeastern Arabian Sea during 1993–2006. *Deep-Sea Research I*, 57, 1–13.

- Romea, R. D., & Allen, J. S. (1983). On vertically propagating coastal Kelvin waves at low latitudes. *J. Phys. Oceanogr.*, *13*, 1241–1254.
- Saji, N. H., Goswami, B. N., Vinayachandran, P. N., & Yamagata, T. (1999). A dipole mode in the tropical Indian Ocean. *Nature*, *401*, 360–363, 1999.
- Saraceno, M., Strub, P. T., & Kosro, P. M. (2008). Estimates of sea surface height and near-surface alongshore coastal currents from combinations of altimeters and tide gauges. *J. Geophys. Res.*, *113*, C11013, doi:10.1029/2008JC004756.
- Schott, F. A., & McCreary, J. P. (2001). The monsoon circulation of the Indian Ocean. *Prog. Oceanogr.*, *51*, 1–123.
- Schott, F. A., Xie, S.-P., & McCreary Jr. J. P. (2009). Indian Ocean circulation and climate variability. *Rev. Geophys.*, *47*, RG1002, doi:10.1029/2007RG000245.
- Senan, R., Sengupta, D., & Goswami, B. N. (2003). Intraseasonal “monsoon jets” in the equatorial Indian Ocean. *Geophys. Res. Lett.*, *30*(14), 1750, doi:10.1029/2003GL017583.
- Sengupta, D., Senan, R., Goswami, B. N., & Vialard, J. (2007). Intraseasonal variability of equatorial Indian Ocean zonal currents. *J. Clim.*, *20*, 3036–3055, doi:10.1175/JCLI4166.1.
- Shankar, D., Aparna, S. G., McCreary, J. P., Suresh, I., Neetu, S., Durand, F., Shenoi, S. S. C., & AlSaafani, M. A. (2010). Minima of interannual sea-level variability in the Indian Ocean. *Prog. Oceanogr.*, *84*(3-4), p. 225-241.
- Shankar, D., McCreary, J. P., Han, W., & Shetye, S. R. (1996). Dynamics of the East India Coastal Current: 1. Analytic solutions forced by interior Ekman pumping and local alongshore winds. *J. Geophys. Res.*, *101*(13), 975–13,991.
- Shankar, D., & Shetye, S. R. (1997). On the dynamics of the Lakshadweep high and low in the southeastern Arabian Sea. *J. Geophys. Res.*, *102*, 12551–12562, doi:10.1029/97JC00465.
- Shankar, D., Vinayachandran, P. N., & Unnikrishnan, A. S. (2002). The monsoon currents in the North Indian Ocean. *Prog. Oceanogr.*, *52*(1), 63–120, doi:10.1016/S0079-6611(02)00024-1.
- Shenoi, S. S. C., Saji, P. K., & Almeida, A. M. (1999). Near-surface circulation and kinetic energy in the tropical Indian Ocean derived from Lagrangian drifters. *J. Mar. Res.*, *57*, 885–907.

- Shetye, S. R. (1998). West India Coastal Current and Lakshadweep high/low. *Sadhana*, 23, 637–651.
- Shetye, S. R., Gouveia, A. D., Shenoi, S. S. C., Michael, G. S., Sundar, D., Almeida, A. M., & Santanam, K. (1991a). The coastal current off western India during the northeast monsoon. *Deep Sea Res.*, 38, 1517–1529.
- Shetye, S. R., Gouveia, A. D., Shenoi, S. S. C., Sundar, D., Michael, G. S., Almeida, A. M. & Santanam, K. (1990). Hydrography and circulation off the west coast of India during the southwest monsoon 1987. *J. Mar. Res.*, 48, 359–378.
- Shetye, S. R., & Shenoi, S. S. C. (1988). Seasonal cycle of surface circulation in the coastal North Indian Ocean. *Proc. Indian Acad. Sci. (Earth Planet Sci.)*, 97, 53–62.
- Shetye, S. R., Shenoi, S. S. C., Gouveia, A. D., Michael, G. S., Sundar, D., & Nampoothiri, G. (1991b). Wind-driven coastal upwelling along the western boundary of Bay of Bengal during southwest monsoon. *Cont. Shelf Res.*, 11, 1397–1408.
- Shetye, S. R., Gouveia, A. D., Shenoi, S. S. C., Sundar, D., Michael, G. S., & Nampoothiri, G. (1993). The western boundary current of the seasonal subtropical gyre in the Bay of Bengal. *J. Geophys. Res.*, 98, 945–954.
- Shetye, S. R., Gouveia, A. D., Shankar, D., Shenoi, S. S. C., Vinayachandran, P. N., Sundar, D., Michael, G. S., & Nampoothiri, G. (1996). Hydrography and circulation in the western Bay of Bengal during the northeast monsoon. *J. Geophys. Res.* 101, 14011–14025.
- Shetye, S. R., Suresh, I., Shankar, D., Sundar, D., Jayakumar, S., Mehra, P., Prabhudesai, R. G., & Pednekar, P. S. (2008). Observational evidence for remote forcing of the West India Coastal Current. *J. Geophys. Res.*, 113, C11001, doi:10.1029/2008JC004874.
- Shi, L., Hendon, H. H., Alves, O., Luo, J.-J., Balmaseda, M., & Anderson, D. (2012). How predictable is the Indian Ocean Dipole? *Mon. Weather Rev.*, 140, 3867–3884.
- Singh, O. P. (2002). Interannual variability and predictability of sea level along the Indian Coast. *Theor. Appl. Climatol.*, 72, 11–28.
- Smith, W.H. F., & Sandwell, D.T. (1997). Global sea floor topography from satellite altimetry and ship depth soundings. *Science*, 277, 5334.

- Srinivas, K., Kumar, P. K. D., & Revichandran, C. (2005). ENSO signature in the sea level along the coastline of the Indian subcontinent. *Indian J. Mar. Sci.*, *34*, 225–236.
- Suresh, I., Vialard, J., Izumo, T., Lengaigne, M., Han, W., McCreary, J., & Muraleedharan, P. M. (2016). Dominant role of winds near Sri Lanka in driving seasonal sea level variations along the west coast of India. *Geophys. Res. Lett.*, *43*, doi:10.1002/2016GL069976.
- Suresh, I., Vialard, J., Lengaigne, M., Han, W., McCreary, J., Durand, F., & Muraleedharan, P. M. (2013). Origins of wind-driven intraseasonal sea level variations in the North Indian Ocean coastal waveguide. *Geophys. Res. Lett.*, *40*, 5740–5744, doi:10.1002/2013GL058312.
- Tozuka, T., Yokoi, T. & Yamagata, T. (2010). A modeling study of interannual variations of the Seychelles Dome. *J. Geophys. Res.*, *115*, C04005, doi:10.1029/2009JC005547.
- Trenberth, K.E., Branstator, G.W., Karoly, D., Kumar, A., Lau N-C., & Ropelewski, C. (1998). Progress during TOGA in understanding and modeling global teleconnections associated with tropical sea surface temperatures. *J. Geophys. Res.*, *103*(C7), 14291–14324, doi:10.1029/97JC01444.
- Verron, J., Sengenes, P., Lambin, J., Noubel, J., Steunou, N., Guillot, A., Picot, N., Coutin-Faye, S., Sharma, R., Gairola, R. M., Raghava Murthy, D. V. A., Richman, J. G., Griffin, D., Pascual, A., Rémy, F., & Gupta, P. K. (2015). The SARAL/AltiKa Altimetry Satellite Mission. *Marine Geodesy*, *38*, DOI: 10.1080/01490419.2014.1000471
- Vialard, J., Drushka, K., Bellenger, H., Lengaigne, M., Pous, S., & Duvel, J. P. (2013). Understanding Madden–Julian-induced sea surface temperature variations in the north western Australian Basin. *Clim. Dyn.*, *41*, 3203–3218.
- Vialard, J., Jayakumar, A., Gnanaseelan, C., Lengaigne, M., Sengupta, D., & Goswami, B. N. (2012). Processes of 30–90 days sea surface temperature variability in the northern Indian Ocean during boreal summer. *Clim. Dyn.*, *38*, 1901. doi:10.1007/s00382-011-1015-3.
- Vialard, J., Shenoi, S. S. C., McCreary, J. P., Shankar, D., Durand, F., Fernando, V., & Shetye, S. R. (2009). Intraseasonal response of the northern Indian Ocean coastal waveguide to the Madden-Julian oscillation. *Geophys. Res. Lett.*, *36*, L14606, doi:10.1029/2009GL038450.

- Vinayachandran, P. N., Shankar, D., Kurian, J., Durand, F., & Shenoi, S. S. C. (2007). Arabian Sea mini warm pool and the monsoon onset vortex. *Curr. Sci.*, *93*(2), 203–214.
- Wang, C., & Picaut, J. (2004). Understanding ENSO physics - A review, in Earth's Climate: The Ocean-Atmosphere Interaction. *Geophys. Monogr. Ser.*, vol. 147, edited by Wang, C., Xie, S.-P., & Carton J. A., pp. 21–48, AGU, Washington, D. C.
- Webber, B. G., Matthews, A. J., Heywood, K. J., & Stevens, D. P. (2012). Ocean Rossby waves as a triggering mechanism for primary Madden–Julian events. *Q. J. R. Meteorol. Soc.*, *138*(663), 514–527, doi:10.1002/qj.936.
- Webster, P.J., Moore, A.M., Loschnigg, J. P., & Leben, R.R. (1999). Coupled oceanic–atmospheric dynamics in the Indian Ocean during 1997– 98. *Nature*, *401*, 356–360.
- Wheeler, M.C., & Hendon, H. H. (2004). An All-Season Real-Time Multivariate MJO Index: Development of an Index for Monitoring and Prediction. *Mon. Wea. Rev.*, *132*, 1917–1932.
- Wolter, K., & Timlin, M. S. (1998). Measuring the strength of ENSO events: How does 1997/98 rank? *Weather*, *53*, 315–324. doi:10.1002/j.1477-8696.1998.tb06408.x
- Xie, S. P., Hu, K., Hafner, J., Tokinaga, H., Du, Y., Huang, G., & Sampe, T. (2009). Indian Ocean capacitor effect on Indo–western Pacific climate during the summer following El Niño. *Journal of Climate*, *22*(3), 730-747.
- Yamagata, T., Behera, S. K., Luo, J. J., Masson, S., Jury, M. R., & Rao, S. A. (2004). Coupled ocean-atmosphere variability in the tropical Indian Ocean. *Geoph. Monog. Series*, *147*, 189–211, doi:10.1029/147GM12.
- Yu, L., O'Brien, J. J., & Yang, J. (1991). On the remote forcing of the circulation in the Bay of Bengal. *J. Geophys. Res.*, *96*(C11), 20449–20454, doi:10.1029/91JC02424.
- Zhang, C. (2005). Madden-Julian Oscillation. *Rev. Geophys.*, *43*, RG2003, doi:10.1029/2004RG000158.
- Zhang, C. (2013). Madden–Julian oscillation: Bridging weather and climate. *Bulletin of the American Meteorological Society*, *94*(12), 1849-1870.
- Zhang, C., & Dong, M. (2004). Seasonality of the Madden-Julian Oscillation. *J. Clim.*, *17*, 3169-3180.